CHARACTERIZATION OF A LITHIUM NIOBATE PIEZOELECTRIC TRANSFORMER

A Dissertation
Presented to
The Faculty of the Graduate School
University of Missouri

In Partial Fulfillment
Of the Requirements for the Degree

Doctor of Philosophy

By

JAMES A. VANGORDON

Dr. Scott D. Kovaleski, Dissertation Supervisor

MAY 2014

The undersigned, appointed by the Dean of the Graduate School, have examined the dissertation entitled

CHARACTERIZATION OF A LITHIUM NIOBATE PIEZOELECTRIC TRANSFORMER

presented by James A. VanGordon,

a candidate for the degree of Doctor of Philosophy in Electrical Engineering, and hereby certify that in their opinion it is worthy of acceptance.

_____
Dr. Scott D. Kovaleski, Dissertation Advisor
Electrical and Computer Engineering

_____
Dr. Jae Wan Kwon
Electrical and Computer Engineering

_____
Dr. Robert A. Winholtz
Mechanical and Aerospace Engineering

_____
Dr. Gregory E. Dale
Los Alamos National Laboratory
University of Missouri Graduate Faculty

ACKNOWLEDGEMENTS

TABLE OF CONTENTS

LIST OF FIGURES

LIST OF TABLES

1. Introduction

Introduction

Applications

Particle accelerators range in size from linear accelerators that are miles long to laser-plasma accelerators that are a few millimeters long [1], [2]. These systems can be used as components for photon, neutron, or charged-particle sources or subatomic particle physics studies [1]–[5]. Photon sources have applications ranging from medical x-rays to cargo interrogation [4], [6]. Neutron sources can also be used for oil-well logging or cancer therapy in addition to cargo interrogation [4], [7], [8]. All of these accelerators have a subsystem that generates the required accelerating potential for the particles to reach the desired energy, but high-voltage sources can be heavy and bulky components. The desire for compact, low-complexity accelerators increases as the applications for this technology become more diverse and widespread. The piezoelectric transformer is a compact, high-voltage source that can be used for some of these accelerator systems.

Piezoelectric Transformers

Piezoelectric devices use the piezoelectric effect to induce a stress in a material from an applied electric field, or vice versa [9], [10]. This effect is commonly used in devices such as stepper motors, precise optical positioning mounts, and various transducers [11]–[14]. These devices have the advantages of being compact, low power, and precise. Common piezoelectric materials include quartz, lithium niobate, lithium tantalate, and lead zirconate titanate (PZT) [9].

Another piezoelectric device uses both the direct piezoelectric effect and the converse piezoelectric effect together to create a voltage transformation similar to that of a traditional ferromagnetic transformer [15]–[17]. These devices, known as piezoelectric transformers (PTs), come in different geometries and use different modes of operation. Two of the most common are the radial mode discs and the length-extensional mode bars [15]–[20]. Unlike traditional transformers which require mutual magnetic flux linkage between two coils to transform an ac voltage, PTs use the vibrational resonance from the piezoelectric effect to transform the voltage [15]–[17]. PTs can be used to step voltages up or down like a traditional ferromagnetic transformer [17]. For a PT that operates in the length-extensional mode, an rf voltage is applied to the input electrodes and a longitudinal mechanical vibration is produced in the crystal. The length-extensional displacement of the material creates high electric fields in the crystal via the converse piezoelectric effect. These electric fields can create high voltages at the output electrodes of the PT [17], [19], [20]. PTs also have the advantage of compact size, low mass, and high efficiency [17].

Investigations have been performed to characterize various geometries and configurations of the PT to maximize the transformer ratio for these devices [21]–[24]. Many of these studies used the PT as a voltage source with voltage gains less than a few hundred [17], [25], while higher transformation ratios are produced for applications such as compact particle accelerators [19], [20], [26]. PTs used for accelerating charged-particle beams have produced voltage transformation ratios in excess of 10,000 [27]. Additionally, the electrical load connected to the output of the PT can have a significant impact on the output of the PT regardless of the magnitude of the transformation ratio [9], [28]–[30]. This dissertation presents modeling and experimental results to characterize a lithium niobate piezoelectric transformer by modifying boundary conditions such as electrical loading and ambient pressure.

Characterization Approach

The primary application of the PTs presented in this dissertation was the acceleration of charged particle beams. Therefore, the PTs were predominantly characterized under electron beam diode loads. External variations such as parasitic load impedance and electric fields were controlled to prevent altering the high-voltage PT operating conditions. Although traditional electrical measurement techniques could be used at the input of the piezoelectric transformer, ultra high-impedance diagnostics had to be used at the output of the PT.

Optical methods of characterizing PTs would limit the reduction in voltage transformation inherent with conventional low-impedance electrical diagnostics. Piezoelectric materials are regularly used as nonlinear optical modulators [31]–[33]. The induced stresses and electric fields due to an externally applied signal modify the

refractive indices of the material based on the photoelastic and electro-optic effects. The modified refractive indices affect the ordinary and extraordinary wave components of an optical wave propagating through the material [34]. While the use of piezoelectric, nonlinear optical components is well understood for phase modulation and polarization modulation, fewer studies have been done to use the photoelastic and/or electro-optic effects to determine stresses or electric fields in resonating crystals [31]–[33], [35], [36].

Norgard and Kovaleski previously evaluated the use of the electro-optic effect to analyze a piezoelectric transformer using the half-wave voltage [36]. This analysis demonstrated that optical diagnostics can be useful for characterizing PTs. However, Norgard and Kovaleski's previous analysis did not include the photoelastic effects that are present in a resonant piezoelectric device. Additionally, the method of using the half-wave voltage is only valid for a constant internal stress, electric field, temperature, et cetera [36]. The half-wave voltage would be different along the length of the PT due to varying magnitudes of internal electric field and stress. As such, the half-wave voltage method is only useful when analyzing a particular point along the length of the PT as was done by Norgard and Kovaleski.

This work suggests an extension of Norgard and Kovaleski's previous analysis that incorporates both the electro-optic and photoelastic effects. The method presented is capable of determining the values of the internal stress, electric field, and electric potential at any point along the length of an operating PT. Rather than using the half-wave voltage that is dependent on the operating conditions, closed-form equations were derived based on the piezoelectric constitutive equations and equations that describe both the electro-optic and photoelastic effects. Detailed presentations of both the

mathematical formulation and experimental setup for the optical diagnostic are given. Simulated and measured values are also presented for the stress and electric field at different positions along the length of the PT for varied PT boundary conditions.

Dissertation Overview

Chapter 2 discusses the theory of piezoelectric transformer operation and different models that were used for modeling the PT. Specifically, a Matlab program was used to analyze the effects of different electrical loads on the operation of the PT via a one-dimensional model [9], [28], [37], and COMSOL Multiphysics was used to provide three-dimensional electrical modeling of the PT for varied electrical loads [38]. Chapter 3 covers the setup of the experiments that were performed to characterize the PT. Descriptions of PT preparation, high-voltage output circuit design, electron-beam load testing, and electric field shaper design are presented. Chapter 4 covers the design of all diagnostics that were used. Specifically, the bremsstrahlung x-ray, optical, and quality factor diagnostics are presented. Chapter 5 presents experimental results such as PT internal stress and electric field, output voltage, and resonant frequency drift. Least-squares curve fitting was used to compare experimental results to the modeling results from Chapter 2. Chapter 6 summarizes and concludes the results presented in the dissertation. Chapter 7 suggests future work based on the findings of this research.

2. Theory and Modeling

A one-dimensional model of the piezoelectric transformer (PT) was created to further analyze the experimental data. This model accounted for variations in a parallel *RC* load impedance to look at the effects of impedance on PT voltage transformation ratio. Additionally, finite-element modeling was performed in COMSOL Multiphysics to analyze the change in output voltage for varying positions of the PT for the electron-beam diode experiments. The 1-D model provided approximate solutions that were less computationally intensive, and the 3-D model provided higher fidelity results that more closely matched experimental results for a wider range of electrical loading. The PT modeling was necessary to predict the nonlinear behavior of the device.

Theory

Piezoelectric Effect

Figure 2.1 shows several of the physical properties of crystals and how they are related to one another [39]. Electrical, mechanical, and thermal variables that can be

directly modified as boundary conditions to the crystal are shown as the outermost corners of the triangle as electric field, stress, and temperature, respectively. The inner triangle consists of variables that cannot be manipulated externally, but are directly related to those variables in the outermost triangle. Arrows denote physical phenomena that link each of the variables. Also denoted is the corresponding tensor rank in parenthesis or square brackets for the variables or material coefficients, respectively. Although mechanical vibration due to the piezoelectric effect can affect the temperature or vice versa, only the electromechanical effects of the crystal are of interest in this work.

An applied stress or electric field can initiate an electromechanical response in a crystal due to the direct or converse piezoelectric effect, respectively. An applied stress causes a compression of the crystal, resulting in the electric flux density change due to the polarization of the crystal lattice. An applied electric field modifies the polarization of the crystal lattice which results in a mechanical displacement to equilibrate the relative positions of bound charge in the lattice. The dependence of mechanical displacement on a polarization of the crystal lattice means that no crystal with a center of symmetry can exhibit the bulk piezoelectric effect. These effects are related by the piezoelectric constitutive equations. The stress-charge and strain-charge forms of these equations are shown consecutively in Equation 2.1 to Equation 2.4 with variable definitions given in Table 2.1 [9]. Because the direct and converse piezoelectric effects directly affect the variables in both equations as shown in Figure 2.1, neither equation can be solved independently.
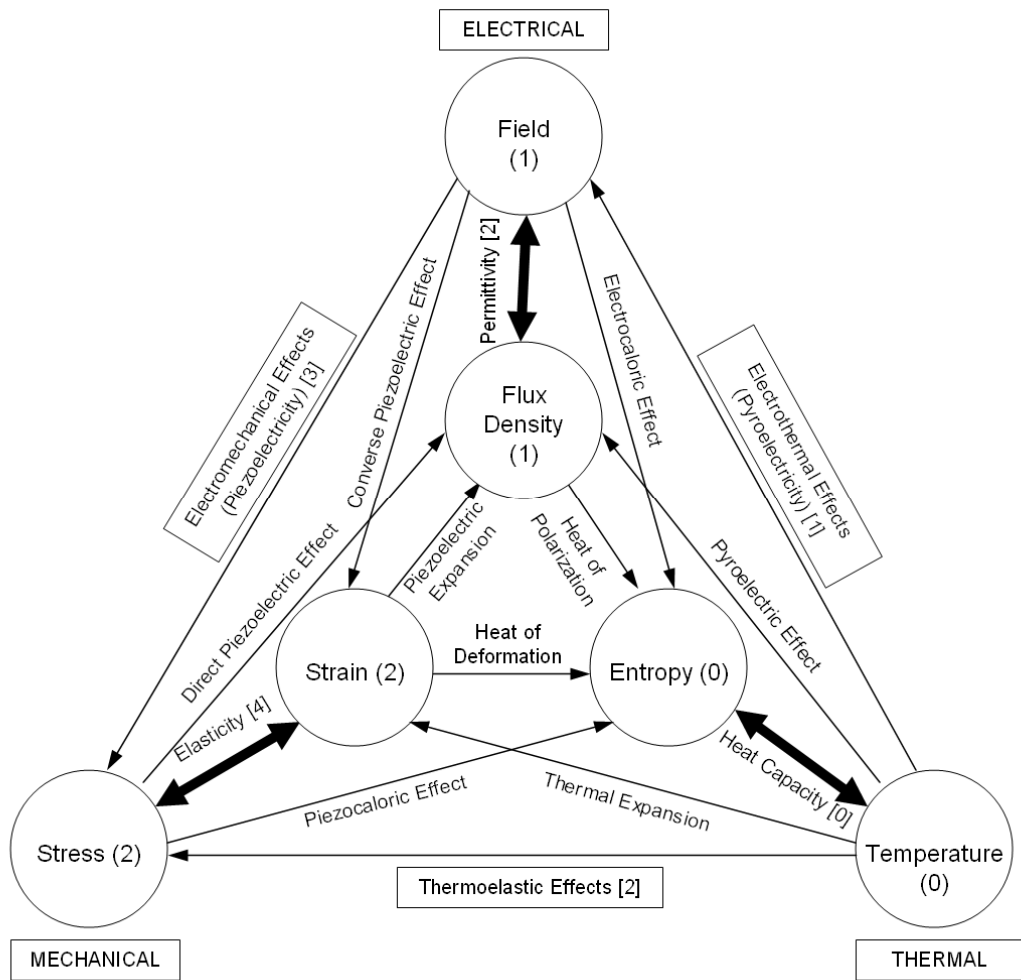
Figure 2.1: Diagram of the physical properties of crystals. Electrical, mechanical, and thermal effects are shown. Variables are shown in the circles while effects are denoted by arrows. The outer triangle includes variables that can be directly affected via the boundary conditions of the crystal. Tensor ranks of variables are shown in parenthesis while tensor ranks of effects are shown in square brackets [39].

$$T_{ij} = c_{ijkl} S_{kl} + e_{kij} E_k$$

Equation 2.1

$$D_i = e_{ijk} S_{jk} + \varepsilon_{ij}^S E_j$$

Equation 2.2

$$S_{ij} = s_{ijkl} T_{kl} + d_{kij} E_k$$

Equation 2.3

$$D_i = d_{ijk} T_{jk} + \varepsilon_{ij}^T E_j$$

Equation 2.4

Piezoelectric Transformer

A diagram of the lithium niobate piezoelectric transformer under test is shown in Figure 2.2. The PT was 100 mm long, 10 mm wide, and 1.5 mm thick. In Figure 2.2 axes x and y correspond to the crystallographic $+a_1$ and $+a_2$ axes, respectively, while the z axis corresponds to the crystallographic $+c$ axis [40]. Electroded regions in Figure 2.2 are denoted by the darkened areas and were made using silver paint. The input electrodes on the top and bottom surfaces were 50 mm long and 10 mm wide while the output

Table 2.1: Definition of variables used in the 1-D model derivation.

Variable	Definition	Units
V_1	voltage applied across the input electrodes	V
V_2	voltage generated across the load impedance	V
I_1	input current	A
I_2	output current	A
Q_1	charge on the input electrode at $x_3 = h$	C
Q_2	charge on the output electrode at $x_2 = b$	C
Z_L	load impedance	Ω
R_L	load resistance	Ω
C_L	load capacitance	F
x_1	position along the global x-axis	m
x_2	position along the global y-axis	m
x_3	position along the global z-axis	m
l	length of the PT	m
w	width of the PT	m
h	thickness of the PT	m
S	strain	—
T	stress	Pa
E	electric field	V/m
D	electric flux density	C/m^2
ϕ	electric potential	V
ρ	mass density	kg/m^3
u	mechanical displacement	m
t	time	s
ω	angular frequency	rad/s

Variable	Definition	Units
f	applied body force	N
s	elastic compliance coefficients	m^2/N
c	elastic stiffness coefficients	N/m^2
d	piezoelectric strain coefficients	C/N
e	piezoelectric coefficients	C/m^2
ε^S	permittivity with respect to constant strain	F/m
ε^T	permittivity with respect to constant stress	F/m
k	electromechanical coupling coefficient	—
Q_m	input mechanical quality factor	—
δ_m	mechanical loss factor	—
γ	dielectric loss factor	—

Figure 2.2: Diagram of the dimensions and rotation of the piezoelectric transformer.

electrode on the end was 10 mm long and 1.5 mm wide. The ground electrode for the input signal also served as the ground electrode for the output voltage.

The rotation angle, θ, of the crystallographic axes with respect to the global axes of the slab in Figure 2.2 was 45°, which corresponds to a 135° rotated y-cut crystal, to provide optimal electromechanical coupling [41], [42]. Due to the rotated crystallographic axes, the material constants of lithium niobate must be rotated for analysis of the PT. The rotated material constants are found by multiplying the material property tensors by the simplified directional cosine rotation matrix as shown in Equation 2.5 [43], [44]. The rotated constants are denoted using a prime notation, where r'_{ij} is the rotated form of the constant r_{ij} as an example.

$$Q_{ij} = \begin{bmatrix} 1 & 0 & 0 \\ 0 & \cos\theta & \sin\theta \\ 0 & -\sin\theta & \cos\theta \end{bmatrix}, \quad \theta = \frac{\pi}{4}$$

Equation 2.5

The PT was operated in the length-extensional mode at one of the first two mechanical resonant frequencies depending on the desired mode of operation. The resonant frequencies were primarily governed by the dimensions of the lithium niobate slab. A low-frequency rf input signal was used to create an electric field between the input electrodes. The electric field produced between the input electrodes initiated the longitudinal vibrational resonance using the converse piezoelectric effect. The vibrational deformation produced a longitudinal stress in the material which resulted in

an internal longitudinal electric field due to the direct piezoelectric effect. The internal electric field between the output electrode and the ground electrode created a high output voltage at the end of the PT.

Since the primary application for the PTs described in this dissertation was to accelerate charged-particle beams, the electrical load was chosen to be a simplified beam equivalent consisting of a parallel resistor-capacitor (*RC*) circuit as shown in Figure 2.3. The capacitive portion of the load was formed between the output electrode and the circuit board, electric field shaper, vacuum chamber, etc. Both intended load capacitance and any stray capacitance were included in the capacitive portion of the load, C_L. The resistive portion of the load, R_L, was formed by the charged-particle beam current. Ohm's law dictates that an increase in beam current must correspond to a proportional decrease in load resistance for a constant voltage. However, the PT output voltage may not be constant for a change in electrical load due to the nonlinear nature of the device. Least-squares curve fitting between experimental results and models was used to characterize the charged-particle beam current interacting with the output of the PT.
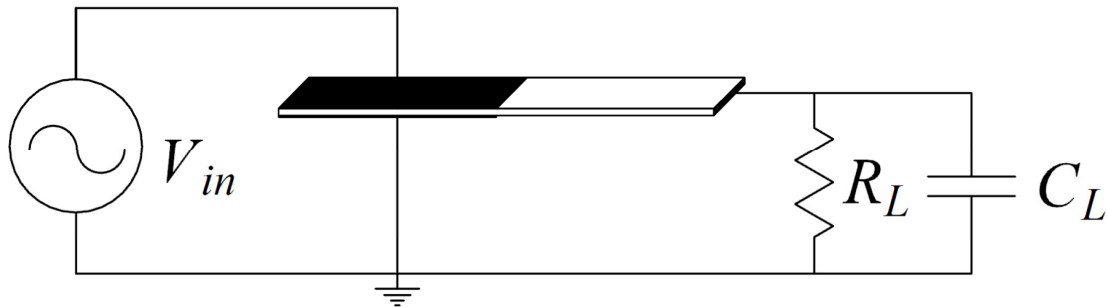
Figure 2.3: Equivalent load circuit attached to the PT.

One-Dimensional Piezoelectric Transformer Model

A one-dimensional model was developed to analyze the PT operating characteristics. This model included three-dimensional (3-D) geometry and constants, but was one-dimensional (1-D) in that it only allowed length-extensional vibration. The 1-D model was based upon the model created by Yang and Zhang, but was modified to include the crystal orientation used in experiments [9], [10], [17], [28]. Additionally, the mechanical loss factor and dielectric loss factor were used to help account for nonidealities of the PT [31], [45]–[47]. The complete mathematical derivation of the 1-D model is shown in Appendix A, and final expressions for mechanical displacement, voltages, and currents are given in this section.

Derivation

The derivation of the 1-D model uses tensor notation that may not be familiar to all readers. Indices from 1-3 correspond to the tensile, or linear, components, while 4-6 correspond to the shear, or tangential, components of the respective variable [34]. If two constants being multiplied together have the same indices, then the denoted product is actually a summation of the product over the range of the repeated index. An example of this is denoted in Equation 2.6. Summations will be from one to three or one to six depending whether the equation uses two-suffix notation or single-suffix notation, respectively [9], [34], [39]. Another notation is that "…a comma followed by an index represents a partial differentiation with respect to the coordinate associated with the index [9]." An example of this is shown in Equation 2.7. If the comma is followed by two indices, a second partial differentiation is denoted as shown in Equation 2.8. Finally, a dot, or series of dots, over a variable denotes partial differentiation with respect to time

14

as shown in Equation 2.9. Table 2.1 shows a list of variable definitions for all variables included in this chapter. All constants are rotated using Equation 2.5, so the prime notation will be dropped throughout this derivation.

$$S_{ij} = s_{ijkl}T_{kl} + d_{kij}E_k = \sum_{k=1}^{3}\sum_{l=1}^{3}s_{ijkl}T_{kl} + \sum_{k=1}^{3}d_{kij}E_k$$

Equation 2.6

$$E_i = -\phi_{,i} = -\frac{\partial \phi}{\partial x_i}$$

Equation 2.7

$$\rho \ddot{u}_2 = \frac{u_{2,22}}{s_{22}} = \frac{1}{s_{22}}\frac{\partial^2 u_2}{\partial x_2^2}$$

Equation 2.8

$$\frac{u_{2,22}}{s_{22}} = \rho \ddot{u}_2 = \rho \frac{\partial^2 u_2}{\partial t^2}$$

Equation 2.9

15

The PT configuration used for the 1-D model is shown in Figure 2.4. The length-extensional transformer is a bar with dimensions such that $a + b >> w >> h$. The polarization of the crystal lattice lies along the P-axis. The driving portion of the PT where the input voltage is applied is defined as the region $-a < x_2 < 0$. A time harmonic driving voltage, $V_1(t)$, is applied across the driving portion to excite the resonant extensional vibration. The receiving portion where the voltage step-up occurs is defined as the region $0 < x_2 < b$. The load impedance, Z_L, is connected between the output electrode and ground. General equations necessary to solve the model are Equation 2.1 to Equation 2.5 and Equation 2.10 to Equation 2.14 [9], [28]. The driving portion and receiving portion of the PT are analyzed separately.
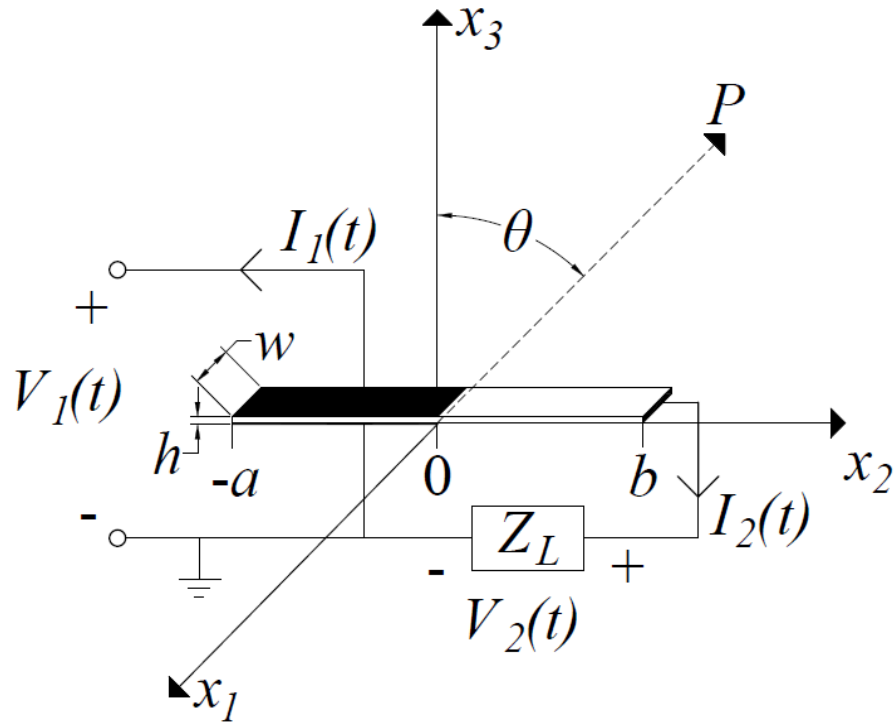
Figure 2.4: Diagram of the PT that was used in the 1-D model.

16

Equation 2.10 restricts displacement and stress in the 1-D model to the longitudinal axis. Equation 2.11 and Equation 2.12 describe the elastic motion occurring within the PT. The applied body force in Equation 2.11 is assumed to be zero, since there is only external electrical excitation of the PT. Equation 2.13 is a form of Gauss's law where there is assumed to be no body charge through the cross-section [9], [48]. Equation 2.14 describes the electric potential and is an electrostatic form of Faraday's law [9], [48].

$$T_1 = T_3 = T_4 = T_5 = T_6 = 0$$

Equation 2.10

$$T_{ji,j} + \rho f_i = \rho \ddot{u}_2$$

Equation 2.11

$$S_{ij} = \frac{\left(u_{i,j} + u_{j,i}\right)}{2}$$

Equation 2.12

$$D_{i,i} = 0$$

Equation 2.13

$$E_i = -\phi_{,i}$$

Equation 2.14

Equation 2.1 and Equation 2.2 or Equation 2.3 and Equation 2.4 describe the stress-charge and strain-charge forms, respectively, of the piezoelectric constitutive equations. However, the necessary coefficients are not always given in the desired form in the literature. Equation 2.15 to Equation 2.17 can be used to conveniently transform given coefficients into the desired form. Equation 2.18, Equation 2.19, and Equation 2.20 give the rotated elastic compliance, piezoelectric strain, and permittivity with respect to constant stress coefficients, respectively, for a 45° rotated lithium niobate slab as shown in Figure 2.4. These can be expressed in matrix form using Voigt's notation due to the symmetry of the tensors that describe the respective coefficients [9], [34], [39], [43]. The superscript "T" for the permittivity with respect to constant stress will be dropped for convenience, since the strain-charge form of the piezoelectric constitutive equations are used.

$$[s] = [c]^{-1}$$

Equation 2.15

$$[d] = [e][c]^{-1}$$

Equation 2.16

$$\left[\varepsilon^{T}\right]=\left[\varepsilon^{S}\right]+\left[e\right]\left[c\right]^{-1}\left[e\right]^{T}$$

Equation 2.17

$$s_{pq} = \begin{pmatrix} 0.0577 & -0.0174 & -0.0073 & -0.0044 & 0 & 0 \\ -0.0174 & 0.0671 & -0.0228 & -0.0091 & 0 & 0 \\ -0.0073 & -0.0228 & 0.0569 & 0.0011 & 0 & 0 \\ -0.0044 & -0.0091 & 0.0011 & 0.1366 & 0 & 0 \\ 0 & 0 & 0 & 0 & 0.1731 & 0.0170 \\ 0 & 0 & 0 & 0 & 0.0170 & 0.1324 \end{pmatrix} \times 10^{-10}$$

Equation 2.18

$$d_{pk} = \begin{pmatrix} 0 & 0 & 0 & 0 & 0.7734 & 0.1867 \\ -0.1533 & 0.3308 & -0.1492 & -0.0984 & 0 & 0 \\ 0.1400 & -0.2959 & 0.1842 & 0.1949 & 0 & 0 \end{pmatrix} \times 10^{-10}$$

Equation 2.19

$$\varepsilon_{ij}^{T} = \begin{pmatrix} 0.7540 & 0 & 0 \\ 0 & 0.5040 & -0.2500 \\ 0 & -0.2500 & 0.5040 \end{pmatrix} \times 10^{-9}$$

Equation 2.20

Forced Vibration Analysis

The time-harmonic elastic motion of the PT is forced by the input voltage, $V_1(t) = \tilde{V}_1 e^{j\omega t}$. The phasor equations in Equation 2.21 to Equation 2.26 describe the PT.

$$\frac{1}{s_{22}}\tilde{u}_{2,22} = -\omega^2 \rho \tilde{u}_2, \quad -a \le x_2 \le 0$$

Equation 2.21

$$\frac{1}{\bar{s}_{22}}\tilde{u}_{2,22} = -\omega^2 \rho \tilde{u}_2, \quad 0 \le x_2 \le b$$

Equation 2.22

$$\frac{1}{s_{22}}\left(\tilde{u}_{2,2} + d_{32}\frac{\tilde{V}_1}{h}\right) = 0, \quad x_2 = -a$$

Equation 2.23

$$\frac{1}{\bar{s}_{22}}\left(\tilde{u}_{2,2} - k_{22}^2 \tilde{c}_1\right) = 0, \quad x_2 = b$$

Equation 2.24

$$\tilde{u}_2\left(0^-\right) = \tilde{u}_2\left(0^+\right)$$

Equation 2.25

$$\frac{1}{s_{22}}\left(\tilde{u}_{2,2}\left(0^-\right) + d_{32}\frac{\tilde{V}_1}{h}\right) = \frac{1}{\overline{s}_{22}}\left(\tilde{u}_{2,2}\left(0^+\right) - k_{22}^2\tilde{c}_1\right)$$

Equation 2.26

Solving the set of differential equations with the corresponding boundary conditions yields Equation 2.27. Simplifying coefficients are shown in Equation 2.28 to Equation 2.36

$$\tilde{u}_2 = \begin{cases} \left(\alpha_{11}\dfrac{d_{32}\tilde{V}_1}{h} + \beta_{11}k_{22}^2\tilde{c}_1\right)\sin\left(kx_2\right) + \left(\alpha_{12}\dfrac{d_{32}\tilde{V}_1}{h} + \beta_{12}k_{22}^2\tilde{c}_1\right)\cos\left(kx_2\right), & -a \leq x_2 \leq 0 \\[3ex] \left(\alpha_{22}\dfrac{d_{32}\tilde{V}_1}{h} + \beta_{22}k_{22}^2\tilde{c}_1\right)\sin\left(\overline{k}x_2\right) + \left(\alpha_{12}\dfrac{d_{32}\tilde{V}_1}{h} + \beta_{12}k_{22}^2\tilde{c}_1\right)\cos\left(\overline{k}x_2\right), & 0 \leq x_2 \leq b \end{cases}$$

Equation 2.27

$$k = \omega\sqrt{\rho s_{22}}, \quad \overline{k} = \omega\sqrt{\rho\overline{s}_{22}}$$

Equation 2.28

$$\bar{s}_{22} = s_{22}\left(1 - k_{22}^2\right), \quad k_{22}^2 = \frac{d_{22}^2}{s_{22}\varepsilon_{22}}$$

Equation 2.29

$$\alpha_{11} = \frac{-1}{\Delta\cos(ka)}\bar{s}_{22}\cos(\bar{k}b)\sin(ka)(\cos(ka) - 1) - \frac{1}{k\cos(ka)}$$

Equation 2.30

$$\beta_{11} = \frac{1}{\Delta}s_{22}\sin(ka)\left(1 - \cos(\bar{k}b)\right)$$

Equation 2.31

$$\alpha_{12} = \frac{1}{\Delta}\bar{s}_{22}\cos(\bar{k}b)(\cos(ka) - 1)$$

Equation 2.32

$$\beta_{12} = \frac{-1}{\Delta}s_{22}\cos(ka)\left(1 - \cos(\bar{k}b)\right)$$

Equation 2.33

$$\alpha_{22} = \frac{1}{\Delta}\bar{s}_{22}\sin(\bar{k}b)(\cos(ka)-1)$$

Equation 2.34

$$\beta_{22} = \frac{-1}{\Delta\cos(\bar{k}b)}s_{22}\sin(\bar{k}b)\cos(ka)(1-\cos(\bar{k}b))+\frac{1}{\bar{k}\cos(\bar{k}b)}$$

Equation 2.35

$$\Delta = s_{22}\bar{k}\sin(\bar{k}b)\cos(ka)+\bar{s}_{22}k\sin(ka)\cos(\bar{k}b)$$

Equation 2.36

The electric potential in the receiving portion can now be described by Equation 2.37 and Equation 2.38. Expressions for the output voltage, output current, and input current are shown in Equation 2.39 to Equation 2.47 along with simplifying coefficient expressions.

$$\tilde{\phi} = \frac{1}{2}\tilde{V}_1 + \frac{1}{\bar{d}_{22}}\left[\tilde{c}_1 x_2 - \left(\alpha_{22}\frac{d_{32}\tilde{V}_1}{h}+\beta_{22}k_{22}^2\tilde{c}_1\right)\sin(\bar{k}x_2)\right.$$
$$\left. + \left(\alpha_{12}\frac{d_{32}\tilde{V}_1}{h}+\beta_{12}k_{22}^2\tilde{c}_1\right)(1-\cos(\bar{k}x_2))\right], \quad 0 \le x_2 \le b$$

Equation 2.37

$$\tilde{c}_1 = \frac{\tilde{I}_2 s_{22}}{j\omega d_{22} hw}$$

Equation 2.38

$$\tilde{V}_2 = \frac{\Gamma_1 \tilde{V}_1 Z_L}{Z_L + Z_2}$$

Equation 2.39

$$\tilde{I}_2 = \frac{\Gamma_1 \tilde{V}_1}{Z_L + Z_2}$$

Equation 2.40

$$\Gamma_1 = \frac{1}{2} + \frac{d_{32}}{\bar{d}_{22} h}\left[\alpha_{12}\left(1 - \cos\left(\bar{k}b\right)\right) - \alpha_{22} \sin\left(\bar{k}b\right)\right]$$

Equation 2.41

$$\bar{d}_{22} = d_{22}\left(1 - \frac{1}{k_{22}^2}\right)$$

Equation 2.42

$$Z_2 = \frac{1}{j\omega\varepsilon_{22}wh(1-k_{22}^2)}\left[b - \beta_{22}k_{22}^2\sin(\bar{k}b) + \beta_{12}k_{22}^2(1-\cos(\bar{k}b))\right]$$

Equation 2.43

$$\tilde{I}_1 = \frac{-\tilde{V}_1}{Z_1} + \Gamma_2\tilde{I}_2$$

Equation 2.44

$$\frac{1}{Z_1} = \frac{j\omega\bar{\varepsilon}_{33}w}{h}\left[a - \frac{k_{32}^2}{1-k_{32}^2}(\alpha_{12} + \alpha_{11}\sin(ka) - \alpha_{12}\cos(ka))\right]$$

Equation 2.45

$$\bar{\varepsilon}_{33} = \varepsilon_{33}(1-k_{32}^2), \quad k_{32}^2 = \frac{d_{32}^2}{\varepsilon_{33}s_{22}}$$

Equation 2.46

$$\Gamma_2 = \frac{k_{22}^2 d_{32}}{hd_{22}}(\beta_{12} + \beta_{11}\sin(ka) - \beta_{12}\cos(ka))$$

Equation 2.47

25

The 1-D model derivation to this point has not included loss factors. Substituting the lossy elastic compliance and permittivity with respect to constant stress coefficients, s_L and ε_L^T, respectively, into the model derivation accounts for the mechanical and dielectric loss factors. The inclusion of loss factors introduces complex numbers into the material coefficients. The mechanical loss factor is inversely proportional to the input mechanical quality factor (Q-value) and affects the elastic compliance coefficients isotropically as shown in Equation 2.48 [45]. The input mechanical Q-value is approximately equal to the Q-value of the PT input impedance [45], [49]. Common input mechanical Q-values were measured to be between $2,500 - 5,000$ depending on the electrical and mechanical load. The dielectric loss factors affect the permittivity with respect to constant stress as shown in Equation 2.49. However, the dielectric loss factors must be implemented prior to any rotation using Equation 2.5, since these loss factors correspond to the crystallographic axes. Dielectric loss factors for lithium niobate used in the 1-D model are shown in Equation 2.50 [31], [46], [47].

$$s_L = s\left(1 - j\delta_m\right) = s\left(1 - j\frac{1}{Q_m}\right)$$

Equation 2.48

$$\varepsilon_L^T = \varepsilon_{ij}^T\left(1 - j\gamma_{ij}\right)$$

Equation 2.49

26

$$\gamma_{ij} = \begin{pmatrix} 5 & 0 & 0 \\ 0 & 5 & 0 \\ 0 & 0 & 3.4 \end{pmatrix} \times 10^{-4}$$

Equation 2.50

1-D Modeling Results

PT analysis was conducted using the 1-D model. Unless otherwise noted, all modeling results presented correspond to a 10 V amplitude input voltage, input mechanical quality factor of 5,000, lossy permittivity, and a constant load capacitance of 50 fF. The load capacitance was chosen based on 3-D finite-element simulations of the PT in the vacuum chamber. Physicality of the model was verified using the electrical efficiency as defined by the ratio of the output average power to the input average power. Any non-physical results produced efficiencies greater than 100 %.

Figure 2.5 shows the electrical input impedance of the PT as a function of frequency for varied resistive load components. The resonant frequencies occurred where the input impedance was minimized. Both the fundamental harmonic and second harmonic frequencies are shown in Figure 2.5 at approximately 31 kHz and 62 kHz, respectively. Although difficult to see in Figure 2.5, the resonant frequency does shift slightly depending on the load impedance. The input impedance was maximized at the anti-resonance frequency immediately following the resonant frequency. The PT voltage transformation ratio was maximized at the resonant frequency as shown in Figure 2.6. The PT transformer ratio was dependent on the magnitude of the resistive portion of the

27
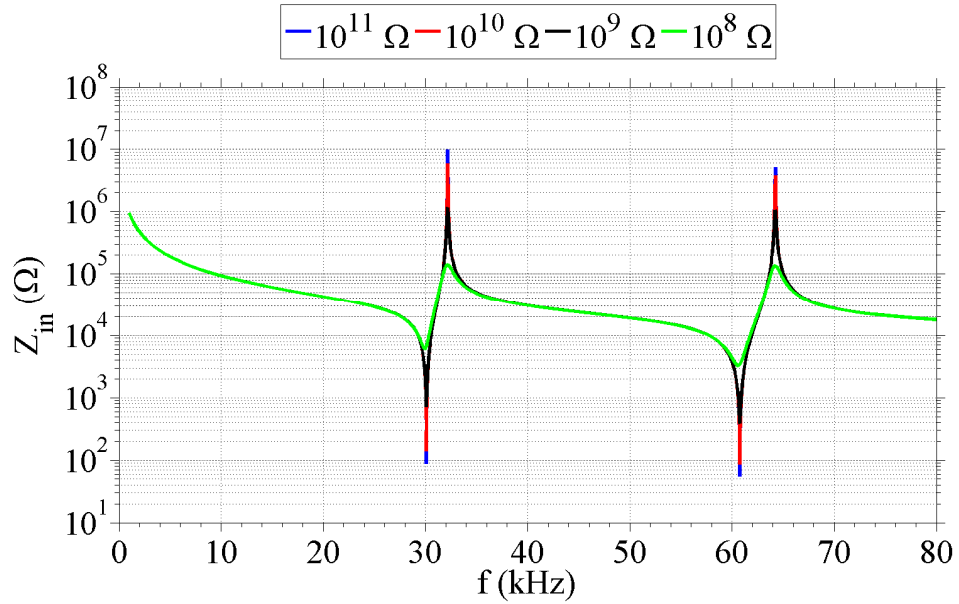
Figure 2.5: 1-D simulated results of the PT input impedance versus frequency for varying load resistances.
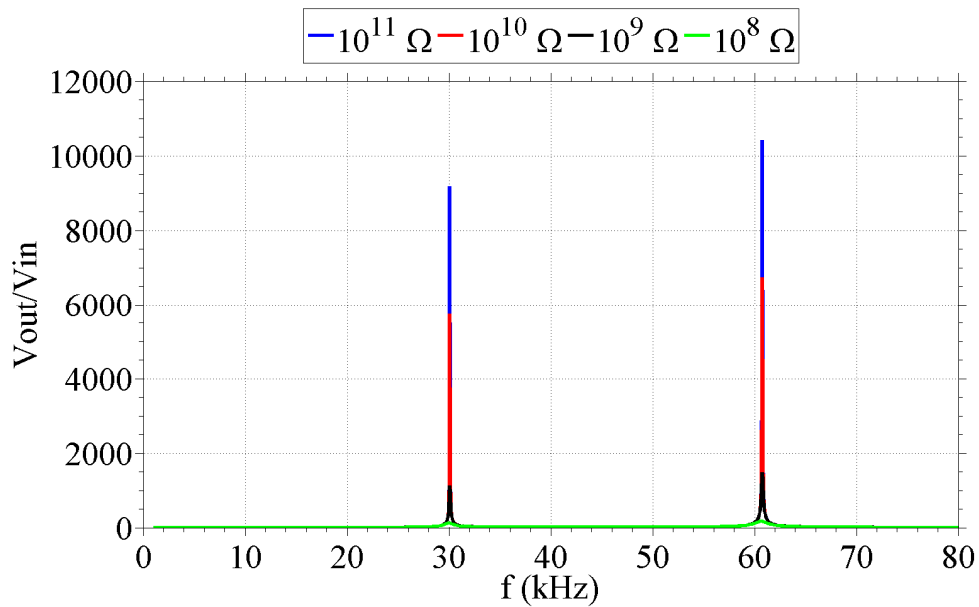
Figure 2.6: 1-D simulated results of the PT voltage transformation ratio versus frequency for varying load resistances. Note that peak transformation ratios occur at resonant frequencies where the input impedance is minimized.

28

load. In mode 2, transformation ratios of approximately 10,500 were simulated for resistive load components of 10^{11} Ω, while transformation ratios of less than 1,000 were simulated for resistive load components of 10^8 Ω.

Figure 2.7 shows the simulated mechanical displacement and longitudinal stress within the PT as a function of length along the PT for varied resistive load components. Two maximum stress values occurred at the points where the mechanical displacement was minimized. Experimentally, this was observed because the PT tended to fracture at the holder where the PT was mechanically clamped. The fracture limit of lithium niobate is between 30 – 150 MPa [50]. Both the displacement and stress achieved in the PT increased as the resistive component of the load was increased.

Figure 2.8 shows the longitudinal electric field magnitude and the corresponding electric potential generated as a function of length for varied resistive load components. The electric field near the end of the PT decreased to zero and reversed polarity due to the boundary conditions at the output electrode. This resulted in a slight decrease in electric potential near the end of the PT, and the highest voltage on the surface of the PT does not occur at the output electrode. Consequently, charged-particle beams accelerated by the PT were directed toward the region of higher electric potential rather than the output electrode unless electric field shaping was used [51]. Higher output voltages were achieved for increased resistive load components.

Figure 2.9 and Figure 2.10 show the simulated PT voltage transformation ratio and the output current, respectively, for varied load resistance and capacitance. The

(a)

(b)

(c)
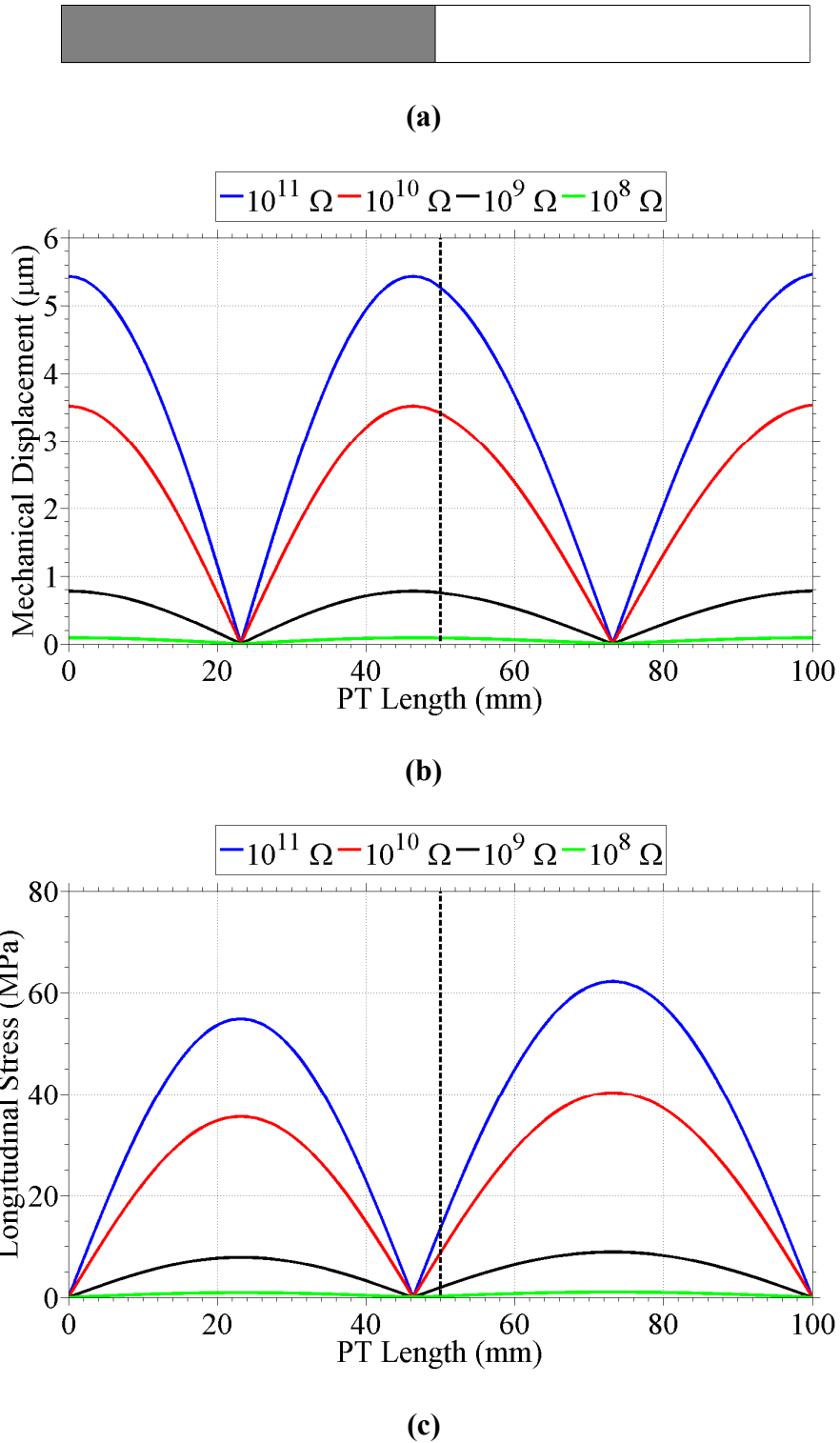
Figure 2.7: A top-down view of the PT in Figure 2.4 is shown for reference in (a). 1-D simulated (b) displacement and (c) longitudinal stress along the length of the PT for second harmonic operation and varying load resistances.

(a)

(b)

(c)
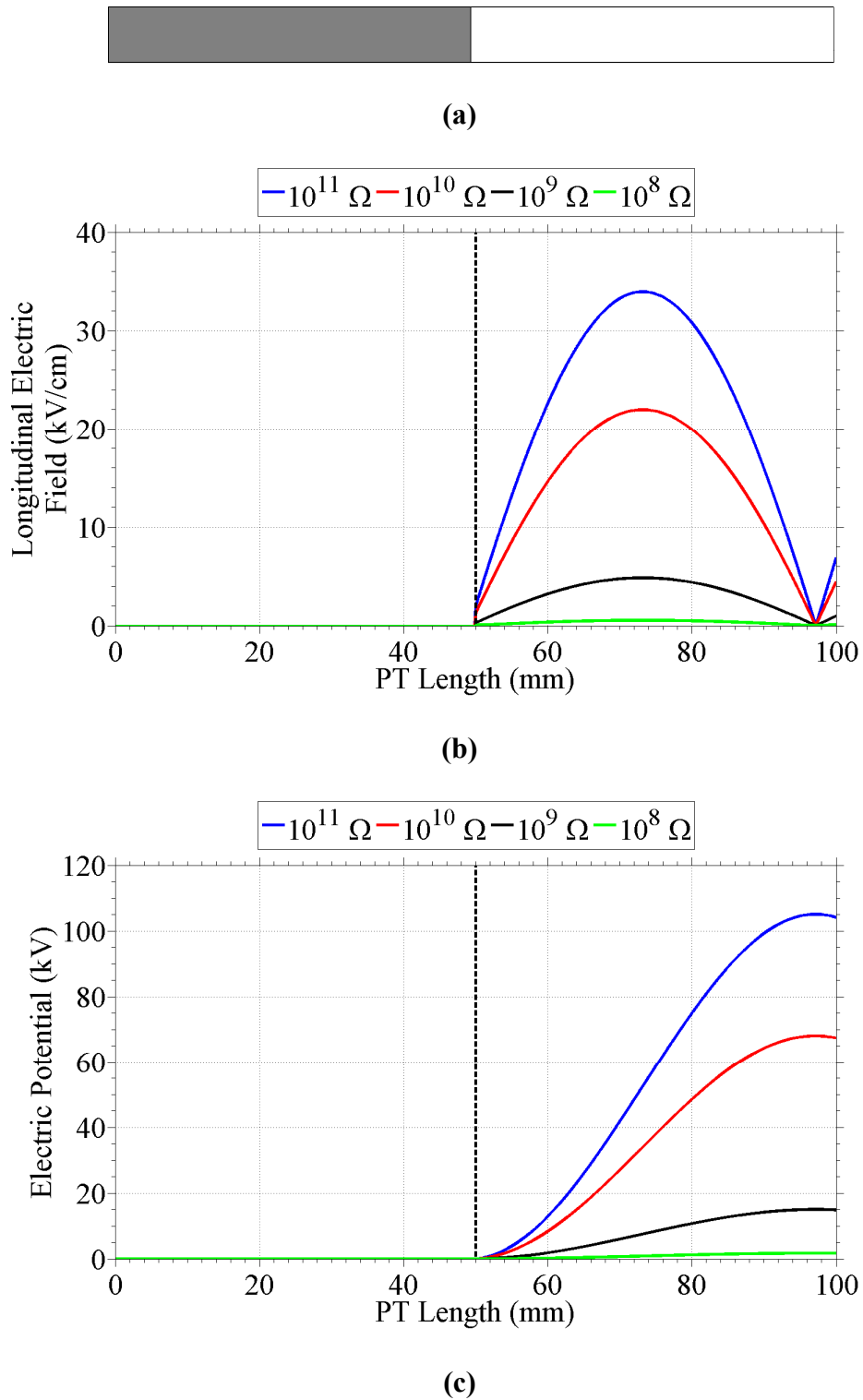
Figure 2.8: A top-down view of the PT in Figure 2.4 is shown for reference in (a). 1-D simulated (b) electric field and (c) potential along the length of the PT for second harmonic operation and varying load resistances.
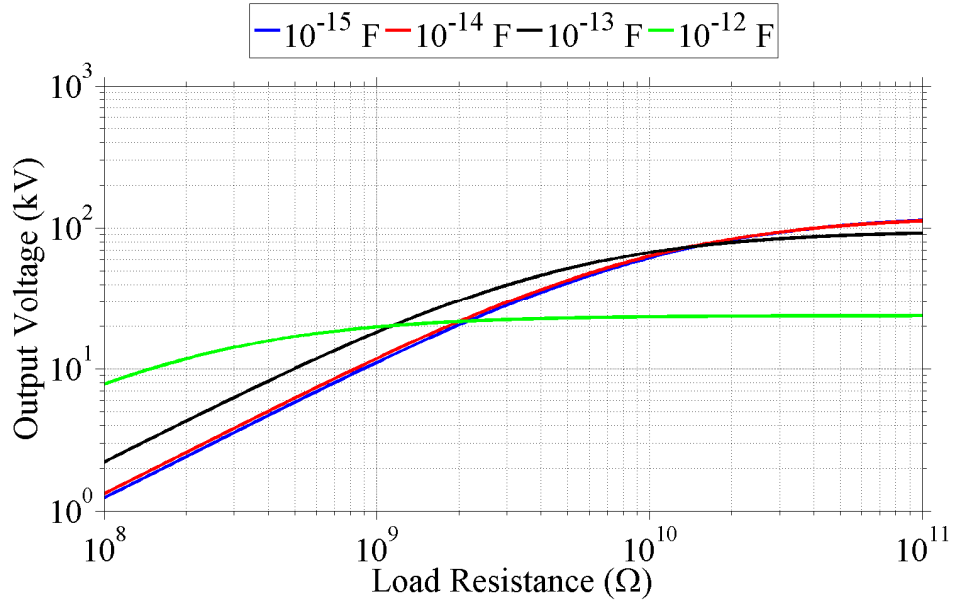
(a)
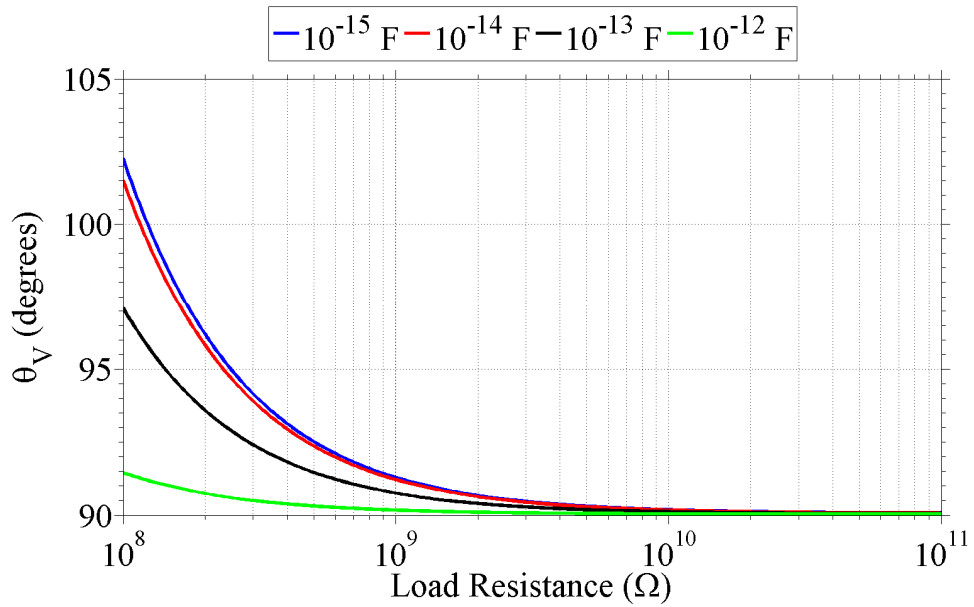
(b)

Figure 2.9: 1-D simulated second harmonic (a) PT output voltage and (b) output voltage phase angle for varied load resistance and capacitance. Note that the output voltage is 90° out of phase with respect to the input voltage.
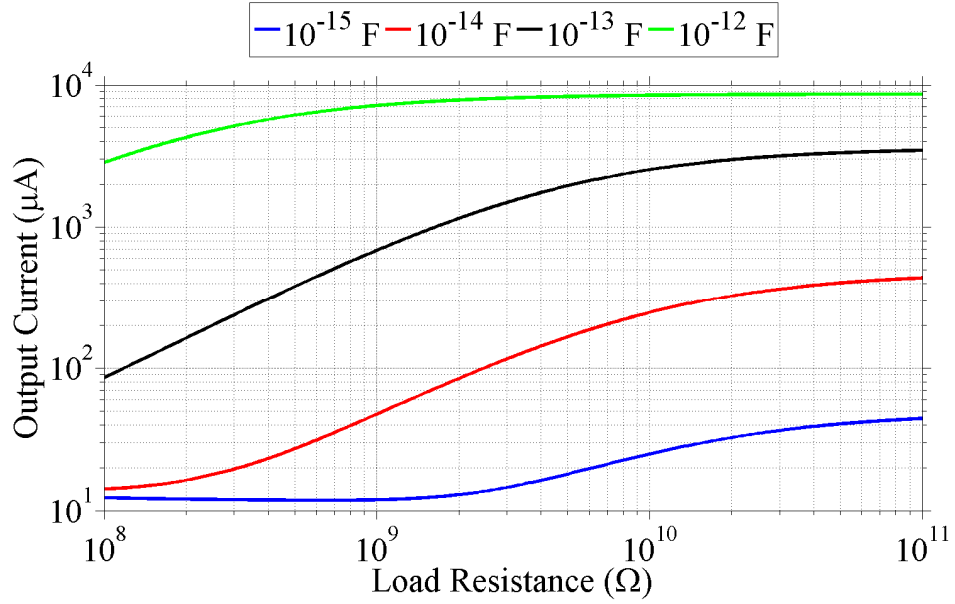
(a)
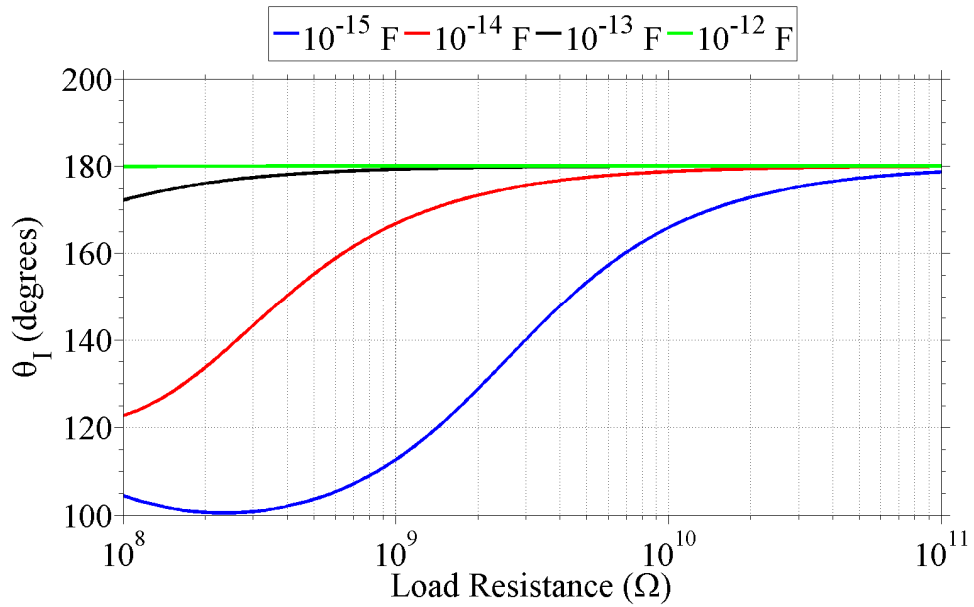
(b)

Figure 2.10: 1-D simulated second harmonic (a) PT output current and (b) output current phase angle for varied load resistance and capacitance.

highest output voltages and currents occurred as the load capacitance was increased toward the output capacitance of the PT of 10^{-13} F. The output voltage approached 90° out of phase with respect to the 0° reference phase of the input voltage for all load capacitances as load resistance increased. PT output voltage amplitudes of approximately 90 kV were simulated with output current amplitudes of approximately 3.2 mA for 10^{11} Ω, 10^{-13} F loads. However, it is important to note that the output current amplitudes included both conduction and displacement currents due to the parallel *RC* load.

The PT output average power is shown in Figure 2.11 along with the phase difference between the output voltage and current. The greatest output average power simulated was approximately 0.32 W for a load capacitance of 10^{-12} F and load resistance of approximately 2×10^8 Ω. Figure 2.11b shows the phase difference between the PT output voltage and current. The voltage and current approached the characteristic -90° phase difference for a capacitive load in all cases. The rate at which the -90° phase difference was achieved was dependent on the respective impedance of the resistive and capacitive portions of the load. Figure 2.12 shows the electrical efficiency of the PT with respect to average input and output power. PT efficiency decreased greatly as load capacitance increased.

Finite-Element Modeling

COMSOL Multiphysics finite-element simulation software was also used to simulate the PT in three dimensions [38]. The finite-element simulations had the same boundary conditions as the 1-D model, but the PT was allowed to have mechanical displacement in all directions. A system of partial differential equations describing the
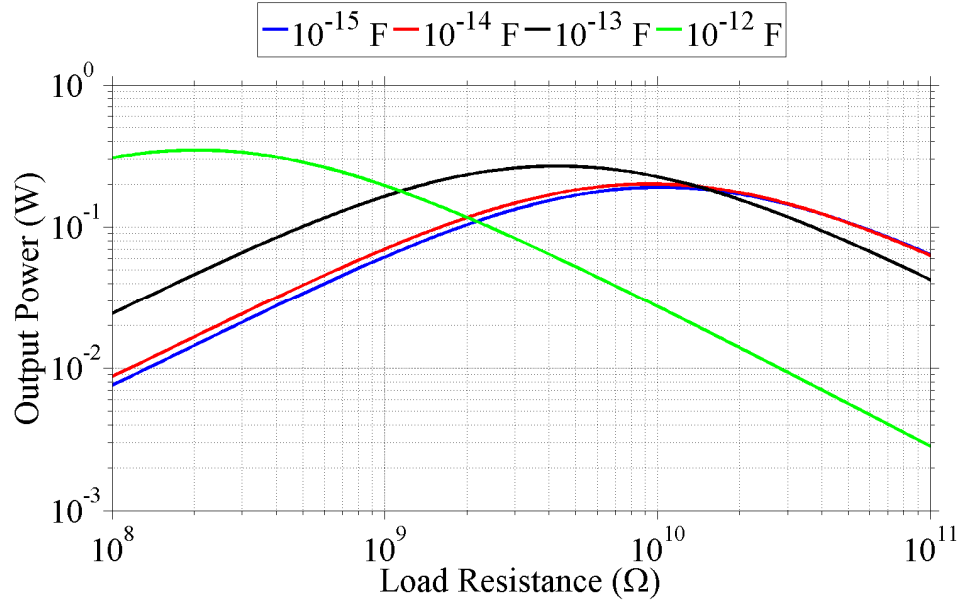
(a)
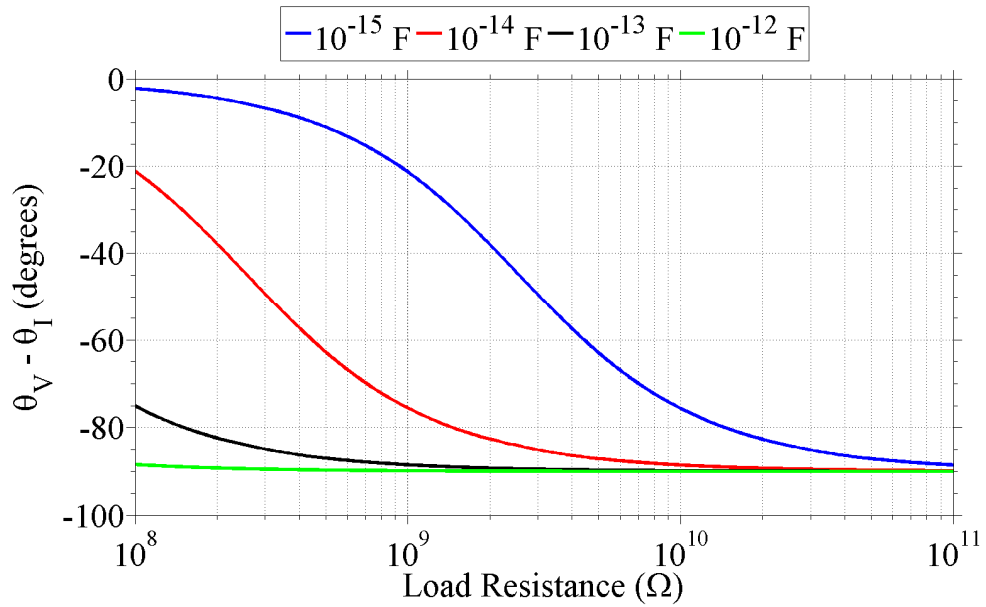
(b)

Figure 2.11: **1-D simulated second harmonic (a) PT output average power for varied load resistance and capacitance. (b) The phase difference between the voltage and current is also shown. Note that the phase difference approaches -90° for the primarily capacitive load.**
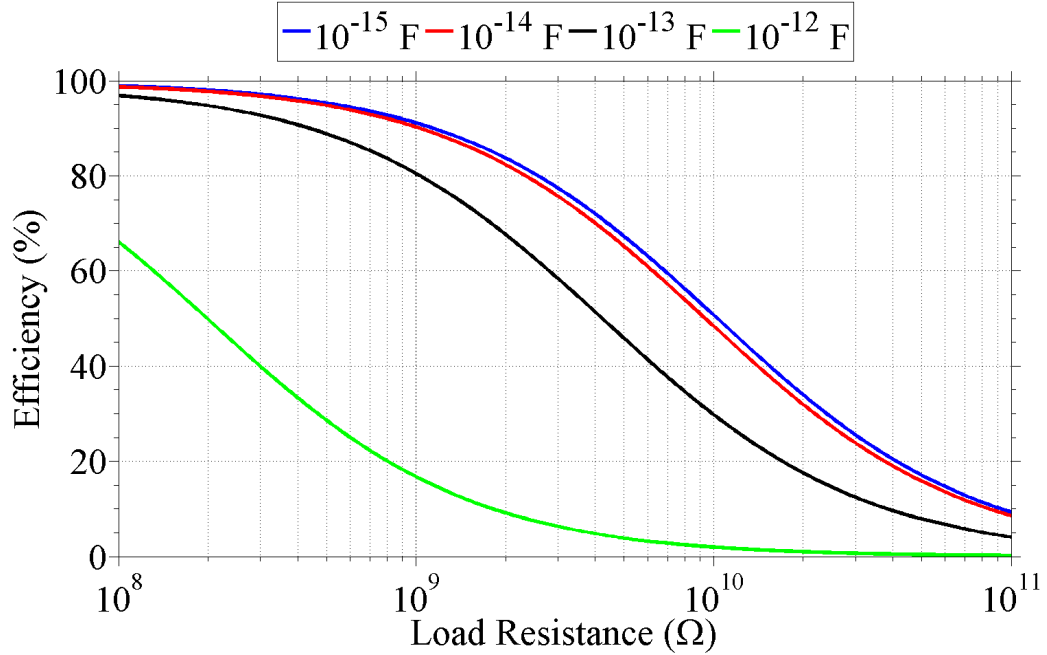
Figure 2.12: 1-D simulated second harmonic efficiency as calculated using the electrical input average power and the electrical output average power.

simulation space was solved to determine the PT operating characteristics [38]. Since the simulation was not solving a simplified system of differential equations as in the 1-D model, the results should have been more physically accurate. The computation time required to solve the system of partial differential equations made the finite-element simulations impractical to use for least-squares curve fitting. Consequently, finite-element simulations were only used to verify the results from the 1-D model.

Figure 2.13 shows the simulated PT voltage transformation ratio as a function of frequency for varied resistive components of the load. Only the frequency space surrounding the second harmonic frequency was simulated for the finite-element
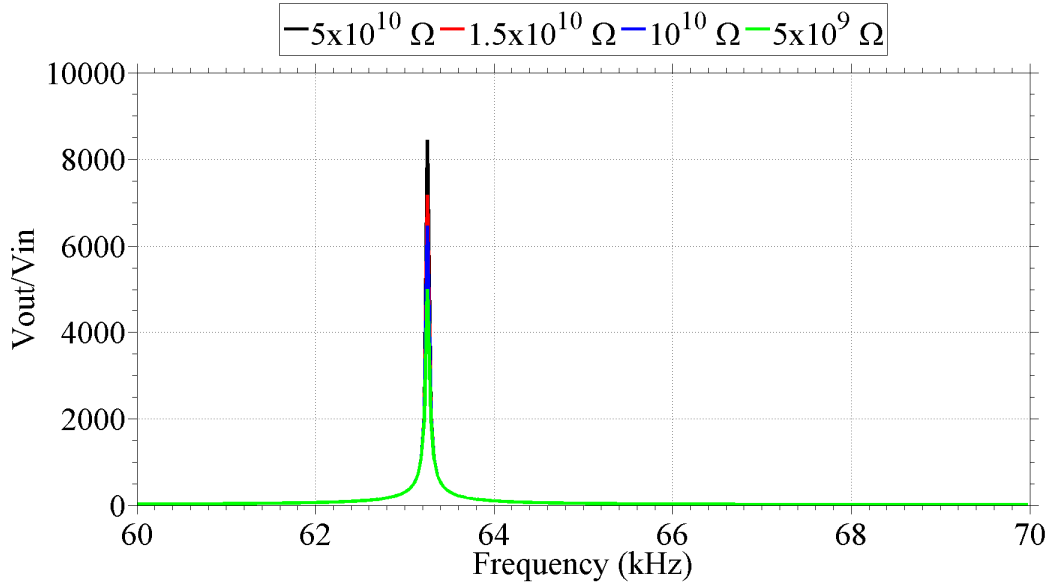
Figure 2.13: Finite-element simulated second harmonic PT voltage transformation ratio versus frequency for varied load resistance.

simulations. The transformation ratio peaked at the resonant frequency similar to the 1-D model. Voltage transformation ratios of approximately 8,500 were simulated for resistive load components of $5x10^{10}$ Ω, while voltage transformation ratios of 5,000 were simulated for resistive load components of $5x10^{9}$ Ω.

Figure 2.14 shows the mechanical displacement and the longitudinal stress in the PT. The finite-elements simulations generated a greater mechanical displacement in the PT than the 1-D model. However, mechanical displacements in the two models were both on the order of a few micrometers. The increased mechanical displacement did not necessarily result in increased stress within the PT because the freedom of the PT to have mechanical displacement in all directions allowed higher order vibrational modes to superimpose on the primary vibrational mode. This was observed as displacement in

other directions and distortion of the longitudinal component of the stress. The occurrence of simultaneous higher-order vibrational modes and any differences in the implementation of loss factors in three dimensions would have accounted for the slight discrepancies between the two models.

The simulated longitudinal electric field and corresponding electric potential are shown in Figure 2.15. The simulated electric fields followed the same trend as the stresses and were slightly lower for the finite-element model than in the 1-D model. Again, a decrease to zero and reversal of polarity was observed for the electric field near the output electrode. The corresponding electric potential profiles are shown in Figure 2.15c. Similarly to the 1-D modeled electric potentials, the finite-element simulations resulted in output voltages on the order of tens of kilovolts.

(a)

(b)

(c)
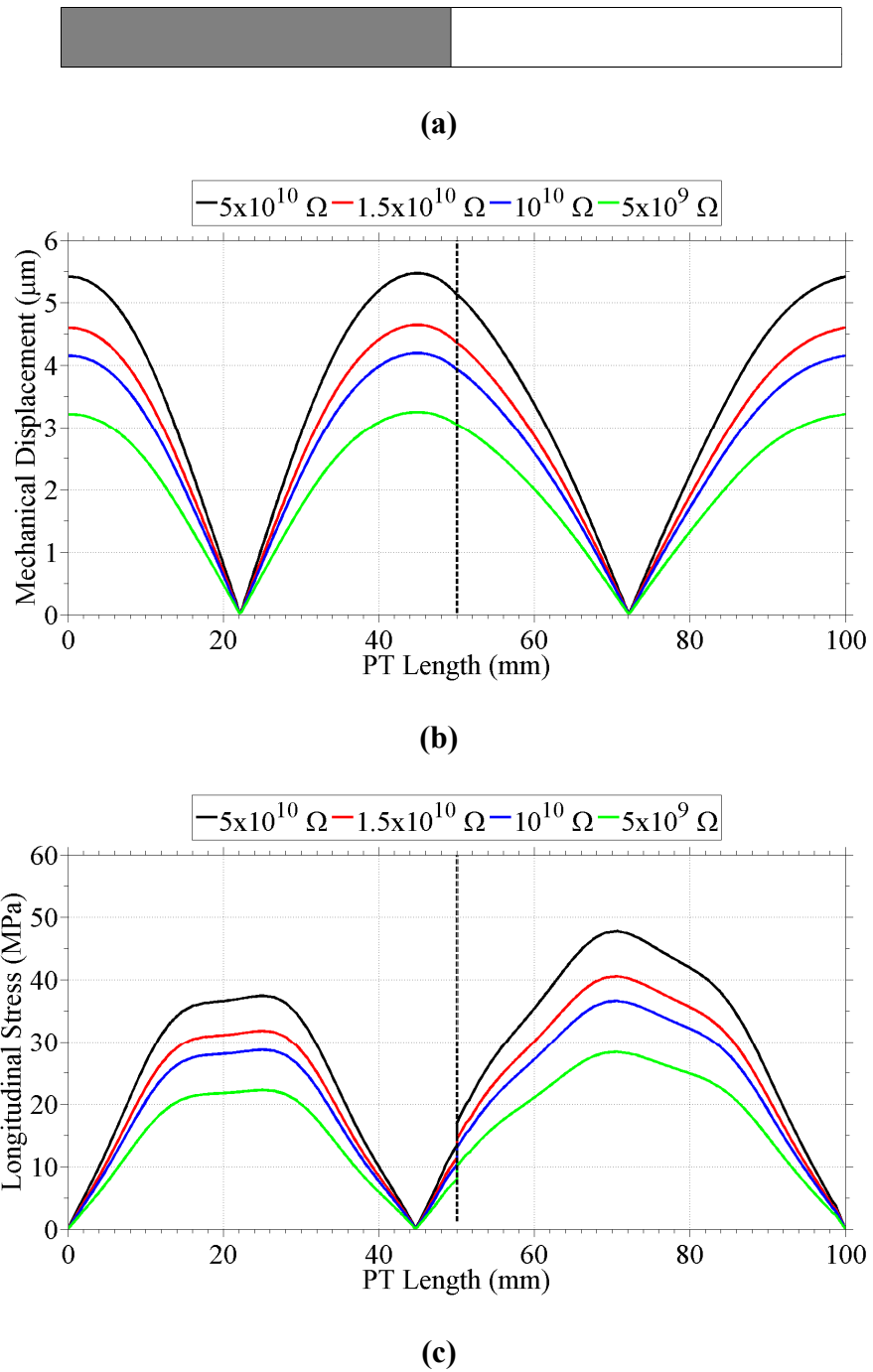
Figure 2.14: A top-down view of the PT in Figure 2.4 is shown for reference in (a). Finite-element simulated (b) mechanical displacement and (c) stress along the length of the PT for second harmonic operation and varying load resistances.

(a)

(b)

(c)
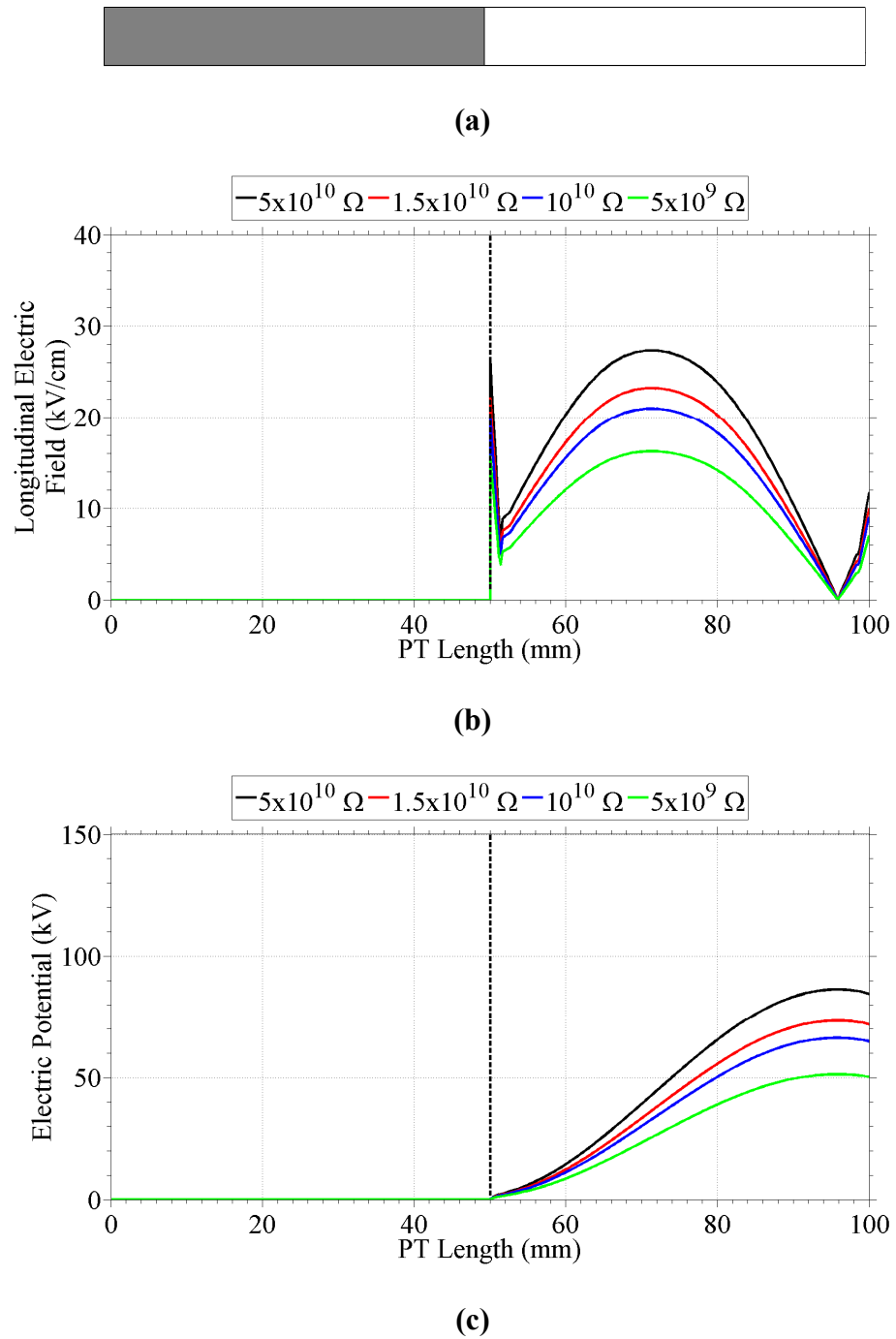
Figure 2.15: A top-down view of the PT in Figure 2.4 is shown for reference in (a). Finite-element simulated (b) electric field and (c) potential along the length of the PT for second harmonic operation and varying load resistances.

3. Experiment Setup

Overview

This chapter is separated into five sections. An overview of the piezoelectric transformer (PT) is presented for both the bipolar and unipolar PT configurations. Initial experiment setups are discussed that were used to demonstrate the PT output voltage dependence on electrical load impedance. These early setups include the bipolar PT connected to high-voltage and initial electron-beam diode experiments where the electron beam current was varied. The primary experiment setup used to characterize the PT for varied electrical load impedances is discussed and includes a system diagram of the setup. The design of an electric field shaper is discussed, and finally, the experimental setup for x-ray fluorescence experiments is given.

Piezoelectric Transformer

The PT was made from a 135° rotated y-cut lithium niobate (LiNbO$_3$) crystal as described in the previous chapter. The PT was held at its vibrational null point(s), the location of which depended on the mode of operation. The first harmonic of the resonant frequency at approximately 31 kHz, or mode 1, had a single vibrational null point located approximately 0.5 cm towards the input side from the center. Experiments operated in mode 1 used either compressed foam pads or a spring-compressed holder with rubber pads to hold the crystal. The second harmonic of the resonant frequency at approximately 62 kHz, or mode 2, had two vibrational null points located approximately 2.5 cm from either end of the crystal. Experiments operated in mode 2 used 3-D printed wedges of photopolymer resin clamped with ultra-precision compression springs to hold the crystal. Examples of mode 1 and mode 2 holders are shown in Figure 3.1 and Figure 3.2, respectively. Initial experiments were conducted in mode 1; however, subsequent experiments were conducted in mode 2 for better precision of PT placement.
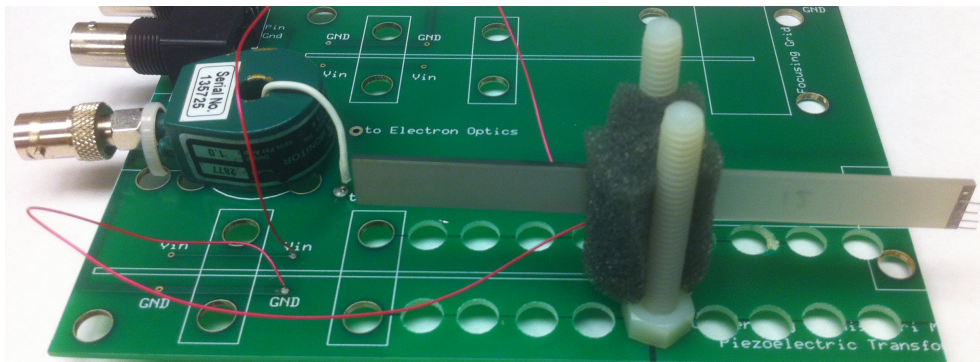
Figure 3.1: Photograph of an experiment operated in mode 1 with the PT held with compressed foam pads.
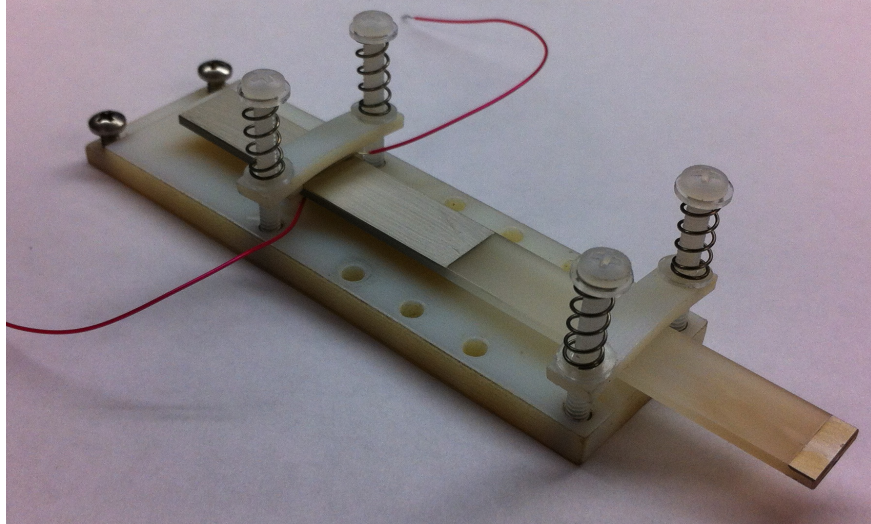
Figure 3.2: Photograph of a PT in a mode 2 holder made of photopolymer resin clamped with ultra-precision compression springs.

Two configurations of the PT were tested: the bipolar and unipolar configurations. The primary difference between the two is the configuration of the electrodes and the resultant operating conditions for those electrode configurations. Both configurations operate in the length-extensional resonance mode and were typically modulated at a rate of once per second with a duty cycle of 0.048 to reduce the likelihood of fracturing the crystal. The unipolar configuration was operated in both modes 1 and 2, while the bipolar configuration was only operated in mode 1. Although the bipolar PT produced an isolated output voltage, the necessary precision required to operate both sides exactly 180° out of phase made this configuration difficult to operate reliably. Because of this, the unipolar PT is the primary configuration discussed in this paper.
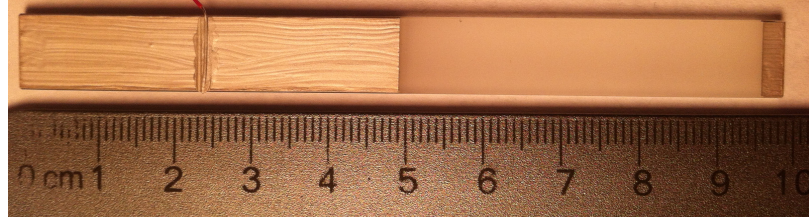
Figure 3.3: Photograph of the unipolar lithium niobate, length-extensional piezoelectric transformer. Dimensions are 100 mm long, 10 mm wide, and 1.5 mm thick.

Unipolar PT

The unipolar PT design can be seen in Figure 3.3. Fifty percent of the surface at one end of the crystal was covered on each side with a conductive silver paint to create the two input electrodes. The silver paint was also used to attach wires to these input electrodes. An output electrode with a surface area of 25 mm^2 was painted onto the top and bottom at the opposite end of the crystal as well as the end plane of the crystal. A wire was attached to the output electrode of the PT to make electrical connections when experiments used discrete circuit loads. Platinum-iridium (PtIr) wires with a diameter of 100 μm and length of 1 cm were attached to the output electrodes using the silver paint and were cleaved to create sharp, field-emitting structures for the initial electron-beam diode experiments that are discussed later in this chapter. The output electrode was left bare for experiments not using discrete electrical loads or field-emitting structures.

The unipolar PT was driven in either mode 1 or mode 2. Typical input voltages and currents had amplitudes of $7 - 10$ V and $75 - 115$ mA, respectively. This PT operating in length-extensional mode was shown to be capable of producing output

voltages in excess of 120 kV for an input voltage of approximately 10 V which corresponds to a voltage gain greater than 11,700.

Bipolar PT

An example of the bipolar PT is shown in Figure 3.4. The mechanical resonant frequency of this PT was approximately 30 kHz in mode 1. Electrodes were applied using conductive silver paint. The input electrodes were applied on each side of the crystal at the midpoint of the crystal with a length of 1 cm, while the output electrodes were painted onto each end of the crystal.

An applied low-frequency rf signal of approximately 25 V amplitude at the input electrodes established a longitudinal resonant vibration, which in turn generated high voltage at each output. Input current amplitudes were on the order of 50 mA. Due to the bipolar design, each output was equal in magnitude but 180° out of phase with respect to one another. A differential measurement from end to end described the output voltage of the PT. End-to-end voltages in excess of 30 kV were demonstrated with this
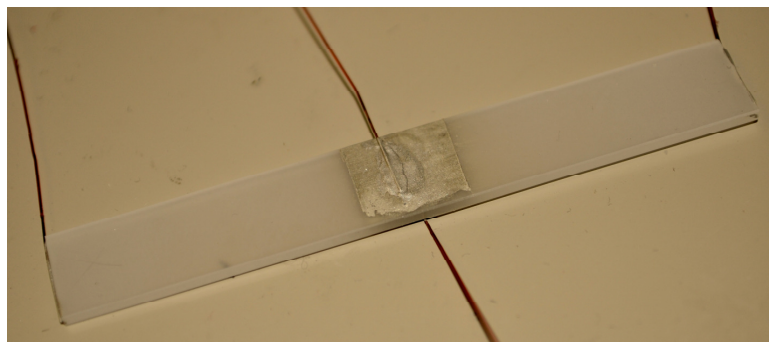
Figure 3.4: **Photograph of the bipolar length-extensional LiNbO$_3$ piezoelectric transformer. Dimensions are 100 mm long, 10 mm wide, and 1.5 mm thick.**

PT using a bremsstrahlung x-ray diagnostic described later in this document. This configuration also made it possible to attach a full-wave Cockcroft-Walton voltage multiplier, but the losses proved too great to make this approach successful at producing high voltage.

Initial Piezoelectric Transformer Experiments

PT Output Circuits

Capacitive Voltage Divider

A capacitive divider was constructed in an attempt to measure the PT output voltage without electrically loading the PT. The capacitive divider used the output electrode of the crystal and a copper tape electrode across a 15 mm air gap as the low-capacitance, high-voltage side of a voltage divider. The second capacitance was formed between an aluminum ground plane and the copper tape with a kapton tape dielectric of
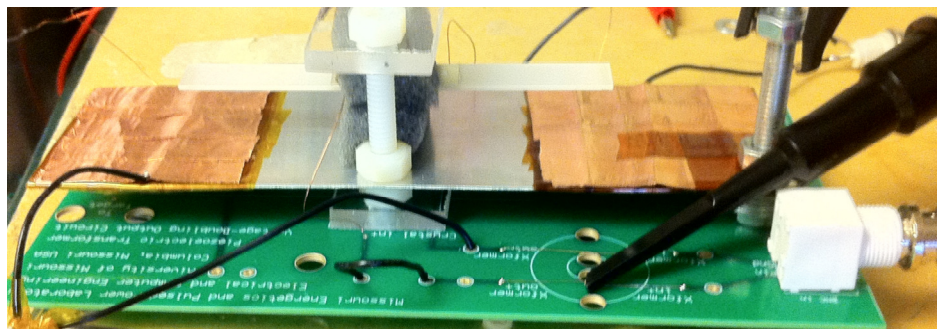
Figure 3.5: Photograph of the capacitive divider circuit with the PT

0.6 mm. This configuration was done on both ends of the PT to achieve a differential measurement. A photograph of the capacitive divider can be seen in Figure 3.5.

To characterize the capacitive divider, an inductor-capacitor (LC) resonant circuit was used. By connecting a 2.8 mH inductor in series with each of the capacitances, the resonant frequency of the LC circuit could be determined. From that resonant frequency, the capacitance was calculated using Equation 3.1 where L is the inductance, C is the capacitance, and f is the LC resonant frequency. It was determined that the capacitance values were approximately 250 fF and 270 pF, creating an approximately 1,000 times divider for each side of the PT. By subtracting the two output voltages, the end-to-end output voltage was determined.

$$f = \frac{1}{2\pi LC}$$

Equation 3.1

Cockcroft-Walton Output Circuit

To further increase the output voltage, a full-wave Cockcroft-Walton (CW) voltage multiplier circuit was attached to the PT. This circuit converts ac to dc and can be implemented in multiple stages to further multiply the voltage. The circuit schematic for a three-stage CW circuit can be seen in Figure 3.6. The theoretical output voltage from a CW circuit with ideal diodes can be calculated as shown in Equation 3.2, where V_{out} is the output voltage, n is the number of stages, and V_{in} is the input voltage from one

side. Each end of the PT acted as an input voltage while 100 pF capacitors were used for

each stage.

$$V_{out} = 2nV_{in}$$

Equation 3.2
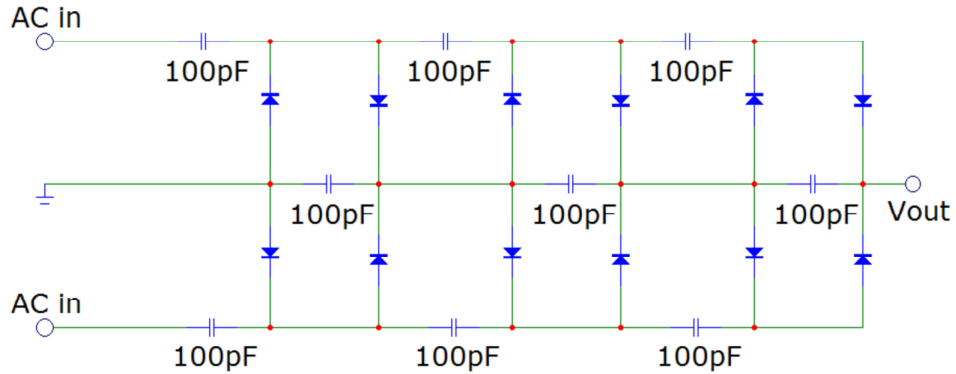
Figure 3.6: Three-stage, full-wave Cockcroft-Walton circuit.

Electron-Beam Diode Loads

The unipolar, mode 1 PT with field-emitting tips shown in Figure 3.1 was used as

the high-voltage source to drive an electron beam diode. The mean free path describes

the mean path between collisions for particles and for electrons in air it can be calculated

using Equation 3.1 where L_e is the electron mean free path in air [cm], T is the

temperature of the air [K], and P is the air pressure [Torr] [52]. Since the electron mean

free path for electrons in air at STP is only approximately 0.4 µm, the electrons would

rarely make it from the source to the target without colliding with air molecules. Consequently, the electron beam diode configuration was operated in vacuum at approximately 1 μTorr to yield an electron mean free path of approximately 40 cm. Additionally, operation in vacuum prevented corona discharge and surface flashover at the electrodes. Figure 3.7 shows a diagram of the PT in the vacuum chamber being directed down a port of the vacuum chamber.

$$L_e = 9.427 \times 10^{-5} \frac{T}{P}$$

Equation 3.3
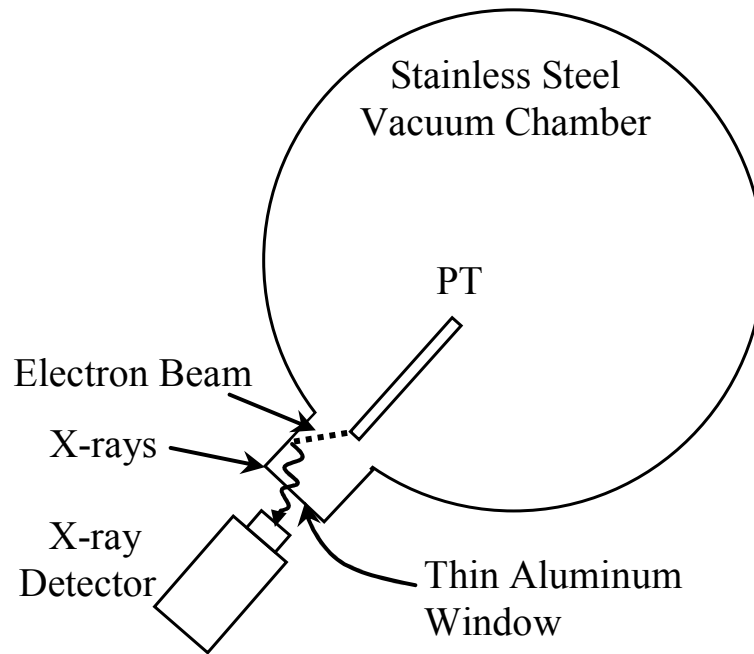
Figure 3.7: Diagram of the PT with respect to the vacuum chamber (not to scale). Bremsstrahlung x-rays are produced from the electrons interacting with the stainless steel vacuum chamber walls. The PT can be positioned at varying distances with respect to the vacuum chamber port.

The rf input voltage used to drive the PT resulted in a high output voltage with the same frequency. On the negative half-cycle of the output voltage, electrons were field emitted from the PtIr wires at the output electrode of the PT. Bremsstrahlung x-rays were produced as electrons interacted with the stainless steel vacuum chamber walls. The x-rays passed through a 30 μm aluminum foil window and were measured with an Amptek cadmium-telluride (CdTe) x-ray detector. By measuring the endpoint energy of the resulting x-rays, the output voltage of the PT was indirectly measured. The PT was repositioned with respect to the vacuum chamber port to analyze the effects of varying the load capacitance on the output voltage of the PT. The electron beam also serves as a parallel resistive component to the load.

High-Voltage Load Testing in Vacuum

Since the initial experiments showed that low-impedance loads caused the PT to have decreased output voltages, the PT was characterized for varying load impedances. Since the primary application for the PT was to accelerate charged-particle beams, an electron beam current was varied to test the effects of load impedance on the PT. This section describes the setup for the varied electron-beam diode load, the use of an electric field shaper to manipulate the trajectory of the electron beam, and the setup for x-ray fluorescence experiments.

Electron-Beam Diode Loads

The PT was operated in a cylindrical vacuum chamber with a thermionic filament to produce and accelerate an electron beam. The PT was operated in a vacuum chamber

at a pressure between $10^{-6} - 10^{-5}$ Torr. A thermionic filament made of 3% rhenium-doped tungsten alloy was heated using dc currents between 2.0 to 2.5 A. Thermionic emission current was accelerated by the electric fields generated by the output of the PT on one half-cycle of operation. This configuration is shown in Figure 3.8. Input impedances were measured directly using a voltage probe and a current transformer. Incident electron energy was attenuated by the silver paint output electrodes, yielding bremsstrahlung radiation. The bremsstrahlung x-rays were measured using a CdTe x-ray detector on the opposite side of a 635 μm (0.050") aluminum window. Additionally, an optical diagnostic was used to probe the internal characteristics of the PT during operation.

A more detailed system diagram for the characterization of the PT for varied load impedances is shown in Figure 3.9. The diagram is color coded for convenience. Blue corresponds to diagnostic reading devices for the direct experimental measurements.
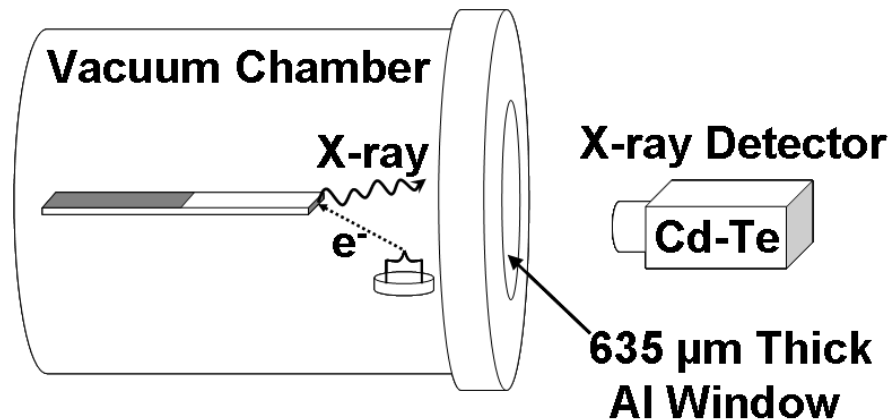
Figure 3.8: Diagram of the thermionic filament with a PT in the vacuum chamber. X-rays are detected outside the vacuum chamber through a 635 μm (0.050") thick aluminum window with a cadmium-telluride x-ray detector.

Orange corresponds to the PT driving circuitry. Green corresponds to the optical diagnostic. Gray corresponds to the x-ray detection system. Pink corresponds to the linear translation stage system. Yellow corresponds to the vacuum system and diagnostics. Dotted lines for the current transformer, vacuum chamber, electric field shaper, and laser beam denote objects that have feedthroughs, viewports, or otherwise can have physical passage through the object.

An Agilent 33220A 20 MHz function/arbitrary waveform generator was used to initiate the driving signal for the PT. The function generator was set to output a sine wave with a 60.0 mV$_{pp}$ output voltage and 0 V offset. The frequency was varied until the input voltage and current were in phase which corresponded to mode 2 operation of the PT near 62 kHz. The function generator was set to operate in burst mode with 3,000 cycles per burst and a 1.0 s period. The "sync" output from the function generator was used as the trigger signal to sync the Tektronix TDS 2024C oscilloscope to the PT driving signal. The output signal from the function generator went to an Amplifier Research KAA1020 23 W, 43 dB gain rf amplifier. However, due to the impedance mismatch between the PT resonant input impedance of approximately 75 Ω and the rf amplifier output impedance of 50 Ω, 43 dB gain was never achieved. The output voltage amplitude from the rf amplifier varied from 7 – 12 V and was connected to the PT via a vacuum chamber feedthrough. The input current to the PT was measured using a Pearson 2877 1 V/A current transformer on the PT circuit board and was connected directly to the oscilloscope via the vacuum chamber feedthrough. Typical input current amplitudes were between 75 – 120 mA. Sample input current and voltage waveforms can be seen in Figure 3.10.
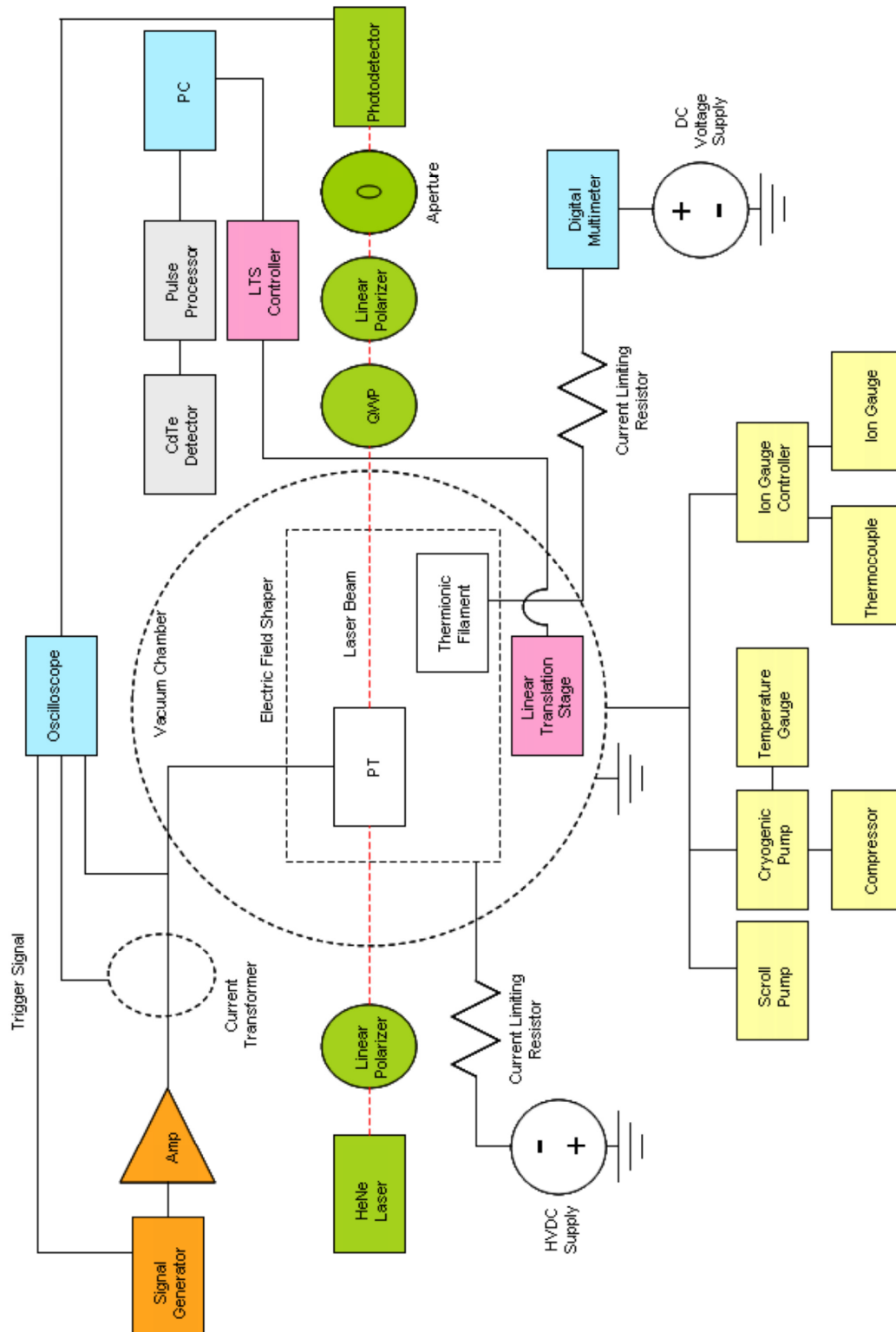
Figure 3.9: Experimental system diagram for characterizing the PT for varied load impedances.
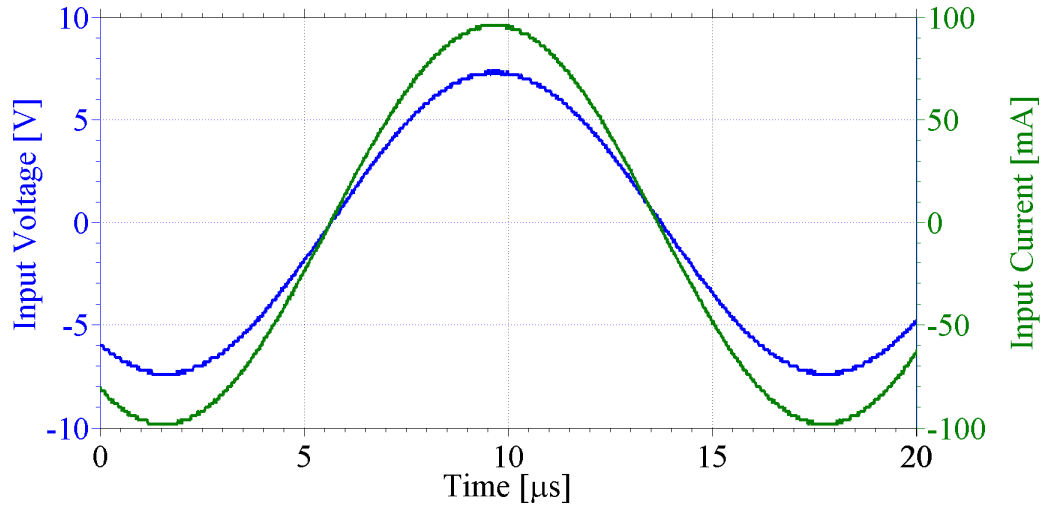
Figure 3.10: Sample input voltage and current waveforms for the PT operating in mode 2.

The Cambridge S style thermionic filament was heated using a BK Precision 1672 dc power supply in series with a 3 Ω, 25 W current limiting resistor and RadioShack digital multimeter. The filament current most frequently used was 2.3 A. This corresponded to sufficient electron emission to generate measurable x-ray count rates while reducing the risk of burning out the filament. As will be mentioned in more detail in the following section, a cylindrical electric field shaper was used to manipulate the trajectory of the electron beam. The electric field shaper was biased at a negative dc voltage, since the PT and the thermionic filament were inside the field shaper. A Power Design 2K20 high-voltage dc power supply was used to vary the bias voltage on the electric field shaper in series a 100 MΩ current limiting resistor in case of electrical breakdown. The bias voltage on the field shaper was varied between -1 kV – 0 V to vary the PT output current by changing the amount of electron beam current that hit the output

electrode. As previously mentioned, the x-rays were detected using an Amptek XR-100T x-ray detector with a 25 mm^2 detection area on the opposite side of a 635 μm thick aluminum window. The x-ray detector was controlled using an Amptek PX4 digital pulse processor, and the multichannel analyzer (MCA) spectrum was observed and recorded on a PC.

The optical diagnostic was used to measure the changing phase difference between the ordinary and extraordinary wave components of a laser beam due to the change in the refractive indices within the PT. The internal stress, electric field, and electric potential were calculated based on the phase change. The optical diagnostic is described in more detail in Chapter 4. Primary components of the optical diagnostic included a Melles Griot 5 mW, 632.8 nm helium neon (HeNe) laser, two linear polarizers, a quarter-wave plate, an aperture, and a ThorLabs DET110 photodetector. The laser beam entered the vacuum chamber via two optically transmissive vacuum viewports. The photodetector output was directly viewed and recorded on the oscilloscope. All optical components were on linear translation stages external to the vacuum chamber. This allowed for the PT to be probed at various positions along the length to generate profiles of electric field, stress, and electric potential. Additionally, the circuit board containing the PT, thermionic filament, and electric field shaper was mounted to a Micronix VT-21L linear translation stage controlled with a PC and Micronix MMC-200 controller. The vacuum-rated translation stage allowed for more lengths along the PT to be probed without restraint due to the diameter of the vacuum chamber viewports.

The vacuum system was evacuated down to 50 mTorr using a Varian TriScroll pump. A CTI-Cryogenics Cryo-Torr 100 cryogenic vacuum pump was capable of evacuating the system to less than 1 µTorr, but operating pressures of $10^{-6} - 10^{-5}$ Torr were most commonly used. A CTI-Cryogenics Model SC compressor was used to operate the cryogenic pump. A CTI-Cryogenics temperature indicator was used to measure the temperature of the cryogenic system. Temperatures less than 10 K were within the operating range of the pump. A Kurt J. Lesker KJL 600C-MC thermocouple was used to measure low vacuum pressures, while an ion gauge was used to measure high vacuum pressures. The readings from both vacuum pressure diagnostics were viewed on a JC Controls IG4500 ion gauge controller.

Electric Field Shaping

Initial electron-beam diode experiment results showed that the bremsstrahlung x-ray yield was greatly dependent on the relative PT placement within the vacuum chamber. This was attributed to unconstrained electric fields accelerating electrons such that they missed the target output electrode on the PT. Consequently, an electric field shaper was designed to constrain the electric fields in the vicinity of the PT and manipulate the trajectory of the electron beam. The electric field shaper was simulated using finite-element simulation software and successfully used in the experiment. By varying the bias potential on the field shaper, reliable high-energy x-ray count rates could be achieved and measured.

The chosen electric field shaper design used a cylindrical equipotential surface that surrounded the PT. The thermionic filament could be placed internally or externally to the field shaper depending on the polarity of the bias voltage. The chosen design for

the experiment had the thermionic filament internal to the field shaper with a negative field shaper bias voltage. In practice, the field shaper was a biased wire array in the form of a cylinder. A photograph of the field shaper is shown in Figure 3.11. A grounded wire mesh end cap was also used to constrain the axial electric fields (not shown in Figure 3.11). The wire cylinder had a 6 cm diameter and a 7.54 cm length with the PT radially centered in the cylinder. Lengthwise, the cylinder began at the midpoint (end of the input electrodes) of the PT and extended past the end of the PT. The thermionic filament was 1.4 – 1.5 cm axially away from the end of the PT and was at the radial edge of the cylinder.
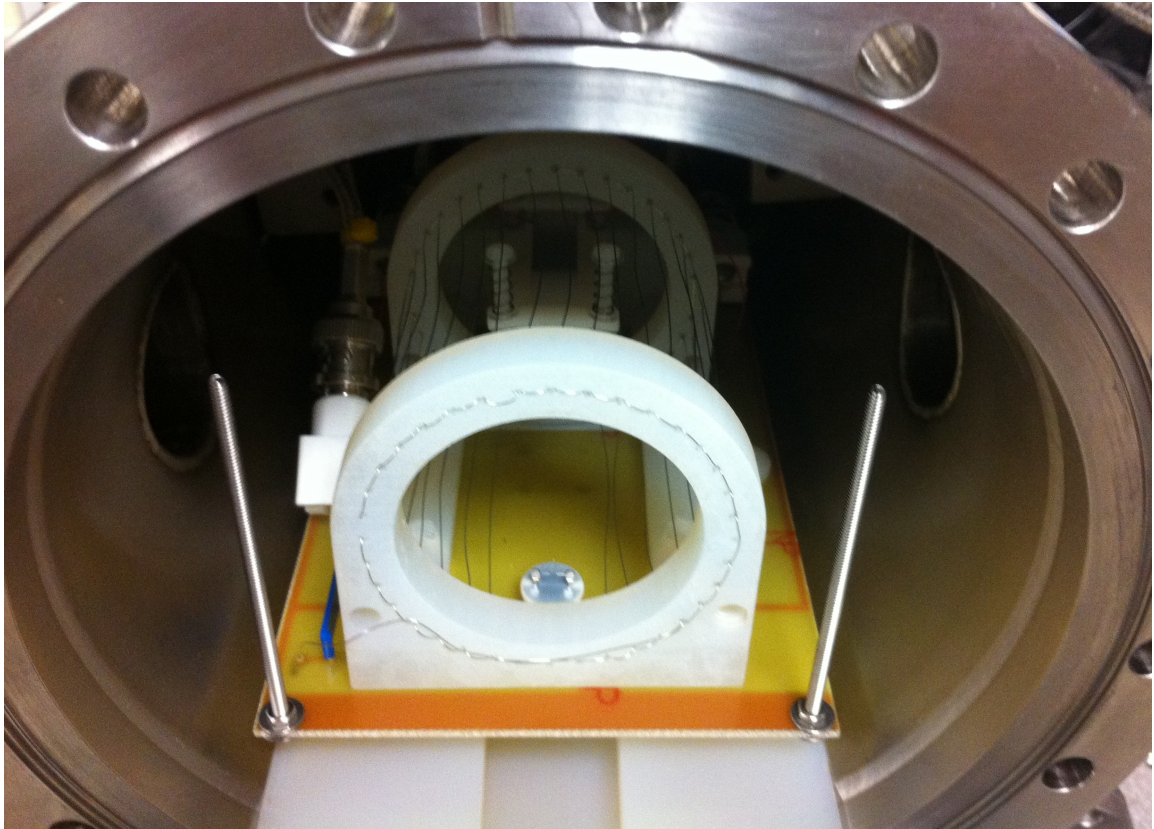
Figure 3.11: PT with electric field shaping cylinder inside the vacuum chamber.

Finite-element, particle ray tracing results are shown in Figure 3.12 to Figure 3.14. The finite-element simulations used a solid-walled, cylindrical tube with a solid disk end-cap. The output electrode of the PT was biased to +30 kV and the field shaper was biased to -300 V, while the thermionic filament and end-cap were grounded. The color scale in the figures represents the electric potential in volts in the plane of the PT. The particle ray tracing for the electrons is shown as the red lines in the figures. With the electric field shaper and PT in this configuration the electrons clearly impact the output electrode of the PT.

Experimentally, the electric field shaper shown in Figure 3.11 produced reliable high-energy x-ray spectra. A sample x-ray spectrum is shown in Figure 3.15 for a grounded electric field shaper. As will be shown in Chapter 5, the grounded field shaper did not necessarily result in the most electron current on the PT output electrode but did result in the highest x-ray count rate. Additionally, the discoloration on the PT shown in Figure 3.2 was due to operation of the PT with the electric field shaper. This discoloration was likely due to increased electron current impacting the PT surface which resulted in reduction/oxidation chemistry at the crystal surface. Such discoloration was not observed for a PT operated with a thermionic filament current under similar conditions without the electric field shaper.

X-Ray Fluorescence Experiments

In addition to using the endpoint energy of the x-ray spectra to verify the output voltage of the PT, x-ray fluorescence experiments were performed to measure x-ray fluorescence peaks at high energies. The PT was operated with the setup shown in
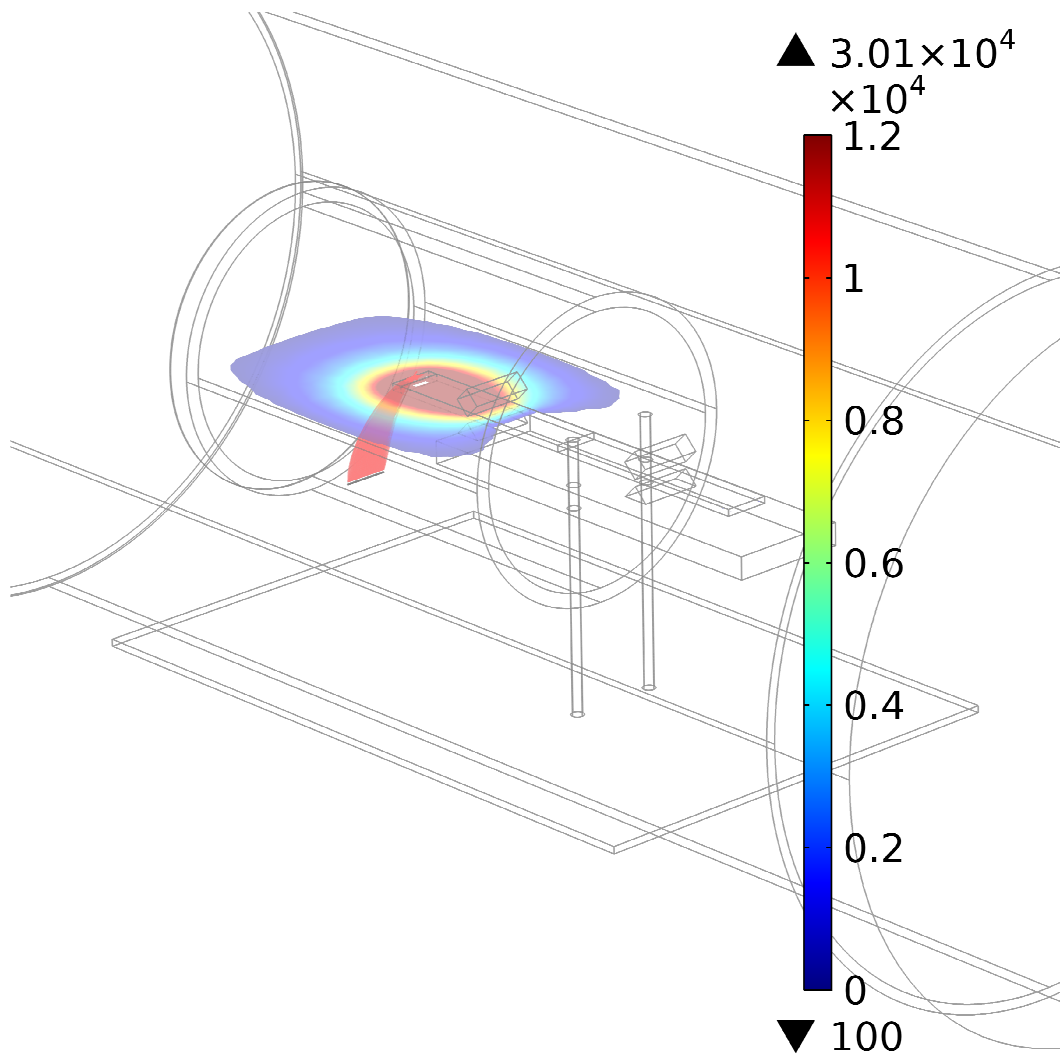
Figure 3.12: **Finite-element simulation results of the electric field shaper. The color bar corresponds to the electric potential in volts.**
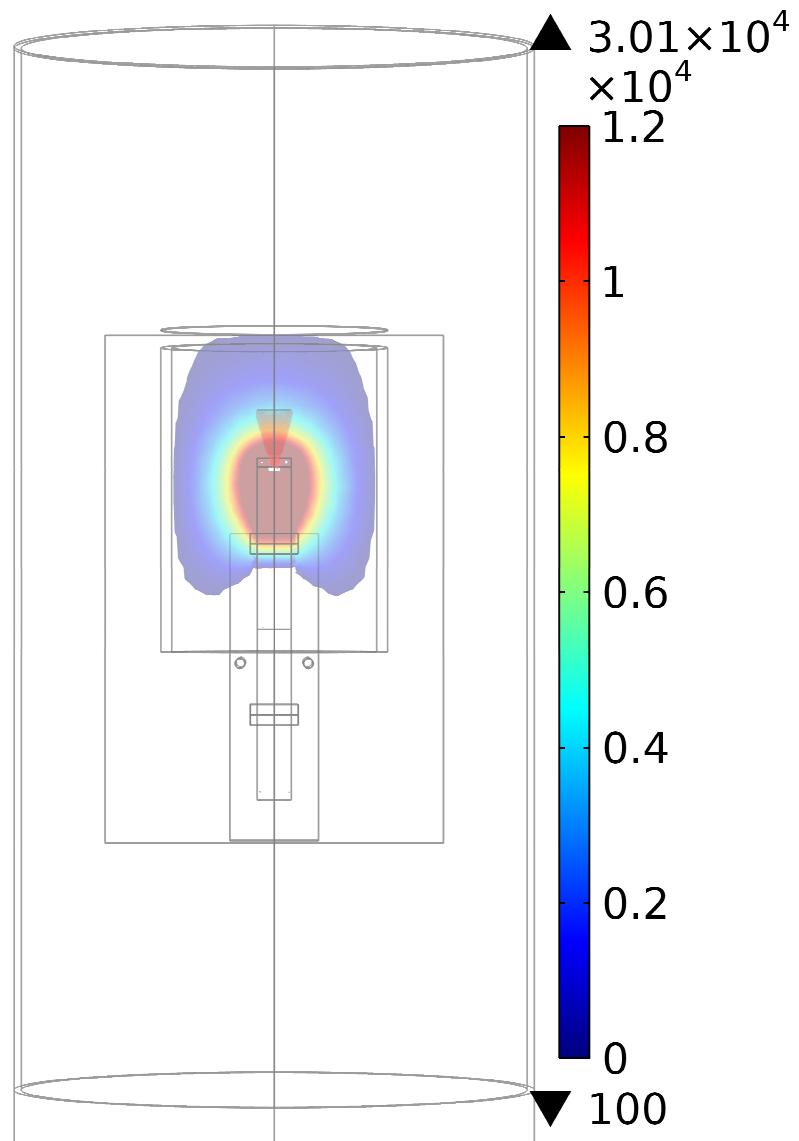
Figure 3.13: (Top-down view) Finite-element simulation results of the electric field shaper. The color bar corresponds to the electric potential in volts.
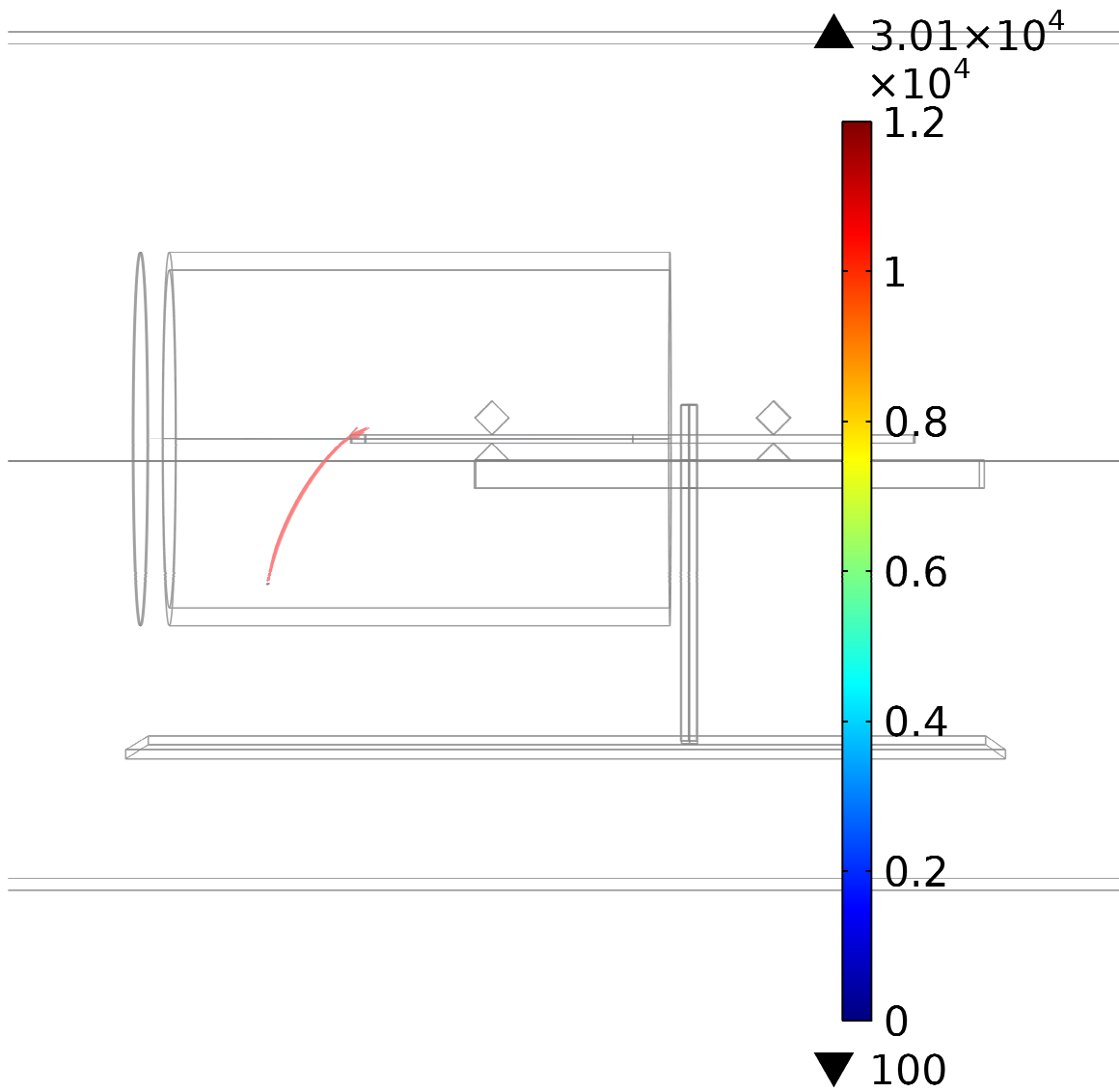
Figure 3.14: (Side view) Finite-element simulation results of the electric field shaper. The color bar corresponds to the electric potential in volts.
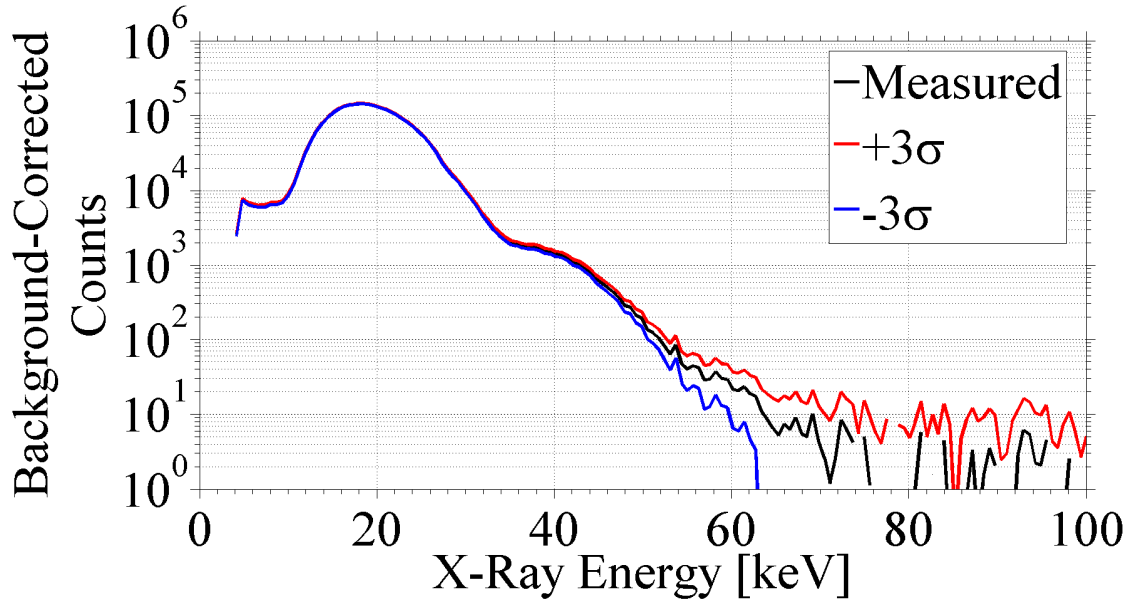
Figure 3.15: **X-ray spectrum with a background pressure of approximately 5 μTorr. Measured data along with ± 3 standard deviations are shown.**

Figure 3.11 inside the vacuum chamber and Figure 3.16 outside the vacuum chamber. The excitation of fluorescence peaks in the lead (Pb) and molybdenum (Mo) targets due to the x-rays generated by the PT were measured using the CdTe x-ray detector. A lead shield was used to prevent the x-ray detector from directly measuring the bremsstrahlung x-rays. The PT was operated at its second harmonic frequency of approximately 62 kHz with a 20% duty cycle on 500 ms burst periods. The CdTe detector was gated such that counts were only detected during the times that the PT was resonating. High-voltage PT operation was verified using both the endpoint energy of the x-ray signal scattered off of the targets and the observed fluorescence peaks [53], [54]. A sample spectrum for this experiment is shown in Figure 3.17.
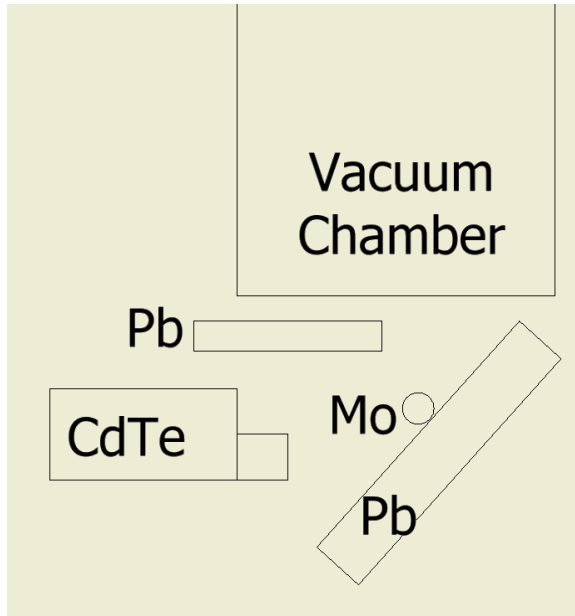
Figure 3.16: Experimental setup for the fluorescence peak counting.
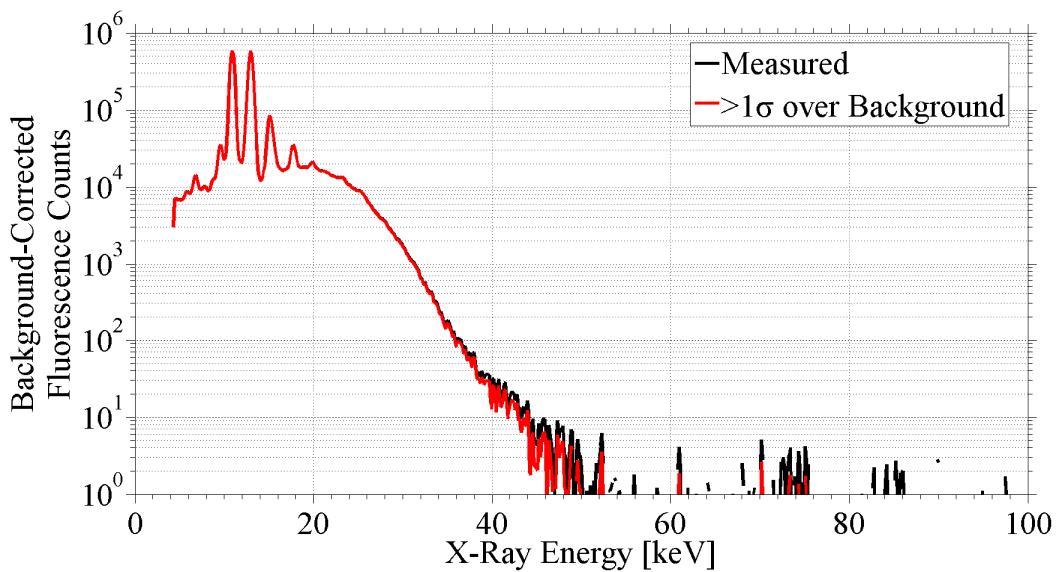
Figure 3.17:   Sample x-ray fluorescence spectrum with lead and molybdenum fluorescence peaks.   The bremsstrahlung-like portion of the spectrum is due to scattered x-rays off of the fluorescence targets.

4. Diagnostic Design

This chapter outlines the diagnostics used to characterize the piezoelectric transformer (PT). A bremsstrahlung x-ray diagnostic previously used by other researchers is briefly discussed. The development of an optical diagnostic to probe the internal characteristics of the PT such as stress, electric field, and electric potential is presented. Finally, a diagnostic based on the input and output quality factors (Q-values) of the PT that was used to confirm the optical diagnostic is presented.

Bremsstrahlung X-Ray Diagnostic

As the electrons were accelerated by the PT in the electron-beam diode experiments, the electrons achieved an energy approximately equal to the accelerating potential (i.e. 10 keV of final electron kinetic energy corresponds to a 10 kV accelerating potential produced by the PT). The interaction between the electrons and the atoms in the silver paint of the PT output electrode resulted in a conversion of energy from electron kinetic energy to photon energy in the form of x-rays. This is known as bremsstrahlung,

or braking, radiation and is energetically broadband radiation [54]. The maximum, or endpoint, energy of the broadband x-ray radiation corresponds to the maximum incident electron energy. Since the electron kinetic energy was approximately equal to the accelerating potential, the endpoint energy of the x-ray spectrum was used as a diagnostic to characterize the output voltage of the PT. The same approach for determining the PT output voltage was previously used by Benwell and Gall [19], [20], [26], [27].

The bremsstrahlung x-rays were detected using a cadmium telluride (CdTe) x-ray detector and the energy spectrum was viewed using a 1,024 channel multichannel analyzer (MCA). A 14 hour background count was normalized to the counting time of each spectrum and subtracted from the corresponding collected spectrum to determine the number of counts due to the x-ray source. The energy distribution for each channel of the MCA can be assumed to be a Poisson distribution about the mean energy of the respective channel [55]. The source and background standard deviations were calculated using Equation 4.1 and Equation 4.2, respectively, where σ_S is the standard deviation of the source counts, N_S is the number of background-corrected counts in the channel due to the source, σ_B is the standard deviation of the background counts, and N_B is the number of counts in the channel due to background. The standard deviation for each channel was determined using Equation 4.3 where σ_T is the total standard deviation [55].

$$\sigma_S = \sqrt{N_S}$$

Equation 4.1

65

$$\sigma_B = \sqrt{N_B}$$

Equation 4.2

$$\sigma_T = \sqrt{\sigma_S^2 + \sigma_B^2}$$

Equation 4.3

Equation 4.4 was used to determine whether the number of counts due to the source was statistically above background radiation levels where N is the number of counts statistically above background, N_T is the detected number of counts and n is the chosen number of standard deviations. The mean energy of the highest channel that had counts statistically above background was said to have been the PT output voltage. Table 4.1 shows the probabilities that the background-corrected number of counts was actually above background radiation levels [55], [56]. Channels that had background-corrected counts greater than one standard deviation above zero had a 84.13 % probability of being above background, while channels that had background-corrected counts greater than three standard deviation above zero had a 99.87 % probability of being above

$$N = \left(N_T - N_B\right) - n\sigma_T$$

Equation 4.4

Table 4.1: Probabilities that detected counts were above background based on the number of standard deviations above background.

Number of Standard Deviations above Background	Probability that Detected Counts Were above Background
1	84.13 %
1.64	94.95 %
2	97.72 %
3	99.87 %

background.   A common standard of 1.64 standard deviations above zero corresponds to an approximately 95 % probability that the counts were above background [55], [57].

Optical Diagnostic

An optical diagnostic was developed to measure the internal longitudinal stress and electric field within the operating PT [58]. This diagnostic takes advantage of the photoelastic and electro-optic effects that occur within lithium niobate by modulating the intensity of an externally supplied laser probe. Although lithium niobate is a naturally birefringent material, the combined effects of the electric field and stress in the resonating PT cause the polarization phase difference to be time dependent [31]. A linearly polarized laser beam entering the PT along the x'-direction, as shown in Figure 2.2, exits the PT with a time-dependant elliptical polarization due to the change in the refractive indices. As such, the optical diagnostic may be used to determine the frequency, time-varying output electric field, and phase difference of the output voltage with respect to

the input voltage, but the profiles of the electric field and stress magnitudes as a function of position that are of primary interest in this work to describe internal PT operation.

Mathematical Theory

Photoelastic Effect

The photoelastic effect is the linear change in a material's refractive index due to an applied stress [34]. The change in the refractive index is typically found using the difference between the impermeability tensors for the stressed crystal and the undeformed state of the crystal which are denoted by B_i and B_i^0, respectively, when written using the single-suffix notation, also known as Einstein notation [32], [34]. The general form of this expression is shown in different forms in Equation 4.5 and Equation 4.6 where n_i' are the rotated stressed refractive indices, $n_i'^0$ are the rotated undeformed refractive indices, q_{ij}' are the rotated stress-optical coefficients, and T_j are the applied stresses. Subscripts i and j correspond to the direction of the subscripted variables. For instance, n_1' corresponds to the rotated refractive index for wave components in the x'-direction, while n_3' corresponds to the rotated refractive index for wave components in the z'-direction. Values of i or j from 1-3 correspond to the tensile, or linear,

$$\Delta B_i = B_i - B_i^0 = \left(\frac{1}{n_i'}\right)^2 - \left(\frac{1}{n_i'^0}\right)^2 = \Delta\left(\frac{1}{n_i'}\right)^2 \quad i = 1...6$$

Equation 4.5

$$\Delta \left(\frac{1}{n_i'} \right)^2 = \sum_{j=1}^{6} q_{ij}' T_j \quad i = 1...6$$

Equation 4.6

components, while 4-6 correspond to the shear, or tangential, components of the respective variable [34].

Stress in the output section of the PT is induced from the vibrational resonance established by the applied input voltage and the converse piezoelectric effect. Assuming that motion in the PT is limited only to deformation along the *y*-direction due to the length-extensional mode of operation, Equation 4.6 can be simplified further to Equation 4.7 to obtain the equations needed to determine the refractive indices for an optical signal propagating in the *-x'*-direction as shown in Figure 2.2 [9], [19], [20]. The change in refractive indices can be determined using the approximation $\Delta(1/n)^2 \approx -2n^{-3}\Delta n$ and algebraic manipulation [33], [34]. Simplified expressions for the relevant changes in refractive indices due to the photoelastic effect are shown in Equation 4.8 and Equation 4.9. Equation 4.8 corresponds to the extraordinary wave component, and Equation 4.9 corresponds to the ordinary wave component of an optical wave propagating in the *-x'*-direction. The ordinary wave component along the optic axis propagates at a constant velocity, while the extraordinary wave component propagates at a velocity dependent on the angle between the optic axis and the direction of propagation [59].

$$\Delta\left(\frac{1}{n'_2}\right)^2 = q'_{22}T_2$$

$$\Delta\left(\frac{1}{n'_3}\right)^2 = q'_{32}T_2$$

Equation 4.7

$$\Delta n'_2 = \Delta n'_o = -\frac{1}{2}\left(n'^0_y\right)^3\left(q'_{22}T_2\right)$$

Equation 4.8

$$\Delta n'_3 = \Delta n'_e = -\frac{1}{2}\left(n'^0_z\right)^3\left(q'_{32}T_2\right)$$

Equation 4.9

Electro-optic Effect

The first-order electro-optic effect, also known as the Pockels effect, is the linear change in the refractive index of a material due to an applied electric field [34]. The Pockels effect can appear as a "false" photoelastic effect in a piezoelectric material because an applied stress will induce an electric field based on the direct piezoelectric effect [39]. Higher order effects of the electro-optic response are neglected due to the dominance of the first order effect. The general form for the change in the refractive

index takes a similar form to that of the photoelastic effect as is shown in Equation 4.10 where r'_{ij} are the rotated electro-optic coefficients and E_j are the applied electric fields.

$$\Delta\left(\frac{1}{n'_i}\right)^2 = \sum_{j=1}^{3} r'_{ij} E_j \quad i = 1...6$$

Equation 4.10

Working under the assumption that the PT is limited only to deformation along the y'-direction due to the length-extensional mode of operation, Equation 4.10 can be simplified to determine only the relevant changes in refractive indices as shown in Equation 4.11. Simplification yields the changes in refractive indices shown in Equation 4.12 and Equation 4.13 for the ordinary and extraordinary wave components, respectively, of the propagating optical wave due to the first-order electro-optic effect.

$$\Delta\left(\frac{1}{n'_2}\right)^2 = r'_{22} E_2$$
$$\Delta\left(\frac{1}{n'_3}\right)^2 = r'_{32} E_2$$

Equation 4.11

$$\Delta n_2' = \Delta n_o' = -\frac{1}{2}\left(n_y'^0\right)^3 \left(r_{22}' E_2\right)$$

Equation 4.12

$$\Delta n_3' = \Delta n_e' = -\frac{1}{2}\left(n_z'^0\right)^3 \left(r_{32}' E_2\right)$$

Equation 4.13

Linear Superposition of Effects

Although the photoelastic and electro-optic effects are two distinct phenomena, their individual effects on the change in refractive index for a piezoelectric material cannot be observed directly. Instead, a linear superposition of the two effects must be used to account for both the stress in the output section of the PT due to the mechanical vibration and the electric field induced by the stress. The resultant changes in the relevant refractive indices due to the superposition of the two effects are shown in Equation 4.14 and Equation 4.15

$$\Delta n_2' = \Delta n_o' = -\frac{1}{2}\left(n_y'^0\right)^3 \left(q_{22}' T_2 + r_{22}' E_2\right)$$

Equation 4.14

$$\Delta n_3' = \Delta n_e' = -\frac{1}{2}\left(n_z'^0\right)^3 \left(q_{32}' T_2 + r_{32}' E_2\right)$$

Equation 4.15

As an optical wave propagates through the material in the x'-direction, the changes in refractive indices result in a change in relative phase between the ordinary and extraordinary components of the propagating wave. The change in relative phase difference between the ordinary and extraordinary wave components, $\Delta\phi$, in Equation 4.16 is a function of the length, L, traveled through the medium, the wavelength of the optical traveling wave, λ [32], [33], [39]. This change in relative phase difference corresponds to a change in polarization state of the traveling wave. For the case of the PT, the internal stress and electric field are constantly changing due to the sinusoidal nature of the input voltage.

$$\Delta\phi = \frac{2\pi L}{\lambda}\left(\Delta n_e' - \Delta n_o'\right)$$

Equation 4.16

It now becomes convenient to expand the constants' subscript indices into two-suffix notation to directly correspond to the constants' relative matrix positions. The piezoelectric constitutive relationship between the longitudinal electric flux density, D_2, electric field, E_2, and stress, T_2, is shown in Equation 4.17 where ε_{22}' is the rotated

permittivity of the material and d'_{22} is the rotated piezoelectric strain coefficient. The final expression for the longitudinal stress in the PT is found using Equation 4.14 - Equation 4.17 and is shown in Equation 4.18. It is necessary to use the boundary conditions of the device to determine the longitudinal electric flux density, D_2. Assuming one-dimensional displacement as was done previously, the stress at the output electrode of the PT must be equal to zero. Therefore, the entire change in phase difference at the output electrode is due to the electro-optic effect, and D_2 can be found using Equation 4.17 and Equation 4.19. Since D_2 is constant throughout the output section of the PT, the longitudinal electric field and stress can also be determined throughout the output section of the PT using Equation 4.17 and Equation 4.18 [28]. Table 4.2 shows the specific values for lithium niobate material constants and laser parameters that were used for optical diagnostic calculations.

$$D_2 = \varepsilon'_{22} E_2 + d'_{22} T_2$$

Equation 4.17

$$T_2 = \frac{\pi D_2 L \left(n'^{0^3}_{22} r'_{22} - n'^{0^3}_{33} r'_{32} \right) - \varepsilon'_{22} \lambda (\Delta\phi)}{\pi L \left[d'_{22} \left(n'^{0^3}_{22} r'_{22} - n'^{0^3}_{33} r'_{32} \right) - \varepsilon'_{22} \left(n'^{0^3}_{22} q'_{22} - n'^{0^3}_{33} q'_{32} \right) \right]}$$

Equation 4.18

$$E_2 = \frac{\lambda(\Delta\phi)}{\pi L\left(n_{22}'^{0\,3} r_{22}' - n_{33}'^{0\,3} r_{32}'\right)} \; , \quad T_2 = 0$$

Equation 4.19

Optical Diagnostic Setup

The experimental setup shown in Figure 4.1 was used to determine the change in phase difference between the ordinary and extraordinary wave components for the optical traveling wave when the PT was operating at the resonant frequency. The long edges of

Table 4.2. Parameters used for optical diagnostic calculations.

Unrotated Parameters		Rotated Parameters	
Parameter	Value	Parameter	Value
n_2^0 [unitless]	2.291	$n_2'^0$ [unitless]	2.2458
n_3^0 [unitless]	2.2005	$n_3'^0$ [unitless]	2.2458
q_{32} [m^2/N]	7.597 x 10^{-13}	q_{32}' [m^2/N]	-2.074 x 10^{-12}
q_{22} [m^2/N]	-1.349 x 10^{-13}	q_{22}' [m^2/N]	1.965 x 10^{-12}
r_{32} [m/V]	0	r_{32}' [m/V]	1.24 x 10^{-12}
r_{22} [m/V]	3.40 x 10^{-12}	r_{22}' [m/V]	2.698 x 10^{-11}
ε_{22} [F/m]	7.439 x 10^{-10} $- j7.78$ x 10^{-13}	ε_{22}' [F/m]	5.041 x 10^{-10} $- j4.24$ x 10^{-12}
d_{22} [C/N]	2.074 x 10^{-11}	d_{22}' [C/N]	3.308 x 10^{-11}
L [m]	0.01	L' [m]	0.01
λ [m]	632.8 x 10^{-9}	λ' [m]	N/A

the lithium niobate slab were polished using the procedure outlined by Norgard and Kovaleski to reduce optical loss at the crystal boundaries [36]. The PT was operated in a vacuum chamber to prevent corona discharge at the electrodes and to permit electron-beam loads. The laser and associated optical components were moved with respect to the PT along the longitudinal axis of the PT to measure the change in phase difference at different positions. Due to the limited viewing range on the vacuum chamber viewports, only a 25 mm section near the output electrode of the PT (corresponding to 75 mm to 100 mm of the overall 100 mm length) was probed during the optical diagnostic verification. Additional positions along the length of the PT were accessible for the results in Chapter 5 by using a vacuum-rated linear translation stage to move the PT position within the vacuum chamber.
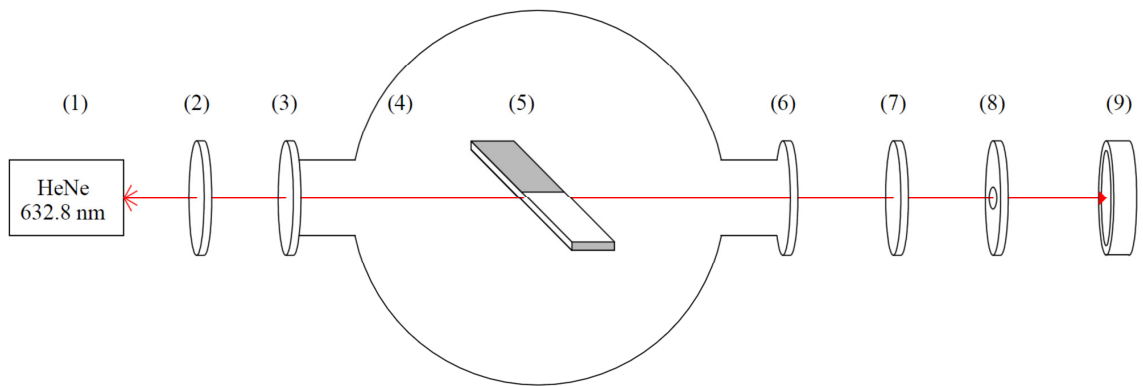
Figure 4.1: Optical diagnostic setup. (1) Helium-neon (HeNe) laser (632.8 nm), (2) Linear polarizer, (3) Vacuum chamber viewport, (4) Vacuum chamber, (5) Piezoelectric transformer (PT), (6) Vacuum chamber viewport, (7) Analyzing linear polarizer, (8) Aperture, (9) Photodetector

A 5 mW, helium-neon (HeNe) laser with a 632.8 nm ± 0.5 nm wavelength was used as the light source for the optical diagnostic. The laser beam passed through a linear polarizer oriented along the z'-axis of the PT as shown in Figure 2.2 (or 45° rotated from the polarization axis of the lithium niobate bar) such that ordinary and extraordinary wave components had equal intensities as the beam entered the cross-section of the PT. Conflat flange viewports were used to pass the beam into the vacuum chamber and back out again. These viewports were shown to have negligible effects on intensity and polarization of the beam. An analyzing polarizer was used to filter out the ordinary wave component and yield a sinusoidal beam intensity for the varying change in phase difference. A 6.35 mm (0.25 in) diameter aperture was used immediately prior to the photodetector to reduce noise on the photodetector signal due to ambient light.

The optical diagnostic was tested at various positions along the final 25 mm section of the PT for two different electrical loads. The first load was an electron beam accelerated by the PT where the electrons were emitted from a thermionic filament. This configuration was similar to that described in the "High-Voltage Load Testing in Vacuum" section of Chapter 3 but without the electric field shaper. Bremsstrahlung x-rays produced at the output electrode were used as a voltage diagnostic for the PT output voltage when using the electron beam load [19], [20]. The second load was a Tektronix P6015A voltage probe. The output signal for the voltage probe was used to measure the output voltage when using the voltage probe load. The voltage probe could not be used as a PT output voltage diagnostic for electron beam experiments due to the low total impedance of the probe which was approximately 850 kΩ. The PT voltage transformation ratio was dependent on load impedance and high accelerating potentials

for the electron beam could not be achieved with lower load impedance [9], [28], [29]. Even a capacitive divider with a total capacitance of 1 pF, which corresponds to an impedance of approximately 2.5 MΩ at the mode 2 resonant frequency, would result in lower PT voltage transformation ratios.

Diagnostic Verification

Figure 4.2 shows a sample of the photodetector output signal versus the input voltage where each signal is averaged over 64 burst cycles of the PT to filter out ambient optical noise on the photodetector. Based on the linear polarizer configuration described in the previous section, each change in the slope of the photodetector output signal from positive to negative, or vice versa, corresponded to a change in phase difference, $\Delta\phi$, of $\pi/2$ radians between the ordinary and extraordinary wave components of the laser beam. The period of the output stress, electric field, and voltage were each approximately 16 μs, since each parameter had the same period as the applied input voltage. The magnitudes of the stress and electric field were determined using Equation 4.20 where $\Delta\phi$ was the total change in phase difference for a quarter period of the applied input voltage and a was the number of zero crossings in the slope of the photodetector signal [45]. For instance, if there were ten zero crossings ($a = 7$) in the slope of the photodetector signal within a quarter period of the input voltage, then the magnitude of the stress and electric field at that point can be found using a total change in phase difference of 3.5π radians $\pm$ $\pi/2$ radians.
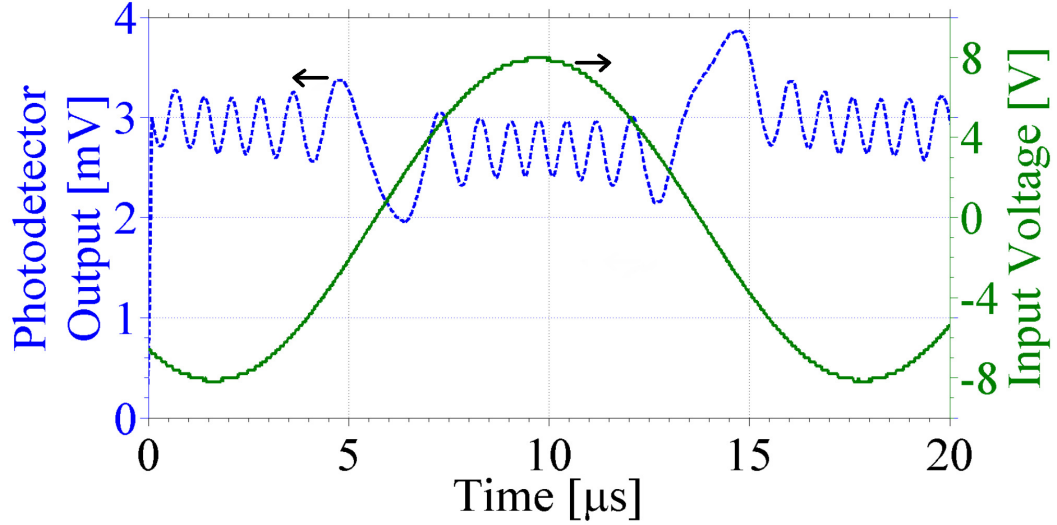
Figure 4.2: Sample waveforms of the PT input voltage signal (solid and green) and optical detector signal (dotted and blue). One period for the input voltage corresponds to one period for the output voltage, electric field, and stress.

$$\Delta\phi = a\frac{\pi}{2} \quad \text{[radians]}$$

Equation 4.20

Sénarmont compensator

Although not used during the optical diagnostic verification process described in this chapter, a quarter-wave plate (QWP) was added to the optical diagnostic for the results shown in Chapter 5. The addition of the QWP was to make the optical signal more symmetric about the mean of the signal. The altered configuration with optical components (7) and (8) as shown in Figure 4.3 is known as a Sénarmont compensator which is used for characterizing elliptical polarization [60]. The quarter-wave plate

introduced an additional 90° phase shift between the ordinary and extraordinary wave-components of the time-changing elliptical polarization state that exited the PT.

For comparison, the optical diagnostic was tested under the same PT operating conditions of 4.5 mTorr vacuum with an "open-circuit" load both with and without the quarter-wave plate. Figure 4.4 shows the photodetector signal from the optical diagnostic without the QWP (i.e. using only linear polarizers). Although the number of $\pi/2$ phase transitions can be counted manually, there is no simple algorithm for determining the number of transitions computationally. This was due to the asymmetry of the photodetector signal. Figure 4.5 shows the optical diagnostic output signal when the quarter-wave plate was inserted with the QWP's fast axis aligned with the axis of the analyzing linear polarizer. The number of $\pi/2$ phase transitions was the same, but the photodetector signal with the QWP was nearly symmetric about a 5 mV value. In theory,
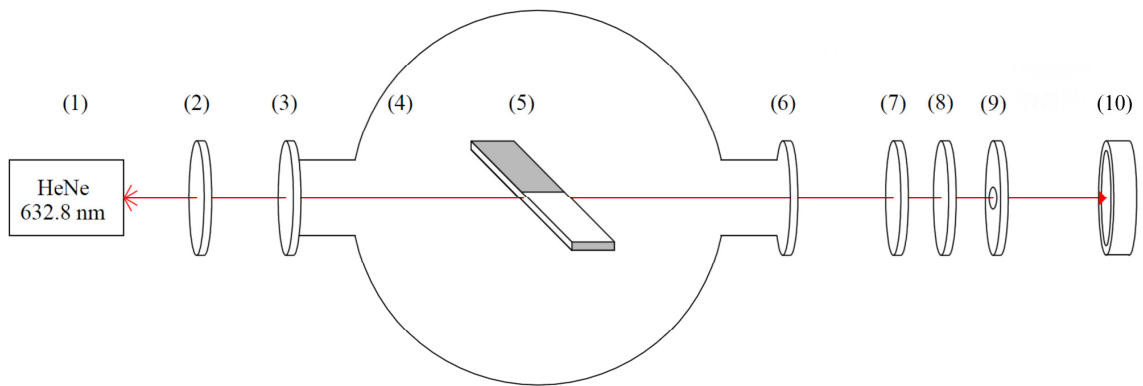
Figure 4.3: Optical diagnostic setup. (1) Helium-neon (HeNe) laser (632.8 nm), (2) Linear polarizer, (3) Vacuum chamber viewport, (4) Vacuum chamber, (5) Piezoelectric transformer (PT), (6) Vacuum chamber viewport, (7) Quarter-Wave Plate, (8) Analyzing linear polarizer, (9) Aperture, (10) Photodetector
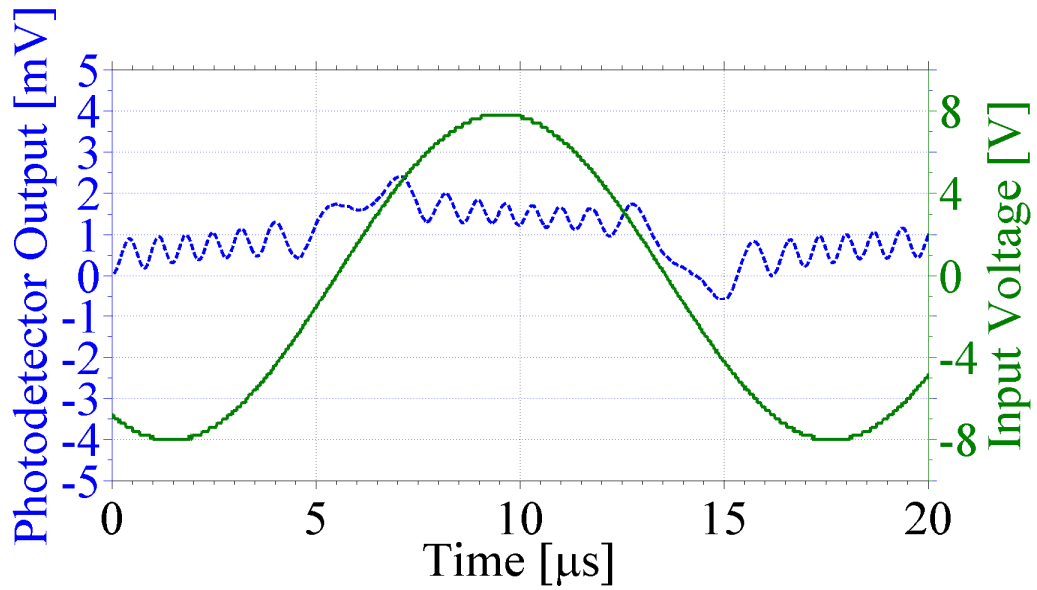
Figure 4.4: Optical diagnostic signal without the quarter-wave plate. The input voltage signal for the PT is also shown for reference purposes.
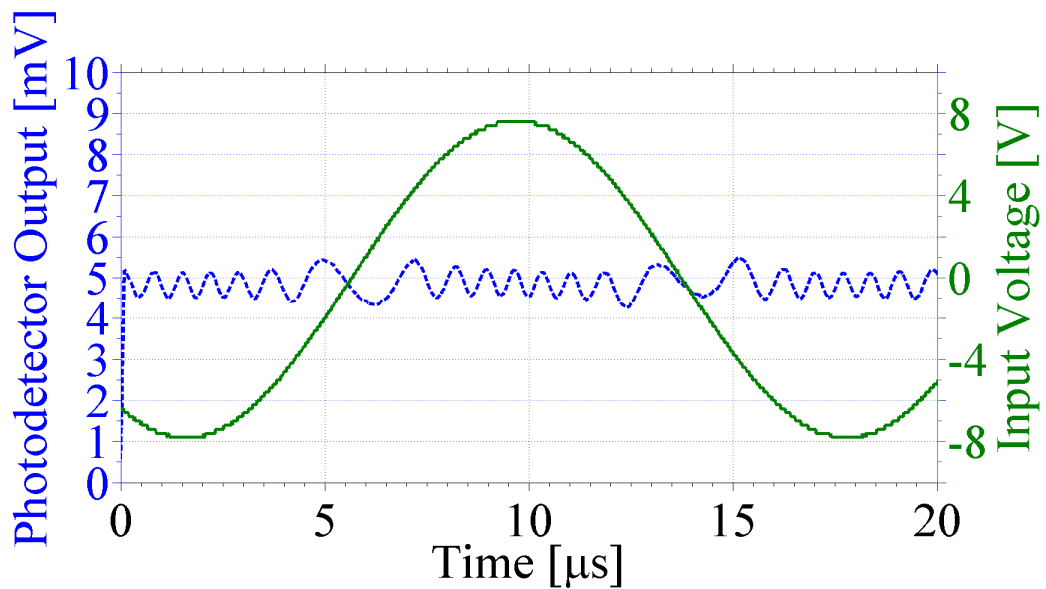
Figure 4.5: Optical diagnostic signal with the quarter-wave plate. The input voltage signal for the PT is also shown for reference purposes. Note the symmetry of the photodetector output about 5 mV.

this symmetry should have simplified data analysis. The mean voltage of the photodetector output could be calculated. The number of times that the photodetector signal crossed that mean is then equal to the number of $\pi/2$ phase transitions due to the photoelastic and electro-optic effects in the PT. However, the optical rotation of the elliptical wave exiting the crystal was dependent on the position along the length. Although the Sénarmont compensator configuration was useful at certain positions along the PT length, the number of $\pi/2$ phase transitions had to be counted manually to ensure that the correct number of $\pi/2$ phase transitions.

Comparison with Models

Experimental results were compared to simulated results from two different models of the PT. The first model assumed one-dimensional (1-D) motion in the PT due to a single longitudinal mode of vibration, while the second model was a three-dimensional finite-element model that accounted for 3-D motion due to simultaneous higher-order modes of vibration being established. Both simulation methods used the geometry of the PT shown in Figure 2.2, the parallel *RC* load configuration shown in Figure 2.3 and solved the piezoelectric equations with material constants that were rotated using Equation 2.5. The models included identical loss factors for the mechanical and dielectric losses and were simulated for the same input voltages and electrical loads [38], [45], [61]. The 1-D model provided approximate solutions that were less computationally intensive, and the 3-D model provided higher fidelity results that more closely matched experimental results for a wider range of electrical loading.

The 1-D model assumed motion in the PT only along the longitudinal direction as developed by Yang and Zhang and solved the piezoelectric constitutive equations shown

82

in Equation 4.21 and Equation 4.22 where S_{ij} are the internal strains and s'_{ijkl} are the

rotated elastic compliance coefficients [28]. As shown in Figure 2.2, the input voltage

was applied across the thickness along half the PT, while the output voltage was formed

between the electrode on the end of the PT and the grounded input electrode. The

necessary boundary conditions used to solve the equations in the 1-D model included the

stress and electric field being continuous between the input and output sections and the

stress at each end of the PT must equal zero [9], [28]. Time-harmonic solutions at the

resonant frequency were determined for output voltage, internal electric fields, and

internal stresses. This 1-D model was a fast-executing approximation that yielded

solutions for the electric field and stress components in minutes.

$$D_i = \varepsilon'_{ij} E_j + d'_{ijk} T_{jk} \quad i,j,k = 1,2,3$$

Equation 4.21

$$S_{ij} = s'_{ijkl} T_{kl} + d'_{kij} E_k \quad i,j,k,l = 1,2,3$$

Equation 4.22

The 3-D model was simulated using a commercially-available three-dimensional

finite-element simulation package and solved partial differential equations of the system

for the respective stresses, electric fields, and strains in all directions [38]. The boundary

conditions for the 3-D model were the same as 1-D model with the exception that

83

mechanical displacement was permitted in all three principal axes rather than just along one axis. First-order vibrational modes resulted in similar longitudinal vibration as in the 1-D model, but higher-order modes due to system nonlinearity were also allowed to form in any direction. As such, the 3-D model produced results that were more physical in nature but could take several hours to solve depending on the desired resolution.

A least-squares curve fitting technique relating the 1-D simulated and experimental results was used to identify the load impedance values for both the voltage probe and electron beam loads [62], [63]. The load impedance was varied in the model to determine the impedance that minimized the error between the simulated and measured electric field, stress, and output voltage. For the voltage probe load, an additional arbitrary constant was fit as a scaling factor for the electric field, stress, and output voltage to place added emphasis on the zero crossing point in the electric field profile. Curve fitting was used to determine the stray capacitance formed due to a wire that ran along the vacuum chamber wall to connect the output electrode of the PT to the voltage probe. The known 100 MΩ, 3 pF impedance of the probe in parallel with the fitted stray capacitance was used as the modeled load impedance. Curve fitting results from the 1-D model were used as initial estimates for the 3-D model. Due to the differences between the 1-D and 3-D models for the lower impedance load, discussed in more detail in subsequent sections, a curve fitting was also done in the 3-D model to better match the experimental results. The impedance that minimized the error between 3-D results and experimental results was then simulated in both the 1-D and 3-D models. For the case of the electron beam load, the beam resistance and capacitance were determined using the

1-D curve fitting. The determined electron beam load impedance was then simulated using the computationally intensive 3-D finite-element model.

Electron Beam Load

The electrical equivalent of the electron beam load was determined to be an approximately 94 GΩ resistance in parallel with a 0.05 pF capacitance by using the mechanical quality factor, the effective electrical quality factor, and the PT equivalent electromechanical circuit [15]. Figure 4.6 shows the simulated and measured number of $\pi/2$ phase changes that occurred within a quarter period of the input voltage for varying positions along the length of the PT for the electron beam load. Simulated results after curve fitting correspond to an electrical load of 91.2 GΩ in parallel with 0.047 pF. Figure 4.6 also shows the simulated number of $\pi/2$ phase changes that occurred due to the individual electro-optic and photoelastic effects. The number of $\pi/2$ phase changes due to the photoelastic effect was greater than the number due to the electro-optic effect with the exception of the end near the output electrode. The total simulated number of $\pi/2$ phase changes accounted for the relative time-harmonic phase difference between the stress and electric field caused by the various loss mechanisms in the PT [45]. Because the relative directions of the stress and electric field were not in phase throughout the length of the PT, the photoelastic and electro-optic effects add or subtract from one another accordingly. The greatest change in optical phase difference occurred near a vibrational null point of the PT, further indicating that the photoelastic effect had a greater influence than the electro-optic effect.

Figure 4.7 shows the simulated and measured longitudinal stress magnitudes along the PT, while Figure 4.8 shows the simulated and measured longitudinal electric
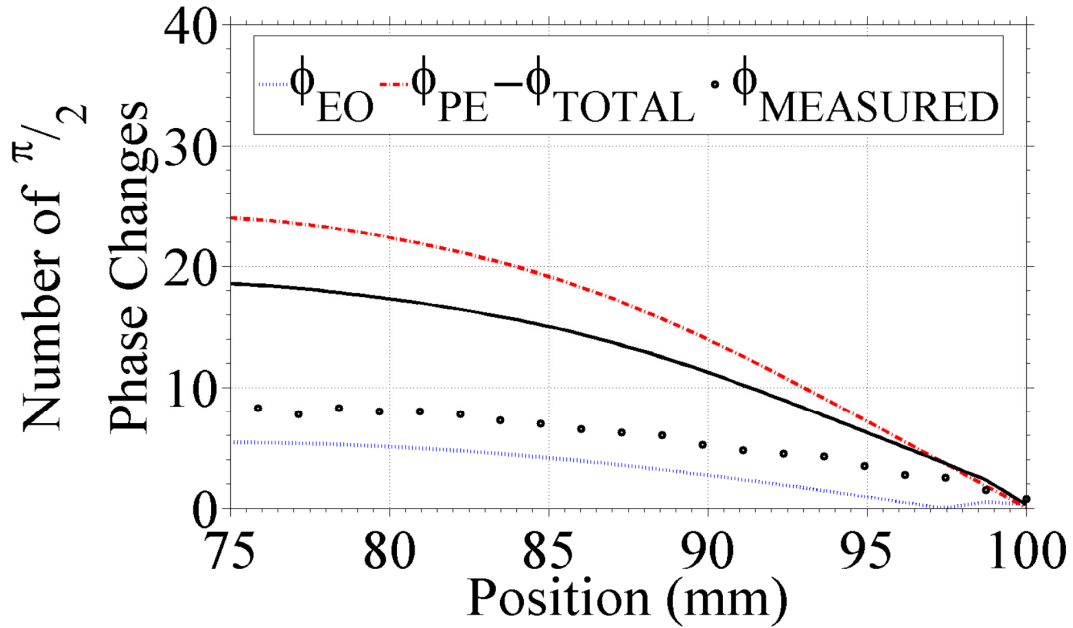
Figure 4.6: Number of π/2 phase changes for an electron beam as a load that was used to determine electric field and stress in the PT.

field magnitudes for the electron beam load. The maximum measured stress occurred near the vibrational null point, and the minimum stress occurred near the output electrode. The stress at these two points corresponds to the boundary conditions of the device. Additionally, the 10 MPa maximum stress was below the 30 − 150 MPa yield stress of lithium niobate [50]. The maximum electric field observed in the probed section of the PT was approximately 5.5 kV/cm which was well below 200 kV/cm where dielectric breakdown has been observed for lithium niobate [64]. The abrupt change in electric field magnitude between 95 mm and 100 mm corresponded to a 180° phase change in the electric field due to a local maximum in the electric potential profile. Although the 3-D model results showed stresses that were higher than the 1-D model results, the simulated electric fields for both models were in agreement with the measured

values. Both sets of simulated results followed the same qualitative profile including positions of the zero crossings.

The difference between the 3-D simulated stress and the measured stress was likely due to higher order modes that were present in the 3-D simulations being suppressed in the experiment. The effects of such higher order modes would have been due to slight variations in the mechanical boundary conditions imposed by the experimental configuration. Although similar higher order modes can also be due to electrical loading, the electrical boundary conditions imposed by the load appear to be more strongly coupled to the resonance mode than the mechanical boundary conditions. Therefore, changes in the mechanical boundary conditions result in less amplification of
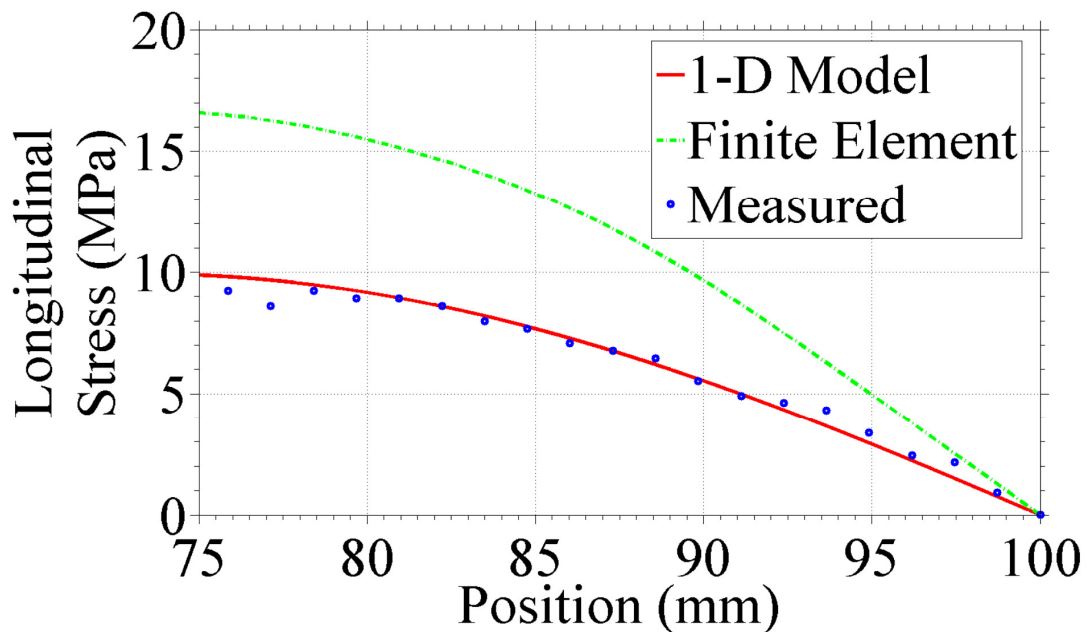
Figure 4.7: Magnitude of stress profile with an electron beam load.
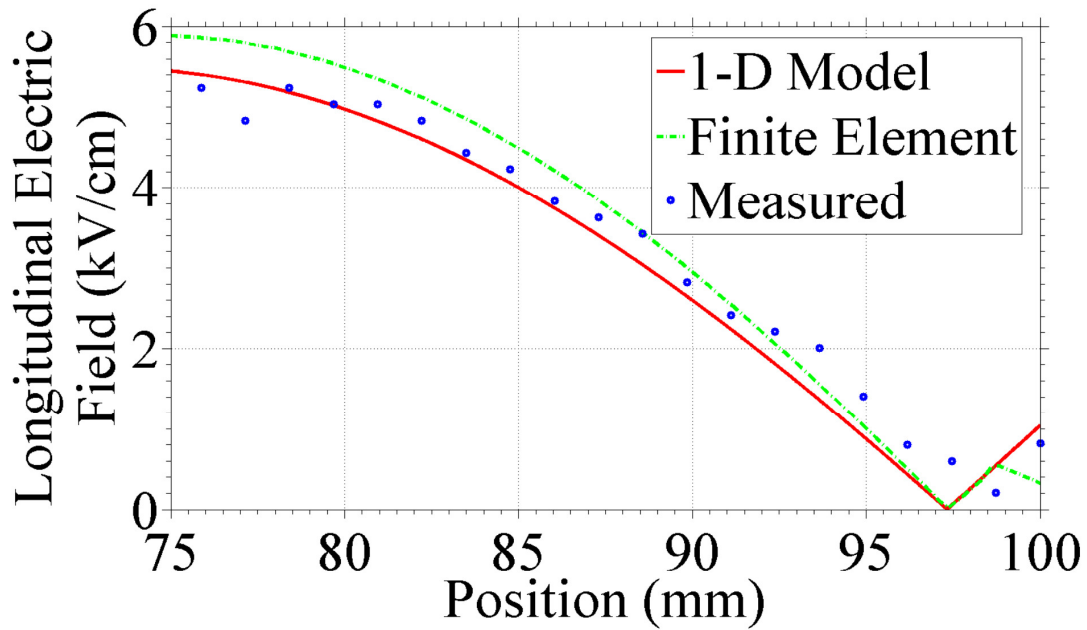
Figure 4.8: Magnitude of electric field profile with an electron beam load.

higher order resonances than the electrical boundary conditions.   The resultant discrepancies in stress and electric field due to higher order modes caused primarily by electrical loading are shown in the next section for the voltage probe load.

Voltage Probe Load

Figure 4.9 shows the simulated and measured number of $\pi/2$ phase changes that occurred within a quarter period of the input voltage for varying positions along the length of the PT with the voltage probe load. The simulated changes in phase difference are shown for the individual responses due to the photoelastic effect and electro-optic effect.   The simulated change in phase difference was influenced more by the photoelastic effect than by the electro-optic effect, as was the case for the electron beam load.
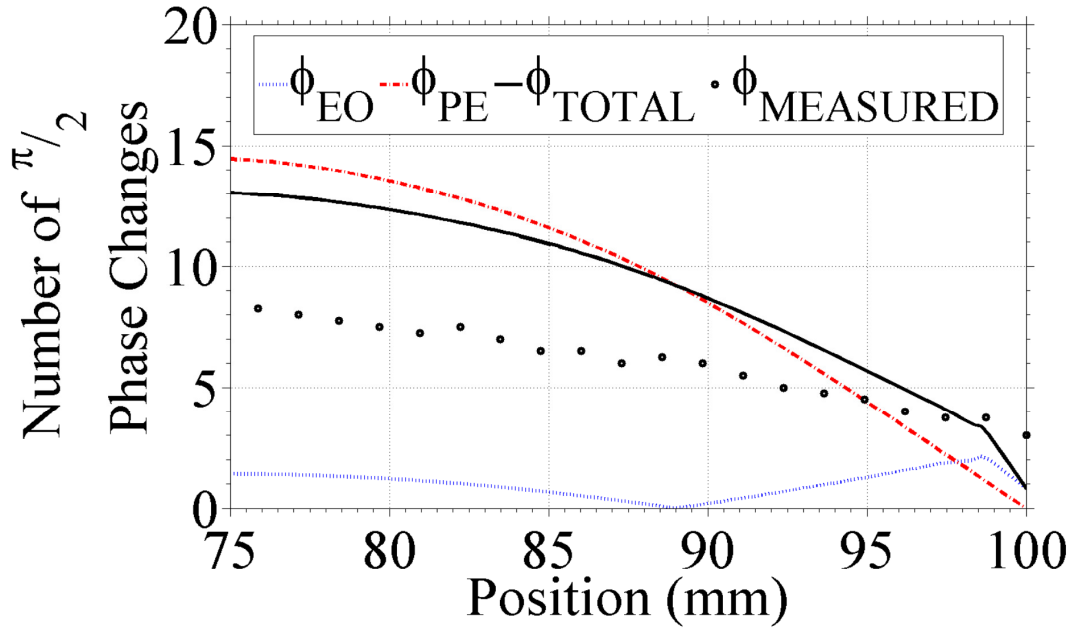
Figure 4.9: Number of π/2 phase changes with an electrical voltage probe load that was used to determine electric field and stress in the PT.

Figure 4.10 shows the simulated and measured longitudinal stress, while Figure 4.11 shows the longitudinal electric field for the voltage probe load. The maximum stress occurred near the vibrational null point. The maximum measured stress of 7 MPa was similar to the 3-D simulated maximum stress of 10 MPa. The 1-D simulated results showed a higher maximum stress of approximately 28 MPa. The measured stresses and both of the simulated stresses were below the yield stress of lithium niobate. The maximum measured electric field of 3 kV/cm was also similar to the 3-D simulated maximum electric field of 2.5 kV/cm. Again, the maximum electric field for the 1-D simulated case was much higher at approximately 12 kV/cm. The zero crossing between 80 mm and 90 mm was shifted towards the center of the PT with respect to the electron

beam load case. Both simulated results showed a similar qualitative profile for the internal stresses and electric fields.

The measured data and the 3-D simulated results were in agreement for the voltage probe load. However, the 1-D simulated results were in worse agreement for the voltage probe load than with the electron beam load. Observed variations between the mechanical displacement and resonant frequency in the 3-D simulations for the electron beam and voltage probe loads demonstrated that higher order modes of vibration had a greater effect in the PT for the lower impedance electrical load. Such higher order modes of vibration would distribute input energy away from the desired resonance mode and degrade the performance of the PT. The 3-D model accounted for the displacement in different directions due to the higher order vibrational modes, but the 1-D model would have only accounted for the lowest order mode of vibration. Thus, three-dimensional modeling is necessary when predicting the performance of a wide range of electrical load impedances, specifically for low impedance loads. The effect of such higher order modes of vibration due to low impedance electrical loading further indicates the need for high impedance diagnostics in the characterization of high transformation ratio PTs. Other diagnostics that do not share the same level of high impedance as the optical diagnostic, such as D-dot probes, may provide additional insight into the operation of PTs for lower impedance electrical loads when high transformation ratios are not as important.

Output Voltages

Table 4.3 shows the measured and simulated output voltage from the PT for the two load impedances. The experimentally measured output voltages were 17 kV and
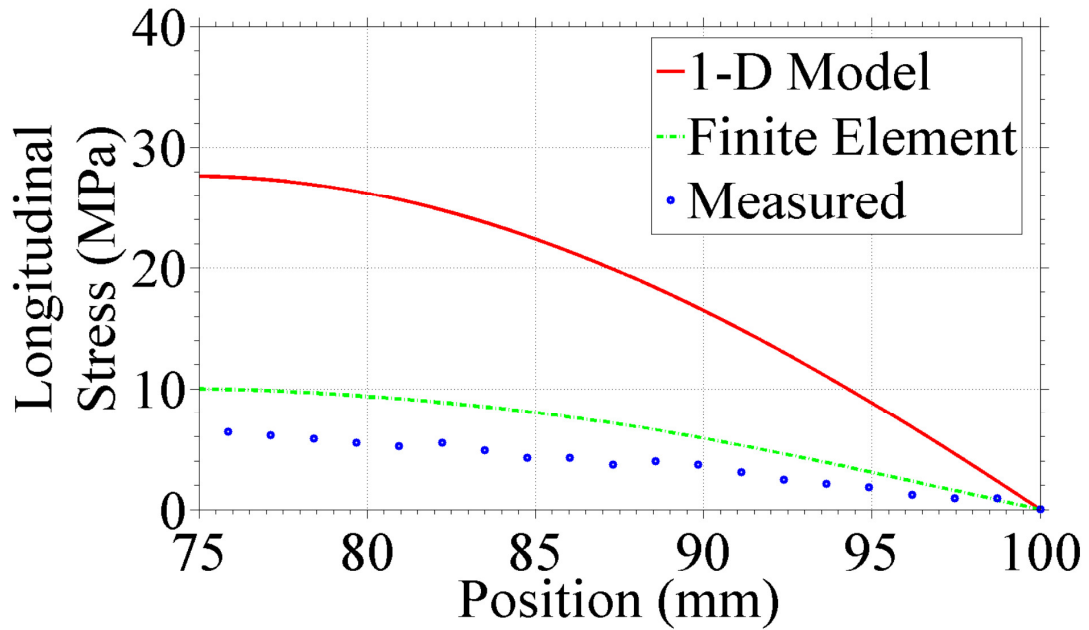
Figure 4.10: Magnitude of stress profile with an electrical voltage probe load.
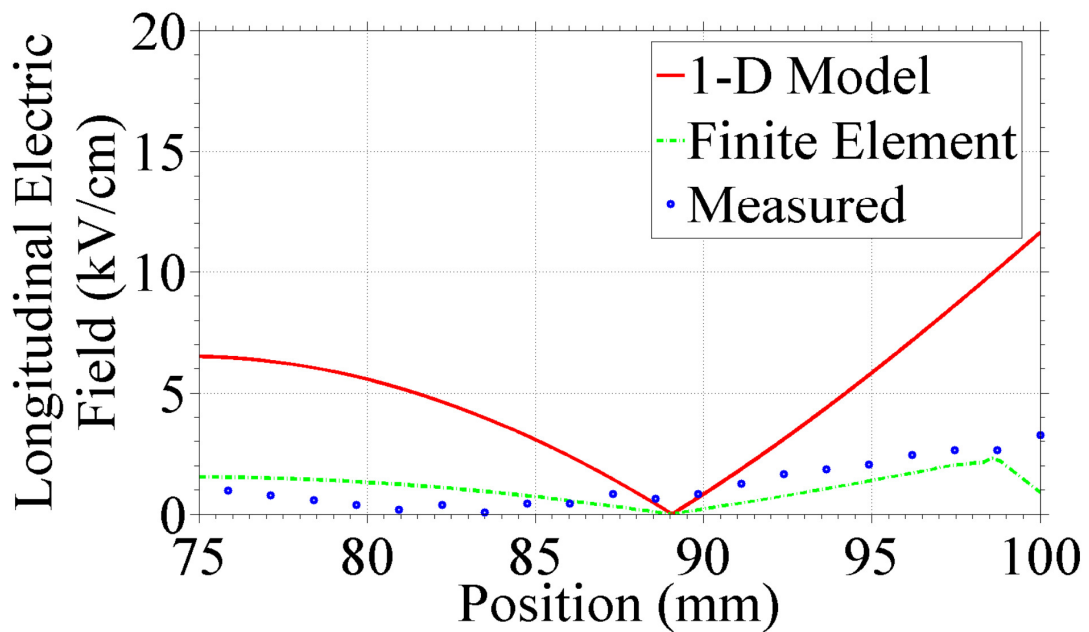
Figure 4.11: Magnitude of electric field profile with an electrical voltage probe load.

Table 4.3. Piezoelectric transformer output voltages as determined via experiment, 1-D simulations, and 3-D finite-element simulations.

Load	Experimental Output Voltage	1-D Simulated Output Voltage	3-D Simulated Output Voltage
Electron Beam	17 kV	16.94 kV	17.00 kV
Voltage Probe	250 V	1,065 V	250 V

250 V for the electron beam and voltage probe loads, respectively. The simulated output voltages were found by using the load impedances as determined with the least-squares curve fitting in the 1-D and 3-D models. The 3-D model predicted output voltages that were approximately the same as the measured values. However, the 1-D model only predicted the correct output voltage for the electron beam load. The inaccuracy of the 1-D model's output voltage for the voltage probe load as due to the inability of the 1-D model to simulate conflicting resonant modes as discussed in the previous sections. The 1-D model's PT output voltage with the voltage probe load was approximately four times higher than the measured value which was similar to the scaling of the internal stress and electric field. The similarity between the measured output voltages and the 3-D simulated output voltages further verifies the optical diagnostic that was used as a fitting parameter for the least-squares curve fitting technique.

A discrete integration of the internal electric fields in Figure 4.8 using Equation 4.23 was performed to determine the electric potential profile along the PT. Because the reference point of ground (0 V) was the input electrodes and the nearest measurement was 25 mm from the input electrodes, it was anticipated that the measured voltage should
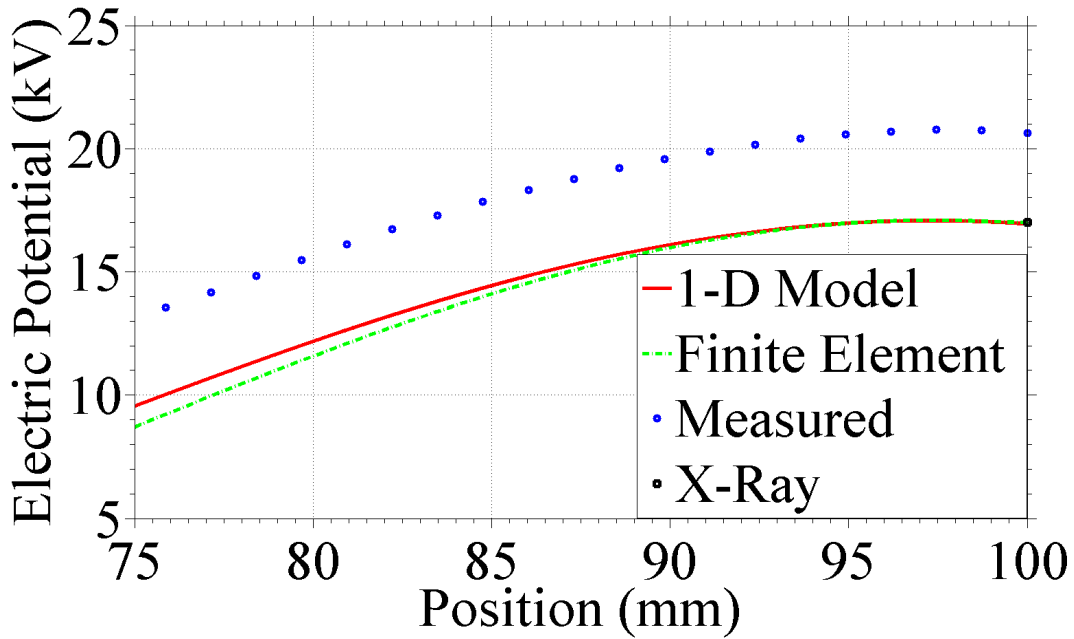
Figure 4.12: Electric potential profile for a PT operated with an electron beam load. Simulated data correspond to 91.2 GΩ in parallel with 0.046 pF. The output voltage determined by the x-ray diagnostic is also shown.

be higher than experimental value. The electric potential profile is shown in Figure 4.12. The output voltage from the PT was 20.5 kV based on the optical diagnostic with the approximate discrete integral. The measured output voltage from the x-ray diagnostic was 17 kV.

$$E = \frac{-\Delta\phi}{\Delta x}$$

Equation 4.23

Optical Diagnostic Summary

An optical diagnostic has been developed that uses the photoelastic and electro-optic effects in lithium niobate to measure the internal stresses and electric fields in a resonating length-extensional piezoelectric transformer. This diagnostic allows profiles of the stress and electric field to be mapped along the length of the PT for characterizing the operation without any additional electrical loading on the PT. The measured values shared the same qualitative shape as both modeled results. Measured values of stress and electric field were shown to be within an order of magnitude of simulated values for the 1-D model and much closer for the 3-D model. The 3-D model simulated with a load impedance determined from curve fitting the optically measured values also matched the measured output voltages for both the electron beam load and the voltage probe load. Additionally, the optical diagnostic could be used to determine temporal information such as the operating frequency of the PT or the load impedance of unknown loads when using curve fitting to match simulated and measured results. Future expansion of this derivation to include increased dimensionality with respect to the direction of vibration, stress, and electric field may help to account for the effects of higher order vibrational modes.

Quality Factor Diagnostic

The quality factor is a dimensionless parameter for resonators that describes the ratio of the energy stored to the energy dissipated in the resonator. A diagnostic based on the PT input and output quality factors and the equivalent electromechanical circuit was used to further verify the optical diagnostic. Although this diagnostic did help to verify

the optical diagnostic, it was not used for additional PT characterization. The reliance of this diagnostic on the x-ray count rate at frequencies off of resonance made it a valid but inefficient method of gathering data about the PT. The PT resonant frequency drifted during operation which made statistically significant x-ray counting times difficult to achieve. Further detail is given in Chapter 5 regarding resonant frequency drift and the unreliability of x-rays as a method of determining output voltage.

Electromechanical Equivalent Circuit

Rosen presented a method of using the input quality factor with a known load to determine the effective output quality factor based on the equivalent electromechanical circuit [15]. The simplified electromechanical equivalent at resonance is shown in Figure 4.13, where V_s is the voltage from the signal generator, aR and bR are the effective impedances of the generator and load, respectively, and R, L, and C are the internal mechanical resistance, inductance and capacitance of the PT, respectively. The value of
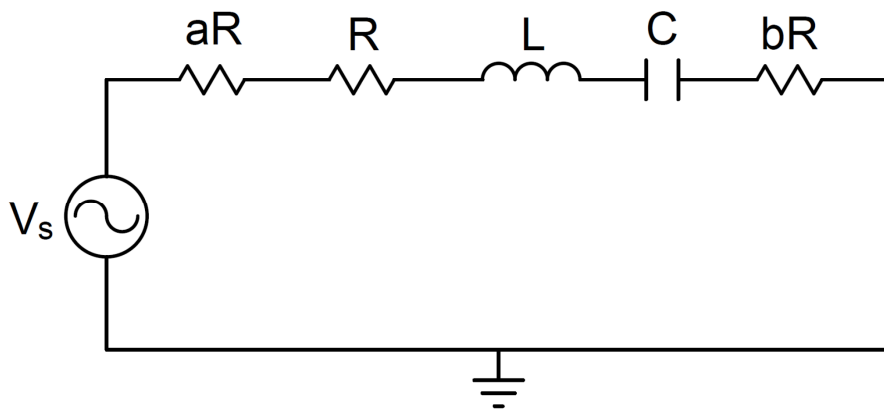
Figure 4.13: Simplified electromechanical equivalent circuit.

a can be assumed to be zero if the input voltage is measured at the input to the PT rather than at the source.

The effective output electrical quality factor can be found by treating the electromechanical equivalent circuit as a resonant *RLC* network. The resulting expression is shown in Equation 4.24, where Q_e is the effective output electrical quality factor and ω_o is the angular resonant frequency of the fundamental mode. Equation 4.24 can be simplified further to yield Equation 4.25, where Q_m is the input mechanical Q-value [15]. If the material properties, input mechanical Q-value, and effective output electrical Q-value are known from experiment and the load capacitance can be approximated, then the load resistance can be found using Equation 4.25 – Equation 4.28, where X_L is the load reactance, ω is the electrically loaded resonant frequency, C_L is the load capacitance, k_{22} is the electromechanical coupling coefficient, d_{22} is the piezoelectric strain coefficient, s_{22} is the elastic compliance coefficient, ε_{22} is the permittivity of the material, *l* is the length of the PT, R_L is the load resistance, *t* is the thickness of the PT, and *w* is the width of the PT [15]. The load resistance and load capacitance in Equation 4.26 and Equation 4.28 are in a parallel *RC* configuration as shown in Figure 2.3. The specific material constants for lithium niobate that were used include the PT dimensions and the values shown in Table 4.2.

$$Q_e = \frac{\omega_o L}{R(1 + a + b)}$$

Equation 4.24

$$Q_e = \frac{Q_m}{1 + a + b}$$

Equation 4.25

$$X_L = \frac{1}{\omega C_L}$$

Equation 4.26

$$k_{22}^2 = \frac{d_{22}^2}{s_{22}\varepsilon_{22}}$$

Equation 4.27

$$b = \frac{7486 k_{22}^2 l R_L X_L^2}{\left(1 - k_{22}^2\right)\pi^2 tw\varepsilon_{22}\omega\left(R_L^2\left(X_L + \frac{l}{2\left(1 - k_{22}^2\right)tw\varepsilon_{22}^2\omega}\right)^2 + \left(\frac{lX_L}{2\left(1 - k_{22}^2\right)tw\varepsilon_{22}\omega}\right)^2\right)}$$

Equation 4.28

Figure 4.14 and Figure 4.15 demonstrate the sensitivity of the effective output electrical quality factor to the electrical load. The sensitivity analysis was calculated assuming an input mechanical Q-value of 5,000 and a parallel *RC* load. Figure 4.14

97
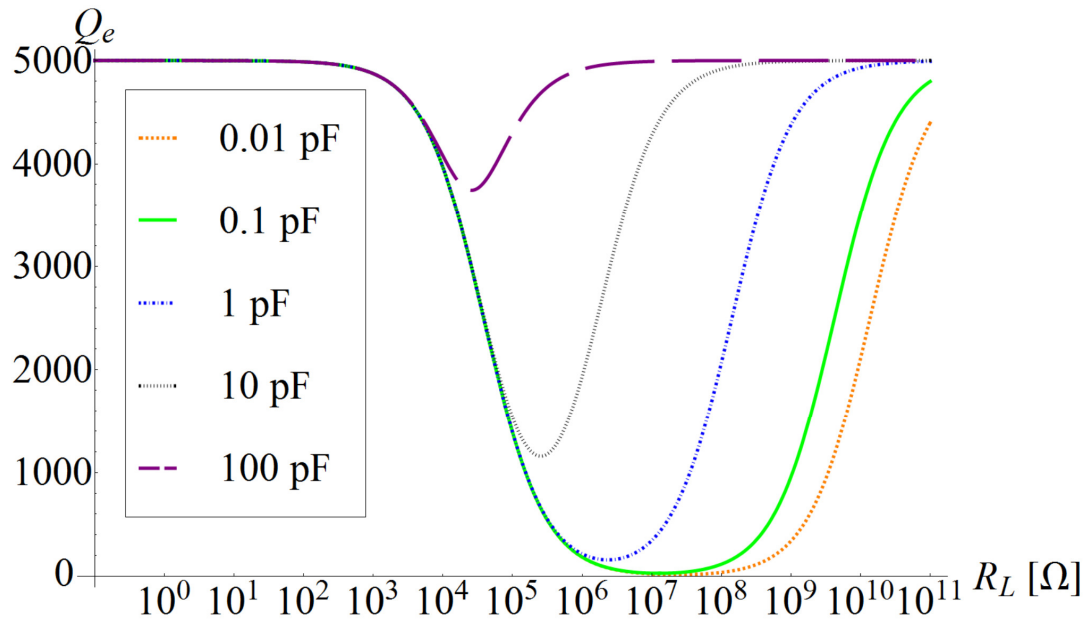
Figure 4.14: Effective output electrical quality factor as a function of load resistance for varying load capacitances.
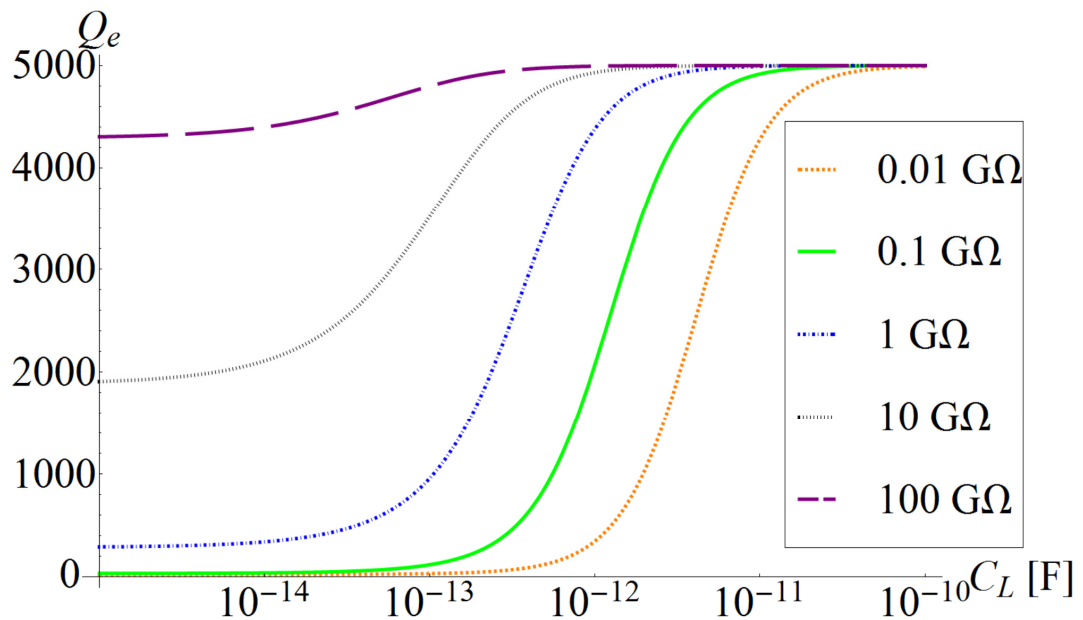
Figure 4.15: Effective output electrical quality factor as a function of load capacitance for varying load resistances.

shows the output electrical Q-values as a function of the load impedance for five different load capacitances. All load capacitances resulted in a decrease in the electrical Q-value for load resistances between 100 kΩ and 100 GΩ. The relative sensitivity of the Q-value was dependent on the load capacitance. The Q-value was less sensitive to the magnitude of the load resistance for the 100 pF load capacitance, while the 0.01 pF capacitance had a negligible effect on the electrical Q-value for load resistances between 100 kΩ and 100 GΩ.

Figure 4.15 shows the output electrical Q-values as a function of load capacitance for five different load resistances. All load resistances result in a decreased electrical Q-value for load capacitances less than 10 pF. The electrical Q-value is less sensitive to changes in load capacitance for higher load resistances. A 100 GΩ load resistance caused an output electrical Q-value that was greater than 80% of the input mechanical Q-value over the entire range of load capacitances.

Quality Factor Diagnostic Verification

The electrical and mechanical Q-values were measured for a resonating PT coupled with an electron beam load. Figure 4.16 shows the frequency sweep of the input voltage that was used to calculate the Q-values based on Equation 4.29 where Q is the Q-value, $f_{resonant}$ is the resonant frequency, and Δf_{3dB} is the full-width, half-maximum (FWHM) of the measured values. The load for measurements shown in Figure 4.16 was an electron beam produced by a thermionic filament with a 2.3 A filament current. Gaussian curves were fitted to the measured values to determine the full-width, half-maximum (FWHM) of the curves. A measured input mechanical Q-value of 3,851 was based on the measured electrical input impedance. The measured output electrical Q-

value of 3,607 was based on the PT voltage transformation ratio. Since the Q-value is only dependent on the FWHM and resonant frequency, the measured output electrical Q-value is insensitive to minor deviations in the output voltage due to any associated counting error in the x-ray voltage measurement.

$$Q = \frac{f_{resonant}}{\Delta f_{3dB}}$$

Equation 4.29
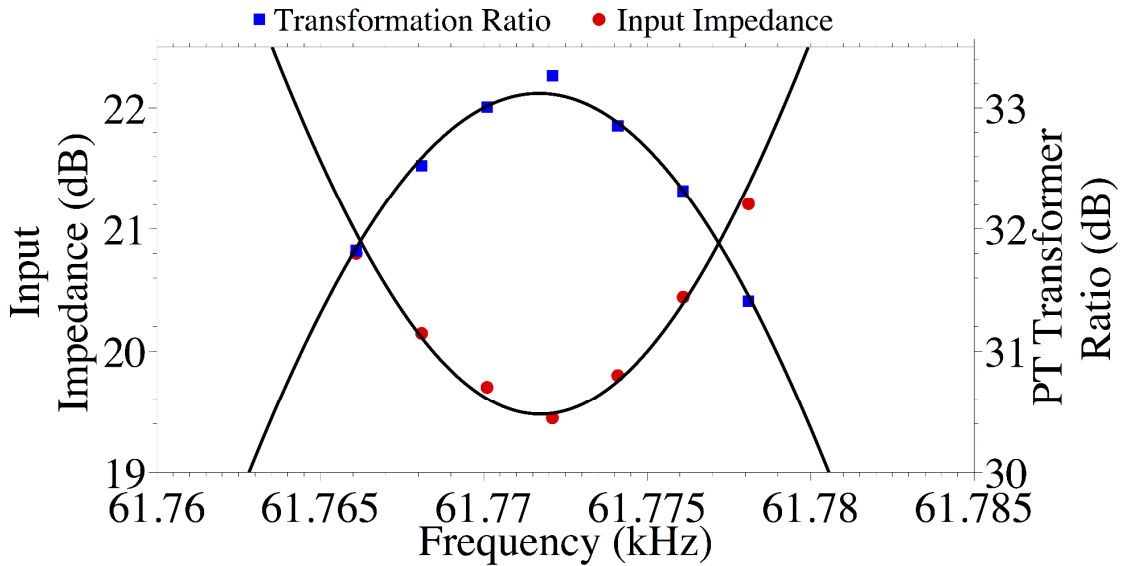
Figure 4.16: Frequency sweep of the PT input voltage to determine the mechanical and electrical quality factors for the PT with a thermionic filament operating at 2.3 A. The mechanical and electrical quality factors were determined to be 3,851 and 3,607, respectively.

Finite-element simulations were used to approximate the load capacitance as 0.050 pF. Using Equation 4.25 – Equation 4.27, the load resistance was determined to be 93.67 GΩ. The measured output voltage for the 2.3 A filament current was 17 kV based on the endpoint energy of the x-ray measurement. Using Ohm's Law, the approximated electron beam current was 0.181 μA.

Comparison of Diagnostic Results

A summary of the results comparing the Q-value diagnostic with the optical diagnostic least-squares curve fitting is shown in Table 4.4 [58]. The *RC* loads determined using each diagnostic were similar. The approximated load capacitance used in the Q-value diagnostic, 0.050 pF, was determined from finite-element models of the PT. The curve fitting from the optical diagnostic resulted in a load capacitance of 0.046 pF. The load resistance values were 93.67 GΩ and 91.20 GΩ for the Q-value diagnostic and optical diagnostic, respectively. The load values determined with the Q-value diagnostic were within 10 % for both the resistive and capacitive components. Additionally, the 0.181 μA electron beam current found using the Q-value diagnostic was within 3 % of the 0.186 μA current found using the optical diagnostic.

Table 4.4: Electron beam currents from two different diagnostic methods

Diagnostic Method	Load Capacitance [pF]	Load Resistance [GΩ]	Electron Beam Current [μA]
Q-value	0.050	93.67	0.181
Optical	0.046	91.20	0.186

5. Results

The piezoelectric transformer (PT) was characterized as a high-voltage source for compact particle accelerators. The primary characteristics to be verified for PT-based accelerator designs were the accelerated beam current, accelerating potential, and dissipated beam power. Figure 5.1 shows a map of how each of these three parameters was determined via experiment. Six separate experiments were performed that led to the experimental conclusion that the PT was capable of accelerating approximately 2.5 μA of electron beam current to 16 keV for an average beam power of approximately 20 mW. Accelerating potentials greater than 120 kV were measured, but simultaneous beam current and/or power measurements were not achieved for the higher PT output voltages. It was also observed that the PT output voltage decreased for decreasing load impedance.

Initial experiments were performed to verify high-voltage production from the PT. These experiments used different methods to measure the output voltage, and each had a different electrical load impedance. A capacitive voltage divider circuit, Cockcroft-
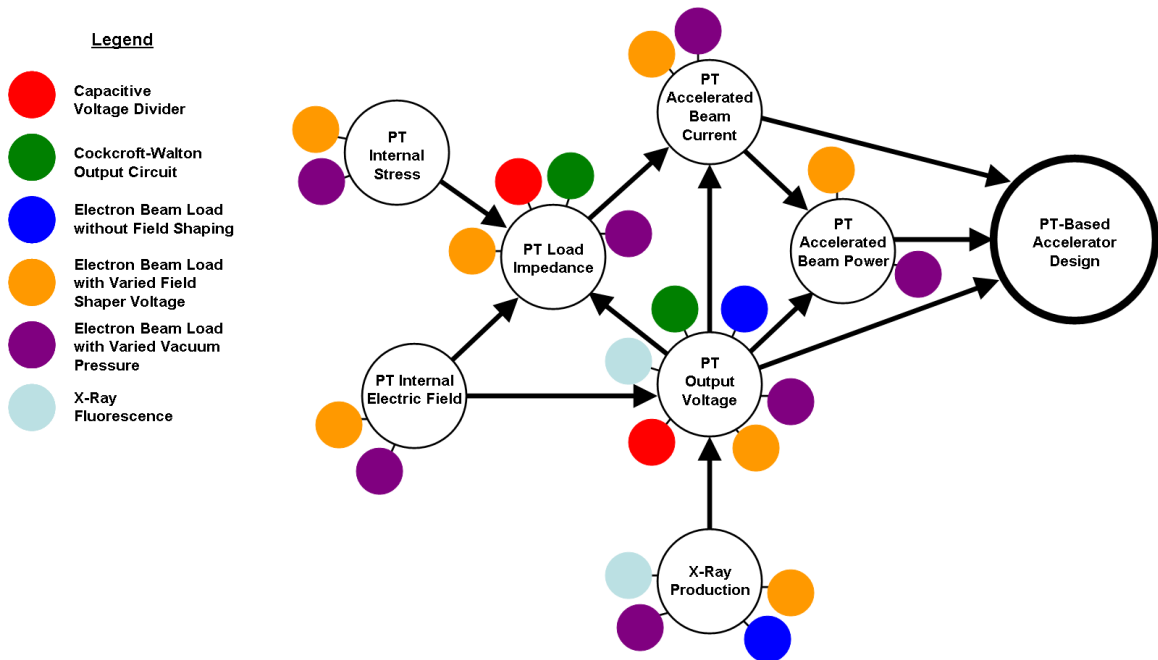
Figure 5.1: **Experiment map for characterizing PTs as high-voltage sources for compact particle accelerators. Colored dots correspond to each of the experiments that were performed.**

Walton circuit, and electron beam diode load were all tested. Each of the discrete circuit loads resulted in output voltages less than 12 kV, but the electron beam diode load resulted in output voltages in excess of 120 kV as measured with an x-ray diagnostic. Although each of these experiments generated high PT voltage transformation ratios, these initial experiments indicated the dependence of PT output voltage on the load impedance.

Later electron beam loads were accelerated to the PT from a thermionic filament using the electric field shaper configuration shown in Figure 3.11. The electron beam current was varied by adjusting the bias voltage of the field shaper or the vacuum

chamber pressure during two separate experiments. The optical diagnostic developed in

Chapter 4 was used to measure the internal stress, electric field, and electric potential of

the PT during operation with these electron beam loads.   Simultaneous x-ray

measurements were also used to measure the accelerating potential for each electron

current. A least-squares curve fitting algorithm was used to compare data from the

optical diagnostic to the 1-D modeled results to determine the load resistance of the

electron beam. The electron beam currents and beam powers were determined using

curve-fitted beam resistances and measured PT output voltages. Finally, the PT output

voltage was further verified using an x-ray fluorescence experiment.

This chapter describes how each of the experiments from Figure 5.1 was executed

and the results from each. Other operating parameters of the PT were also measured

during operation, such as the input mechanical quality factor, PT resonant frequency, and

x-ray count rate. These parameters did not necessarily verify the accelerating conditions

for the electron beam, but did provide insight into how to effectively operate the PT-

based accelerator system.

Initial Experiment Results

PT Output Circuits

Capacitive Voltage Divider

Input and output voltage traces for the capacitive divider circuit from Figure 3.5

are shown in Figure 5.2. For an input voltage of 26 V, the PT had an output voltage of

approximately 12 kV. The voltage across the high capacitance side of the divider was

measured at each end of the bipolar configuration and the voltage division ratio of

approximately 1,000 was used to determine the output voltage at each end. The overall output voltage was the difference between the voltage at each end of the PT as described in the "PT Output Circuits" section of Chapter 3. The capacitive divider had a load capacitance that was equivalent to approximately 130 fF from one end of the crystal to the other. The stray capacitance from the PT to the vacuum chamber on the order of 1 pF dominated the PT load capacitance and was in parallel with the total divider capacitance. The resistive component of the impedance from the air gap in parallel with the capacitance was assumed to have a negligible effect on the load impedance.
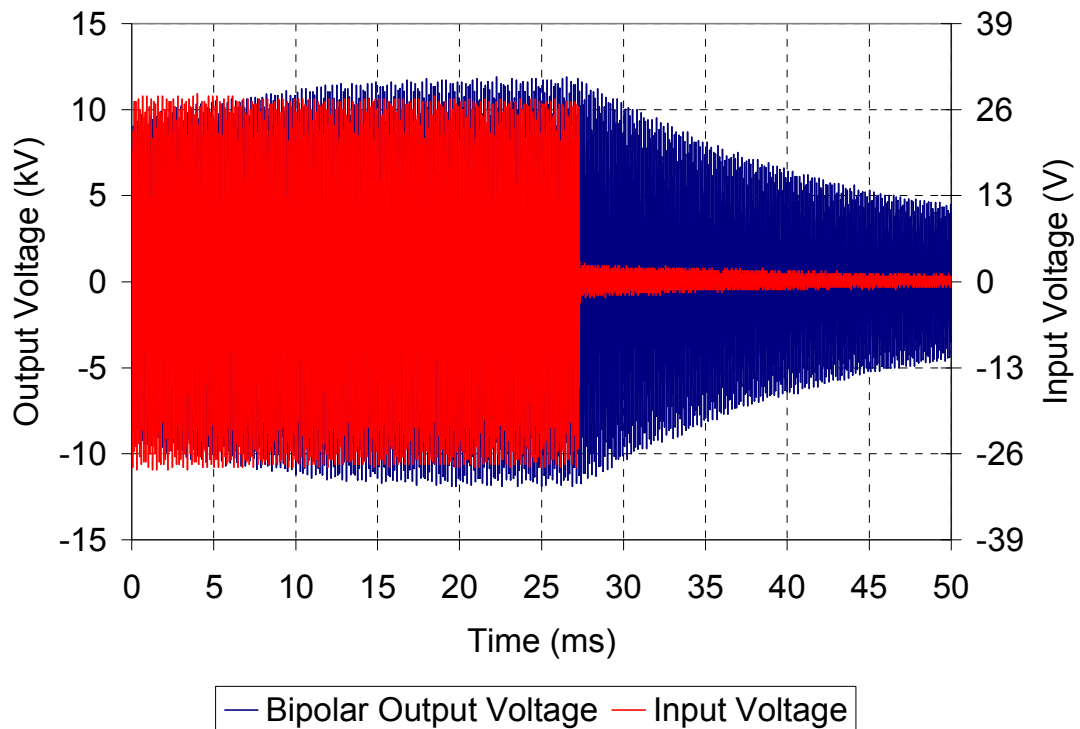
Figure 5.2: Input and output voltage traces for a bipolar PT when connected to the capacitive divider. An isolated voltage transformation ratio of approximately 460 was achieved.

Cockcroft-Walton Output Circuit

The bipolar PT was used to drive a full-wave Cockcroft-Walton (CW) circuit as shown in Figure 3.6. Results for a single-stage and three-stage CW circuit are shown in Figure 5.3. The output voltage for the single-stage CW circuit attached to the PT was only 2.4 kV_{DC} as measured with a Tektronix P6015A at the output of the CW circuit. This was due to the significantly lower load impedance than the electron beam diode and the capacitive divider. The three-stage CW circuit should have been approximately 7.2 kV_{DC}, but the measured output voltage was only 2.9 kV_{DC}. This discrepancy was due to the decrease in load impedance as more stages were added to the CW circuit. The single-stage and three-stage CW circuits had parallel RC loads of 130 MΩ, 0.4 pF and
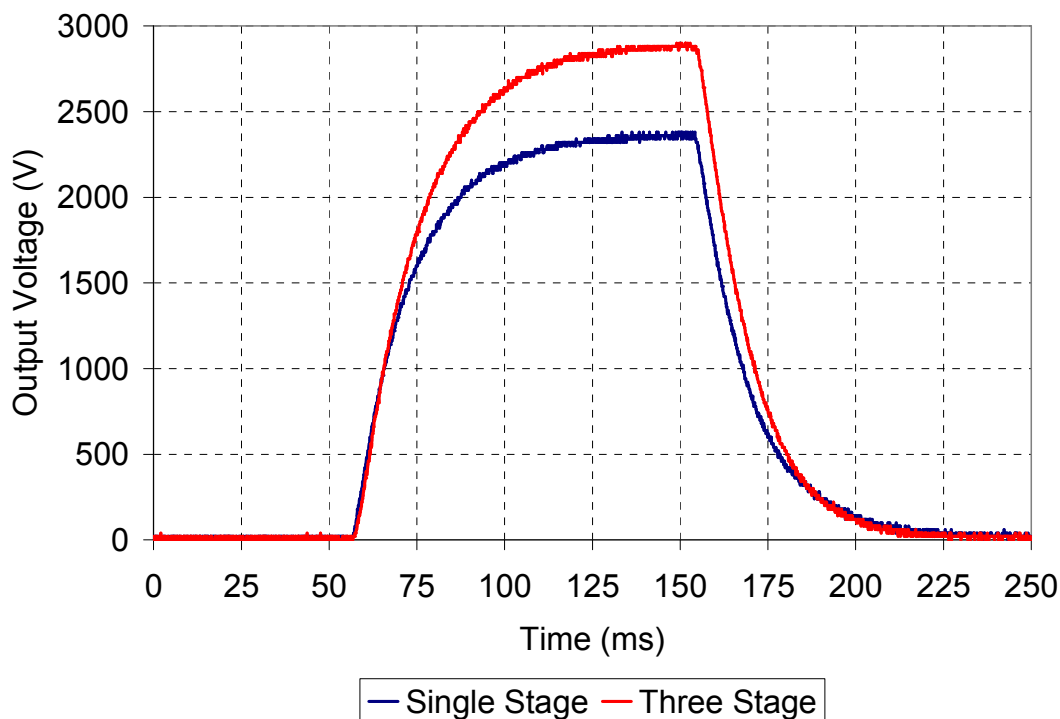
Figure 5.3: Voltage output for a single-stage and three-stage CW circuit attached to the bipolar PT.

15.5 MΩ, 2.6 pF, respectively, as measured with an *LCR* meter. This order of magnitude drop in load impedance also lowered the output voltage from the PT that was supplying the CW circuit. Using Equation 3.2, the PT output voltages were approximately 1.2 kV and 480 V for the single-stage and three-stage CW circuits, respectively. The decrease in output voltage for decreased load impedance was similar to the simulated trends shown in Figure 2.9.

Electron Beam Diode Loads

Initially, the PT was operated at five different positions with respect to the vacuum chamber port as shown in Figure 3.7 to analyze the effects of varying electron-beam diode loads at the output of the PT. These relative positions and the corresponding results are shown in Table 5.1. The load capacitance was a result of PT position in the Multiphysics [38]. Simulated load capacitances for the electron-beam diode ranged from 0.76 pF to 1.0 pF as shown in Table 5.1. Although the load capacitance for the electron-

Table 5.1: Summary of experimental results for different PT positions in the vacuum chamber.

PT Placement with Respect to Vacuum Chamber Port	Simulated Capacitance [pF]	V_{in} [V]	Endpoint X-ray Energy [keV]
3 cm outside port	0.76	10.8	>123
2 cm outside port	0.76	10.7	>123
1 cm outside port	0.80	10.6	64
0 cm outside port	0.84	10.6	30
3 cm inside port	1.0	10.5	14

vacuum chamber and was approximated using finite-element simulations in COMSOL beam diode load was similar to the capacitive divider, the mode 1, unipolar PT configuration generated higher output voltages than the bipolar configuration used for the capacitive divider.

The x-ray endpoint energies for each of the positions with respect to the vacuum chamber port as shown in Figure 3.7 are also shown in Table 5.1. Endpoint energies greater than 123 keV could not be directly measured due to the maximum calibrated energy on the x-ray detector. A transformation ratio in excess of 11,000 was observed when the PT was 3 cm outside the port. However, the transformation ratio decreased to approximately 1,300 when the PT was 3 cm inside the port. The large decrease in output voltage for the electron-beam diode positions inside the vacuum chamber port was likely not due to the relatively small increase in load capacitance. It was more likely that the load resistance due to the electron beam was being decreased as the PT became closer to the vacuum chamber walls. As the PT was repositioned, the traveled electron distance decreased which increased the space-charge limited current. Additionally, the electric field at the field emission tips would have increased and extracted additional electron current from the tips.

$$ I_{SCL} = \frac{\pi}{0.78} \varepsilon \mu \frac{V_{out}^2}{d} $$

Equation 5.1

The change in traveled electron distance was shown using finite-element, particle ray tracing simulations. The relative space-charge limited current can be used as an approximation of the decrease in load resistance. The simulated traveled electron distance decreased from 3.6 cm to 0.5 cm between the 0 cm outside the port and 3 cm inside the port cases as shown in Figure 5.4. This decrease in distance may have resulted in a space-charge limited current increase by a factor of approximately 7 as calculated using Equation 5.1 where I_{SCL} is the space-charge limited current, ε is the permittivity, μ is the permeability, V_{out} is the PT output voltage, and d is the electron beam length [65]. The increase in current would correspond to a decrease in load resistance by a factor of 7.

(a)   (b)
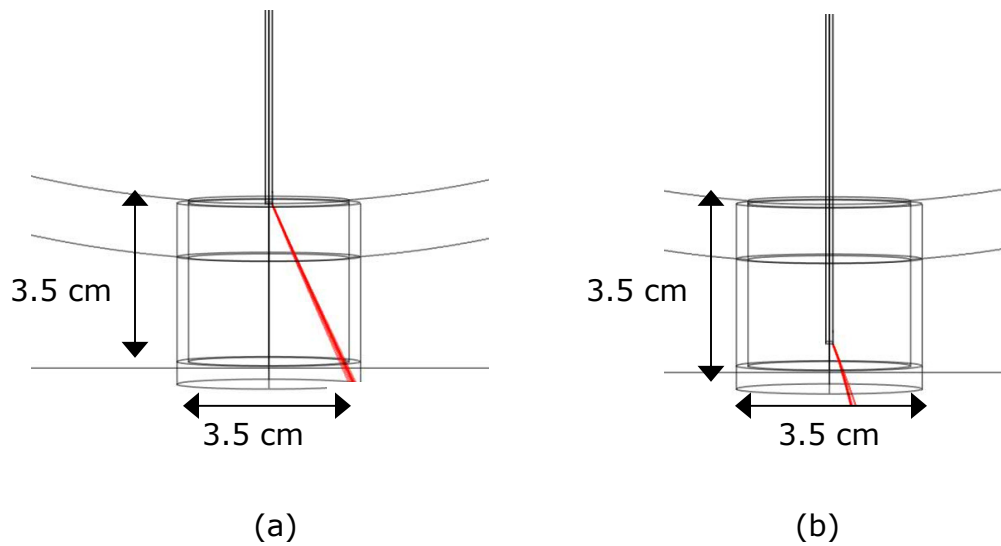
Figure 5.4: Simulated particle ray tracing showing a decrease in traveled electron beam distance for the case where the PT is inside the vacuum chamber port. (a) PT even with the port has an electron beam length of 3.6 cm (b) PT 3 cm inside the port has an electron beam length of 0.5 cm.

Electron Beam Diode Loads with Electric Field Shaping

Although the initial experiments demonstrated high voltage production at the output of the PT, voltage amplitudes greater than 10 kV were never observed for a PT load circuit comprised of discrete components. The initial results supported the simulation results from Chapter 2 which indicated that electrical load impedance could adversely affect the voltage transformation ratio of the PT. A mode 2 PT was operated with an electron beam load in an electric field shaper as shown in Figure 3.11 to further study the PT for varied electron beam currents. The electron beam current was varied by adjusting the bias voltage on the electric field shaper to adjust the trajectories of the electron beams. Additionally, the vacuum chamber pressure was varied to determine the effect of the electron beam operated in a grounded electric field shaper at different ambient pressures. Higher ambient pressures could result in beam current variations due to charge extraction from plasma or secondary electron emission.

A least squares curve fitting technique was used to determine the load resistance and capacitance attached to the output of the PT as shown in Figure 2.3. After the optical diagnostic data was collected and analyzed, Matlab was used to compare the 1-D modeled results for varied loads to the measured values [66]. The load resistance and capacitance were changed to minimize the error using an algorithm called particle swarm analysis [62], [63]. The error in the algorithm was calculated using the sum of squares of the residuals between the simulated and measured values. Coefficients of determination, R^2, were calculated for the modeled results using Equation 5.2 to Equation 5.4 where $SS_{residuals}$ is the sum of squares of the residuals and SS_{total} is the sum of squares of the measured values minus the mean of all measured values [67].

$$R^2 = 1 - \frac{SS_{residuals}}{SS_{total}}$$

Equation 5.2

$$SS_{residuals} = \sum_i (x_i - y_i)^2$$

Equation 5.3

$$SS_{total} = \sum_i (y_i - \bar{y})^2$$

Equation 5.4

Effect of Duty Factor on Polished Crystals

The duty factor used in Chapter 4 was increased from 5 % to 20 % in an attempt to increase the x-ray count rate. However, it was found that lithium niobate crystals polished for optical transmission fractured at an increased rate with respect to unpolished crystals at the higher duty factor. An experiment was performed to determine the cause of the increased fracture rate for the polished crystals. The duty factor and burst period were varied with a grounded electric field shaper. It was determined that the previous number of PT resonant periods, 3,000, was not sufficient to reach a stable resonance mode. The mechanical displacement in the PT was still increasing at the end of the burst period. However, a higher duty factor operated at 6,000 resonant periods was sufficient to reach the full resonance. The results from the experiment are summarized in Table

5.2. The 3,000 cycle operation only yielded an x-ray endpoint energies of 26.7 keV, while the 6,000 cycle operation yielded endpoint energies of 32.6 keV. The x-ray endpoint energies were approximately the same for a given number of resonant periods despite a change in duty factor.

While the unpolished crystals were operated without fracturing throughout the operating region shown in Table 5.2, the polished PTs fractured at both the higher duty factors and lower duty factors with an increased number of resonant periods. This increase in fracture rate was attributed to minor chips or microfractures occurring during the polishing process. When the PT reached the full, stable resonance, a greater stress was produced for a given strain which exceeded the yield stress of a crystal with such imperfections. Consequently, the PT was operated at a 5 % duty factor with a modulation period of 1 s for all experiments using the optical diagnostic to reduce the likelihood of crystal fracture. All optical data was taken during the last PT resonant

Table 5.2: Experimental results for varied duty factors and number of PT resonant periods. Error bars correspond to three standard deviations.

Number of Resonant Periods	Burst Period (s)	Duty Factor	X-Ray Endpoint Energy (keV)
3,000	0.5	10 %	26.7 ± 1.8
3,000	1	5 %	26.9 ± 2.1
4,000	1	6.5 %	29.7 ± 2.2
6,000	0.5	20 %	32.6 ± 1.9
6,000	1	10 %	32.7 ± 2.0

period of each burst to determine the maximum stress, electric field, and electric potential magnitudes that were produced. The effect of the decreased duty factor was resolved by using a parallel operating load resistance in the electron beam equivalent load circuit as will be described in the following section of this chapter.

Table 5.3: Summary of operating conditions and results for the PT with an "open-circuit" load. Coefficients of determination are with respect to the 1-D model.

Parameters	Value	Units
Vacuum chamber pressure	$1.0\text{-}1.2 \times 10^{-6}$	Torr
Input voltage amplitude	7.4	V
Input current amplitude	100	mA
Input mechanical quality factor	3,641	—
Output voltage amplitude	21.55	kV
Maximum internal stress	10.77	MPa
Maximum internal electric field	6.25	kV/cm
Average resonant frequency drift rate	-3.52×10^{-3}	Hz/s
Electric field shaper bias voltage	0	V
Thermionic filament current	0	A
X-ray count rate	0	cps
Curve-fitted load resistance	2.647	GΩ
Curve-fitted load capacitance	0.040	pF
Stress R^2 value	0.890	—
Electric field R^2 value	0.936	—
Electric potential R^2 value	0.950	—

"Open-Circuit" Load

The PT was operated with an "open-circuit" load and analyzed with x-ray and optical diagnostics. The "open-circuit" load consisted of operating the PT in vacuum with a grounded electric field shaper and no dc current passing through the thermionic filament. Table 5.3 summarizes the operating conditions and results for the PT operating with the "open-circuit" load. The input voltage amplitude was 7.4 V, and the optically determined output voltage from the PT was 21.55 kV. Another important value to note from Table 5.3 is the average resonant frequency drift rate of -3.52 x 10^{-3} Hz/s. The resonant frequency drift rates for the PT with a heated thermionic filament were increased by approximately an order of magnitude and are shown in the following sections.
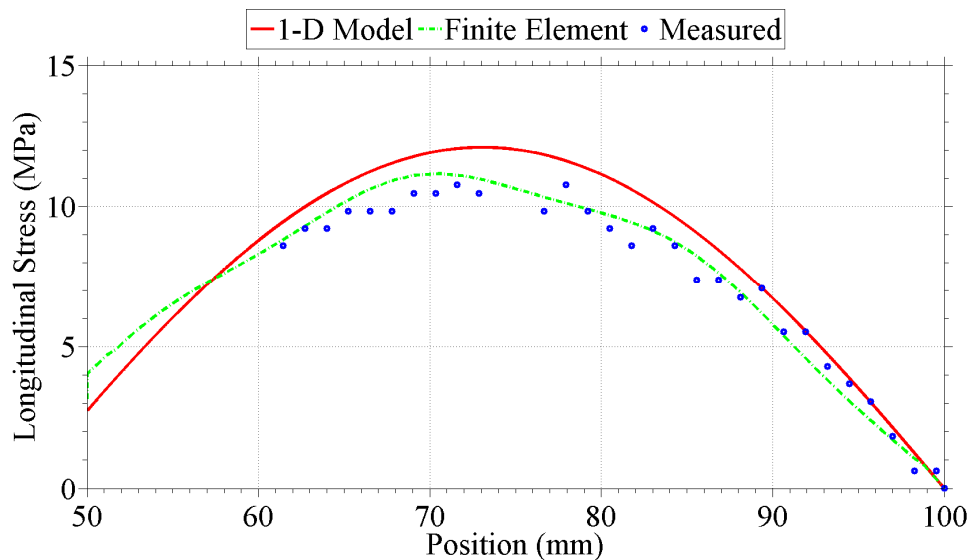
Figure 5.5: **Internal stress for an "open-circuit" load attached to the PT. The "open-circuit" load corresponded to the PT operating in a grounded electric field shaper with the thermionic filament turned "off".**

The internal longitudinal stress magnitudes that were determined with the optical diagnostic for the "open-circuit" load are shown in Figure 5.5. The 1-D model and finite element model simulated results are also shown in Figure 5.5 for reference. The maximum measured stress was 10.77 MPa which was below the lowest quoted yield stress for lithium niobate of 30 MPa [50]. The 1-D model had an R^2 value of 0.890. The 3-D finite element model produced a better fit to the measured stress than the 1-D model with an R^2 value of 0.972. Any distortion of the stress in the 3-D model was likely due to simultaneous higher order vibrational modes as described in Chapter 4 that were not permitted in the 1-D model.

The longitudinal electric field magnitude and electric potential for the "open-circuit" load are shown in Figure 5.6 and Figure 5.7, respectively. The maximum internal electric field in the PT was measured to be 6.25 kV/cm, and the output voltage was measured to be 21.55 kV. The R^2 values for the electric field were 0.936 for the 1-D model and 0.882 for the finite element simulations. The primary difference between the simulated electric fields in the two models was an offset of the zero crossing as shown in Figure 5.6. The R^2 values for the electric potential were 0.950 for the 1-D model and 0.991 for the finite element simulations.

The simulated load that minimized the error between the 1-D model and the optical data for the "open-circuit" load was a parallel 2.65 GΩ, 0.04 pF load. However, the thermionic filament was not emitting electrons. Any resistive component of the load was due to a combination of field-emitted electrons from the corners of the output electrode and electromechanical loss factors that were not included in the models [20].

115
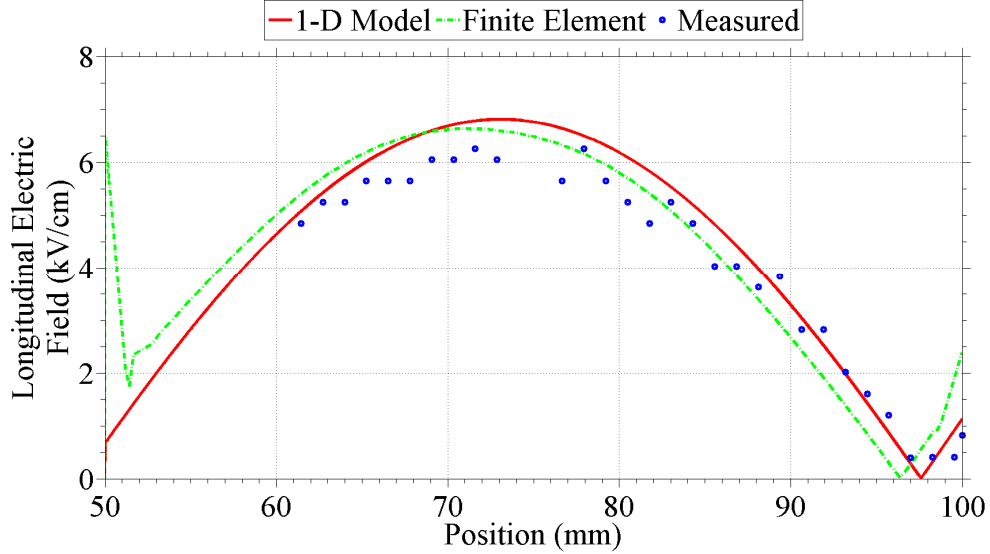
Figure 5.6: **Internal electric field for an "open-circuit" load attached to the PT. The "open-circuit" load corresponded to the PT operating in a grounded electric field shaper with the thermionic filament turned "off".**
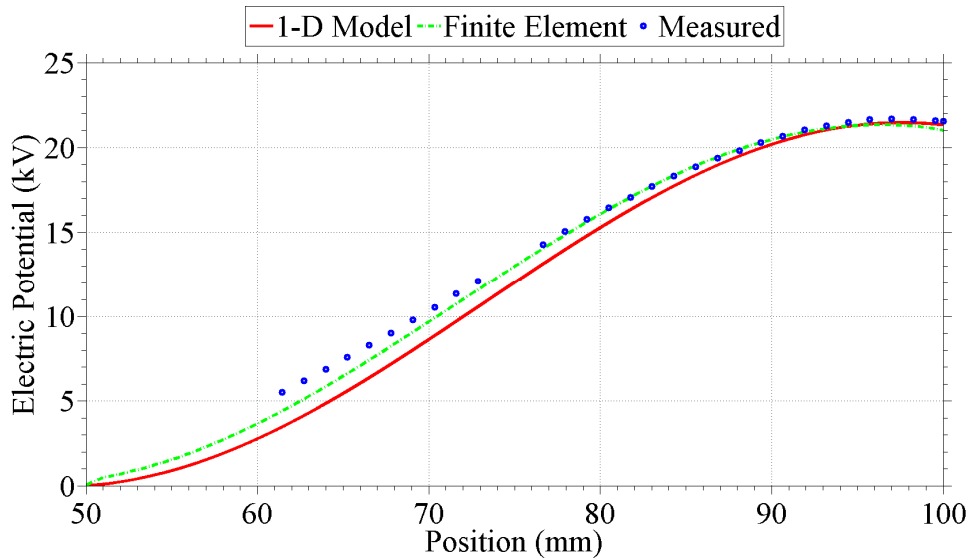
Figure 5.7: **Internal electric potential for an "open-circuit" load attached to the PT. The "open-circuit" load corresponded to the PT operating in a grounded electric field shaper with the thermionic filament turned "off".**

116

The modeled electrical load was modified as shown in Figure 5.8 to include a parallel operating resistance, R_o, with the RC beam load. The operating resistance was assumed to be constant, so any variations in the curve-fitted values of the equivalent parallel resistance were due to the beam resistance.

The operating resistance was chosen to be equal to the highest curve-fitted value of the parallel combination of R_L and R_o when no electron current was thought to be incident on the PT output electrode. Ideally, the operating resistance would be determined as the maximum "open-circuit" load resistance for each operating regime of varied duty factors, vacuum chamber pressures, etc. Once the operating resistance was determined, the resistance due to the electron beam was calculated using Equation 5.5 where $R_{\|}$ is the parallel combination of R_L and R_o as determined by least-squares curve fitting.
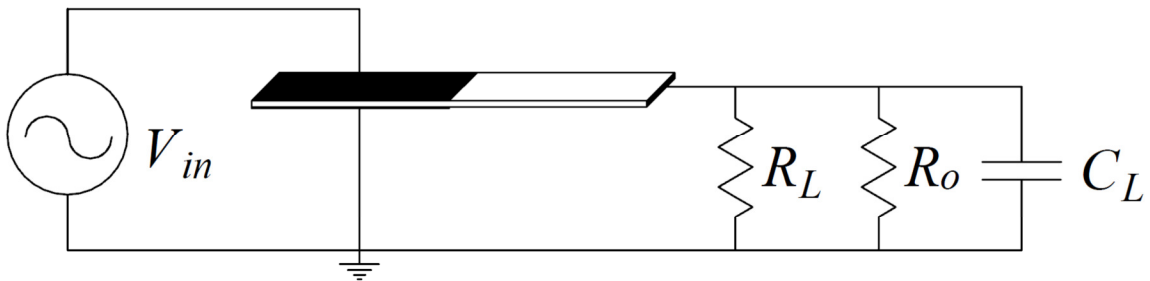
Figure 5.8: Modified PT load model that includes a parallel operating resistance in addition to the parallel RC load.

$$R_L = \frac{R_o R_\parallel}{R_o - R_\parallel}$$

Equation 5.5

Varied Electric Field Shaper Bias Voltage

The primary method of varying the electron beam current at the output electrode of the PT was by varying the electric field shaper bias voltage. Bias voltages of -1,000 – 0 V were tested with PT input voltage amplitudes of approximately 7.4 V and dc thermionic filament currents of approximately 2.3 A for all tests. A summary of the experimental data collected for the varied field shaper bias voltage is shown in Table 5.4. Two different thermionic filaments were used due to the first filament burning out midway through the experiment. Results from the least-squares curve fitting of optical diagnostic data and x-ray data are presented in Table 5.4. All x-ray data was analyzed for x-ray counts greater than 1.64 standard deviations above background.

Input Mechanical Quality Factor

One variable use in the models for the least-squares curve fitting was the mechanical loss factor. The mechanical loss is inversely proportional to the input mechanical quality factor (Q-value), so the input mechanical Q-value was measured for each electric field shaper bias voltage. The input mechanical Q-values were determined by performing a frequency sweep about the resonance and measuring the input impedance [45], [49]. The measured input mechanical Q-values are shown in Table 5.4

118

Table 5.4: **Summary of experimental data for varied electric field shaper bias voltage.**

Vgrid (V_{DC})	Input Mechanical Q-Value	Total Load Resistance (GΩ)	Beam Resistance (GΩ)	Optically Determined Voltage (kV)	Output Current (µA)	X-Ray Endpoint Energy (keV)	Total X-Ray Counts	Counting Time (s)	Time-Averaged Count Rate (cps)	Standard Deviations above Background	Thermionic Filament Number
0	3,533	2.619	36.08	21.13	0.59	21.42	2,195	171.4	12.81	1.64	1
-20	3,172	2.768	139.59	21.48	0.15	21.17	1,550	129.8	11.94	1.64	2
-40	3,436	2.749	103.51	21.98	0.21	20.65	1,023	150.0	6.82	1.64	2
-50	3,342	2.657	44.93	21.14	0.47	21.04	756.0	131.0	5.77	1.64	1
-60	3,255	2.791	238.84	21.78	0.09	21.30	969.7	146.0	6.64	1.64	2
-80	3,255	2.664	47.02	21.14	0.45	20.78	853.6	148.6	5.74	1.64	2
-100	2,943	2.824	∞	20.40	0	20.91	953.4	186.5	5.12	1.64	1
-120	3,256	2.097	8.15	16.86	2.07	21.04	269.2	150.0	1.79	1.64	2
-140	3,436	2.662	46.40	21.42	0.46	20.27	715.3	150.0	4.77	1.64	2
-150	3,255	2.061	7.63	16.78	2.20	19.24	164.4	128.4	1.28	1.64	2
-160	3,436	2.717	71.71	21.71	0.30	20.65	327.1	124.1	2.64	1.64	2
-180	3,174	2.209	10.14	17.31	1.71	16.28	28.87	131.0	0.22	1.64	2
-200	3,092	1.984	6.67	15.86	2.38	14.48	9.75	143.0	6.82×10^{-2}	1.64	1
-220	3,171	2.130	8.67	16.94	1.95	18.85	2.12	138.0	1.54×10^{-2}	1.64	2
-240	3,344	2.099	8.18	17.01	2.08	17.30	1.69	146.0	1.16×10^{-2}	1.64	2
-250	3,256	2.824	∞	21.91	0	N/A	0	129.6	0	1.64	2
-260	3,255	1.994	6.78	16.21	2.39	N/A	0	150.0	0	1.64	2
-280	3,171	2.102	8.22	16.79	2.04	17.69	0.29	150.0	1.90×10^{-3}	1.64	2
-300	3,344	2.721	74.60	21.57	0.29	N/A	0	97.5	0	1.64	2
-400	3,434	2.530	24.30	20.58	0.85	N/A	0	138.0	0	1.64	1
-600	3,255	2.698	60.47	21.21	0.35	N/A	0	150.0	0	1.64	1
-800	3,747	2.559	27.27	21.34	0.78	N/A	0	128.0	0	1.64	1
-1,000	3,747	2.479	20.29	20.76	1.02	N/A	0	128.0	0	1.64	1
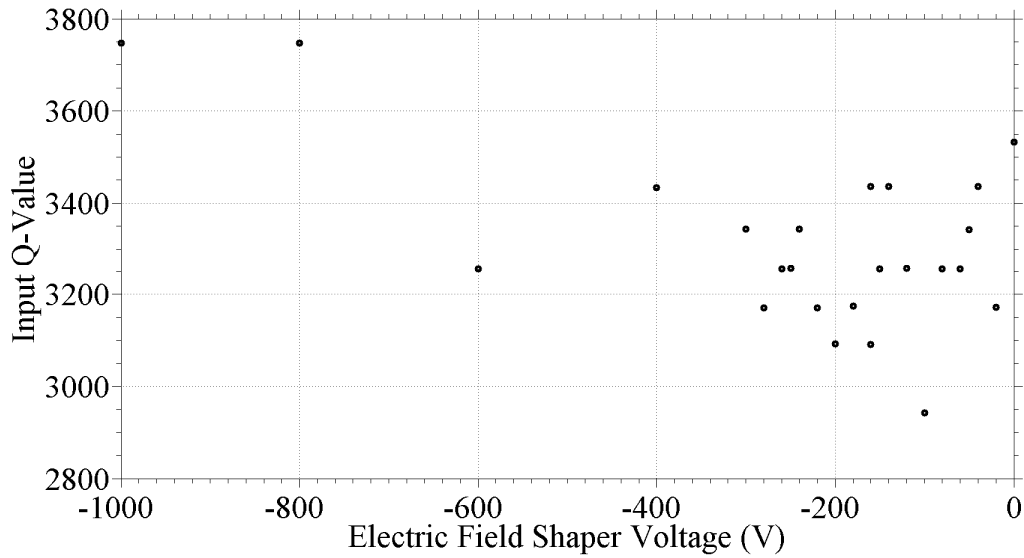
Figure 5.9: Input mechanical quality factor as determined using the PT electrical input impedance for varied electric field shaper bias voltage.

and plotted as a function of field shaper voltage in Figure 5.9. The input mechanical Q-values varied about the mean value of 3,300 for electric field shaper bias voltages that resulted in electron beam current at the output of the PT. The Q-values increased to approximately 3,700 for the lowest field shaper bias voltages. The respective mechanical loss factors for each of the least-squares curve fits were calculated using Equation 2.48. The average mechanical loss factor was 3.03 x 10^{-4}.

PT Resonant Frequency

It was observed that the PT resonant frequency, defined as the PT input voltage and current being in phase, continuously decreased as a function of time during operation. Figure 5.10 shows the resonant frequency versus time for all experiments that
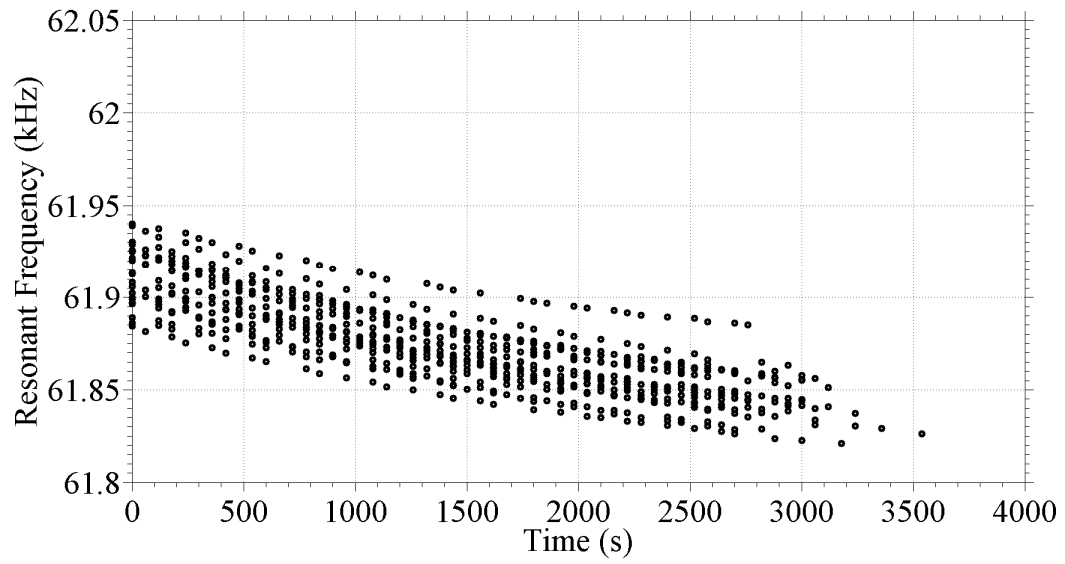
Figure 5.10: PT resonant frequencies as a function of operating time.
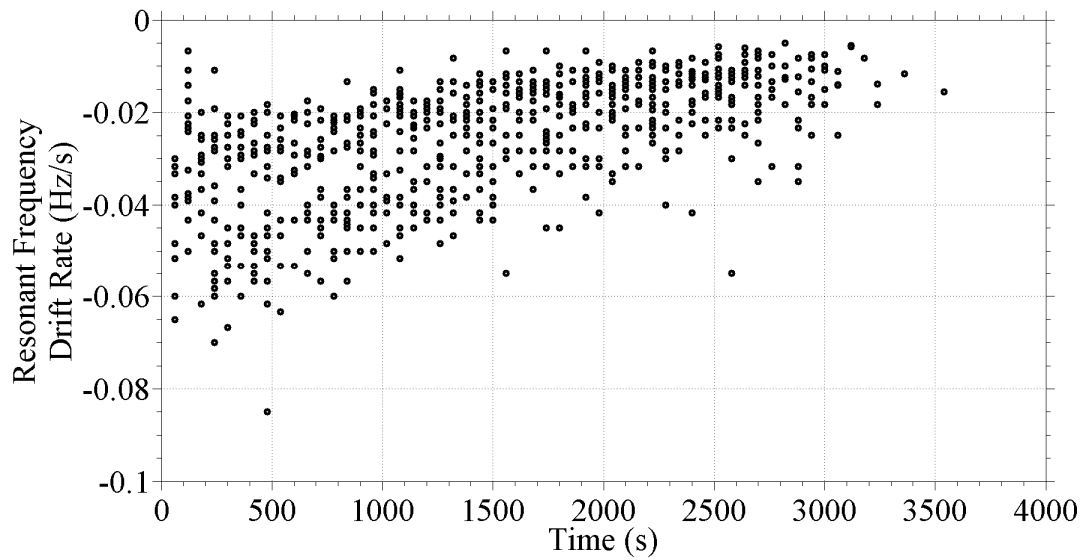
Figure 5.11: PT resonant frequency drift rates as a function of operating time.

121

were conducted with varied electric field shaper bias voltages. Typical operating times to collect optical data for each varied field shaper voltage were between 45 minutes to 1 hour. The average decrease over a 45 minute operating time was approximately 70 Hz. The PT input frequency was adjusted throughout the operating time to maintain a near 0° phase difference between the input voltage and current.

Although the PT resonant frequency did drift over the entire operating time, the resonant frequency drift rate was not constant. Figure 5.11 shows the resonant frequency drift rate as a function of time. The resonant frequency drifted more rapidly at the beginning of the operating time than at the end of the operating time. Although the resonant frequency also decreased for the "open-circuit" load, the average drift rate was an order of magnitude less than for the tests with a heated thermionic filament. The resonant frequency drift was likely due to heating from a combination of ohmic heating from the electron beam and radiation from the thermionic filament. The decrease in drift rate over time would correspond to the PT approaching a thermo-electro-mechanical equilibrium.

The time-averaged resonant frequency drift rates for the varied electric field shaper bias voltages are shown in Figure 5.12. The time-averaged drift rates may have varied slightly for field shaper voltages between -300 V and -150 V which will be shown to correspond to increased beam current at the output of the PT. However, the time-averaged frequency drift rate did not vary by more than one standard deviation about the mean frequency drift rate of -0.026 Hz/s. This may indicate that the radiant heat from the thermionic filament had more influence over the resonant frequency drift rate than any
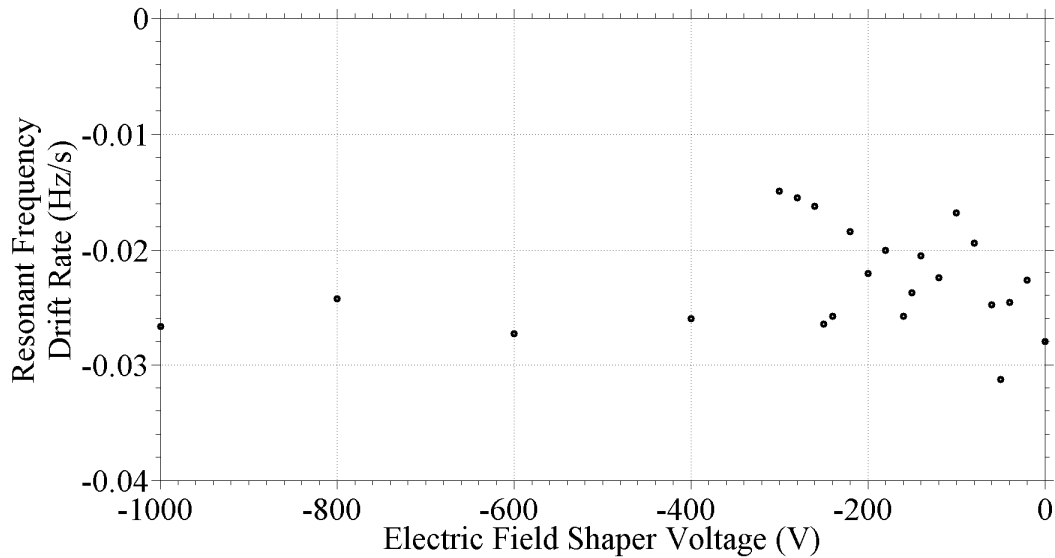
Figure 5.12: Time-averaged resonant frequency drift rates for varied electric field shaper bias voltage.

ohmic heating from the electron beam. The significance of heating as an explanation for resonant frequency drift rate is further demonstrated by the fact that the time-averaged resonant frequency drift rate for the "open-circuit" load was an order of magnitude less than the values shown in Figure 5.12. Since the "open-circuit" load was predominantly influenced electromechanical effects rather than thermal effects, it is likely that any deviation of the resonant frequency drift rate from the "open-circuit" case was due to the thermal effects of the filament.

PT Output Voltage

Both the bremsstrahlung x-ray diagnostic and the optical diagnostic were used to determine the output voltage of the PT. The results from each diagnostic are shown in
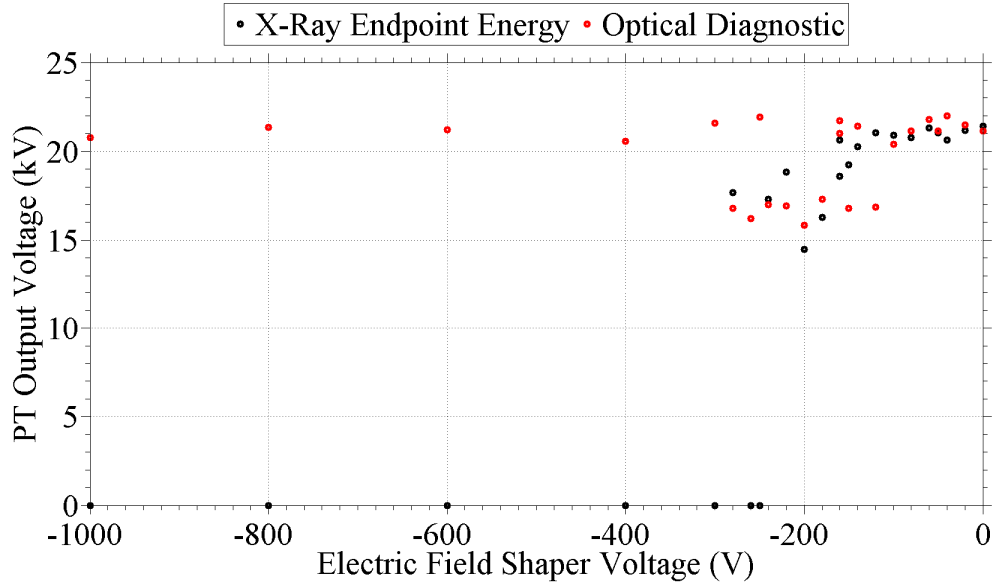
Figure 5.13: PT output voltage determined by both the x-ray endpoint energy and the optical diagnostic for varied electric field shaper bias voltage. X-ray endpoint energies correspond to counts greater than 1.64 standard deviations above background for a 95 % confidence interval.

Figure 5.13. The x-ray diagnostic results correspond to x-ray counts that were greater than 1.64 standard deviations above background based on 95 % confidence limits of detection [55], [57]. The optical diagnostic and x-ray diagnostic are in agreement down to field shaper voltages of -300 V. The few optical diagnostic voltages in Figure 5.13 that were not in agreement with the x-ray diagnostic were in regions when the output voltage was changing. Analysis of the optical diagnostic for discrete values of $\pi/2$ phase transitions made it appear that the output voltages oscillated about the x-ray detected values of output voltage in these regions. The x-ray diagnostic did not detect sufficient counts to determine the PT output voltage for field shaper bias voltages less than -300 V, so the PT output voltage was denoted as 0 V in Figure 5.13. Based on a combination of

124

modeling and experimental data, the decrease in x-ray counts for the lowest tested field shaper voltages was due to electrons striking the PT in areas where resultant photons could not be measured by the cadmium telluride (CdTe) detector or electrons missing the PT entirely. X-ray count rates and angular photon emission profiles will be presented later in this chapter.

Table 5.5: Coefficient of determination, R^2, values for 1-D modeled stress, electric field, and electric potential for each of the electric field shaper bias voltages.

Vgrid (V_{DC})	Input Mechanical Q-Value	Total Load Resistance (GΩ)	Total Load Capacitance (fF)	Stress R^2 Value	Electric Field R^2 Value	Electric Potential R^2 Value
0	3,533	2.619	40	0.853	0.909	0.932
-20	3,172	2.768	40	0.864	0.918	0.950
-40	3,436	2.749	40	0.855	0.904	0.957
-50	3,342	2.657	40	0.870	0.924	0.943
-60	3,255	2.791	40	0.865	0.919	0.953
-80	3,255	2.664	40	0.891	0.928	0.967
-100	2,943	2.824	40	0.851	0.905	0.977
-120	3,256	2.097	40	0.994	0.894	0.959
-140	3,436	2.662	40	0.884	0.932	0.960
-150	3,255	2.061	40	0.975	0.893	0.974
-160	3,436	2.717	40	0.866	0.918	0.952
-180	3,174	2.209	40	0.976	0.836	0.928
-200	3,092	1.984	40	0.991	0.893	0.973
-220	3,171	2.130	40	0.991	0.892	0.961
-240	3,344	2.099	40	0.990	0.916	0.973
-250	3,256	2.824	40	0.873	0.926	0.954
-260	3,255	1.994	40	0.991	0.916	0.976
-280	3,171	2.102	40	0.988	0.880	0.958
-300	3,344	2.721	40	0.867	0.920	0.949
-400	3,434	2.530	40	0.905	0.944	0.962
-600	3,255	2.698	40	0.865	0.915	0.944
-800	3,747	2.559	40	0.863	0.915	0.948
-1,000	3,747	2.479	40	0.905	0.947	0.962

Least-Squares Curve Fitting Results for PT Load Impedance

The particle swarm algorithm was used to perform a least-squares curve fit of the PT load resistance and capacitance based on the configuration shown in Figure 2.3. Equal weighting was given to the stress, electric field, and electric potential in the determination of the residual sum of squares. The resulting load resistances and capacitances for each of the electric field shaper bias voltages are shown in Table 5.5 as well as the R^2 values for the stress, electric field, and electric potential. All of the 1-D modeled results had R^2 values greater than 0.83, where 1.0 is an exact match to the experimental data. Although an R^2 value of 0.8 indicates a 20 % error in the fit of a given parameter, the equal weighting among each of the three factors minimized the overall error in the curve fitting algorithm.

The load resistance determined by the least-squares curve fitting was equal to the parallel combination of the operating resistance and electron beam resistance as shown in Figure 5.8. The PT equivalent load resistance versus electric field shaper bias voltage is shown in Figure 5.14. The resistance values ranged from 1.98 GΩ to 2.82 GΩ. The equivalent load resistance was lowest for field shaper voltages between -300 V and -150 V. Increased electron beam current at the PT output electrode decreased the beam resistance and brought down the equivalent parallel combination of the operating and beam resistances.

The output voltage as determined using the optical diagnostic was plotted versus equivalent load resistance as shown in Figure 5.15. The results showed a nearly linear increase in PT output voltage for increasing load resistance. The experimental results
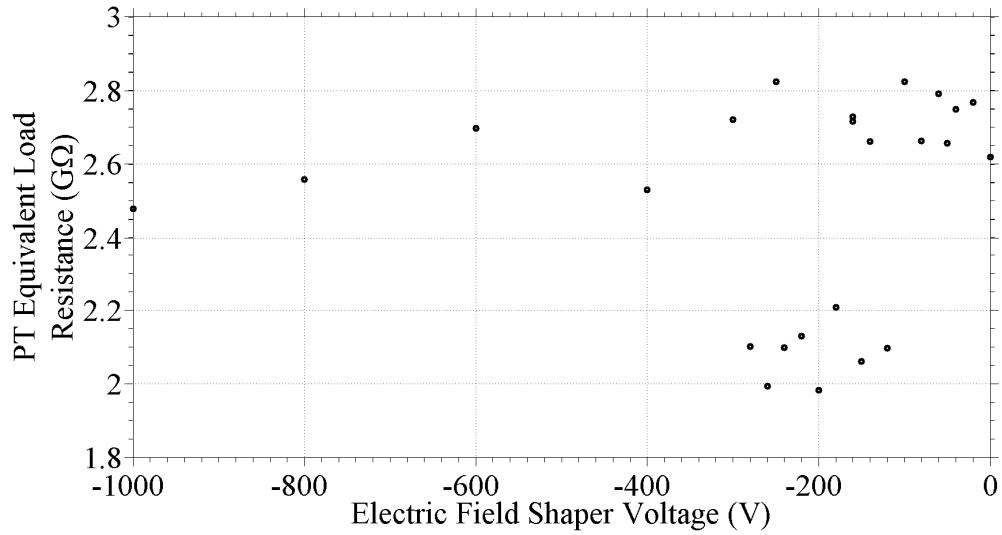
Figure 5.14: PT equivalent load resistance as determined by least-squares curve fitting for varied electric field shaper bias voltage. The equivalent load resistance is the simplified resistance of the parallel operating resistance and electron beam resistance.
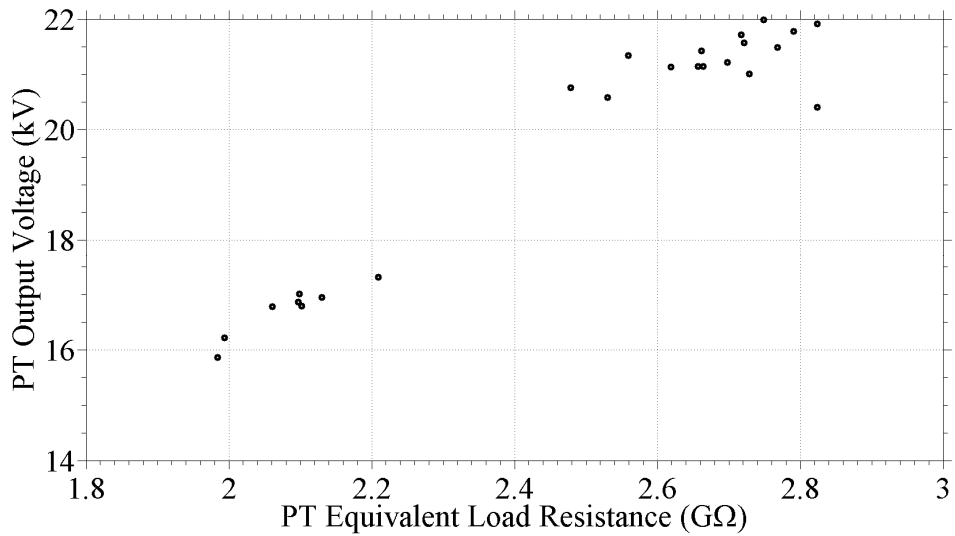
Figure 5.15: PT output voltage for varied equivalent load resistance. The equivalent load resistance is the simplified resistance of the parallel operating resistance and electron beam resistance.

127

follow the modeled trends from Chapter 2 shown in Figure 2.9. This corroboration should be expected given that the 1-D model was used for the least-squares curve fitting, but Figure 5.15 does help to validate the curve fitting algorithm that was used. It was also interesting to note that for a change in equivalent load resistance less than 1 GΩ, the output voltage varied by up to 25 %.

Electron Beam Current

The electron beam current could not be directly measured during experimentation. However, the electron beam resistance at the output of the PT was determined using the least-squares curve fitting and Equation 5.5. The electron beam current that was incident on the PT for varied electric field shaper bias voltages was calculated using Ohm's law and is shown in Figure 5.16. As expected, the field shaper voltage had an effect on the
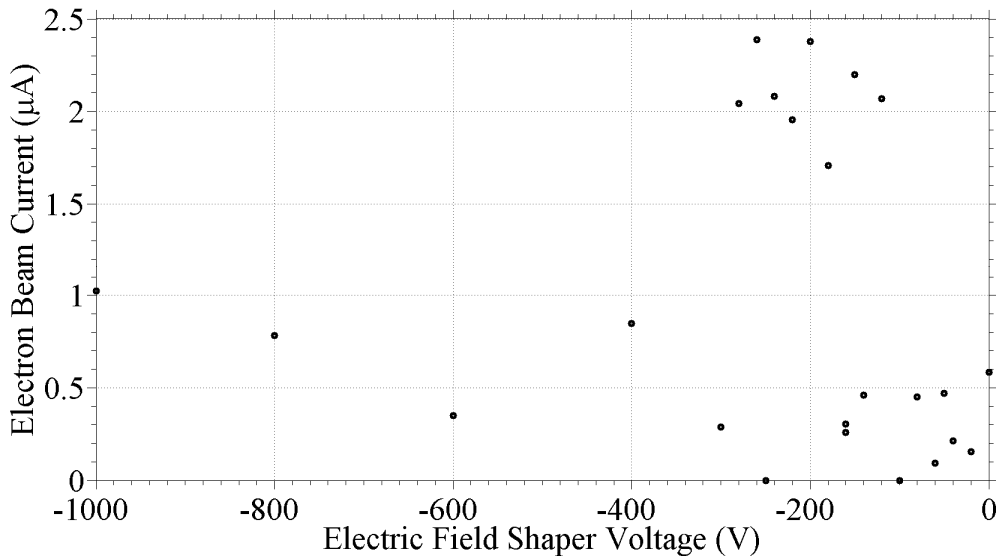
Figure 5.16: Electron beam current incident on the PT as determined by least-squares curve fitting and Ohm's law for varied electric field shaper bias voltage.

electron beam current that interacted with the PT. The electron beam currents incident on the PT output electrode were between $0 - 2.39$ µA. The range of field shaper voltages between approximately -300 V and -150 V corresponded to increased electron beam current at the output of the PT.

The PT output voltage was also plotted as a function of electron beam current that was incident on the PT as shown in Figure 5.17. The PT output voltage dropped from approximately 22 kV to 16 kV as the electron beam current increased from 0 to 2.5 µA. Figure 5.17 does not directly correspond to Figure 5.15, but Figure 5.17 does show a similar trend. As the PT output current was increased, the output voltage dropped to compensate for the finite amount of charge that could be sourced by the PT during a given resonant period. Figure 5.17 is also of particular interest for using the PT as a particle accelerator for energy conversion. Increasing beam current for increased output
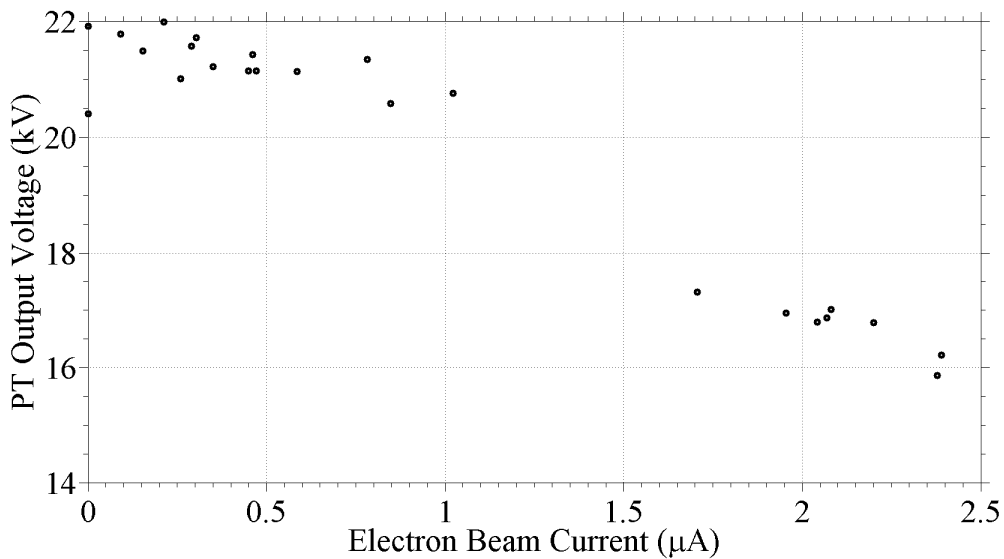
Figure 5.17: PT output voltage for varied electron beam current.

particle flux in the conversion of incident particle energy to photon or neutron energy may not be a viable option for PT-based accelerator designs. The decrease in acceleration potential would decrease the maximum energy for electron to photon energy conversions and decrease the reaction cross-section for an ion to neutron energy conversion.

Electron Beam Power Dissipation

Once the electron beam load resistance was determined from the curve fitting, the dissipated beam power was calculated using Equation 5.6 where P_{beam} is the dissipated electron beam power, V_{out} is the PT output voltage, and R_L is the electron beam load resistance as shown in Figure 5.8. The dissipated beam power is shown in Figure 5.18 as a function of electric field shaper bias voltage. The dissipated beam power was between
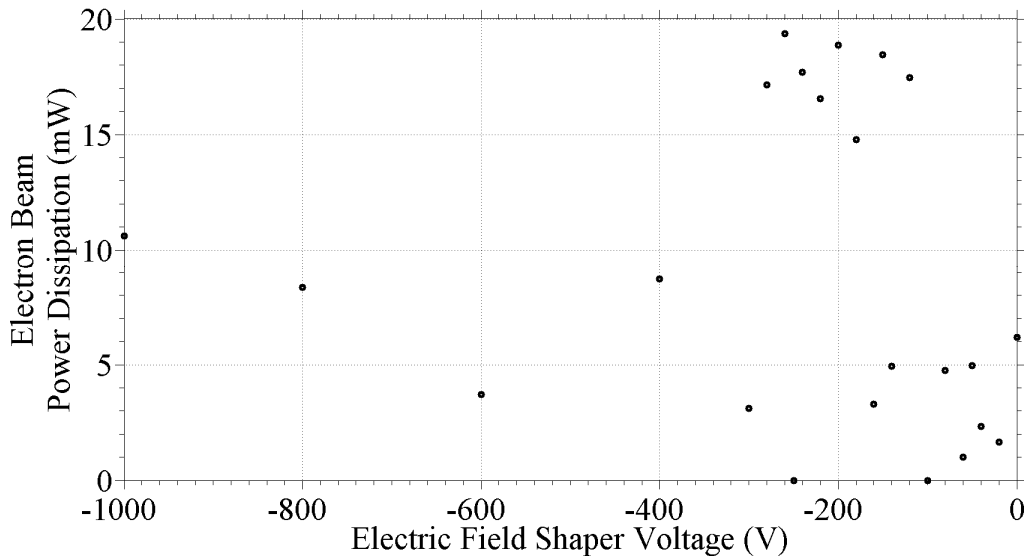
Figure 5.18: Electron beam power dissipation as determined by least-squares curve fitting and optical voltage measurements for varied electric field shaper bias voltage.

$$P_{beam} = \frac{V_{out}^2}{2R_L}$$

Equation 5.6

$15 - 20$ mW for the field shaper range that had the highest electron beam current. Tens of milliwatts of power was also less than the maximum simulated PT output power from Chapter 2 shown in Figure 2.11.

The dissipated electron beam power was plotted as a function of incident electron beam current in Figure 5.19. It is important to note that Figure 5.19 does not necessarily need to follow the same trend of Figure 2.11 due to the parallel operating and
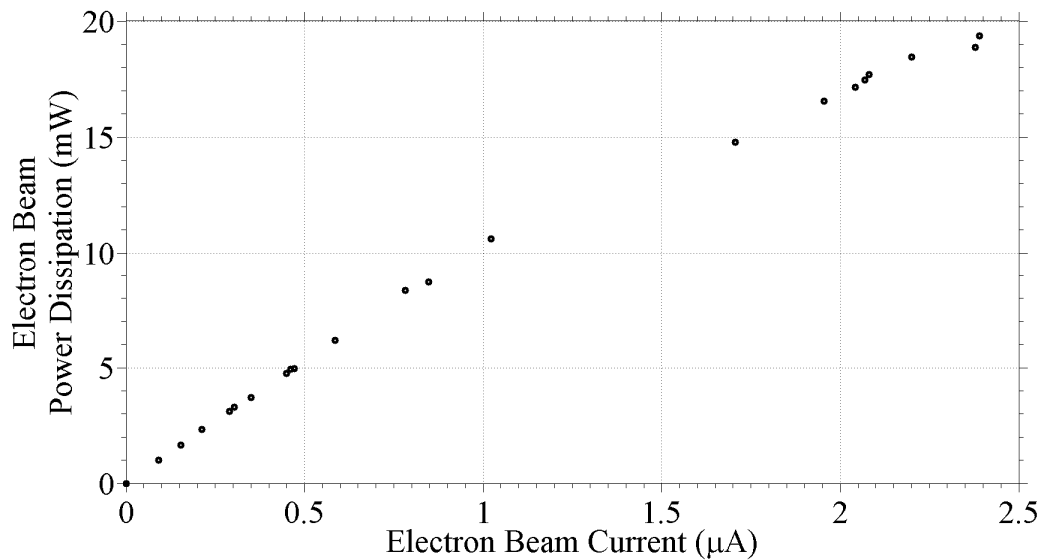
Figure 5.19: Electron beam power dissipation for varied electron beam current. The linear increase in power indicates that the PT output voltage decreased at a slower rate than the beam current increased.

beam resistances. However, Figure 5.15 demonstrates that the curve-fitted load resistances do follow the simulated trends for PT output average power shown in Figure 2.11. The dissipated beam power increases nearly linearly for increasing electron beam current. This linear trend of power with respect to current indicates that the PT output voltage decreases at a slower rate than the electron beam current increases. Thus, a PT-based accelerator system could use additional beam current to deliver increased power to an application if maintaining high particle energies is not of concern.

X-Ray Count Rates and Angular X-Ray Intensity Distribution

The x-ray count rate in counts per second (cps) generated by the PT for varied electric field shaper bias voltages is shown in Figure 5.20. Both 1.64 and 3.00 standard
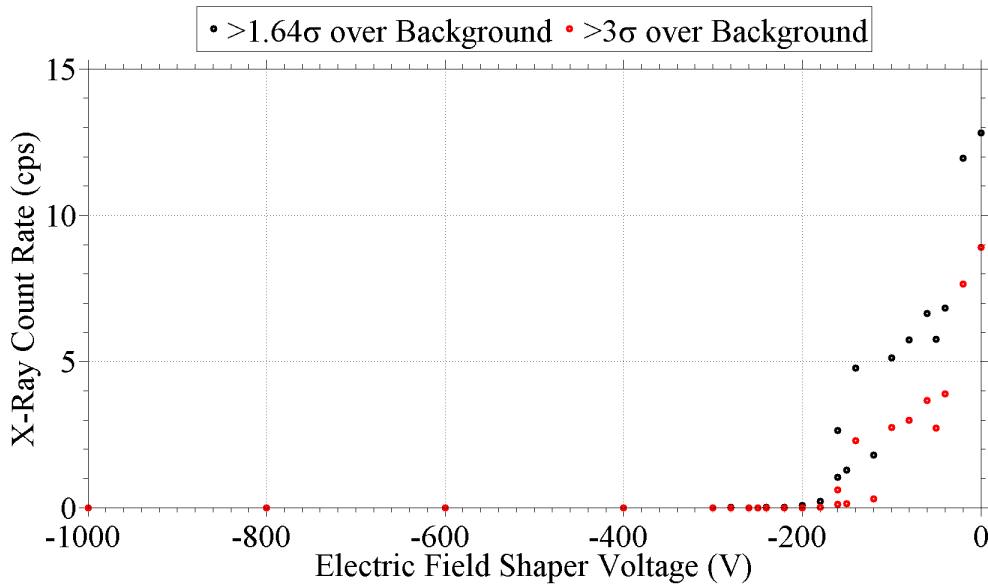
Figure 5.20: Time-averaged x-ray count rate over all energies for varied electric field shaper bias voltage. Both 1.64 and 3 standard deviations over background are shown.

deviations above background are shown to correspond to the 95 % and 99.9 % confidence intervals, respectively. The x-ray count rate decreases exponentially as the field shaper voltage is decreased. This x-ray count rate is dependent on incident electron beam current, accelerating potential, and the generated x-ray intensity angular distribution.

The total number of bremsstrahlung photons generated from an electron beam incident on an anode is proportional to the square of the accelerating potential [54]. Thus, the x-ray count rate should decrease in this fashion for a field shaper voltage between -100 V and -200 V. A combination of decreasing accelerating potential and varied electron beam current may account for the decrease in count rate for a field shaper voltage from 0 V to -100 V. However, another phenomenon that may be contributing to a decrease in x-ray count rate is the angular distribution of x-ray intensities, specifically the angular distribution based on the electron angle of incidence. This phenomenon would explain why the x-ray count rate does not increase for field shaper voltages below -300 V despite the PT output voltage increasing as indicated by the optical diagnostic.

An electron beam impacting a thick target yields bremsstrahlung radiation in the reflected direction with respect to the acceleration vector of the incident electrons. The Kirkpatrick-Wiedmann-Statham (KWS) equation describes the angular dependent intensity of the resultant photons [68]–[73]. A modification of the KWS equation to describe only reflected x-ray intensity is shown in Equation 5.7, where I is intensity, θ is the angle between the electron acceleration vector (as transmitted through the target) and the location of x-ray detection, and β is the ratio of electron velocity, v_e, to the speed of light in vacuum, c, as shown in Equation 5.9. Equation 5.8 relates the angle, θ, to the

angle between the normal to the target surface and the incoming electron acceleration vector, ϕ, and the angle between the target surface and the location of x-ray detection, ψ.

$$I(\cos\theta) = \frac{3}{8}\left[1 + \left(\frac{\cos\theta - \beta}{1 - \beta\cos\theta}\right)^2\right]\left[\frac{1-\beta^2}{(1-\beta\cos\theta)^2}\right], \quad 0° \leq \theta \leq 180°$$

Equation 5.7

$$\cos\theta = -\cos\phi\sin\psi - \sin\phi\cos\psi, \quad 0° \leq \phi, \ \psi \leq 180°$$

Equation 5.8

$$\beta = \frac{v_e}{c}$$

Equation 5.9

Figure 5.21 shows the theoretical angular distribution of the reflected bremsstrahlung x-ray intensity as calculated using Equation 5.7 to Equation 5.9. The electron beam in Figure 5.21 was normally incident on the target from the 90° polar coordinate, and x-ray intensities were normalized to the maximum x-ray intensity for each of the incident electron beam energies. The lowest incident electron energies correspond to the greatest x-ray intensities in the direction of electron origin, while the higher incident electron energies have the greatest x-ray intensities in the directions orthogonal to electron origin. Note the symmetric angular distribution of x-ray intensity
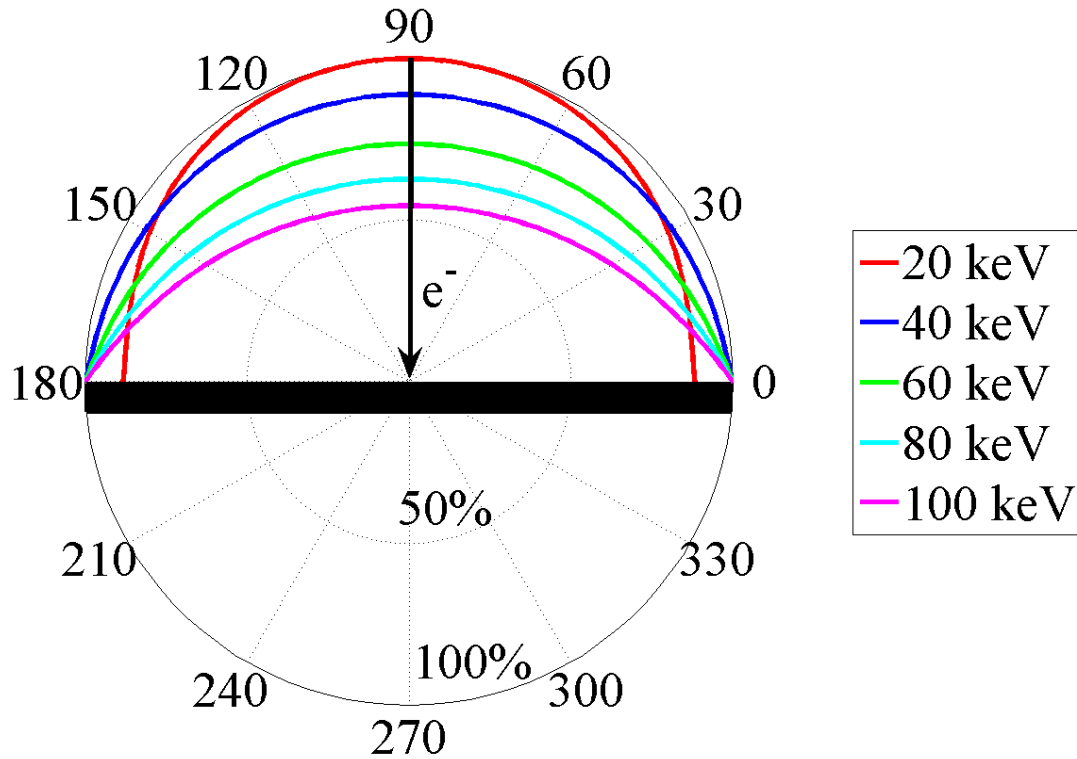
Figure 5.21: **Theoretical angular distribution of bremsstrahlung reflected x-ray intensity for a normally incident electron beam at different energies. Intensities are in terms of a percentage of the maximum reflected x-ray intensity for each of the incident electron beam energies.**

regardless of incident electron energy. This symmetric distribution only occurs for normally incident electrons.

The KWS equation can also be used to analyze the angular distribution of x-ray intensity for oblique electron incidence angles. Figure 5.22 shows such an angular distribution for varied electron incident angles for both 20 keV and 100 keV incident electron energies. The angles denoted in Figure 5.22 are the angle between the acceleration vector of electrons and the target surface. The anode target has been defined

as the polar plane between 0° and 180° such that the plotted polar angle directly corresponds to the angle of incidence for the electrons. Both 20 keV and 100 keV incident electron energies demonstrated an anisotropic angular distribution of x-ray intensities as the electrons approached glancing angles with the anode. The resultant distributions were similar to optical ray tracing diagrams describing angles of incidence and reflection.

Recall from Figure 3.2 that the output electrode of the PT had three geometric surfaces on the crystal: the top, bottom, and end. Based on Figure 5.22, any electrons that were incident on the top or bottom portions of the PT output electrode would have produced less than maximal x-ray intensities for the CdTe detector aligned along the longitudinal axis of the PT. Additionally, electrons that were incident on the portion of output electrode at the end of the PT would have yielded maximal x-ray intensities for low energy photons in the direction of the detector, but submaximal intensities for higher energy photons. If the directionality of emitted photons was the cause of the decrease in x-ray count rate for the lowest field shaper voltages, then it is implied that any incident electrons were striking surfaces such that the resultant photons were emitted preferentially away from the CdTe detector. The top and/or bottom surfaces of the PT output electrode would correspond to such surfaces. Similarly, the electrons may have missed the output electrode entirely as decreasing field shaper voltages continued to force electron incidence points toward the input electrode of the PT.

Figure 5.23 shows particle ray tracing diagrams produced from electrostatic finite-element simulations. Top-down and side views are shown of the PT output

20 keV electrons
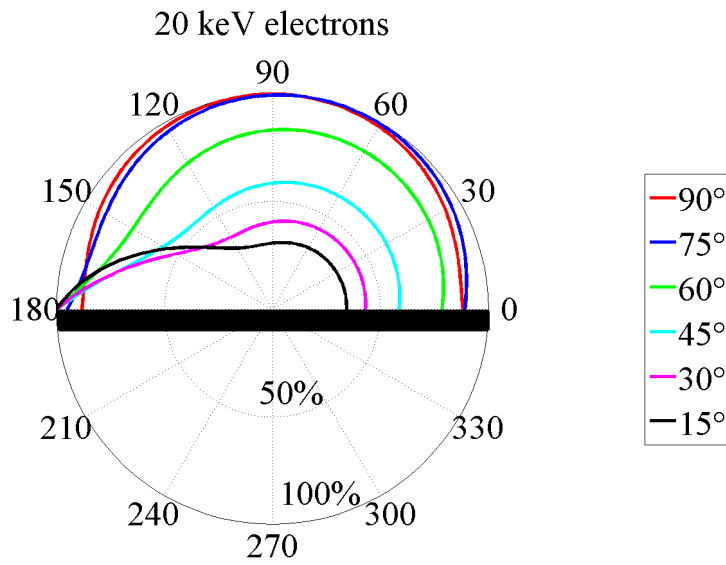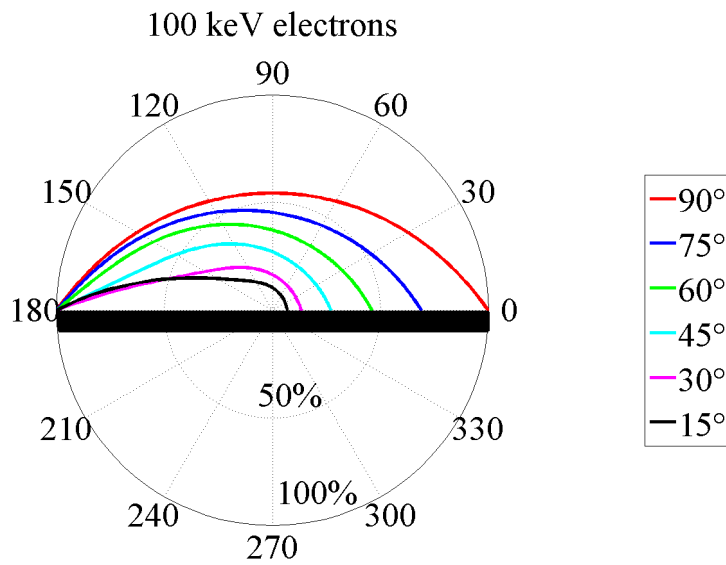
100 keV electrons

Figure 5.22: **Bremsstrahlung radiation patterns for varied incident electron angles. Angles denoted are the points of origin for electrons of (a) 20 keV and (b) 100 keV energies.**

electrode for PT output voltages of 10 kV and 25 kV and electric field shaper bias voltages of 0 V and -500 V. Accelerating potentials of 10 kV produced electron points of incidence on the top of the output electrode for a grounded electric field shaper, but produced a less focused electron beam in the side view shown in Figure 5.23a for field shaper bias voltages of -500 V. Accelerating potentials of 25 kV produced electron points of incidence nearer to the input electrode for a grounded field shaper, but focused the electrons onto the end of the PT for a -500 V field shaper voltage. The particle ray tracing diagrams shown in Figure 5.23 approximate the thermionic filament as a cylinder rather than the inverted "V" shape of a Cambridge S style filament and do not include any space-charge effects at the region of electron origin surrounding the filament. However, these diagrams do indicate that the electron trajectories and final electron points and angles of incidence on the PT are being varied among the three geometric surfaces of the PT output electrode for varied electric field shaper bias voltages. Such results further support the claim that the directionality of resultant photons may have had an effect on the measured x-ray count rate.

Varied Vacuum Chamber Pressure

A brief experiment was also conducted to use the optical diagnostic and x-ray diagnostic in conjunction to analyze a PT operating in varied vacuum chamber pressures. The gate valve between the cryopump and the vacuum chamber was partially closed to vary the effective pumping speed of the cryopump and, thus, the pressure in the vacuum chamber. Partially closing the gate valve allowed for pressures between 10^{-7} Torr and 10^{-4} Torr to be tested. Completely closing the gate valve and using a vacuum scroll pump

(a)   **(b)**

(c)   **(d)**
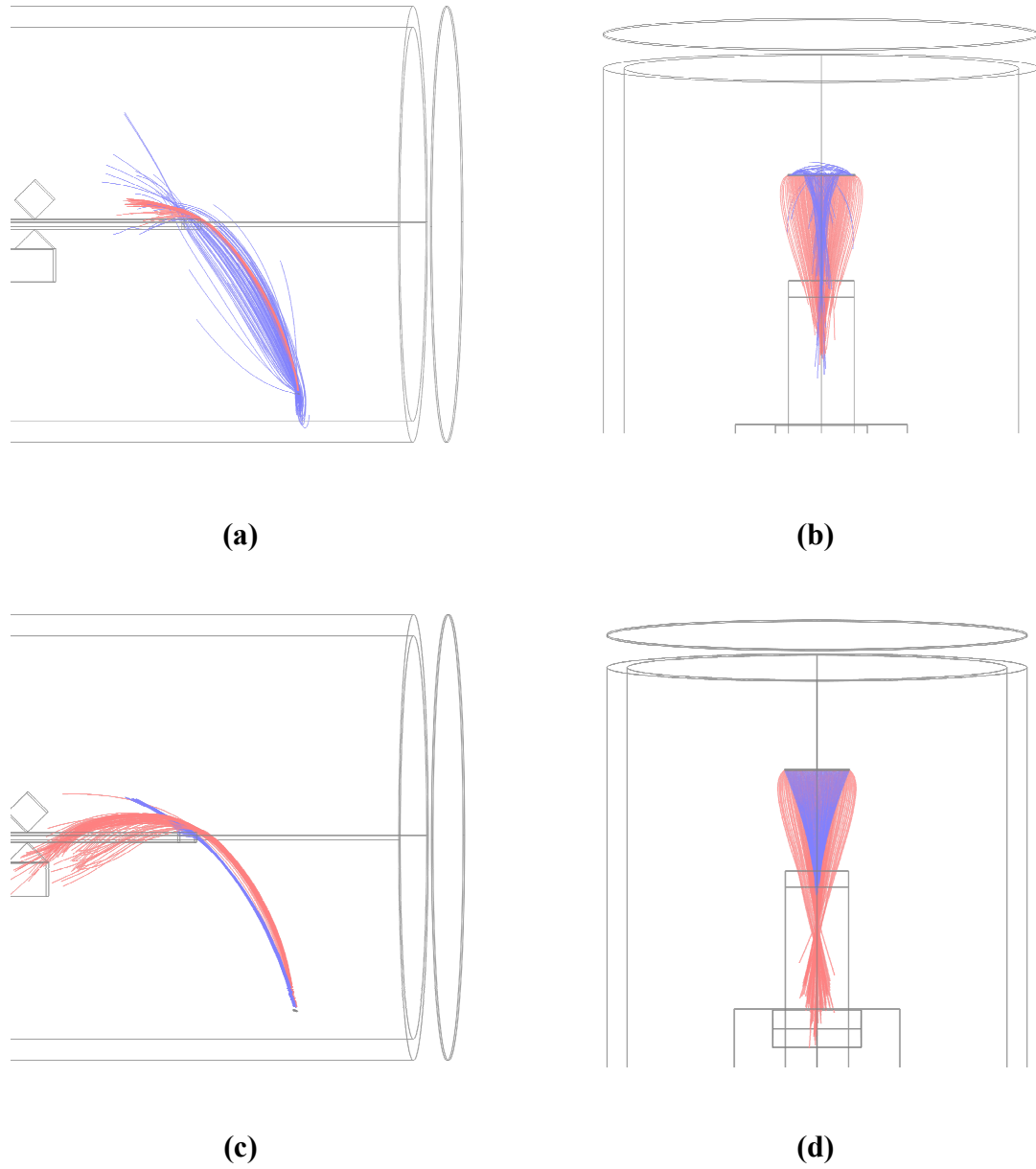
Figure 5.23: Finite-element simulated electron particle ray tracing diagrams for a 10 kV PT output voltage showing (a) side view and (b) top-down view and a 25 kV PT output voltage showing (c) side view and (d) top-down view. Red lines correspond to an electric field shaper bias voltage of 0 V, while blue lines correspond to a shaper bias voltage of -500 V in (a) through (d).

allowed for pressures on the order of 10^{-3} Torr to be tested. The electric field shaper bias voltage was grounded for all pressures tested and the dc thermionic filament current was maintained at approximately 2.3 A.

The results from the varied vacuum chamber pressure experiments are summarized in Table 5.6. The maximum curve-fitted equivalent resistance was used as the operating resistance for the PT electrical load as described in the previous section. The output voltages as determined by the x-ray diagnostic and optical diagnostic were not in agreement for the higher pressures. This may indicate that the assumptions used for the optical diagnostic analysis are not valid at higher operating pressures. The decrease in input mechanical quality factor by a factor of two for the highest pressure likely indicates that higher order vibrational modes were superimposed with the intended mode. The effect of the higher order modes due to increased vacuum chamber pressure is similar in nature to the higher order modes established by the high-voltage probe impedance in Chapter 4.

One significant result from the varied pressure experiments was the effect on measured x-ray count rate. The x-ray count rate increased by three orders of magnitude as the pressure was increased from 10^{-7} Torr to 10^{-3} Torr. The increased count rate may have been due to bremsstrahlung radiation from secondary electrons generated at the higher pressures. Positively ionized gas molecules would impact the PT on the opposite half cycle as electrons and produce secondary electron emission. Positive ion current due to charge extraction from a plasma would have also helped to maintain the PT output voltage as shown in Table 5.6 due to an increase in effective load resistance. Secondary

140

Table 5.6: Summary of experimental data for varying vacuum chamber pressure.

Vacuum Chamber Pressure (Torr)	Field Shaper Bias Voltage (V)	Input Mechanical Q-Value	Average Frequency Drift Rate (Hz/s)	Total Load Resistance (GΩ)	Beam Resistance (GΩ)	Optically Determined Voltage (kV)	Output Current (µA)	X-Ray Endpoint Energy (keV)	Total X-Ray Counts	Counting Time (s)	Time-Averaged Count Rate (cps)	Standard Deviations above Background	Thermionic Filament Number
$1.0\text{-}2.5 \times 10^{-7}$	0	3,344	-0.018	2.097	7.12	17.10	2.40	20.91	302	173.5	1.74	1.64	2
$1.0\text{-}3.6 \times 10^{-6}$	0	3,533	-0.028	2.619	22.00	21.13	0.96	21.42	2,195	171.4	12.81	1.64	2
$1.1\text{-}2.6 \times 10^{-5}$	0	3,256	-0.026	2.873	85.41	22.24	0.26	21.68	6,446	120.0	53.72	1.64	2
$1.3\text{-}2.2 \times 10^{-4}$	0	3,255	-0.025	2.025	6.35	16.33	2.57	22.97	1.05×10^{5}	131.8	794.51	1.64	2
$4.5\text{-}4.7 \times 10^{-3}$	0	1,671	-0.025	1.177	1.95	13.13	6.74	17.18	1.88×10^{5}	112.0	1682.10	1.64	2

electron emission and any invalid assumptions in the analysis of the optical diagnostic at higher pressures made the charged-particle beam current magnitude unreliable to characterize as a function of operating pressure.

X-Ray Fluorescence Experiment

X-ray fluorescence experiments were conducted for an operating PT using the configuration shown in Figure 3.16 with simultaneous target materials of lead and molybdenum. Figure 5.24 shows the results for a 1.4 hour counting time (or 7 hours real time) after correcting for background counts. Figure 5.24 also shows the counts that were greater than one standard deviation over the background. X-ray fluorescence peaks generated by the bremsstrahlung x-ray spectrum were observed based on the atomic
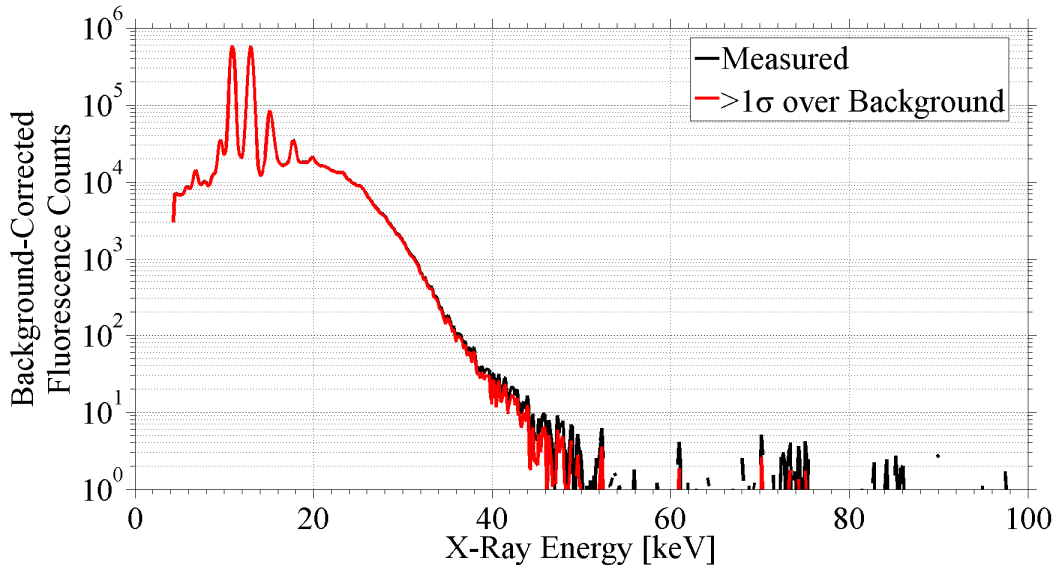
Figure 5.24: X-ray fluorescence spectrum with lead and molybdenum fluorescence peaks. The bremsstrahlung-like portion of the spectrum is due to scattered x-rays off of the fluorescence targets.

energy levels of the targets [74]. Lead L_α, L_β, L_γ, and L_l peaks were clearly observed at 10.45 keV, 12.60 keV, 14.76 keV, and 9.18 keV, respectively. The lead K_α peak at 72.80 keV had a few counts greater than one standard deviation above background. Molybdenum K_α and K_β peaks were observed at 17.37 keV and 19.60 keV, respectively. Iron K_α and K_β peaks at 6.39 keV and 7.11 keV, respectively, were also observed due to the stainless steal vacuum chamber. The bremsstrahlung-like portion of the spectrum below approximately 50 keV was due to photons from the source getting scattered in the lead target [53]. Consequently, there was a 99 % certainty that the PT was generating output voltages greater than 50 keV and 84 % certainty that output voltages greater than 72 keV were produced.

Summary of Results

The piezoelectric transformer was characterized for use as a compact particle accelerator. Although the PT output voltage was dependent on the load impedance, high accelerating potentials were achieved by using optical methods as an ultra-high impedance diagnostic. A least-squares curve fitting algorithm was used to determine the resistance of an electron beam under varied conditions. Using the experimental data and curve fitting results, the PT was shown to be capable of accelerating approximately 2.5 μA of electron beam current with an acceleration potential of 16 kV. Similarly, the maximum dissipated beam power was determined to be approximately 20 mW. Higher PT output voltages in excess of 120 kV were measured, but current measurements could not be taken due to the increased fracture rate of polished crystals. Additional parameters such as resonant frequency drift rate and input mechanical quality factor were also presented to characterize the PT operation while accelerating electron beam loads.

6. Conclusions

A high-voltage, length-extensional piezoelectric transformer (PT) was characterized using both modeling and experimental results for varied electrical load impedances. The PT was made of 135° rotated y-cut lithium niobate (LiNbO$_3$) and had dimensions of 100 mm x 10 mm x 1.5 mm. Three PT configurations were used including mode 1 bipolar, mode 1 unipolar, and mode 2 unipolar. The primary configuration was mode 2 unipolar. The mode 2 resonant frequency was at approximately 62 kHz and was modulated at duty factors from 5 % – 20 % with 1 s burst periods. Typical input voltage and current amplitudes were between 7.5 – 12 V and 100 – 160 mA, respectively. PT voltage transformation ratios in excess of 10,000 were observed for some electron-beam diode loads. However, the PT was operated at transformation ratios closer to 3,000 for much of the data presented to prevent exceeding the yield stress of the LiNbO$_3$.

Modeling of the PT was performed to analyze the theoretical effects of varied parallel *RC* load impedances on the operating characteristics of the PT. A model that assumed only one-dimensional vibration along the length of the PT (1-D model) was

developed based on the works of Yang and Zhang for the PT geometry being tested [9], [10], [17], [28]. Additionally, the mechanical loss factor and dielectric loss factor were implemented to help account for nonidealities of the PT [31], [45]–[47]. The model solved a set of differential equations and corresponding boundary conditions based on the piezoelectric constitutive equations and Maxwell's equations. Analytical solutions were generated to describe the time-harmonic elastic motion, stress, electric field, electric potential, and input and output voltages and currents. Results of the 1-D model were verified using 3-D finite element simulations that solved a set of partial differential equations to describe the PT system.

Simulated load resistances and capacitances were varied exponentially from 10^8 Ω to 10^{11} Ω and 10^{-15} F to 10^{-12} F, respectively. Mechanical displacement, stress, electric field, and electric potential were all found to increase as the load resistance was increased. The PT voltage transformation ratio was found to increase logarithmically as the load resistance increased exponentially. The output current was found to vary in a similar fashion with asymptotic current values for the lowest load impedances. Simulated maximum output voltages and currents were greater than 100 kV and 9 mA, respectively, including displacement current, although maximum current and voltage values did not occur simultaneously. Simulated maximum output average powers were in excess of 300 mW for a 2 x 10^8 Ω, 10^{-12} F load. The simulated efficiency at the point of maximum power was approximately 50 % when defined as the ratio of output electrical average power to input electrical average power, but efficiencies approaching 100 % were simulated for lower output powers on the order of 10 mW.

An optical diagnostic was developed to use in conjunction with an x-ray diagnostic to characterize the PT experimentally during operation with an electron-beam diode load. The optical diagnostic was based on the inherent photoelastic and electro-optic properties of lithium niobate. A laser beam was propagated through the PT, and the resulting change in optical polarization from linear to elliptical was measured. The measurement was performed at different positions along the length of the PT to generate a profile of the changes in phase angle between the ordinary and extraordinary wave components of the propagating laser beam. The internal stress, electric field, and electric potential profiles along the length of the PT were generated using the optical data. The optical diagnostic was validated using simulated data, the x-ray diagnostic, and a quality factor diagnostic.

Initial experimental results with a Cockcroft-Walton circuit, capacitive voltage divider, and electron-beam diode loads at the output of the PT indicated a need for characterization of the PT with varied electrical load impedances. The bias voltage of a cylindrical electric field shaper surrounding the PT was varied from -1 kV to 0 V to modify the electron beam current that was incident on the PT output electrode. The equivalent parallel load capacitances and resistances were determined using a least-squares curve fitting algorithm known as particle swarm analysis with the 1-D model and optical diagnostic results for the varied field shaper voltages. A parallel operating resistance value was defined as the highest curve-fitted load resistance, and the electron beam resistance was determined. The electron beam current incident on the PT and beam power dissipated were analyzed using measured data and curve fitting results.

The PT operating parameters were plotted versus the varied electric field shaper bias voltages. The range of field shaper voltages between -300 V and -150 V resulted in the highest electron beam currents of approximately 2.5 μA. PT output voltages were observed to decrease from approximately 22 kV to 16 kV for the highest electron beam currents. The resonant frequency decreased throughout the operating time for all experiments at an average rate of 0.026 Hz/s. The average input mechanical quality factor was 3,300. The maximum dissipated electron beam power was determined to be approximately 20 mW.

X-ray measurements were taken simultaneously with the optical measurements for the varied electric field shaper voltage experiments. The measured x-ray count rate decreased exponentially as the field shaper voltage was decreased from ground potential to -1 kV. This decrease in count rate was partially caused by the decrease in PT output voltage and electrons missing the output electrode. However, one other possible cause of the decreased x-ray count rate is the directionality of bremsstrahlung photons for oblique electron incidence angles on an anode target. The Kirkpatrick-Wiedmann-Statham (KWS) equation was used to generate polar plots of the angular distribution of bremsstrahlung x-ray intensity [68]–[73]. The maximum x-ray intensity in the direction of the x-ray detector for 20 keV electrons was for normal incidence on the PT output electrode. Approximately 25% of the maximum intensity would have been generated in the direction of the x-ray detector for 20 keV electrons incident at an angle of 15° with respect to the PT output electrode. Additionally, an x-ray fluorescence experiment was conducted at higher PT voltage transformation ratios to verify the production of high-energy photons using the PT. Observed lead L_α, L_β, and K_α and molybdenum K_α, and K_β

fluorescence peaks indicated that there was an 84 % certainty that photon energies in excess of 72 keV were produced.

The research presented in this dissertation has shown that the operation of piezoelectric transformers can be analyzed using optical methods as an ultra-high impedance diagnostic. PTs can be operated with charged-particle beam loads, but the magnitude of the beam current has an effect on the output voltage that is produced. The effects of different beam current magnitudes can be studied using experimental data and curve fitting techniques with modeled results. However, an equivalent operating resistance that includes the field-emission of electrons from the PT and electromechanical losses must be empirically determined for a given operating regime to determine the electron beam currents incident on the PT.

7. Future Work

The research presented in this dissertation was for the purpose of characterizing a piezoelectric transformer (PT) as a high-voltage source for compact particle accelerators. However, extensions of this research could provide useful tools in other research areas. This chapter will briefly describe two such extensions: an optical PT-based external electric field measurement for high voltage applications and an x-ray source that maximizes the measured intensity of both high energy and low energy photons.

Optical External Electric Field Measurement

The optical diagnostic designed in Chapter 4 was for the purpose of measuring the internal stress, electric potential, and electric field within a resonating PT. However, the electro-optic and photoelastic effects are also valid for the non-resonant case. A lithium niobate slab with a geometry similar to that of the PTs used in this dissertation would be under the influence of the electro-optic and photoelastic effects when placed into a high electric field region as shown in Figure 7.1. Such a measurement would not be valid for
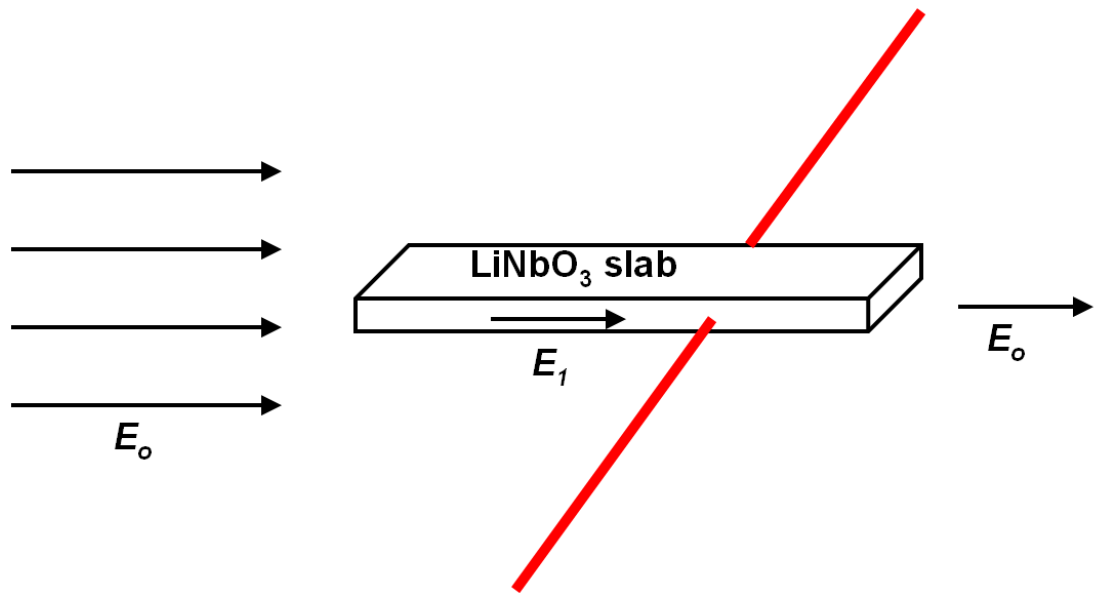
Figure 7.1: Diagram of proposed external electric field measurement.

the dc electric field case as the optical polarization would achieve a final state and $\pi/2$ phase transitions could not be counted. This measurement would be better suited for measuring pulsed electric fields by counting the number of $\pi/2$ phase transitions during the rise time of the pulse.

The external electric field, E_o, in Figure 7.1 would induce an electric field in the lithium niobate slab, E_{1o}, based on Equation 7.1 where ε_o is the permittivity of vacuum, ε_1 is the permittivity of lithium niobate, and ρ_s is the surface charge density at the boundary [48]. The electric field, E_{1o}, in the slab would generate a stress, T_1, and additional electric field component, E_{11}, based on the piezoelectric effect described in Equation 2.1 and Equation 2.2. The linear superposition of the electric fields within the slab would generate the total electric field within the slab, E_1, as shown in Figure 7.1.

$$\varepsilon_o E_o - \varepsilon_1 E_{1o} = \rho_s$$

Equation 7.1

A helium-neon (HeNe) laser beam propagating through the system shown in Figure 4.3 and Figure 7.1 would have a change in phase difference between the ordinary and extraordinary wave components entering and exiting the slab. If a pulsed electric field had a rise time of approximately 16 μs, then the number of $\pi/2$ phase transitions could be counted during the rise time to yield the total phase transition based on Equation 4.16. Rise times faster than 16 μs could be measured, but a 16 μs rise time would correspond to a similar time period for manually counting the number of $\pi/2$ phase transitions. It may be difficult to manually determine the total phase transition for faster rise times.

The relationship between the induced internal stress and electric field and the number of $\pi/2$ phase transitions during the rise time of the pulse would yield the magnitude of the externally applied electric field. A similar effect could be produced for a resonant PT, but the magnitudes of the PT-based electric field would be mathematically and analytically difficult to distinguish from the externally induced electric field. This measurement could aid in the design of anode-cathode gaps for spark-gap switches, electron-beam diodes, etc.

X-Ray Source

The x-ray diagnostic used in this dissertation was a byproduct of the electron-beam interactions with the PT. Neither x-ray production nor measured intensity was

optimized during the experiments conducted for this research. Consequently, gains in both x-ray flux and intensity in a desired direction could be improved by redesigning the system. The Kirkpatrick-Wiedmann-Statham (KWS) equation and Figure 5.22 suggest that electrons interacting at a glancing angle with the bottom portion of the output electrode would yield higher x-ray intensities in the longitudinal direction for high energy electrons. Resultant photons with a low angle of incidence with respect to the electrode would have maximized x-ray intensities in the direction of the detector for both high and low energy incident electrons.

One possible design that would improve the x-ray intensity along the longitudinal axis of the PT would involve an electron beam originating near the input electrodes as shown in Figure 7.2. The accelerated electrons would have a low angle of incidence, so
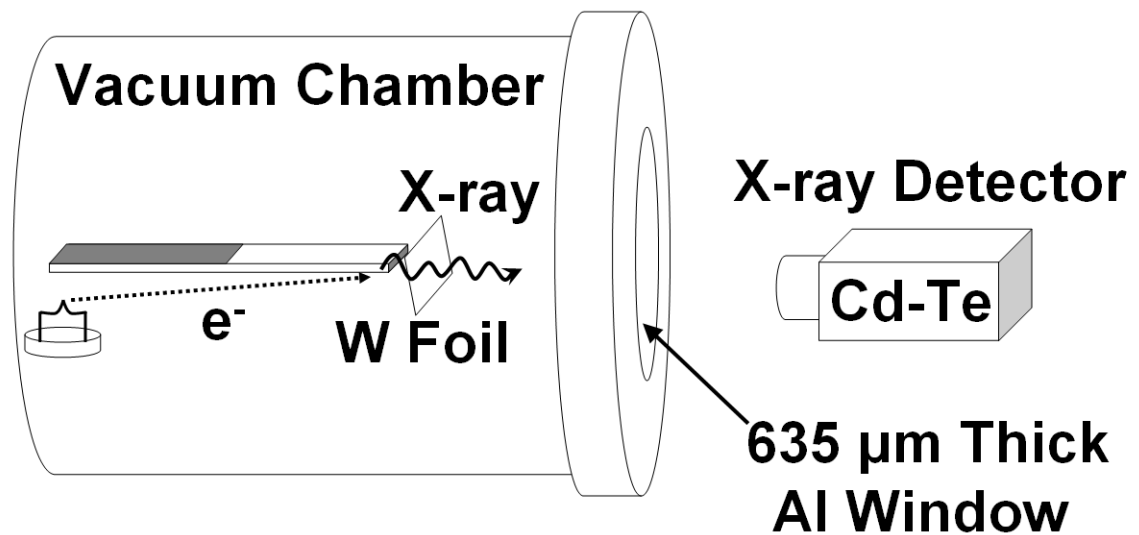
Figure 7.2: Proposed x-ray source. The electrons are accelerated along the length of the PT and strike either the PT output electrode or a thin capacitvely coupled tungsten (W) foil to generate bremsstrahlung x-rays.

152

20 keV and 100 keV photons would have optimal production in the direction of the detector. The gain in directional x-ray intensity for high energy incident electrons is of particular interest because the resultant bremsstrahlung spectrum would also increase the low energy count rate.

Figure 5.23 also suggests that the electrons may not be incident on the desired location throughout the sinusoidal range of the acceleration potential. The implementation of a tungsten foil near the end of the PT as shown in Figure 7.2 could result in the additional transmission-mode photons at the detector. The thin foil would capacitively couple to the output of the PT to a voltage less than but near the PT output voltage. The load capacitance would need to be less than the PT output capacitance of 0.1 pF to prevent decreasing the PT output as shown in Figure 2.9. Any electrons that overshoot the target would be incident on the foil. The radiated photons in the direction of electron acceleration would be attenuated slightly by the foil, but transmit to the detector. This design would both maximize the intensities of the high and low energy reflection-mode x-rays and introduce additional transmission-mode x-rays to increase photon energy and flux at the detector.

A. Detailed 1-D Model Derivation

The derivation of the 1-D model uses tensor notation that may not be familiar to all readers. Indices from 1-3 correspond to the tensile, or linear, components, while 4-6 correspond to the shear, or tangential, components of the respective variable [34]. If two constants being multiplied together have the same indices, then the denoted product is actually a summation of the product over the range of the repeated index. An example of this is denoted in Equation A.1. Summations will be from one to three or one to six depending whether the equation uses two-suffix notation or single-suffix notation, respectively [9], [34], [39]. Another notation is that "…a comma followed by an index represents a partial differentiation with respect to the coordinate associated with the index [9]." An example of this is shown in Equation A.2. If the comma is followed by two indices, a second partial differentiation is denoted as shown in Equation A.3. Finally, a dot, or series of dots, over a variable denotes partial differentiation with respect to time as shown in Equation A.4. Table A.1 shows a list of variable definitions for all variables included in this chapter. All constants are rotated using Equation A.5, so the prime notation will be dropped throughout this derivation.

$$S_{ij} = s_{ijkl}T_{kl} + d_{kij}E_k = \sum_{k=1}^{3}\sum_{l=1}^{3} s_{ijkl}T_{kl} + \sum_{k=1}^{3} d_{kij}E_k$$

Equation A.1

154

$$E_i = -\phi_{,i} = -\frac{\partial \phi}{\partial x_i}$$

Equation A.2

$$\rho \ddot{u}_2 = \frac{u_{2,22}}{s_{22}} = \frac{1}{s_{22}} \frac{\partial^2 u_2}{\partial x_2^2}$$

Equation A.3

$$\frac{u_{2,22}}{s_{22}} = \rho \ddot{u}_2 = \rho \frac{\partial^2 u_2}{\partial t^2}$$

Equation A.4

$$Q_{ij} = \begin{bmatrix} 1 & 0 & 0 \\ 0 & \cos\theta & \sin\theta \\ 0 & -\sin\theta & \cos\theta \end{bmatrix}, \quad \theta = \frac{\pi}{4}$$

Equation A.5

The PT configuration used for the 1-D model is shown in Figure A.1. The length-extensional transformer is a bar with dimensions such that $a + b \gg w \gg h$. The polarization of the crystal lattice lies along the P-axis. The driving portion of the PT where the input voltage is applied is defined as the region $-a < x_2 < 0$. A time harmonic

Table A.1: Definition of variables used in the 1-D model derivation.

Variable	Definition	Units
V_1	voltage applied across the input electrodes	V
V_2	voltage generated across the load impedance	V
I_1	input current	A
I_2	output current	A
Q_1	charge on the input electrode at $x_3 = h$	C
Q_2	charge on the output electrode at $x_2 = b$	C
Z_L	load impedance	Ω
R_L	load resistance	Ω
C_L	load capacitance	F
x_1	position along the global x-axis	m
x_2	position along the global y-axis	m
x_3	position along the global z-axis	m
l	length of the PT	m
w	width of the PT	m
h	thickness of the PT	m
S	strain	—
T	stress	Pa
E	electric field	V/m
D	electric flux density	C/m^2
ϕ	electric potential	V
ρ	mass density	kg/m^3
u	mechanical displacement	m
t	time	s
ω	angular frequency	rad/s

Variable	Definition	Units
f	applied body force	N
s	elastic compliance coefficients	m^2/N
c	elastic stiffness coefficients	N/m^2
d	piezoelectric strain coefficients	C/N
e	piezoelectric coefficients	C/m^2
ε^S	permittivity with respect to constant strain	F/m
ε^T	permittivity with respect to constant stress	F/m
k	electromechanical coupling coefficient	—
Q_m	input mechanical quality factor	—
δ_m	mechanical loss factor	—
γ	dielectric loss factor	—

Figure A.1: Diagram of the PT that was used in the 1-D model.

driving voltage, $V_1(t)$, is applied across the driving portion to excite the resonant extensional vibration. The receiving portion where the voltage step-up occurs is defined as the region $0 < x_2 < b$. The load impedance, Z_L, is connected between the output electrode and ground. General equations necessary to solve the model are Equation A.6 to Equation A.14 [9], [28]. The driving portion and receiving portion of the PT are analyzed separately.

Equation A.6 restricts displacement and stress in the 1-D model to the longitudinal axis. Equation A.7 and Equation A.8 describe the elastic motion occurring within the PT. The applied body force in Equation A.7 is assumed to be zero, since there is only external electrical excitation of the PT. Equation A.9 is a form of Gauss's law where there is assumed to be no body charge through the cross-section [9], [48]. Equation A.10 describes the electric potential and is an electrostatic form of Faraday's law [9], [48].

$$T_1 = T_3 = T_4 = T_5 = T_6 = 0$$

Equation A.6

$$T_{ji,j} + \rho f_i = \rho \ddot{u}_2$$

Equation A.7

$$S_{ij} = \frac{\left(u_{i,j} + u_{j,i} \right)}{2}$$

Equation A.8

$$D_{i,i} = 0$$

Equation A.9

$$E_i = -\phi_{,i}$$

Equation A.10

$$T_{ij} = c_{ijkl} S_{kl} + e_{kij} E_k$$

Equation A.11

$$D_i = e_{ijk} S_{jk} + \varepsilon_{ij}^S E_j$$

Equation A.12

$$S_{ij} = s_{ijkl} T_{kl} + d_{kij} E_k$$

Equation A.13

$$D_i = d_{ijk} T_{jk} + \varepsilon_{ij}^T E_j$$

Equation A.14

Equation A.11 and Equation A.12 or Equation A.13 and Equation A.14 describe the stress-charge and strain-charge forms, respectively, of the piezoelectric constitutive equations. However, the necessary coefficients are not always given in the desired form in the literature. Equation A.15 to Equation A.17 can be used to conveniently transform given coefficients into the desired form. Equation A.18, Equation A.19, and Equation A.20 give the rotated elastic compliance, piezoelectric strain, and permittivity with respect to constant stress coefficients, respectively, for a 45° rotated lithium niobate slab as shown in Figure A.1. These can be expressed in matrix form using Voigt's notation due to the symmetry of the tensors that describe the respective coefficients [9], [34], [39], [43]. The superscript "T" for the permittivity with respect to constant stress will be dropped for convenience, since the strain-charge form of the piezoelectric constitutive equations are used.

$$[s] = [c]^{-1}$$

Equation A.15

$$[d] = [e][c]^{-1}$$

Equation A.16

$$\left[\varepsilon^T\right]=\left[\varepsilon^S\right]+\left[e\right]\left[c\right]^{-1}\left[e\right]^T$$

Equation A.17

$$s_{pq}=\begin{pmatrix} 0.0577 & -0.0174 & -0.0073 & -0.0044 & 0 & 0 \\ -0.0174 & 0.0671 & -0.0228 & -0.0091 & 0 & 0 \\ -0.0073 & -0.0228 & 0.0569 & 0.0011 & 0 & 0 \\ -0.0044 & -0.0091 & 0.0011 & 0.1366 & 0 & 0 \\ 0 & 0 & 0 & 0 & 0.1731 & 0.0170 \\ 0 & 0 & 0 & 0 & 0.0170 & 0.1324 \end{pmatrix}\times10^{-10}$$

Equation A.18

$$d_{pk}=\begin{pmatrix} 0 & 0 & 0 & 0 & 0.7734 & 0.1867 \\ -0.1533 & 0.3308 & -0.1492 & -0.0984 & 0 & 0 \\ 0.1400 & -0.2959 & 0.1842 & 0.1949 & 0 & 0 \end{pmatrix}\times10^{-10}$$

Equation A.19

$$\varepsilon_{ij}^T=\begin{pmatrix} 0.7540 & 0 & 0 \\ 0 & 0.5040 & -0.2500 \\ 0 & -0.2500 & 0.5040 \end{pmatrix}\times10^{-9}$$

Equation A.20

161

Driving Portion

The driving portion of the PT is the region where a time-harmonic voltage is applied across the input electrodes to produce an electric field through the thickness of the crystal. The electric potential through the thickness of the crystal is assumed to vary linearly and is based on the input voltage as shown in Equation A.21. The electric field in the driving portion of the PT can be found using Equation A.10 and Equation A.21 and is shown in Equation A.22. Relevant indices of Equation A.7, Equation A.13, and Equation A.14 can be simplified for the driving portion to yield Equation A.23, Equation A.24, and Equation A.25, respectively.

$$\phi = \frac{x_3}{h} V_1$$

Equation A.21

$$E_1 = E_2 = 0, \quad E_3 = \frac{-V_1}{h}$$

Equation A.22

$$T_{2,2} = \rho \ddot{u}_2$$

Equation A.23

$$S_2 = s_{22}T_2 + d_{33}E_3$$

Equation A.24

$$D_3 = d_{32}T_2 + \varepsilon_{33}E_3$$

Equation A.25

Equating the strain in the x_2 direction from Equation A.8 and Equation A.24 yields the longitudinal stress generated in the driving portion due to the applied voltage as shown in Equation A.26. The first derivative of Equation A.26 can be equated to Equation A.23 to yield an expression for the elastic motion. Equation A.26 is substituted into Equation A.25 to express the electric flux density in terms of the elastic motion in Equation A.28.

$$T_2 = \frac{1}{s_{22}}\left(u_{2,2} + d_{32}\frac{V_1}{h}\right)$$

Equation A.26

$$\frac{u_{2,22}}{s_{22}} = \rho\ddot{u}_2$$

Equation A.27

$$D_3 = \frac{d_{32}}{s_{22}} u_{2,2} - \bar{\varepsilon}_{33} \frac{V_1}{h}$$

Equation A.28

$$\bar{\varepsilon}_{33} = \varepsilon_{33}\left(1 - k_{32}^2\right), \quad k_{32}^2 = \frac{d_{32}^2}{\varepsilon_{33} s_{22}}$$

Equation A.29

The boundary conditions in the driving portion govern the stress at the end of the PT at $x_2 = -a$ and the current flowing into the input electrodes. The stress at the boundary is equal to zero because there is no applied body force at the boundary. The boundary condition for the stress is expressed in Equation A.30. Equation A.31 shows the charge on the input electrode at $x_3 = h$ which was found using Gauss's law. The input current is the time derivative of the charge on the input electrode at $x_3 = h$ as shown in Equation A.32.

$$T_2 = \frac{1}{s_{22}}\left(u_{2,2} + d_{32}\frac{V_1}{h}\right) = 0, \quad x_2 = -a$$

Equation A.30

$$Q_1 = -w \int_{-a}^{0} D_3 \, dx_2$$

Equation A.31

$$I_1 = -\dot{Q}_1$$

Equation A.32

Receiving Portion

In the receiving portion of the PT, the stress is induced by the elastic motion established in the driving portion. The stress generates an electric field based on the direct piezoelectric effect. Since the output electrode is only at the end of the receiving portion, the electric flux density is zero in the x_1 and x_3 directions as shown in Equation A.33. Therefore the electric field only exists in the x_2 direction as shown in Equation A.34. Relevant indices of the general equations are shown in Equation A.35 to Equation A.38.

$$D_1 = D_3 = 0$$

Equation A.33

$$E_1 = E_3 = 0, \quad E_2 = -\phi_{,1}$$

Equation A.34

$$D_{2,2} = 0$$

Equation A.35

$$T_{2,2} = \rho \ddot{u}_2$$

Equation A.36

$$S_2 = s_{22} T_2 + d_{22} E_2$$

Equation A.37

$$D_2 = d_{22} T_2 + \varepsilon_{22} E_2$$

Equation A.38

The longitudinal electric flux density component must be constant along the x_2 direction based on Equation A.35. As such, the electric flux density can be chosen to be in terms of material constants and an unknown integration constant, c_1, as shown in

Equation A.39. Equating the strain in Equation A.8 and Equation A.37, the stress in the receiving portion can be found as shown in Equation A.40. The elastic motion in the receiving portion can be described by equating the first derivative of Equation A.40 with Equation A.36 as shown in Equation A.42. Substituting Equation A.40 into Equation A.38 yields an expression shown in Equation A.43 for the electric potential in the receiving portion in terms of the mechanical displacement and an unknown integration constant, c_2.

$$D_2 = \frac{d_{22}}{s_{22}} c_1$$

Equation A.39

$$T_2 = \frac{1}{\bar{s}_{22}} \left(u_{2,2} - k_{22}^2 c_1 \right)$$

Equation A.40

$$\bar{s}_{22} = s_{22} \left(1 - k_{22}^2 \right), \quad k_{22}^2 = \frac{d_{22}^2}{s_{22} \varepsilon_{22}}$$

Equation A.41

$$\frac{u_{2,22}}{\overline{s}_{22}} = \rho \ddot{u}_2$$

Equation A.42

$$\phi_2 = \frac{1}{\overline{d}_{22}}\left(c_1 x_2 - u_2\right) + c_2$$

Equation A.43

$$\overline{d}_{22} = d_{22}\left(1 - \frac{1}{k_{22}^2}\right)$$

Equation A.44

Similar to the boundary conditions for the driving portion, the stress at the end of the PT at $x_2 = b$ must be equal to zero. This is shown in Equation A.45. Additionally, the electric potential at $x_2 = b$ is equal to the output voltage, V_2. Gauss's law can be used to determine the charge at the output electrode as shown in Equation A.46. The output current is shown in Equation A.47 as the time derivative of the charge on the output electrode.

$$T_2 = \frac{1}{\overline{s}_{22}}\left(u_{2,2} - k_{22}^2 c_1\right) = 0, \quad x_2 = b$$

Equation A.45

$$D_2 = \frac{d_{22}}{s_{22}} c_1 = \frac{-Q_2}{hw}$$

Equation A.46

$$I_2 = -\dot{Q}_2$$

Equation A.47

Interface Conditions

The boundary between the driving portion and receiving portions of the PT at $x_2 = 0$ must be continuous in terms of the mechanical displacement and the stress. The continuity equation for the mechanical displacement is shown in Equation A.48, while the continuity of the stress is shown in Equation A.49. The electric potential at $x_2 = 0^+$ can be taken as the average value of the electric potential over the cross section, since the electric potential in the receiving portion is not dependent on w or h. This is expressed in Equation A.50. The PT is operated by a time-harmonic input voltage, so the vibration analysis is conducted in the frequency domain. As such, all time-dependent variables are

expressed in phasor form. The interface between the PT and the electrical load can be expressed by the phasor form of Ohm's law shown in Equation A.51. The impedance for a parallel RC load as shown in Figure A.2 is expressed in Equation A.52.
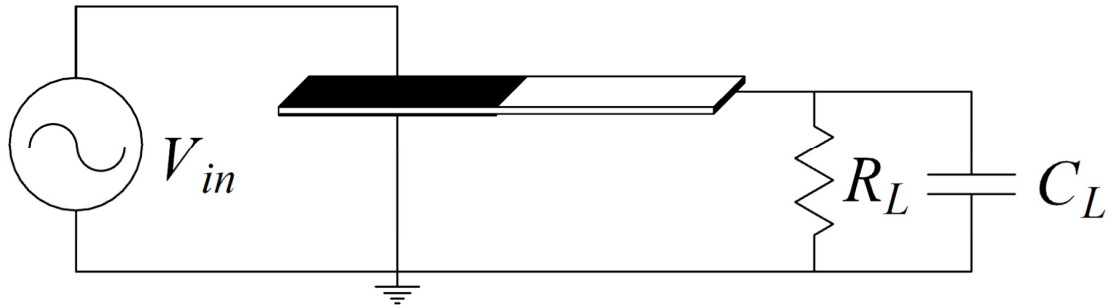
Figure A.2: Equivalent load circuit attached to the PT.

$$u_2\left(0^-\right) = u_2\left(0^+\right)$$

Equation A.48

$$T_2\left(0^-\right) = \frac{1}{s_{22}}\left(u_{2,2} + d_{32}\frac{V_1}{h}\right)\Bigg|_{x_2=0^-} = \frac{1}{s_{22}}\left(u_{2,2} - k_{22}^2 c_1\right)\Bigg|_{x_2=0^+} = T_2\left(0^+\right)$$

Equation A.49

$$\phi(0^+) = \frac{1}{2}V_1$$

Equation A.50

$$\tilde{V}_2 = \tilde{I}_2 Z_L$$

Equation A.51

$$Z_L = \frac{jR_L}{j - \omega R_L C_L}$$

Equation A.52

Forced Vibration Analysis

The time-harmonic elastic motion of the PT is forced by the input voltage, $V_1(t) = \tilde{V}_1 e^{j\omega t}$. Solving the system of phasor equations described in Equation A.53 to Equation A.58 yields the solution for the mechanical displacement due to the elastic motion of the PT.

$$\frac{1}{s_{22}}\tilde{u}_{2,22} = -\omega^2 \rho \tilde{u}_2, \quad -a \leq x_2 \leq 0$$

Equation A.53

$$\frac{1}{\overline{s}_{22}}\tilde{u}_{2,22} = -\omega^2 \rho \tilde{u}_2, \quad 0 \le x_2 \le b$$

Equation A.54

$$\frac{1}{s_{22}}\left(\tilde{u}_{2,2} + d_{32}\frac{\tilde{V}_1}{h}\right) = 0, \quad x_2 = -a$$

Equation A.55

$$\frac{1}{\overline{s}_{22}}\left(\tilde{u}_{2,2} - k_{22}^2 \tilde{c}_1\right) = 0, \quad x_2 = b$$

Equation A.56

$$\tilde{u}_2\left(0^-\right) = \tilde{u}_2\left(0^+\right)$$

Equation A.57

$$\frac{1}{s_{22}}\left(\tilde{u}_{2,2}\left(0^-\right) + d_{32}\frac{\tilde{V}_1}{h}\right) = \frac{1}{\overline{s}_{22}}\left(\tilde{u}_{2,2}\left(0^+\right) - k_{22}^2 \tilde{c}_1\right)$$

Equation A.58

Solving the set of differential equations with the corresponding boundary conditions yields Equation A.59.

$$\tilde{u}_2 = \begin{cases} \left(\alpha_{11} \dfrac{d_{32} \tilde{V}_1}{h} + \beta_{11} k_{22}^2 \tilde{c}_1 \right) \sin(kx_2) + \left(\alpha_{12} \dfrac{d_{32} \tilde{V}_1}{h} + \beta_{12} k_{22}^2 \tilde{c}_1 \right) \cos(kx_2), & -a \le x_2 \le 0 \\[4mm] \left(\alpha_{22} \dfrac{d_{32} \tilde{V}_1}{h} + \beta_{22} k_{22}^2 \tilde{c}_1 \right) \sin(\bar{k}x_2) + \left(\alpha_{12} \dfrac{d_{32} \tilde{V}_1}{h} + \beta_{12} k_{22}^2 \tilde{c}_1 \right) \cos(\bar{k}x_2), & 0 \le x_2 \le b \end{cases}$$

Equation A.59

$$k = \omega \sqrt{\rho s_{22}}, \quad \bar{k} = \omega \sqrt{\rho \bar{s}_{22}}$$

Equation A.60

$$\alpha_{11} = \frac{-1}{\Delta \cos(ka)} \bar{s}_{22} \cos(\bar{k}b) \sin(ka)(\cos(ka) - 1) - \frac{1}{k \cos(ka)}$$

Equation A.61

$$\beta_{11} = \frac{1}{\Delta} s_{22} \sin(ka)(1 - \cos(\bar{k}b))$$

Equation A.62

173

$$\alpha_{12} = \frac{1}{\Delta} \bar{s}_{22} \cos(\bar{k}b)(\cos(ka)-1)$$

Equation A.63

$$\beta_{12} = \frac{-1}{\Delta} s_{22} \cos(ka)(1-\cos(\bar{k}b))$$

Equation A.64

$$\alpha_{22} = \frac{1}{\Delta} \bar{s}_{22} \sin(\bar{k}b)(\cos(ka)-1)$$

Equation A.65

$$\beta_{22} = \frac{-1}{\Delta \cos(\bar{k}b)} s_{22} \sin(\bar{k}b)\cos(ka)(1-\cos(\bar{k}b)) + \frac{1}{\bar{k}\cos(\bar{k}b)}$$

Equation A.66

$$\Delta = s_{22}\bar{k}\sin(\bar{k}b)\cos(ka) + \bar{s}_{22}k\sin(ka)\cos(\bar{k}b)$$

Equation A.67

Using Equation A.43, Equation A.50, and Equation A.59, the electric potential in the receiving portion can now be described by Equation A.68. However, Equation A.68 is still in terms of the unknown phasor constant, $\tilde{c}_1$. Substituting Equation A.46 and Equation A.47 into Equation A.68 at $x_2 = b$ yields the expression for the PT phasor output voltage shown in Equation A.69.

$$
\tilde{\phi} = \frac{1}{2}\tilde{V}_1 + \frac{1}{\bar{d}_{22}}\left[\tilde{c}_1 x_2 - \left(\alpha_{22}\frac{d_{32}\tilde{V}_1}{h} + \beta_{22}k_{22}^2\tilde{c}_1\right)\sin\left(\bar{k}x_2\right)\right.
$$
$$
\left. + \left(\alpha_{12}\frac{d_{32}\tilde{V}_1}{h} + \beta_{12}k_{22}^2\tilde{c}_1\right)\left(1-\cos\left(\bar{k}x_2\right)\right)\right], \quad 0 \leq x_2 \leq b
$$

Equation A.68

$$
\tilde{V}_2 = \tilde{\phi}(b) = \Gamma_1\tilde{V}_1 - Z_2\tilde{I}_2
$$

Equation A.69

$$
\Gamma_1 = \frac{1}{2} + \frac{d_{32}}{\bar{d}_{22}h}\left[\alpha_{12}\left(1-\cos\left(\bar{k}b\right)\right)-\alpha_{22}\sin\left(\bar{k}b\right)\right]
$$

Equation A.70

$$Z_2 = \frac{1}{j\omega\varepsilon_{22}wh\left(1-k_{22}^2\right)}\left[b - \beta_{22}k_{22}^2\sin\left(\bar{k}b\right) + \beta_{12}k_{22}^2\left(1-\cos\left(\bar{k}b\right)\right)\right]$$

Equation A.71

Substituting Equation A.28, Equation A.31, Equation A.46, Equation A.47, and Equation A.59 into Equation A.32 yields an expression for the phasor input current to the PT shown in Equation A.72.

$$\tilde{I}_1 = \frac{-\tilde{V}_1}{Z_1} + \Gamma_2\tilde{I}_2$$

Equation A.72

$$\frac{1}{Z_1} = \frac{j\omega\bar{\varepsilon}_{33}w}{h}\left[a - \frac{k_{32}^2}{1-k_{32}^2}\left(\alpha_{12} + \alpha_{11}\sin\left(ka\right) - \alpha_{12}\cos\left(ka\right)\right)\right]$$

Equation A.73

$$\Gamma_2 = \frac{k_{22}^2 d_{32}}{hd_{22}}\left(\beta_{12} + \beta_{11}\sin\left(ka\right) - \beta_{12}\cos\left(ka\right)\right)$$

Equation A.74

176

Substituting Equation A.51 into Equation A.69 provides an equation for the PT phasor output voltage in terms of the load impedance and the phasor input voltage as shown in Equation A.75. Finally, using the phasor output current expression in Equation A.76, the phasor constant, $\tilde{c}_1$, can be found using Equation A.77 and substituted to solve the mechanical displacement shown in Equation A.59.

$$\tilde{V}_2 = \frac{\Gamma_1 \tilde{V}_1 Z_L}{Z_L + Z_2}$$

Equation A.75

$$\tilde{I}_2 = \frac{\Gamma_1 \tilde{V}_1}{Z_L + Z_2}$$

Equation A.76

$$\tilde{c}_1 = \frac{\tilde{I}_2 s_{22}}{j\omega d_{22} hw}$$

Equation A.77

The 1-D model derivation to this point has not included loss factors. Substituting the lossy elastic compliance and permittivity with respect to constant stress coefficients,

s_L and ε_L^T, respectively, into the model derivation accounts for the mechanical and dielectric loss factors. The inclusion of loss factors introduces complex numbers into the material coefficients. The mechanical loss factor is inversely proportional to the input mechanical quality factor (Q-value) and affects the elastic compliance coefficients isotropically as shown in Equation A.78 [45]. The input mechanical Q-value is approximately equal to the Q-value of the PT input impedance [45], [49]. Common input mechanical Q-values were measured to be between 2,500 — 5,000 depending on the electrical and mechanical load. The dielectric loss factors affect the permittivity with respect to constant stress as shown in Equation A.79. However, the dielectric loss factors must be implemented prior to any rotation using Equation A.5, since these loss factors correspond to the crystallographic axes. Dielectric loss factors for lithium niobate used in the 1-D model are shown in Equation A.80 [31], [46], [47].

$$s_L = s\left(1 - j\delta_m\right) = s\left(1 - j\frac{1}{Q_m}\right)$$

Equation A.78

$$\varepsilon_L^T = \varepsilon_{ij}^T\left(1 - j\gamma_{ij}\right)$$

Equation A.79

$$\gamma_{ij} = \begin{pmatrix} 5 & 0 & 0 \\ 0 & 5 & 0 \\ 0 & 0 & 3.4 \end{pmatrix} \times 10^{-4}$$

Equation A.80

$i_1(t)$

$v_1(t)$

$\phi = v_1$

$\phi = 0$

$t \ w$

h

a

z_L

$V_2(t)$

$\hat{x}_3 \quad \theta \quad x_3'$

$\hat{x}_1$

θ

$i_2(t)$

$\hat{x}_2$

x_2'

①

$T_1 = T_3 = T_4 = T_5 = T_6 = 0 \ , \ T_2 \neq 0$

General Eqns:

$$T_{ji,j} + \rho f_i = \rho \ddot{u}_i$$

$$D_{i,i} = 0$$

$$T_{ij} = c_{ijk\ell} S_{k\ell} - e_{kij} E_k$$

$$D_i = e_{ijk} S_{jk} + \varepsilon_{ij}^S E_j$$

$$S_{ij} = (u_{i,j} + u_{j,i})/2$$

$$E_i = -\phi_{,i}$$

$$S_{ij} = s_{ijk\ell} T_{k\ell} + d_{kij} E_k$$

$$D_i = d_{ijk} T_{jk} + \varepsilon_{ij}^T E_j$$

Driving Portion

$$T_1 = T_3 = T_4 = T_5 = T_6 = 0$$

$$\phi = \frac{x_3}{h} V_1 \qquad \text{assuming linear increase in potential through the thickness}$$

$$E_1 = E_2 = 0 \ , \qquad E_3 = \frac{-V_1}{h} \ , \qquad V_1 = V_1(t)$$

b/c no external force, $T_{22} = \rho \ddot{u}_2$

$$S_{ij} = s_{ijk\ell} T_{k\ell} + d_{kij} E_k = \sum_{k=1}^{3} \sum_{\ell=1}^{3} s_{ijk\ell} T_{k\ell} + \sum_{k=1}^{3} d_{kij} E_k$$

$$= s_{ij11} \cancel{T_{11}}^0 + s_{ij12} \cancel{T_{12}}^0 + s_{ij13} \cancel{T_{13}}^0 + s_{ij21} \cancel{T_{21}}^0 + s_{ij22} T_{22} + s_{ij32} \cancel{T_{32}}^0$$

$$+ s_{ij31} \cancel{T_{31}}^0 + s_{ij32} \cancel{T_{32}}^0 + s_{ij33} \cancel{T_{33}}^0 + d_{1ij} \cancel{E_1}^0 + d_{2ij} \cancel{E_2}^0 + d_{3ij} E_3$$

Figure A.3: Page 1 of handwritten 1-D model derivation notes.

180

$$S_1 = s_{12} T_2 + d_{31} E_3 \qquad S_4 = s_{42} T_2 + d_{34} E_3$$
$$S_2 = s_{22} T_2 + d_{32} E_3 \qquad S_5 = s_{52} T_2 + d_{35} E_3$$
$$S_3 = s_{32} T_2 + d_{33} E_3 \qquad S_6 = s_{62} T_2 + d_{36} E_3$$

$$D_i = d_{ijk} T_{jk} + \varepsilon_{ij} E_j = \sum_{j=1}^{3} \sum_{k=1}^{3} d_{ijk} T_{jk} + \sum_{j=1}^{3} \varepsilon_{ij} E_j$$

$$= d_{i11} \cancel{T_{11}}^0 + d_{i12} \cancel{T_{12}}^0 + d_{i13} \cancel{T_{13}}^0 + d_{i21} \cancel{T_{21}}^0 + d_{i22} T_{22} + d_{i23} \cancel{T_{23}}^0$$
$$+ d_{i31} \cancel{T_{31}}^0 + d_{i32} \cancel{T_{32}}^0 + d_{i33} \cancel{T_{33}}^0 + \varepsilon_{i1} \cancel{E_1}^0 + \varepsilon_{i2} \cancel{E_2}^0 + \varepsilon_{i3} E_3$$

$$D_1 = d_{12} T_2 + \varepsilon_{13} E_3$$
$$D_2 = d_{22} T_2 + \varepsilon_{23} E_3$$
$$D_3 = d_{32} T_2 + \varepsilon_{33} E_3$$

$$S_{ij} = (u_{i,j} + u_{j,i})/2 \implies S_1 = 0, \quad S_2 = u_{2,2}, \quad S_3 = S_4 = S_5 = S_6 = 0$$

$$0 = s_{12} T_2 + d_{31} E_3 \qquad 0 = s_{42} T_2 + d_{34} E_3$$
$$u_{2,2} = s_{22} T_2 + d_{32} E_3 \qquad 0 = s_{52} T_2 + d_{35} E_3$$
$$0 = s_{32} T_2 + d_{33} E_3 \qquad 0 = s_{62} T_2 + d_{36} E_3$$

$$T_2 = \frac{u_{2,2} - d_{32} E_3}{s_{22}} = \frac{u_{2,2} + d_{32}\frac{V_1}{h}}{s_{22}}$$

$$\boxed{T_2 = \frac{1}{s_{22}}\left(u_{2,2} + d_{32}\frac{V_1}{h}\right)}$$

$$T_{2,2} = \rho \ddot{u}_2 \implies \frac{1}{s_{22}} u_{2,22} + 0 = \rho \ddot{u}_2 \implies \boxed{\frac{u_{2,22}}{s_{22}} = \rho \ddot{u}_2}$$

$$D_1 = d_{12}\left[\frac{1}{s_{22}}\left(u_{2,2} + d_{32}\frac{V_1}{h}\right)\right] + \varepsilon_{13}\left(\frac{-V_1}{h}\right)$$
$$= \frac{d_{12}}{s_{22}} u_{2,2} + \frac{d_{12}d_{32}}{s_{22}}\frac{V_1}{h} - \varepsilon_{13}\left(\frac{V_1}{h}\right)$$
$$= \frac{d_{12}}{s_{22}} u_{2,2} + \frac{V_1}{h}\left(\frac{d_{12}d_{32}}{s_{22}} - \varepsilon_{13}\right)$$

$$D_2 = d_{22}\left[\frac{1}{s_{22}}\left(u_{2,2} + d_{32}\frac{V_1}{h}\right)\right] + \varepsilon_{23}\left(\frac{-V_1}{h}\right)$$
$$= \frac{d_{22}}{s_{22}} u_{2,2} + \frac{V_1}{h}\left(\frac{d_{22}d_{32}}{s_{22}} - \varepsilon_{23}\right)$$

Figure A.4: Page 2 of handwritten 1-D model derivation notes.

181

$$D_3 = d_{32}\left[\frac{1}{s_{22}}\left(u_{2,2} + d_{32}\frac{V_1}{h}\right)\right] + \varepsilon_{33}\left(\frac{-V_1}{h}\right)$$

$$= \frac{d_{32}}{s_{22}}u_{2,2} + \frac{V_1}{h}\left(\frac{d_{32}^2}{s_{22}} - \varepsilon_{33}\right)$$

only need D_3 in order to find I_1, b/c D_3 is normal to electrodes for Gauss's Law

$$\bar{\varepsilon}_{33} = \varepsilon_{33}(1 - k_{32}^2)$$

$$k_{32}^2 = \frac{d_{32}^2}{\varepsilon_{33}s_{22}}$$

$$D_3 = \frac{d_{32}}{s_{22}}u_{2,2} - \frac{V_1}{h}\varepsilon_{33}\left(1 - \frac{d_{32}^2}{\varepsilon_{33}s_{22}}\right) = \boxed{\frac{d_{32}}{s_{22}}u_{2,2} - \bar{\varepsilon}_{33}\frac{V_1}{h} = D_3}$$

Boundary Condition

$$T_2 = \frac{1}{s_{22}}\left(u_{2,2} + d_{32}\frac{V_1}{h}\right) = 0 \quad @ \ x_2 = -a$$

$$I_1 = \dot{Q}_1 \qquad \text{b/c defined as going into electrode}$$

from pg 204-205 of Ulaby (also pg 207)

$$\hat{n}\cdot D_3 = \hat{n}\,\rho_s\cdot\hat{n} \implies \int_s D_3\cdot\hat{n}\,dA = \int_s \rho_s = Q_1$$

$$\int_{-w}^{0}\int_{-a}^{0} D_3\cdot(-\hat{x}_3)\,dx_2\,dx_1 = Q_1$$

$$Q_1 = (0-(-w))\int_{-a}^{0}-D_3\,dx_2 \implies \boxed{-w\int_{-a}^{0}D_3\,dx_2 = Q_1}$$

pg 208 Ulaby

$J_{1n}\uparrow$ Medium 1 (metal) $\qquad J_{1n}\left(\frac{\varepsilon_1}{\sigma_1} - \frac{\varepsilon_2}{\sigma_2}\right) = \rho_s$

$J_{2n}\uparrow$ Medium 2 (LiNbO$_3$) $\qquad J_{1n}\left(0 - \frac{\varepsilon_2}{\sigma_2}\right) = \rho_s \implies J_{1n} \propto -\rho_s$

but I_1 is defined coming out so

$$I_1 = \frac{-dQ_1}{dt} = -\dot{Q}_1$$

$$\boxed{I_1 = -\dot{Q}_1}$$

Figure A.5: Page 3 of handwritten 1-D model derivation notes.

Receiving Portion

$T_1 = T_3 = T_4 = T_5 = T_6 = 0$

$D_1 = D_3 = 0$ b/c no electrodes to accumulate charge

$D_i = d_{ijk} T_{jk} + \varepsilon_{ij} E_j \Rightarrow E_1 = E_3 = 0$

$E_2 = -\phi_{,2}$, $\phi = \phi(x, t)$

$\boxed{T_{2,2} = \rho \ddot{u}_2}$ $\boxed{D_{2,2} = 0}$ from general eqns

$S_{ij} = s_{ij11} \cancel{T_{11}}^0 + s_{ij12} \cancel{T_{12}}^0 + s_{ij13} \cancel{T_{13}}^0 + s_{ij21} \cancel{T_{21}}^0 + s_{ij22} T_{22} + s_{ij23} \cancel{T_{23}}^0$

$\qquad + s_{ij31} \cancel{T_{31}}^0 + s_{ij32} \cancel{T_{32}}^0 + s_{ij33} \cancel{T_{33}}^0 + d_{1ij} \cancel{E_1}^0 + d_{2ij} E_2 + d_{3ij} \cancel{E_3}^0$

$S_{ij} = s_{ij22} T_{22} + d_{2ij} E_2$

$\begin{cases} S_1 = s_{12} T_2 + d_{21} E_2 \\ S_2 = s_{22} T_2 + d_{22} E_2 \\ S_3 = s_{32} T_2 + d_{23} E_2 \end{cases}$ $\begin{array}{l} S_4 = s_{42} T_2 + d_{24} E_2 \\ S_5 = s_{52} T_2 + d_{25} E_2 \\ S_6 = s_{62} T_2 + d_{26} E_2 \end{array}$

$D_i = d_{i11} \cancel{T_{11}}^0 + d_{i12} \cancel{T_{12}}^0 + d_{i13} \cancel{T_{13}}^0 + d_{i21} \cancel{T_{21}}^0 + d_{i22} T_{22} + d_{i23} \cancel{T_{23}}^0$

$\qquad + d_{i31} \cancel{T_{31}}^0 + d_{i32} \cancel{T_{32}}^0 + d_{i33} \cancel{T_{33}}^0 + \varepsilon_{i1} \cancel{E_1}^0 + \varepsilon_{i2} E_2 + \varepsilon_{i3} \cancel{E_3}^0$

$D_i = d_{i22} T_{22} + \varepsilon_{i2} E_2$

$\boxed{D_2 = d_{22} T_2 + \varepsilon_{22} E_2}$

$S_{ij} = (u_{i,j} + u_{j,i})/2 \Rightarrow S_1 = 0,\ S_2 = u_{2,2},\ S_3 = S_4 = S_5 = S_6 = 0$

$\begin{cases} 0 = s_{12} T_2 + d_{21} E_2 & 0 = s_{42} T_2 + d_{24} E_2 \\ u_{2,2} = s_{22} T_2 + d_{22} E_2 & 0 = s_{52} T_2 + d_{25} E_2 \\ 0 = s_{32} T_2 + d_{23} E_2 & 0 = s_{62} T_2 + d_{26} E_2 \end{cases}$

$\Rightarrow T_2 = \dfrac{u_{2,2} - d_{22} E_2}{s_{22}}$

$D_2 = d_{22} T_2 + \varepsilon_{22} E_2 \Rightarrow E_2 = \frac{1}{\varepsilon_{22}} (D_2 - d_{22} T_2)$

Figure A.6: Page 4 of handwritten 1-D model derivation notes.

$$T_2 = \frac{1}{s_{22}}\left(u_{2,2} - \frac{d_{22}}{\varepsilon_{22}}(D_2 - d_{22} T_2)\right)$$

$$T_2 - \frac{d_{22}^2}{s_{22}\varepsilon_{22}} T_2 = \frac{1}{s_{22}}\left(u_{2,2} - \frac{d_{22}}{\varepsilon_{22}} D_2\right)$$

$$T_2 = \frac{u_{2,2} - \frac{d_{22}}{\varepsilon_{22}} D_2}{s_{22} - \frac{d_{22}^2}{\varepsilon_{22}}}$$

$$T_{2,2} = \frac{u_{2,22}}{s_{22} - \frac{d_{22}^2}{\varepsilon_{22}}} \qquad \text{b/c } D_{2,2} = 0 \quad \text{from general eqns}$$

$$\boxed{\frac{u_{2,22}}{s_{22} - \frac{d_{22}^2}{\varepsilon_{22}}} = \rho \ddot{u}_2}$$

$$\bar{s}_{22} = s_{22}(1 - k_{22}^2)$$

$$k_{22}^2 = \frac{d_{22}^2}{s_{22}\varepsilon_{22}}$$

$$\bar{d}_{22} = d_{22}\left(1 - \frac{1}{k_{22}^2}\right)$$

$$\bar{s}_{22} = s_{22}\left(1 - \frac{d_{22}}{s_{22}\varepsilon_{22}}\right) = s_{22} - \frac{d_{22}}{\varepsilon_{22}}$$

$$\boxed{\frac{u_{2,22}}{\bar{s}_{22}} = \rho \ddot{u}_2}$$

$$\underset{x_2=b}{@} \left\{ \begin{array}{l} \nabla \cdot D = \rho_s \implies \int D_{2,2}\, dx_2 = \int_0^h \int_{-w}^0 D_2 \cdot (-\hat{x}_2)\, dx_2 = -D_2 hw = Q_2 \\[2mm] \int_0^h \int_{-w}^0 \rho_s = Q_2 \equiv \text{charge on output electrode} \\[2mm] \boxed{D_2 = \frac{-Q_2}{hw}} \end{array} \right.$$

If $D_{2,2} = 0$, then D_2 is a constant

$$D_2 = \int D_{2}\, dx_2 = \frac{d_{22}}{s_{22}} c_1$$

can choose constant to be in terms of material constants that will simplify later

Figure A.7: Page 5 of handwritten 1-D model derivation notes.

184

$$T_2 = \frac{u_{2,2} - \frac{d_{22}}{\varepsilon_{22}} D_2}{S_{22} - \frac{d_{22}^2}{\varepsilon_{22}}} \qquad \text{from } pg \; ⑤$$

$$\text{let } \quad \bar{S}_{22} = S_{22}(1 - k_{22}^2)$$

$$k_{22}^2 = \frac{d_{22}^2}{S_{22}\varepsilon_{22}}$$

$$T_2 = \frac{1}{\bar{S}_{22}}\left[u_{2,2} - \frac{d_{22}}{\varepsilon_{22}} D_2 \right]$$

$$D_2 = \frac{d_{22}}{S_{22}} c_1 \qquad \text{from } pg \; ⑤$$

$$T_2 = \frac{1}{\bar{S}_{22}}\left[u_{2,2} - \frac{d_{22}^2}{S_{22}\varepsilon_{22}} c_1 \right] = \boxed{\frac{1}{\bar{S}_{22}}\left[u_{2,2} - k_{22}^2 c_1 \right] = T_2}$$

$$E_2 = \frac{1}{\varepsilon_{22}}\left(D_2 - d_{22} T_2 \right) \qquad \text{from } pg \; ④$$

$$E_2 = \frac{1}{\varepsilon_{22}}\left[\frac{d_{22}}{S_{22}} c_1 - d_{22} \frac{1}{\bar{S}_{22}}\left(u_{2,2} - k_{22}^2 c_1 \right) \right]$$

$$\phi_2 = - \int E_2 \, dx_2 \qquad \text{from } pg \; ④$$

$$\phi_2 = -\frac{1}{\varepsilon_{22}} \int \left(\frac{d_{22}}{S_{22}} + \frac{d_{22} k_{22}^2}{\bar{S}_{22}} \right) c_1 \, dx_2 + \frac{1}{\varepsilon_{22}} \int \frac{d_{22} u_{2,2}}{\bar{S}_{22}} \, dx_2$$

$$\phi_2 = \frac{d_{22} u_2}{\varepsilon_{22} \bar{S}_{22}} + c_a - \frac{d_{22}}{S_{22}\varepsilon_{22}} \int \left(1 + \frac{k_{22}^2}{1 - k_{22}^2} \right) c_1 \, dx_2$$

$$\phi_2 = \frac{d_{22} u_2}{\varepsilon_{22} \bar{S}_{22}} + c_a - \frac{d_{22}}{S_{22}\varepsilon_{22}} \int \left(\frac{1 - k_{22}^2 + k_{22}^2}{1 - k_{22}^2} \right) c_1 \, dx_2$$

$$\phi_2 = \frac{d_{22} u_2}{\varepsilon_{22}(S_{22}(1 - k_{22}^2))} + c_a - \frac{d_{22}}{S_{22}\varepsilon_{22}} \left[\frac{1}{1 - k_{22}^2} \right] c_1 x_2 + c_b$$

$$c_\alpha = c_a + c_b$$

$$\phi_2 = \frac{k_{22}^2}{d_{22}(1 - k_{22}^2)} u_2 - \frac{k_{22}^2}{d_{22}} \left[\frac{1}{1 - k_{22}^2} \right] c_1 x_2 + c_\alpha$$

$$\phi_2 = \frac{-u_2}{d_{22}(1 - \frac{1}{k_{22}^2})} + \frac{c_1 x_2}{d_{22}(1 - \frac{1}{k_{22}^2})} + c_2$$

$$\text{let } \quad \bar{d}_{22} = d_{22}\left(1 - \frac{1}{k_{22}^2}\right)$$

$$\boxed{\phi_2 = \frac{1}{\bar{d}_{22}}\left(c_1 x_2 - u_2 \right) + c_2}$$

Figure A.8: Page 6 of handwritten 1-D model derivation notes.

Boundary conditions at $x_2 = b$

$$T_2 = \frac{1}{s_{22}}(u_{2,2} - k_{22}^2 c_1) = 0$$

$$\phi = V_2(t)$$

$$\boxed{D_2 = \frac{d_{22}}{s_{22}} c_1 = \frac{-Q_2}{A_w}} \quad \text{from} \quad pg \; ⑤$$

also $\boxed{I_2(t) = \frac{-dQ_2}{dt}}$

Interface Conditions

$$u_2(0^-) = u_2(0^+)$$

$$T_2(0^-) = \frac{1}{s_{22}}\left(u_{2,2} + \frac{d_{32} V_1}{h}\right)\Big|_{0^-} = \frac{1}{s_{22}}(u_{2,2} - k_{22}^2 c_1)\Big|_{0^+} = T_2(0^+)$$

$$\phi(0^+) = \tfrac{1}{2} V_1$$

↳ assume to be the average of the potential in the driving region / cross-section

b/c there will be a time harmonic V_1, make all values into phasors for easier analysis

$$\widetilde{I}_2 = \frac{\widetilde{v}_2}{z_2}$$

Forced Vibration Analysis

↳ will skip free vibration analysis

from pg ② in frequency domain

$$\frac{1}{s_{22}} \widetilde{u}_{2,22} = (j\omega)^2 \ell \widetilde{u}_2 \Bigg\} \quad -a \leq x_2 \leq 0$$

$$\frac{1}{s_{22}} \widetilde{u}_{2,22} = -\omega^2 \ell \widetilde{u}_2$$

from pg ⑤ in frequency domain

$$\frac{1}{s_{22}} \widetilde{u}_{2,22} = -\omega^2 \ell \widetilde{u}_2 \quad \text{for} \quad 0 \leq x_2 \leq b$$

Figure A.9: Page 7 of handwritten 1-D model derivation notes.

from pg ③ in frequency domain

$$\frac{1}{s_{22}}\left(\widetilde{u}_{2,2} + d_{32}\frac{\widetilde{V}_1}{h}\right) = 0 \quad @ \quad x_2 = -a$$

from pg ⑦ in frequency domain

$$\frac{1}{s_{22}}\left(\widetilde{u}_{2,2} - k_{22}^2 c_1\right) = 0 \quad @ \quad x_2 = b$$

from pg ⑤ in frequency domain

$$\widetilde{u}_2(0^-) = \widetilde{u}_2(0^+)$$

$$\frac{1}{s_{22}}\left[\widehat{u}_{2,2}(0^-) + \frac{d_{32}\widehat{V}_1}{h}\right] = \frac{1}{s_{22}}\left[\widehat{u}_{2,2}(0^+) - k_{22}^2 c_1\right]$$

solving this set of differential equations
with boundary conditions should yield

$$\widetilde{u}_2 = \begin{cases} \left(\alpha_{11}\frac{d_{32}\widetilde{V}_1}{h} + \beta_{11}k_{22}^2 c_1\right)\sin(kx_2) + \left(\alpha_{12}\frac{d_{32}\widetilde{V}_1}{h} + \beta_{12}k_{22}^2 c_1\right)\cos(kx_2) \\ \qquad \text{for } -a \leq x_2 \leq 0 \\ \left(\alpha_{22}\frac{d_{32}\widetilde{V}_1}{h} + \beta_{22}k_{22}^2 c_1\right)\sin(\bar{k}x_2) + \left(\alpha_{12}\frac{d_{32}\widetilde{V}_1}{h} + \beta_{12}k_{22}^2 c_1\right)\cos(\bar{k}x_2) \\ \qquad \text{for } 0 \leq x_2 \leq b \end{cases}$$

$$k = \omega\sqrt{\rho s_{22}}$$

$$\bar{k} = \omega\sqrt{\rho \bar{s}_{22}}$$

$$\alpha_{11} = -\frac{1}{\Delta\cos ka}\,\bar{s}_{22}\cos(\bar{k}b)\sin(ka)(\cos(ka)-1) - \frac{1}{k\cos(ka)}$$

$$\beta_{11} = \frac{1}{\Delta}\,s_{22}\sin(ka)(1-\cos(\bar{k}b))$$

$$\alpha_{12} = \frac{1}{\Delta}\,\bar{s}_{22}\cos(\bar{k}b)(\cos(ka)-1)$$

$$\beta_{12} = \frac{-1}{\Delta}\,s_{22}\cos(ka)(1-\cos(\bar{k}b))$$

$$\alpha_{22} = \frac{1}{\Delta}\,\bar{s}_{22}\sin(\bar{k}b)(\cos(ka)-1)$$

$$\beta_{22} = -\frac{1}{\Delta\cos(\bar{k}b)}\,s_{22}\sin(\bar{k}b)\cos(ka)(1-\cos(\bar{k}b)) + \frac{1}{\bar{k}\cos(\bar{k}b)}$$

$$\Delta = s_{22}\bar{k}\sin(\bar{k}b)\cos(ka) + \bar{s}_{22}k\sin(ka)\cos(\bar{k}b)$$

assuming Yang is correct
   ↳ verified in Mathematica on 3/27/13

Figure A.10: Page 8 of handwritten 1-D model derivation notes.

$$\hat{U}_2 = \phi(b) = \Gamma_1 \tilde{U}_1 - z_2 \tilde{\tilde{I}}_2$$

where
$$\Gamma_1 = \frac{1}{2} + \frac{d_{32}}{\bar{\varepsilon}_{22}} \frac{1}{h} \left[\alpha_{12}(1-\cos(kb)) - \alpha_{22}\sin(kb) \right]$$

$$z_2 = \frac{1}{(1-k_{22}^2)} \frac{1}{b} \left[b - \beta_{22} k_{22}^2 \sin(kb) + \beta_{12} k_{22}^2 (1-\cos(kb)) \right] \frac{b}{j\omega \bar{\varepsilon}_{22} h}$$

verified in Mathematica on 3/27/13

$$D_3 = \frac{d_{32}}{s_{22}} \tilde{u}_{2,2} - \bar{\varepsilon}_{33} \frac{\tilde{U}_1}{h} \qquad \text{from pg ③}$$

$$\tilde{I}_1 = -j\omega Q_1 \quad , \quad Q_1 = -w \int_{-a}^{0} D_3 \, dx_2 \qquad \text{from pg ③}$$

using solution for $\tilde{u}_2$ on pg ⑧

$$\hat{\tilde{I}}_1 = -\frac{\tilde{U}_1}{z_1} + \Gamma_2 \tilde{\tilde{I}}_2$$

where
$$\frac{1}{z_1} = \frac{1}{a} \left[a - \frac{k_{32}^2}{1-k_{32}^2} \left(\alpha_{12} + \alpha_{11}\sin(ka) - \alpha_{12}\cos(ka) \right) \right] \frac{j\omega \bar{\varepsilon}_{33} wa}{h}$$

$$\Gamma_2 = k_{22}^2 \frac{s_{22} d_{32}}{s_{22} d_{22}} \frac{1}{h} \left(\beta_{12} + \beta_{11}\sin(ka) - \beta_{12}\cos(ka) \right)$$

verified in Mathematica on 3/28/13

$$\hat{\tilde{I}}_1 = -\frac{\tilde{U}_1}{z_1} + \Gamma_2 \tilde{\tilde{I}}_2$$

$$\tilde{U}_2 = \Gamma_1 \tilde{U}_1 - z_2 \tilde{\tilde{I}}_2$$

$$\hat{U}_2 = \tilde{I}_2 z_L \qquad \text{from circuit load eqn}$$

$$\tilde{U}_2 = \Gamma_1 \tilde{U}_1 - z_2 \left(\frac{\tilde{U}_2}{z_L} \right)$$

$$\tilde{U}_2 \left(1 + \frac{z_2}{z_L} \right) = \Gamma_1 \tilde{U}_1 \implies \boxed{\tilde{U}_2 = \frac{\Gamma_1 U_1 z_L}{z_L + z_2}}$$

$$\boxed{\frac{\tilde{U}_2}{z_L} = \tilde{\tilde{I}}_2 = \frac{\Gamma_1 \tilde{U}_1}{z_L + z_2}}$$

Figure A.11: Page 9 of handwritten 1-D model derivation notes.

B. Matlab Code for 1-D Model

```
clear;
close all hidden;
pause(1);
clc;
tic;


%************************* SUMMARY OF CODE
*******************************
%  Author:          James A. VanGordon
%  Department:      Electrical and Computer Engineering
%  Organization:    University of Missouri
%  Date:            March 2013
%
%  This code is to be used for performing a 1-dimensional model
of a PT with
%  respect to length-extensional motion.  Although the material
constants
%  are rotated to yield the correct longitudinal stress, strain,
electric
%  field, etc. in the output region of the PT, the model assumes
zero
%  electric field and stress in the transverse direction.  The
material
%  constants for lithium niobate are already inserted and can be
rotated
%  for any rotation about any axis.  This is also true for
rotations about
%  multiple axes.
%
%  This code will also calculate the corresponding phase shift
that should
%  be observed when using an optical diagnostic at any point
along the
%  output section of the PT.  Some references for the 1-D model
derivation
%  are listed.
%
%  REFERENCES
%  [1]     Jiashi Yang, An Introduction to the Theory of
Piezoelectricity.
%       New York: Springer, 2005.
%  [2]     Jiashi Yang, Analysis of Piezoelectric Devices. New
Jersey:
%       World Scientific, 2006.
%  [3]  J. S. Yang and X. Zhang, "Extensional vibration of a
nonuniform
```

```
%        piezoceramic rod and high voltage generation,"
International
%        Journal of Applied Electromagnetics, vol. 16, pp. 29-42,
2002.
%  [4]  Martin Sadd, Elasticity:  Theory, Applications, and
Numerics.
%        Amsterdam: Elsevier Butterworth Heinemann, 2005.
%  [5]    Jiashi Yang, "Piezoelectric transformer structural
modeling - a
%        review," Ultrasonics, Ferroelectrics and Frequency
Control, IEEE
%        Transactions on, vol. 54, no. 6, pp. 1154-1170, 2007.
%  [6]    J. A. VanGordon, B. B. Gall, S. D. Kovaleski, E. A.
Baxter, R.
%        Almeida, and J. W. Kwon, "High Voltage Production from
Shaped
%        Piezoelectric Transformers and Piezoelectric Transformer
Based
%        Circuits," in IEEE International Power Modulators and
High Voltage
%        Conference, Proceedings of the 2010, 2010.
%
%****************************************************************
**********


%*********************** Material Constants
****************************
x_rotation_angle = 45;                        %% rotation for
z-cut PT in degrees
                                              %% rotation for
y-cut PT should be made accordingly
                                              %% (45 degree
rotated z-cut = 135 degree rotated y-cut)
y_rotation_angle = 0;                         %% rotation about
y-axis
z_rotation_angle = 0;                         %% rotation about
z-axis

length = 100e-3;                              %% length of PT
in meters
width = 1e-2;                                 %% width of PT in
meters
a = 50e-3;                                    %% length of
input electrode in meters
b = length - a;                              %% position of
output electrode in meters
thick = 1.5e-3;                              %% thickness of
PT in meters

rho = 4700;                                  %% mass density
in kg/m^3
```

```
                                                        %% should be
4,700 kg/m^3 for LiNbO3

BD_dielectric = 150e6;                                  %% dielectric
breakdown strength in V/m
                                                        %% for LiNbO3
should be ~150 MV/m

T_max = 30 * 10^6;                                      %% maximum stress
before crystal will fracture in Pa
                                                        %% for LiNbO3
should be between 30 MPa and 120 MPa

c = zeros(6,6);                                         %% initialize
size of c               [N/m^2]
e = zeros(3,6);                                         %% initialize
size of e               [C/m^2]
eps_S = zeros(3,3);                                     %% initialize
size of eps_S           [C/(V*m)] aka [F/m]
s = zeros(6,6);                                         %% initialize
size of s               [m^2/N]
d = zeros(3,6);                                         %% initialize
size of d               [C/N]
eps = zeros(3,3);                                       %% initialize
size of eps             [C^2/(N*m^2)] aka [F/m]
r = zeros(6,3);                                         %% initialize
size of r               [m/V]
r_rotated = zeros(6,3);                                 %% initialize
size of rotated r       [m/V]
p = zeros(6,6);                                         %% initialize
size of p               [unitless]
p_rotated = zeros(6,6);                                 %% initialize
size of rotated p       [unitless]
n = zeros(3,3);                                         %% initialize
size of n               [unitless]
n_rotated = zeros(3,3);                                 %% initialize
size of rotated n       [unitless]


% set up elastic constants in matrix "c"               %% for LiNb03
should be
c = [2.03   0.53  0.75   0.09  0     0;                 %% 2.03    0.53
0.75   0.09  0      0
     0.53   2.03  0.75  -0.09  0     0;                 %% 0.53   2.03
0.75  -0.09  0      0
     0.75   0.75  2.45   0     0     0;                 %% 0.75   0.75
2.45   0      0      0
     0.09  -0.09  0      0.60  0     0;                 %% 0.09  -0.09  0
0.60  0      0
     0      0     0      0     0.60  0.09;              %% 0      0      0
0     0.60   0.09
```

191

```matlab
        0       0      0       0       0.09  0.75];        %% 0       0       0
0     0.09   0.75

 c = c * 10^11;                                          %% c = c * 10^11


% set up piezoelectric constants in matrix "e"   %% for LiNbO3
should be
e = [0       0      0       0       3.70  -2.50;        %% 0       0       0
0      3.70  -2.50
     -2.50  2.50  0       3.70  0       0;        %% -2.50  2.50  0
3.70  0       0
      0.20   0.20  1.30  0       0       0];        %% 0.20   0.20
1.30   0       0       0

e = e * 1;                                          %% e = e * 1


% set up dielectric constants in matrix "eps_S"
% this is for constant strain field              %% for LiNbO3
should be
eps_S = [38.9  0      0;                             %% 38.9  0       0
         0      38.9  0;                             %% 0      38.9  0
         0      0      25.7];                        %% 0      0
25.7

eps_S = eps_S * 10^-11;                              %% eps_S = eps_S
* 10^-11


% set up dielectric constants in matrix "eps_T"
% this is for constant stress field             %% for LiNbO3
should be
eps_T = [85.2  0      0;                             %% 38.9  0       0
         0      85.2  0;                             %% 0      38.9  0
         0      0      28.7];                        %% 0      0
25.7

eps_T = eps_T * 8.85e-12;                           %% eps_S =
eps_S * 10^-11


% set up dielectric constants in matrix "n"      %% for LiNbO3
should be
n = [2.2910    0              0;                     %% 2.2910   0
0
     0              2.2910    0;                     %% 0
2.2910  0
     0              0              2.2005];          %% 0              0
2.2005

n = n * 1;                                          %% n = n * 1
```

```matlab
% set up electro-optic constants in matrix "r"
% this is for constant strain field          %% for LiNbO3
should be
r = [0       -3.4     7.7;                    %% 0       -3.4
7.7
     0        3.4     7.7;                    %% 0        3.4
7.7
     0        0       28.8;                   %% 0        0
28.8
     0        18.2    0;                      %% 0        18.2
0
     18.2     0       0;                      %% 18.2     0
0
     -3.4     0       0];                     %% -3.4     0
0

r = r * 10^-12;                               %% r = r * 10^-
12


% set up elastic constants in matrix "p"     %% for LiNb03
should be
p = [0.036  0.072   0.139   0.066   0       0;        %% 0.036
0.072   0.139   0.066   0       0
     0.072  0.036   0.139   -0.066  0       0;        %% 0.072
0.036   0.139   -0.066  0       0
     0.178  0.178   0.060   0       0       0;        %% 0.178
0.178   0.060   0       0       0
     0.154  -0.154  0       0.30    0       0;        %% 0.154
-0.154  0       0.30    0       0
     0      0       0       0       0.30    0.154;    %% 0
0       0       0       0.30    0.154
     0      0       0       0       0.066   -0.019];  %% 0
0       0       0       0.066   -0.019

 p = p * 1;                                   %% p = p
* 1

 dielectric_loss_factor_xy = 5e-4;
 dielectric_loss_factor_z = 3.4e-4;
%  dielectric_loss_factor_xy = 5e-3;
%  dielectric_loss_factor_z = 3.4e-3;

 Q = 5e3;

 % rotate matrices accordingly and return matrices to be used in
calculations
 [s, d, eps, r_rotated, p_rotated, n_rotated, q_rotated] =
rotate3D_RSI_paper1(x_rotation_angle, y_rotation_angle,
```

```
z_rotation_angle, c, e, eps_T, r, p, n,
dielectric_loss_factor_xy,dielectric_loss_factor_z, Q);
s;
d;
eps;
r_rotated;
p_rotated;
n_rotated;
q_rotated;


%*****************************************************************
**********


%*********************** Circuit Parameters
***************************

burst_period = 1;                                  %% burst period
in seconds
cycles_per_burst = 3000;                           %% # cycles per
burst
f_operating = 30e3;                                %% operating
frequency in Hz
Vin_pk = 10;                                       %% amplitude of
input voltage sinusoid
                                                   %% 8.1 V for
ebeam
                                                   %% 10 V for
P6015A

CL = 1e-15;                                        %% load
capacitance
ZL = complex(0,-1/(2*pi()*f_operating*CL));        %% complex
impedance of load
                                                   %% first number
is real,
                                                   %% second number
is imaginary (be sure to include appropriate sign for imaginary
term)

%*****************************************************************
**********




%*********************** Generate Output
*****************************
```

```matlab
% make several generic plots based on geometry from sweeping
parameters
%
output_generator2(rho,s,d,eps,ZL,Vin_pk,f_operating,length,width,
thick,a,b,output_electrode,bipolar);


% n_rotated = n;
% r_rotated(2,2) = r(2,2) + r(2,3);
% r_rotated(3,2) = r(3,2) + r(3,3);
% q_rotated(2,2) = q_rotated(2,2) + q_rotated(2,3);
% q_rotated(3,2) = q_rotated(3,2) + q_rotated(3,3);


matrix = zeros(7901*6:9);
num = 1;
f_operating1 = 1e3;
R = 91.2e9;              %1.5Gohm for Q=3700    % R=37.879G, C=0.8p,
Iout=5.79e-7 for first thermionic data
% R = 1e12;                                     % R=1G  , C=.15p,
Iout= 17e-6 for second thermionic data
C = 0.05e-12;            % Tektronix P6015A, RL = 100 Mohm, CL =
17 pF, Q = 823
Rtest = complex(1,0)*0;        % to account for series R (due to
electrode painting or charge limiting(?))

for m = 6:11
    R = 10^m;
    for i = f_operating1:10:80e3
%         ZL = R;
%         ZL = 1/(1/complex(R,0)+1/complex(0,-1/(2*pi*i*C)));
        ZL = 1/(1/complex(R,0) + 1/complex(0,-1/(2*pi*i*C)));

[uin,uout,Tin,Tout,voltage,E2,E3,Iin,Vout,Iout,f_resonant,n,Pout,
Qout,Pin,Qin,Sin,Sout,gamma1] =
PT_solver(rho,s,d,eps,ZL,Vin_pk,i,length,width,thick,a);
        matrix(num,1) = i;
        matrix(num,2) = n;
        matrix(num,3) = angledim(-
angle(Iin)+angle(Vin_pk),'radians','degrees');
        matrix(num,4) = (abs(Vin_pk)/abs(Iin));
        matrix(num,5) = angledim(-
angle(Iout)+angle(Vout),'radians','degrees');
        matrix(num,6) = abs(Vout)/abs(Iout);
        matrix(num,7) = abs(Pin);
        matrix(num,8) = abs(Pout);
        matrix(num,9) = abs(Sout/Sin)*100;
        num = num + 1;
    end
end
```

```matlab
ZL;
[x,y] = max(matrix(:,2));
f_operating = matrix(y,1);
% f_operating = 28.58e3;

% plot voltage transformation ratio
figure
% subplot(3,1,1)
% semilogy((matrix(1:7901,1))/1e3,matrix(1:7901,2),'b')
% hold on;
% semilogy((matrix(7902:15802,1))/1e3,matrix(7902:15802,2),'r')
% hold on;
semilogy((matrix(39506:47406,1))/1e3,matrix(39506:47406,2),'b')
hold on;
semilogy((matrix(31605:39505,1))/1e3,matrix(31605:39505,2),'r')
hold on;
semilogy((matrix(23704:31604,1))/1e3,matrix(23704:31604,2),'k')
hold on;
semilogy((matrix(15803:23703,1))/1e3,matrix(15803:23703,2),'g')
hold on;
legend('10^1^1 \Omega','10^1^0 \Omega','10^9 \Omega','10^8
\Omega');
grid on;
xlabel('f (kHz)')
ylabel('Vout/Vin')
axis([0  80  0 100])
axis 'auto y'

pause(1)

figure
% subplot(3,1,2)
plot((matrix(1:2500,1))/1e3,matrix(1:2500,3),'b')
hold on;
% plot((matrix(2501:5000,1))/1e3,matrix(2501:5000,3),'r')
% hold on;
% plot((matrix(5001:7500,1))/1e3,matrix(5001:7500,3),'g')
% hold on;
% plot((matrix(7501:10000,1))/1e3,matrix(7501:10000,3),'k')
% hold on;
% plot((matrix(10001:12500,1))/1e3,matrix(10001:12500,3),'c')
% hold on;
% legend('10^6 \Omega','10^7 \Omega','10^8 \Omega','10^9
\Omega','10^1^0 \Omega');
grid on;
xlabel('f (kHz)')
ylabel('\theta_Z_i_n (degrees)')
axis([0  80  0 100])
axis 'auto y'

%  plot input impedance
figure
```

```matlab
% subplot(3,1,3)
% semilogy((matrix(1:7901,1))/1e3,matrix(1:7901,4),'b')
% hold on;
% semilogy((matrix(7902:15802,1))/1e3,matrix(7902:15802,4),'r')
% hold on;
semilogy((matrix(39506:47406,1))/1e3,matrix(39506:47406,4),'b')
hold on;
semilogy((matrix(31605:39505,1))/1e3,matrix(31605:39505,4),'r')
hold on;
semilogy((matrix(23704:31604,1))/1e3,matrix(23704:31604,4),'k')
hold on;
semilogy((matrix(15803:23703,1))/1e3,matrix(15803:23703,4),'g')
hold on;
legend('10^1^1 \Omega','10^1^0 \Omega','10^9 \Omega','10^8
\Omega');
grid on;
xlabel('f (kHz)')
ylabel('Z_i_n (\Omega)')
axis([0  80  0 100])
axis 'auto y'

pause(1)




% GO = 0
fprintf('\n Getting Closer... \n\n')
matrix = zeros(2500*5:10);
stress = zeros(101:2);
efield = zeros(101:2);
potential = zeros(101:2);
num = 1;
fig_num = 1;
i=0;
% f_operating = 31e3;

% m=8;
for m = 6:11
%     R = 100e6;
R = 10^(m);
C = 0.05e-12;
% C = 40e-12;

        % find f_operating
        %%%%%%%%%%%%%%%%%%%%%%%%%%%%%%%%%%%%%%%%%%%%%%%%%%%%%%%
%         ZL = @(f) 1/(1/complex(R,0)+1/complex(0,-
1/(2*pi*f*C)));
        ZL = @(f) 1/(1/complex(R,0)+1/complex(0,-1/(2*pi*f*C)));
%         ZL = @(f) R;
        j = complex(0,1);
        k22 = sqrt(d(2,2)^2/(s(2,2)*eps(2,2)));
        sbar = s(2,2)*(1-k22^2);
```

```
        dbar = d(2,2)*(1-1/k22^2);
        omega = @(f) 2*pi*f;
        k = @(f) omega(f)*sqrt(rho*s(2,2));
        kbar = @(f) omega(f)*sqrt(rho*sbar);

        delta = @(f) s(2,2)*kbar(f)*sin(kbar(f)*b)*cos(k(f)*a) +
sbar*k(f)*sin(k(f)*a)*cos(kbar(f)*b);
        alpha11 = @(f) -
1/(delta(f)*cos(k(f)*a))*sbar*cos(kbar(f)*b)*sin(k(f)*a)*(cos(k(f
)*a)-1) - 1/(k(f)*cos(k(f)*a));
        beta11 = @(f) 1/delta(f)*s(2,2)*sin(k(f)*a)*(1-
cos(kbar(f)*b));
        alpha12 = @(f)
1/delta(f)*sbar*cos(kbar(f)*b)*(cos(k(f)*a)-1);
        beta12 = @(f) -1/delta(f)*s(2,2)*cos(k(f)*a)*(1-
cos(kbar(f)*b));
        alpha22 = @(f)
1/delta(f)*sbar*sin(kbar(f)*b)*(cos(k(f)*a)-1);
        beta22 = @(f) -
1/(delta(f)*cos(kbar(f)*b))*s(2,2)*sin(kbar(f)*b)*cos(k(f)*a)*(1-
cos(kbar(f)*b)) + 1/(kbar(f)*cos(kbar(f)*b));


        gamma1 = @(f) 1/2 + d(3,2)/(thick*dbar)*(alpha12(f)*(1-
cos(kbar(f)*b))-alpha22(f)*sin(kbar(f)*b));
        Z2 = @(f) 1/((1-k22^2)*b)*(b-
beta22(f)*k22^2*sin(kbar(f)*b) + beta12(f)*k22^2*(1-
cos(kbar(f)*b)))*b/(j*omega(f)*eps(2,2)*width*thick);

        n_f = @(f) abs(gamma1(f)*ZL(f)/(ZL(f) + Z2(f)));

        f_operating = fminbnd(@(f) (-n_f(f)),55e3,65e3)
        %%%%%%%%%%%%%%%%%%%%%%%%%%%%%%%%%%%%%%%%%%%%%%%%%%%%%

        ZL = 1/(1/complex(R,0)+1/complex(0,-
1/(2*pi*f_operating*C)));

        if R == 1e6||R==1e7||R==1e8||R==1e9||R==1e10||R==1e11
            R
            f_operating;
            fprintf('\n Getting Closer... \n\n')
        end


[uin,uout,Tin,Tout,voltage,E2,E3,Iin,Vout,Iout,f_resonant,n,Pout,
Qout,Pin,Qin,Sin,Sout,gamma1] =
PT_solver(rho,s,d,eps,ZL,Vin_pk,f_operating,length,width,thick,a)
;
        %       matrix(num,1) = -imag(ZL);
        matrix1(num,1) = abs(ZL);
        matrix(num,2) = n;
        matrix(num,3) = abs(Qin);
```

```
        matrix(num,4) = abs(Qout);
        matrix1(num,5) = abs(Sout/Sin)*100;
        matrix(num,6) = f_operating;
        matrix(num,7) = abs(Iout);
        matrix(num,8) = abs(Vout);
        matrix(num,9) = abs(gamma1);

%         angled = 360-angledim(angle(Vout)-
angle(Iout),'radians','degrees')
%         x = abs(Vout)*abs(Iout)*cosd(angled)*.5
%         x1 = real(Vout*conj(Iout)*.5)
%         y = abs(Vin_pk)*abs(Iin)*.5*cosd(360-
angledim(angle(Vin_pk)-angle(Iin),'radians','degrees'))
%         eff = x/y*100

        lambda = 632.8e-9;
        L = 1e-2;
        length_num = 1;
        for l = -a:1e-5:0
            stress(length_num,1) = (l+.05)*1e3;   % in mm
            stress_matrix(fig_num,1) = (l+.05)*1e3;
            stress(length_num,2) = abs(Tin(l));
            stress_matrix(fig_num,2) = abs(Tin(l))/1e6;  %in MPa
            efield(length_num,1) = (l+.05)*1e3;   % in mm
            efield(length_num,2) = 0;
            stress_matrix(fig_num,3) = 0;  %in kV/cm
            potential(length_num,1) = (l+.05)*1e3;   % in mm
            potential(length_num,2) = 0.5*Vin_pk;
            stress_matrix(fig_num,4) = 0.5*Vin_pk/1e3;  %in kV
            stress_matrix(fig_num,5) = abs(uin(l))*1e6;   % in um
            length_num = length_num + 1;
            fig_num = fig_num+1;

        end
        for l = 1e-5:1e-5:b
            stress(length_num,1) = (l+.05)*1e3;   % in mm
            stress_matrix(fig_num,1) = (l+.05)*1e3;
            stress(length_num,2) = abs(Tout(l));
            stress_matrix(fig_num,2) = abs(Tout(l))/1e6;  %in MPa
            efield(length_num,1) = (l+.05)*1e3;   % in mm
            efield(length_num,2) = abs(E2(l));
            stress_matrix(fig_num,3) = abs(E2(l))/1e5;  %in kV/cm
            potential(length_num,1) = (l+.05)*1e3;   % in mm
            potential(length_num,2) = abs(voltage(l));
            stress_matrix(fig_num,4) = abs(voltage(l))/1e3;  %in
kV
            stress_matrix(fig_num,5) = abs(uout(l))*1e6;   % in um
            phi_EO(length_num,1) =
abs(L*pi*(n_rotated(2,2)^3*r_rotated(2,2) -
n_rotated(3,3)^3*r_rotated(3,2))*(E2(l))/lambda)*180/pi/90;
```

```
            phi_PE(length_num,1) =
abs(L*pi*(n_rotated(2,2)^3*q_rotated(2,2) -
n_rotated(3,3)^3*q_rotated(3,2))*(Tout(l))/lambda)*180/pi/90;
            phi_total(length_num,1) =
abs(L*pi*((E2(l))*(n_rotated(2,2)^3*r_rotated(2,2) -
n_rotated(3,3)^3*r_rotated(3,2)) +
(Tout(l))*(n_rotated(2,2)^3*q_rotated(2,2) -
n_rotated(3,3)^3*q_rotated(3,2)))/lambda)*180/pi/90;
%           phi_total(length_num,1) =
abs(L*pi*((E2(l))*(n_rotated(2,2)^3*r_rotated(2,2) -
n_rotated(3,3)^3*r_rotated(3,2)) +
(Tout(l))*(n_rotated(2,2)^3*q_rotated(2,2) +
n_rotated(3,3)^3*q_rotated(3,2)))/lambda)*180/pi/90;
            T_angle(length_num,1) = angle(Tout(l))*180/pi;
            E_angle(length_num,1) = angle(E2(l))*180/pi;
            length_num = length_num + 1;
            fig_num = fig_num+1;

        end
        [x,y] = max(stress(:,2));
        matrix(num,10) = stress(y,2);

        num = num + 1;
%     end
    ZL
    fprintf('\n Getting Closer... \n\n')
end

% abs(Vout)
% abs(Vout/Vin_pk)



num = 1;
i=0;
% f_operating = 31e3;



for k=1:1:15000
    num_matrix(k,1)=50;
    num_matrix(k,2)=k/100;
end

figure
semilogy(stress_matrix(1:10001,1),stress_matrix(1:10001,4),'b')
grid on;
xlabel('PT Length (mm)')
ylabel('Electric Potential (kV)')


% plot displacement vs length vs RL
```

```
figure
% plot(stress_matrix(1:10001,1),stress_matrix(1:10001,2),'b')
% hold on;
%
plot((stress_matrix(10002:20002,1)),stress_matrix(10002:20002,2),
'r')
% hold on;
plot((stress_matrix(50006:60006,1)),stress_matrix(50006:60006,5),
'b')
hold on;
plot((stress_matrix(40005:50005,1)),stress_matrix(40005:50005,5),
'r')
hold on;
plot((stress_matrix(30004:40004,1)),stress_matrix(30004:40004,5),
'k')
hold on;
plot((stress_matrix(20003:30003,1)),stress_matrix(20003:30003,5),
'g')
hold on;
plot(num_matrix(:,1),num_matrix(:,2),'k--')
hold on;
legend('10^1^1 \Omega','10^1^0 \Omega','10^9 \Omega','10^8
\Omega');
grid on;
xlabel('PT Length (mm)')
ylabel('Mechanical Displacement (\mum)')


% plot stress vs length vs RL
figure
% plot(stress_matrix(1:10001,1),stress_matrix(1:10001,2),'b')
% hold on;
%
plot((stress_matrix(10002:20002,1)),stress_matrix(10002:20002,2),
'r')
% hold on;
plot((stress_matrix(50006:60006,1)),stress_matrix(50006:60006,2),
'b')
hold on;
plot((stress_matrix(40005:50005,1)),stress_matrix(40005:50005,2),
'r')
hold on;
plot((stress_matrix(30004:40004,1)),stress_matrix(30004:40004,2),
'k')
hold on;
plot((stress_matrix(20003:30003,1)),stress_matrix(20003:30003,2),
'g')
hold on;
plot(num_matrix(:,1),num_matrix(:,2),'k--')
hold on;
legend('10^1^1 \Omega','10^1^0 \Omega','10^9 \Omega','10^8
\Omega');
```

```
grid on;
xlabel('PT Length (mm)')
ylabel('Longitudinal Stress (MPa)')

% plot e-field vs length vs RL
figure
% plot(stress_matrix(1:10001,1),stress_matrix(1:10001,3),'b')
% hold on;
%
plot((stress_matrix(10002:20002,1)),stress_matrix(10002:20002,3),
'r')
% hold on;
plot((stress_matrix(50006:60006,1)),stress_matrix(50006:60006,3),
'b')
hold on;
plot((stress_matrix(40005:50005,1)),stress_matrix(40005:50005,3),
'r')
hold on;
plot((stress_matrix(30004:40004,1)),stress_matrix(30004:40004,3),
'k')
hold on;
plot((stress_matrix(20003:30003,1)),stress_matrix(20003:30003,3),
'g')
hold on;
plot(num_matrix(:,1),num_matrix(:,2),'k--')
hold on;
legend('10^1^1 \Omega','10^1^0 \Omega','10^9 \Omega','10^8
\Omega');
grid on;
xlabel('PT Length (mm)')
ylabel('Longitudinal Electric Field (kV/cm)')

% plot electric potential vs length vs RL
figure
% semilogy(stress_matrix(1:10001,1),stress_matrix(1:10001,4),'b')
% hold on;
%
semilogy((stress_matrix(10002:20002,1)),stress_matrix(10002:20002
,4),'r')
% hold on;
plot((stress_matrix(50006:60006,1)),stress_matrix(50006:60006,4),
'b')
hold on;
plot((stress_matrix(40005:50005,1)),stress_matrix(40005:50005,4),
'r')
hold on;
plot((stress_matrix(30004:40004,1)),stress_matrix(30004:40004,4),
'k')
hold on;
plot((stress_matrix(20003:30003,1)),stress_matrix(20003:30003,4),
'g')
hold on;
```

```
plot(num_matrix(:,1),num_matrix(:,2),'k--')
hold on;
legend('10^1^1 \Omega','10^1^0 \Omega','10^9 \Omega','10^8
\Omega');
grid on;
xlabel('PT Length (mm)')
ylabel('Electric Potential (kV)')


pause(1);


matrix = zeros(1505:12);
num = 1;
fig_num = 1;


for m = 12:15
    C = 10^(-m)

    for i = 8:1/100:11
        R = 10^(i);
        stress = zeros(501:2);
        efield = zeros(501:2);
        potential = zeros(501:2);

        % find f_operating
        %%%%%%%%%%%%%%%%%%%%%%%%%%%%%%%%%%%%%%%%%%%%%%%%%%%%%%%
        ZL = @(f) 1/(1/complex(R,0)+1/complex(0,-1/(2*pi*f*C)));
        j = complex(0,1);
        k22 = sqrt(d(2,2)^2/(s(2,2)*eps(2,2)));
        sbar = s(2,2)*(1-k22^2);
        dbar = d(2,2)*(1-1/k22^2);
        omega = @(f) 2*pi*f;
        k = @(f) omega(f)*sqrt(rho*s(2,2));
        kbar = @(f) omega(f)*sqrt(rho*sbar);

        delta = @(f) s(2,2)*kbar(f)*sin(kbar(f)*b)*cos(k(f)*a) +
sbar*k(f)*sin(k(f)*a)*cos(kbar(f)*b);
        alpha11 = @(f) -
1/(delta(f)*cos(k(f)*a))*sbar*cos(kbar(f)*b)*sin(k(f)*a)*(cos(k(f
)*a)-1) - 1/(k(f)*cos(k(f)*a));
        beta11 = @(f) 1/delta(f)*s(2,2)*sin(k(f)*a)*(1-
cos(kbar(f)*b));
        alpha12 = @(f)
1/delta(f)*sbar*cos(kbar(f)*b)*(cos(k(f)*a)-1);
        beta12 = @(f) -1/delta(f)*s(2,2)*cos(k(f)*a)*(1-
cos(kbar(f)*b));
        alpha22 = @(f)
1/delta(f)*sbar*sin(kbar(f)*b)*(cos(k(f)*a)-1);
```

```matlab
        beta22 = @(f) -
1/(delta(f)*cos(kbar(f)*b))*s(2,2)*sin(kbar(f)*b)*cos(k(f)*a)*(1-
cos(kbar(f)*b)) + 1/(kbar(f)*cos(kbar(f)*b));


        gamma1 = @(f) 1/2 + d(3,2)/(thick*dbar)*(alpha12(f)*(1-
cos(kbar(f)*b))-alpha22(f)*sin(kbar(f)*b));
        Z2 = @(f) 1/((1-k22^2)*b)*(b-
beta22(f)*k22^2*sin(kbar(f)*b) + beta12(f)*k22^2*(1-
cos(kbar(f)*b)))*b/(j*omega(f)*eps(2,2)*width*thick);

        n_f = @(f) abs(gamma1(f)*ZL(f)/(ZL(f) + Z2(f)));

        f_operating = fminbnd(@(f) (-n_f(f)),55e3,65e3);
        %%%%%%%%%%%%%%%%%%%%%%%%%%%%%%%%%%%%%%%%%%%%%%%%%%%%%%%

        ZL = 1/(1/complex(R,0)+1/complex(0,-
1/(2*pi*f_operating*C)));

        if R == 1e6||R==1e7||R==1e8||R==1e9||R==1e10||R==1e11
           R
           f_operating;
           fprintf('\n Getting Closer... \n\n')
        end


[uin,uout,Tin,Tout,voltage,E2,E3,Iin,Vout,Iout,f_resonant,n,Pout,
Qout,Pin,Qin,Sin,Sout,gamma1] =
PT_solver(rho,s,d,eps,ZL,Vin_pk,f_operating,length,width,thick,a)
;
        matrix(num,1) = C;
        matrix(num,2) = R;
        matrix(num,3) = n;
        matrix(num,4) = (Pin);
        matrix(num,5) = (Pout);
        matrix(num,6) = abs(Pout)/abs(Pin)*100;
        matrix(num,7) = f_operating;
        matrix(num,8) = abs(Iout)*1e6; % in uA
        matrix(num,9) = abs(Vout)/1e3;
        matrix(num,13) =
angledim(angle(Vout),'radians','degrees');
        matrix(num,14) =
angledim(angle(Iout),'radians','degrees');
        matrix(num,15) = angledim(angle(Vout)-
angle(Iout),'radians','degrees');


        lambda = 632.8e-9;
        L = 1e-2;
        length_num = 1;
        for l = -a:2e-4:0
            stress(length_num,1) = (l+.05)*1e3;   % in mm
```

```
                stress_matrix(fig_num,1) = (l+.05)*1e3;
                stress(length_num,2) = abs(Tin(l));
                stress_matrix(fig_num,2) = abs(Tin(l))/1e6;  %in MPa
                efield(length_num,1) = (l+.05)*1e3;  % in mm
                efield(length_num,2) = 0;
                stress_matrix(fig_num,3) = 0;  %in kV/cm
                potential(length_num,1) = (l+.05)*1e3;  % in mm
                potential(length_num,2) = 0.5*Vin_pk;
                stress_matrix(fig_num,4) = 0.5*Vin_pk/1e3;  %in kV
                length_num = length_num + 1;
                fig_num = fig_num+1;

        end
        for l = 2e-4:2e-4:b
                stress(length_num,1) = (l+.05)*1e3;  % in mm
                stress_matrix(fig_num,1) = (l+.05)*1e3;
                stress(length_num,2) = abs(Tout(l));
                stress_matrix(fig_num,2) = abs(Tout(l))/1e6;  %in MPa
                efield(length_num,1) = (l+.05)*1e3;  % in mm
                efield(length_num,2) = abs(E2(l));
                stress_matrix(fig_num,3) = abs(E2(l))/1e5;  %in kV/cm
                potential(length_num,1) = (l+.05)*1e3;  % in mm
                potential(length_num,2) = abs(voltage(l));
                stress_matrix(fig_num,4) = abs(voltage(l))/1e3;  %in
kV
                phi_EO(length_num,1) =
abs(L*pi*(n_rotated(2,2)^3*r_rotated(2,2) -
n_rotated(3,3)^3*r_rotated(3,2))*(E2(l))/lambda)*180/pi/90;
                phi_PE(length_num,1) =
abs(L*pi*(n_rotated(2,2)^3*q_rotated(2,2) -
n_rotated(3,3)^3*q_rotated(3,2))*(Tout(l))/lambda)*180/pi/90;
                phi_total(length_num,1) =
abs(L*pi*((E2(l))*(n_rotated(2,2)^3*r_rotated(2,2) -
n_rotated(3,3)^3*r_rotated(3,2)) +
(Tout(l))*(n_rotated(2,2)^3*q_rotated(2,2) -
n_rotated(3,3)^3*q_rotated(3,2)))/lambda)*180/pi/90;
                T_angle(length_num,1) = angle(Tout(l))*180/pi;
                E_angle(length_num,1) = angle(E2(l))*180/pi;
                length_num = length_num + 1;
                fig_num = fig_num+1;

        end

        [x,y] = max(stress(:,2));
        matrix(num,11) = stress(y,2)/1e6;  % in MPa
        [x,y] = max(efield(:,2));
        matrix(num,12) = efield(y,2)/1e5;  % in kV/cm

        num = num + 1;
    end
    ZL
    fprintf('\n Getting Closer... \n\n')
```

205

```
end


for n = 1:1204
    if matrix(n,13)<0
        matrix(n,13) = 360 + matrix(n,13);
    end
    if matrix(n,14)<0
        matrix(n,14) = 360 + matrix(n,14);
    end
    matrix(n,15) = matrix(n,13) - matrix(n,14);
%     matrix(n,5) =
matrix(n,8)/1e6*matrix(n,9)*cosd(matrix(n,15));
end




toc;


% plot efficiency vs RL vs CL
figure
% semilogx((matrix(1205:1505,2)),matrix(1205:1505,6),'g')
% hold on;
semilogx((matrix(904:1204,2)),matrix(904:1204,6),'b')
hold on;
semilogx((matrix(603:903,2)),matrix(603:903,6),'r')
hold on;
semilogx((matrix(302:602,2)),matrix(302:602,6),'k')
hold on;
semilogx((matrix(1:301,2)),matrix(1:301,6),'g')
hold on;
legend('10^-^1^5 F','10^-^1^4 F','10^-^1^3 F','10^-^1^2 F');
grid on;
xlabel('Load Resistance (\Omega)')
ylabel('Efficiency (%)')
ylim([0 100])
xlim([1e8 1e11])



% plot Pout vs RL vs CL
figure
% semilogy((matrix(1205:1505,2)),matrix(1205:1505,5),'g')
% hold on;
loglog((matrix(904:1204,2)),matrix(904:1204,5),'b')
hold on;
loglog((matrix(603:903,2)),matrix(603:903,5),'r')
hold on;
loglog((matrix(302:602,2)),matrix(302:602,5),'k')
hold on;
loglog((matrix(1:301,2)),matrix(1:301,5),'g')
```

```
hold on;
legend('10^-^1^5 F','10^-^1^4 F','10^-^1^3 F','10^-^1^2 F');
grid on;
xlabel('Load Resistance (\Omega)')
ylabel('Output Power (W)')
xlim([1e8 1e11])


% plot output power phase angle vs RL vs CL
figure
% semilogx((matrix(1205:1505,2)),matrix(1205:1505,15),'g')
% hold on;
semilogx((matrix(904:1204,2)),matrix(904:1204,15),'b')
hold on;
semilogx((matrix(603:903,2)),matrix(603:903,15),'r')
hold on;
semilogx((matrix(302:602,2)),matrix(302:602,15),'k')
hold on;
semilogx((matrix(1:301,2)),matrix(1:301,15),'g')
hold on;
legend('10^-^1^5 F','10^-^1^4 F','10^-^1^3 F','10^-^1^2 F');
grid on;
ylabel('\theta_V - \theta_I (degrees)')
xlabel('Load Resistance (\Omega)')
xlim([1e8 1e11])


% plot transformer ratio vs RL vs CL
figure
% loglog((matrix(1205:1505,2)),matrix(1205:1505,3),'g')
% hold on;
loglog((matrix(904:1204,2)),matrix(904:1204,3),'b')
hold on;
loglog((matrix(603:903,2)),matrix(603:903,3),'r')
hold on;
loglog((matrix(302:602,2)),matrix(302:602,3),'k')
hold on;
loglog((matrix(1:301,2)),matrix(1:301,3),'g')
hold on;
legend('10^-^1^5 F','10^-^1^4 F','10^-^1^3 F','10^-^1^2 F');
grid on;
ylabel('Vout/Vin')
xlabel('Load Resistance (\Omega)')
xlim([1e8 1e11])


% plot output voltage vs RL vs CL
figure
% loglog((matrix(1205:1505,2)),matrix(1205:1505,9),'g')
% hold on;
loglog((matrix(904:1204,2)),matrix(904:1204,9),'b')
hold on;
```

```
loglog((matrix(603:903,2)),matrix(603:903,9),'r')
hold on;
loglog((matrix(302:602,2)),matrix(302:602,9),'k')
hold on;
loglog((matrix(1:301,2)),matrix(1:301,9),'g')
hold on;
legend('10^-^1^5 F','10^-^1^4 F','10^-^1^3 F','10^-^1^2 F');
grid on;
ylabel('Output Voltage (kV)')
xlabel('Load Resistance (\Omega)')
xlim([1e8 1e11])


% plot output voltage phase angle vs RL vs CL
figure
% semilogx((matrix(1205:1505,2)),matrix(1205:1505,13),'g')
% hold on;
semilogx((matrix(904:1204,2)),matrix(904:1204,13),'b')
hold on;
semilogx((matrix(603:903,2)),matrix(603:903,13),'r')
hold on;
semilogx((matrix(302:602,2)),matrix(302:602,13),'k')
hold on;
semilogx((matrix(1:301,2)),matrix(1:301,13),'g')
hold on;
legend('10^-^1^5 F','10^-^1^4 F','10^-^1^3 F','10^-^1^2 F');
grid on;
ylabel('\theta_V (degrees)')
xlabel('Load Resistance (\Omega)')
xlim([1e8 1e11])


% plot Iout vs RL vs CL
figure
% loglog((matrix(1205:1505,2)),matrix(1205:1505,8),'g')
% hold on;
loglog((matrix(904:1204,2)),matrix(904:1204,8),'b')
hold on;
loglog((matrix(603:903,2)),matrix(603:903,8),'r')
hold on;
loglog((matrix(302:602,2)),matrix(302:602,8),'k')
hold on;
loglog((matrix(1:301,2)),matrix(1:301,8),'g')
hold on;
legend('10^-^1^5 F','10^-^1^4 F','10^-^1^3 F','10^-^1^2 F');
grid on;
xlabel('Load Resistance (\Omega)')
ylabel('Output Current (\muA)')
xlim([1e8 1e11])
```

```
% plot output current phase angle vs RL vs CL
figure
% semilogx((matrix(1205:1505,2)),matrix(1205:1505,14),'g')
% hold on;
semilogx((matrix(904:1204,2)),matrix(904:1204,14),'b')
hold on;
semilogx((matrix(603:903,2)),matrix(603:903,14),'r')
hold on;
semilogx((matrix(302:602,2)),matrix(302:602,14),'k')
hold on;
semilogx((matrix(1:301,2)),matrix(1:301,14),'g')
hold on;
legend('10^-^1^5 F','10^-^1^4 F','10^-^1^3 F','10^-^1^2 F');
grid on;
ylabel('\theta_I (degrees)')
xlabel('Load Resistance (\Omega)')
xlim([1e8 1e11])




% plot Tmax vs RL vs CL
figure
% loglog((matrix(1205:1505,2)),matrix(1205:1505,11),'g')
% hold on;
loglog((matrix(904:1204,2)),matrix(904:1204,11),'b')
hold on;
loglog((matrix(603:903,2)),matrix(603:903,11),'r')
hold on;
loglog((matrix(302:602,2)),matrix(302:602,11),'k')
hold on;
loglog((matrix(1:301,2)),matrix(1:301,11),'g')
hold on;
legend('10^-^1^5 F','10^-^1^4 F','10^-^1^3 F','10^-^1^2 F');
grid on;
xlabel('Load Resistance (\Omega)')
ylabel('Maximum Stress (MPa)')
xlim([1e8 1e11])




% plot Emax vs RL vs CL
figure
% loglog((matrix(1205:1505,2)),matrix(1205:1505,12),'g')
% hold on;
loglog((matrix(904:1204,2)),matrix(904:1204,12),'b')
hold on;
loglog((matrix(603:903,2)),matrix(603:903,12),'r')
hold on;
loglog((matrix(302:602,2)),matrix(302:602,12),'k')
hold on;
loglog((matrix(1:301,2)),matrix(1:301,12),'g')
```

```matlab
hold on;
legend('10^-^1^5 F','10^-^1^4 F','10^-^1^3 F','10^-^1^2 F');
grid on;
xlabel('Load Resistance (\Omega)')
ylabel('Maximum Electric Field (kV/cm)')
xlim([1e8 1e11])




%*************************** Warnings
********************************

% if Tmax_calc > T_max
%     warning('The maximum stress generated is above the fracture
point for this material.')
% end
%
% if Emax_calc > BD_dielectric
%     warning('The maximum electric field generated is above the
dielectric breakdown strength for this material.')
% end
%
% if f_resonant < 10e3
%     warning('The resonant frequency for this PT is less than
the operating range of the Amplifier Research KAA1020 power
amplifier.')
% end

%*************************************************************
**********
```

```matlab
function [s_rotated, d_rotated, eps_rotated, R_rotated,
P_rotated, n_rotated, q_rotated] = rotate3D(x_rotation_angle,
y_rotation_angle, z_rotation_angle, c, e, eps_T, R, P, n,
dielectric_loss_tangent_xy, dielectric_loss_tangent_z, Q)

rotate_x = zeros(3,3);
rotate_y = zeros(3,3);
rotate_z = zeros(3,3);
rotate = zeros(3,3);

rotate_x = [1 0 0;0 cosd(x_rotation_angle)
sind(x_rotation_angle);0 -sind(x_rotation_angle)
cosd(x_rotation_angle)];
rotate_y = [cosd(y_rotation_angle) 0 -sind(y_rotation_angle);0 1
0;sind(y_rotation_angle) 0 cosd(y_rotation_angle)];
rotate_z = [cosd(z_rotation_angle) sind(z_rotation_angle) 0;-
sind(z_rotation_angle) cosd(z_rotation_angle) 0;0 0 1];

rotate = rotate_x*rotate_y*rotate_z;

% Equations needed to turn material constants into constants for
calculations
% s = inv(c)
% d = e*inv(c)
% eps = eps_S + e*inv(c)*transpose(e)


loss_factor = [dielectric_loss_tangent_xy  0      0;
               0      dielectric_loss_tangent_xy  0;
               0      0      dielectric_loss_tangent_z];


%  QipQjqQkrQltApqrt is transformation for fourth order tensors

c_rotated = zeros(6,6);
s_rotated = zeros(6,6);
P_rotated = zeros(6,6);
int1 = zeros(1,2);
int2 = zeros(1,2);


for i = 1:6
    for j = 1:6
        c_rotated_sum = 0;
        P_rotated_sum = 0;
%         s_rotated_sum = 0;
        int1 = fromCompactNotation(i);
        int2 = fromCompactNotation(j);
        for p = 1:3
            for q = 1:3
                for r = 1:3
                    for t = 1:3
```

211

```
                                    c_rotated_sum =
rotate(int1(1,1),p)*rotate(int1(1,2),q)*rotate(int2(1,1),r)*rotat
e(int2(1,2),t)*c(toCompactNotation(p,q),toCompactNotation(r,t)) +
c_rotated_sum;
                                    c_rotated(i,j) = c_rotated_sum;
                                    P_rotated_sum =
rotate(int1(1,1),p)*rotate(int1(1,2),q)*rotate(int2(1,1),r)*rotat
e(int2(1,2),t)*P(toCompactNotation(p,q),toCompactNotation(r,t)) +
P_rotated_sum;
                                    P_rotated(i,j) = P_rotated_sum;
                            end
                        end
                    end
                end
            end
end
c;
c_rotated;  %undo ";" at end for output
s_rotated = inv(c_rotated);
s_lossy = s_rotated*(1-complex(0,1)/Q);
s_rotated = s_lossy;
s = inv(c)*(1-complex(0,1)/Q);   %undo ";" at end for output
P;
P_rotated;  %undo ";" at end for output


%  QipQjqQkrApqr is transformation for third order tensors when
"jk" are in compact notation

e_rotated = zeros(3,6);
d_rotated = zeros(3,6);
int1 = zeros(1,2);

for i = 1:3
    for j = 1:6
        e_rotated_sum = 0;
        int1 = fromCompactNotation(j);
        for p = 1:3
            for q = 1:3
                for r = 1:3
                    e_rotated_sum =
rotate(i,p)*rotate(int1(1,1),q)*rotate(int1(1,2),r)*e(p,toCompact
Notation(q,r)) + e_rotated_sum;
                    e_rotated(i,j) = e_rotated_sum;
                end
            end
        end
    end
end

e;
e_rotated;  %undo ";" at end for output
```

212

```matlab
d_rotated = e_rotated*inv(c_rotated);
d = e*inv(c);   %undo ";" at end for output


%  QipQjqQkrApqr is transformation for third order tensors when
"ij" are in compact notation

R_rotated = zeros(6,3);
int1 = zeros(1,2);

for i = 1:6
    R_rotated_sum = 0;
    int1 = fromCompactNotation(i);
    for j = 1:3
        for p = 1:3
            for q = 1:3
                for r = 1:3
                    R_rotated_sum =
rotate(int1(1,1),p)*rotate(int1(1,2),q)*rotate(j,r)*R(toCompactNo
tation(p,q),r) + R_rotated_sum;
                    R_rotated(i,j) = R_rotated_sum;
                end
            end
        end
    end
end

R;
R_rotated;  %undo ";" at end for output


%  QipQjqApq is transformation for second order tensors

eps_T_rotated = zeros(3,3);
eps = zeros(3,3);
n_rotated = zeros(3,3);
loss_factor_rotated = zeros(3,3);
eps_lossless_rotated  = zeros(3,3);

eps_lossless = eps_T;
eps_lossy = eps_T;
eps_lossy(1,1) = eps_T(1,1)*(1 -
complex(0,1)*dielectric_loss_tangent_xy);
eps_lossy(2,2) = eps_T(2,2)*(1 -
complex(0,1)*dielectric_loss_tangent_xy);
eps_lossy(3,3) = eps_T(3,3)*(1 -
complex(0,1)*dielectric_loss_tangent_z);
eps_T = eps_lossy;


for i = 1:3
    for j = 1:3
```

```
        eps_T_rotated_sum = 0;
        n_rotated_sum = 0;
        eps_lossless_rotated_sum = 0;
        loss_factor_rotated_sum = 0;
        for p = 1:3
            for q = 1:3
%change to eps_lossy below
                eps_T_rotated_sum =
rotate(i,p)*rotate(j,q)*eps_T(p,q) + eps_T_rotated_sum;
                eps_T_rotated(i,j) = eps_T_rotated_sum;
                eps_lossless_rotated_sum =
rotate(i,p)*rotate(j,q)*eps_lossless(p,q) +
eps_lossless_rotated_sum;
                eps_lossless_rotated(i,j) =
eps_lossless_rotated_sum;
                n_rotated_sum = rotate(i,p)*rotate(j,q)*n(p,q) +
n_rotated_sum;
                n_rotated(i,j) = n_rotated_sum;
                loss_factor_rotated_sum =
rotate(i,p)*rotate(j,q)*loss_factor(p,q) +
loss_factor_rotated_sum;
                loss_factor_rotated(i,j) =
loss_factor_rotated_sum;
            end
        end
    end
end

eps_T_rotated
eps_rotated = eps_T_rotated;
eps_lossless_rotated
loss_factor_rotated
eps_lossy = eps_lossless_rotated.*(1-
complex(0,1)*loss_factor_rotated)
eps_rotated = eps_lossy;


n;  %undo ";" at end for output
n_rotated;  %undo ";" at end for output

q = zeros(6,6);

for i = 1:6
    for j =1:6
        q_sum = 0;
        for k = 1:6
            q_sum = P_rotated(i,k)*s_rotated(k,j) + q_sum;
        end
        q(i,j) = q_sum;
    end
end
q_rotated = q;  %undo ";" at end for output
```

```
q = zeros(6,6);

for i = 1:6
    for j =1:6
        q_sum = 0;
        for k = 1:6
            q_sum = P(i,k)*s(k,j) + q_sum;
        end
        q(i,j) = q_sum;
    end
end
q;
q32 = q(3,2);
q22 = q(2,2);
```

```
function [matrix] = fromCompactNotation(compact)

if compact==1
    matrix = [1,1];
elseif compact==2
    matrix = [2,2];
elseif compact==3
    matrix = [3,3];
elseif compact==4
    matrix = [2,3];
elseif compact==5
    matrix = [3,1];
elseif compact==6
    matrix = [1,2];
else
    matrix = [4,4];            %error if i=j=4

end
```

```
function compact = toCompactNotation(i,j)

if i==j,
    compact = i;
elseif (i==2 & j==3) | (i==3 & j==2)
    compact = 4;
elseif (i==3 & j==1) | (i==1 & j==3)
    compact = 5;
elseif (i==1 & j==2) | (i==2 & j==1)
    compact = 6;
else
    compact = 7;  %%error if compact = 7
end
```

```matlab
function
[u2in,u2out,Tin,Tout,voltage,E2,E3,Iin,Vout,Iout,f_resonant,n,Pou
t,Qout,Pin,Qin,Sin,Sout,gamma1] =
PT_solver(rho,s,d,eps,ZL,Vin_pk,f_operating,length,width,thick,a)

V1 = Vin_pk;
f_resonant = 0;

% Iin_max = 0;
% Vout_max = 0;
% Iout_max = 0;
% f_resonant = 100e3;                                 %% for
testing only
% n = 0;
% Emax_calc = 0;
% Tmax_calc = 0;

b = length - a;                                       %% total
length is -a < z < length
                                                      %% input pad
is -a < z < 0

j = complex(0,1);

k32 = sqrt(d(3,2)^2/(eps(3,3)*s(2,2)));
abs(k32);
epsbar = eps(3,3)*(1-k32^2);
k22 = sqrt(d(2,2)^2/(s(2,2)*eps(2,2)));
abs(k22);
dbar = d(2,2)*(1-1/k22^2);
sbar = s(2,2)*(1-k22^2);

omega = 2*pi*f_operating;
k = omega*sqrt(rho*s(2,2));
kbar = omega*sqrt(rho*sbar);

delta = s(2,2)*kbar*sin(kbar*b)*cos(k*a) +
sbar*k*sin(k*a)*cos(kbar*b);
alpha11 = -
1/(delta*cos(k*a))*sbar*cos(kbar*b)*sin(k*a)*(cos(k*a)-1) -
1/(k*cos(k*a));
beta11 = 1/delta*s(2,2)*sin(k*a)*(1-cos(kbar*b));
alpha12 = 1/delta*sbar*cos(kbar*b)*(cos(k*a)-1);
beta12 = -1/delta*s(2,2)*cos(k*a)*(1-cos(kbar*b));
alpha22 = 1/delta*sbar*sin(kbar*b)*(cos(k*a)-1);
beta22 = -1/(delta*cos(kbar*b))*s(2,2)*sin(kbar*b)*cos(k*a)*(1-
cos(kbar*b)) + 1/(kbar*cos(kbar*b));


gamma1 = 1/2 + d(3,2)/(thick*dbar)*(alpha12*(1-cos(kbar*b))-
alpha22*sin(kbar*b));
```

```
Z2 = 1/((1-k22^2)*b)*(b-beta22*k22^2*sin(kbar*b) +
beta12*k22^2*(1-cos(kbar*b)))*b/(j*omega*eps(2,2)*width*thick);

gamma2 = k22^2*s(2,2)*d(3,2)/(s(2,2)*d(2,2)*thick)*(beta12 +
beta11*sin(k*a) - beta12*cos(k*a));
Z1 = 1/(1/a*(a - k32^2/(1-k32^2)*(alpha12 + alpha11*sin(k*a) -
alpha12*cos(k*a)))*j*omega*epsbar*width*a/thick);

I2 = gamma1*V1/(ZL + Z2);
I1 = -V1/Z1 + gamma2*I2;
V2 = gamma1*ZL*V1/(ZL + Z2);
Vout = V2;
Iout = I2;
Iin = -I1;

n = abs(V2/V1);
Sout = 1/2*V2*conj(I2);
Sin = 1/2*V1*conj(I1);
% Sin = (1/4*(I1*conj(V1) + conj(V1)*I1));
% Sout = (1/4*(I2*conj(V2) + conj(V2)*I2));
Pout = real(Sout);
Pin = real(Sin);
Qout = imag(Sout);
Qin = imag(Sin);


c1 = I2*s(2,2)/(j*omega*d(2,2)*thick*width);

u2in = @(x) (alpha11*d(3,2)*Vin_pk/thick +
beta11*k22^2*c1)*sin(k*x) + (alpha12*d(3,2)*Vin_pk/thick +
beta12*k22^2*c1)*cos(k*x);
u2out = @(x) (alpha22*d(3,2)*Vin_pk/thick +
beta22*k22^2*c1)*sin(kbar*x) + (alpha12*d(3,2)*Vin_pk/thick +
beta12*k22^2*c1)*cos(kbar*x);

u2in_prime = @(x) k*(d(3,2)*V1*alpha11/thick +
c1*k22^2*beta11)*cos(k*x) - k*(d(3,2)*V1*alpha12/thick +
c1*k22^2*beta12)*sin(k*x);
u2out_prime = @(x) kbar*(d(3,2)*V1*alpha22/thick +
c1*k22^2*beta22)*cos(kbar*x) - kbar*(d(3,2)*V1*alpha12/thick +
c1*k22^2*beta12)*sin(kbar*x);


voltage = @(x) 1/2*V1 + 1/dbar*(c1*x - (alpha22*d(3,2)*V1/thick +
beta22*k22^2*c1)*sin(kbar*x) + (alpha12*d(3,2)*V1/thick +
beta12*k22^2*c1)*(1-cos(kbar*x)));

Tin = @(x) 1/s(2,2)*(u2in_prime(x) + d(3,2)*V1/thick);
% Tin = @(x) (1/s(2,2)*((k*(d(3,2)*V1*alpha11/thick +
c1*k22^2*beta11)*cos(k*x) - k(d(3,2)*V1*alpha12/thick +
c1*k22^2*beta12)*sin(k*x)) + d(3,2)*V1/thick));
% Tin = @(x) 1/x;
```

```
Tout = @(x) 1/sbar*(u2out_prime(x) - k22^2*c1);

E3 = -V1/thick;
E2 = @(x) 1/eps(2,2)*(d(2,2)*c1/s(2,2) -
d(2,2)/sbar*(u2out_prime(x) - k22^2*c1));




%TEST%

% omega = @(f) 2*pi*f;
% k = @(f) omega*sqrt(rho*s(2,2));
% kbar = @(f) omega*sqrt(rho*sbar);
%
% delta = @(f) s(2,2)*kbar*sin(kbar*b)*cos(k*a) +
sbar*k*sin(k*a)*cos(kbar*b);
% alpha11 = @(f) -
1/(delta*cos(k*a))*sbar*cos(kbar*b)*sin(k*a)*(cos(k*a)-1) -
1/(k*cos(k*a));
% beta11 = @(f) 1/delta*s(2,2)*sin(k*a)*(1-cos(kbar*b));
% alpha12 = @(f) 1/delta*sbar*cos(kbar*b)*(cos(k*a)-1);
% beta12 = @(f) -1/delta*s(2,2)*cos(k*a)*(1-cos(kbar*b));
% alpha22 = @(f) 1/delta*sbar*sin(kbar*b)*(cos(k*a)-1);
% beta22 = @(f) -
1/(delta*cos(kbar*b))*s(2,2)*sin(kbar*b)*cos(k*a)*(1-cos(kbar*b))
+ 1/(kbar*cos(kbar*b));
%
%
% gamma1 = @(f) 1/2 + d(3,2)/(thick*dbar)*(alpha12*(1-
cos(kbar*b))-alpha22*sin(kbar*b));
% Z2 = @(f) 1/((1-k22^2)*b)*(b-beta22*k22^2*sin(kbar*b) +
beta12*k22^2*(1-cos(kbar*b)))*b/(j*omega*eps(2,2)*width*thick);
%
% n_f = @(f) gamma1*ZL/(ZL + Z2);
```

C. Matlab Code for Analyzing Optical Diagnostic

```
clear all;
close all;
clc;

%************************* SUMMARY OF CODE
*******************************
%  Author:          James A. VanGordon
%  Department:      Electrical and Computer Engineering
%  Organization:    University of Missouri
%  Date:            December 2012
%
%  This code is just used for rotating the material constants and
analyzing
%  optical data.
%
%********************************************************************
**********


%*********************** Material Constants
****************************
x_rotation_angle = 45;                      %% rotation for
y-cut PT in degrees
y_rotation_angle = 0;                        %% rotation for
z-cut PT in degrees
z_rotation_angle = 0;                        %% rotation for
x-cut PT in degrees

width = 1e-2;
thick = 1.5e-3;
length1 = 100e-3;
a = 50e-3;
b = length1 - a;

rho = 4700;                                  %% mass density
in kg/m^3
                                             %% should be
4,700 kg/m^3 for LiNbO3

BD_dielectric = 150e6;                       %% dielectric
breakdown strength in V/m
                                             %% for LiNbO3
should be ~150 MV/m

T_max = 30 * 10^6;                           %% maximum stress
before crystal will fracture in Pa
```

```
                                                   %% for LiNbO3
should be between 30 MPa and 120 MPa


c = zeros(6,6);                                    %% initialize
size of c              [N/m^2]
e = zeros(3,6);                                    %% initialize
size of e              [C/m^2]
eps_S = zeros(3,3);                                %% initialize
size of eps_S          [C/(V*m)] aka [F/m]
s = zeros(6,6);                                    %% initialize
size of s              [m^2/N]
d = zeros(3,6);                                    %% initialize
size of d              [C/N]
eps = zeros(3,3);                                  %% initialize
size of eps            [C^2/(N*m^2)] aka [F/m]
r = zeros(6,3);                                    %% initialize
size of r              [m/V]
r_rotated = zeros(6,3);                            %% initialize
size of rotated r      [m/V]
p = zeros(6,6);                                    %% initialize
size of p              [unitless]
p_rotated = zeros(6,6);                            %% initialize
size of rotated p      [unitless]
n = zeros(3,3);                                    %% initialize
size of n              [unitless]
n_rotated = zeros(3,3);                            %% initialize
size of rotated n      [unitless]



% set up elastic constants in matrix "c"     %% for LiNb03
should be
c = [2.03   0.53  0.75   0.09  0     0;      %% 2.03   0.53
0.75   0.09  0      0
     0.53   2.03  0.75  -0.09  0     0;      %% 0.53   2.03
0.75  -0.09  0      0
     0.75   0.75  2.45   0     0     0;      %% 0.75   0.75
2.45   0      0      0
     0.09  -0.09  0      0.60  0     0;      %% 0.09  -0.09  0
0.60   0      0
     0      0     0      0     0.60  0.09;   %% 0      0      0
0      0.60  0.09
     0      0     0      0     0.09  0.75];  %% 0      0      0
0      0.09  0.75

 c = c * 10^11;                                     %% c = c * 10^11

% set up piezoelectric constants in matrix "e"  %% for LiNbO3
should be
e = [0      0     0      0     3.70  -2.50;  %% 0      0      0
0      3.70  -2.50
     -2.50  2.50  0      3.70  0     0;      %% -2.50  2.50  0
3.70   0      0
```

222

```
       0.20    0.20   1.30    0      0      0];            %% 0.20    0.20
1.30    0      0      0

e = e * 1;                                                 %% e = e * 1


% set up dielectric constants in matrix "eps_S"
% this is for constant strain field              %% for LiNbO3
should be
eps_S = [38.9   0      0;                         %% 38.9   0      0
         0      38.9   0;                         %% 0      38.9   0
         0      0      25.7];                      %% 0      0
25.7

eps_S = eps_S * 10^-11;                           %% eps_S = eps_S
* 10^-11

% set up dielectric constants in matrix "eps_T"
% this is for constant strain field              %% for LiNbO3
should be
eps_T = [85.2   0      0;                         %% 38.9   0      0
         0      85.2   0;                         %% 0      38.9   0
         0      0      28.7];                      %% 0      0
25.7

eps_T = eps_T * 8.85e-12;                         %% eps_S =
eps_S * 10^-11


% set up dielectric constants in matrix "n"      %% for LiNbO3
should be
n = [2.2910     0         0;                      %% 2.2910   0
0
     0          2.2910    0;                      %% 0
2.2910  0
     0          0         2.2005];                %% 0         0
2.2005

n = n * 1;                                        %% n = n * 1


% set up electro-optic constants in matrix "r"
% this is for constant strain field              %% for LiNbO3
should be
r = [0      -3.4    7.7;                          %% 0      -3.4
7.7
     0       3.4    7.7;                          %% 0       3.4
7.7
     0       0      28.8;                         %% 0       0
28.8
```

223

```
      0      18.2    0;                                    %% 0        18.2
0
      18.2   0       0;                                    %% 18.2     0
0
      -3.4   0       0];                                   %% -3.4     0
0

r = r * 10^-12;                                            %% r = r * 10^-
12


% set up elastic constants in matrix "p"          %% for LiNb03
should be
p = [-0.026 0.090   0.133   -0.075  0        0;          %% 0.036
0.072   0.139   0.066   0       0
      0.090  -0.026  0.133   0.075   0        0;          %% 0.072
0.036   0.139   -0.066  0       0
      0.133  0.133   0.071   0       0        0;          %% 0.178
0.178   0.060   0       0       0
      -0.151 0.151   0       0.146   0        0;          %% 0.154
-0.154  0       0.30    0       0
      0      0       0       0       0.146    -0.151;     %% 0
0       0       0       0.30    0.154
      0      0       0       0       -0.075   -0.058];    %% 0
0       0       0       0.066   -0.019

 p = p * 1;                                               %% p = p
* 1

 dielectric_loss_factor_xy = 5e-4;
 dielectric_loss_factor_z = 3.4e-4;

 Q = 3255;


 % rotate matrices accordingly and return matrices to be used in
calculations
 [s, d, eps, r_rotated, p_rotated, n_rotated, q_rotated] =
rotate3D_RSI_paper1(x_rotation_angle, y_rotation_angle,
z_rotation_angle, c, e, eps_T, r, p, n,
dielectric_loss_factor_xy,dielectric_loss_factor_z, Q);
s;
d;
eps;
r_rotated;
p_rotated;
n_rotated;
abs(q_rotated)


%***************************************************************
**********
```

```
% for y = 1:11
% test to see what the maximum electric field would be based on
% calculations for the number of light-to-dark transitions we are
seeing
%         ---->1 light-to-dark transtion corresponds to a phase
change of pi/2

E = 0;
T = 0;
D2 = 0;
I = 0;

f = 61.6470e3
D_transitions = 13;


transitions = 14


lambda = 632.8e-9;
L = 1e-2;
phase_change = (transitions/4)*pi/2;
D_phase_change = (D_transitions/4)*pi/2;
D2 =
eps(2,2)*lambda*D_phase_change/(L*pi*(n_rotated(2,2)^3*r_rotated(
2,2) - n_rotated(3,3)^3*r_rotated(3,2)));
d(2,2)

I = abs(D2*complex(0,1)*2*pi*f*width*thick)

T_numerator = D2*L*pi*(n_rotated(2,2)^3*r_rotated(2,2) -
n(3,3)^3*r_rotated(3,2)) - eps(2,2)*lambda*phase_change;
T_denominator = L*pi*(d(2,2)*n_rotated(2,2)^3*r_rotated(2,2) -
d(2,2)*n_rotated(3,3)^3*r_rotated(3,2) -
n_rotated(2,2)^3*q_rotated(2,2)*eps(2,2) +
n_rotated(3,3)^3*q_rotated(3,2)*eps(2,2));

T = abs(T_numerator/T_denominator)
T = (T_numerator/T_denominator);

E = abs(((D2 - d(2,2)*-T)/eps(2,2)))
E = ((D2 - d(2,2)*-T)/eps(2,2));

D2 =
abs(eps(2,2)*lambda*D_phase_change/(L*pi*(n_rotated(2,2)^3*r_rota
ted(2,2) - n_rotated(3,3)^3*r_rotated(3,2))))
abs(d(2,2)*T)
% T=0
```

```matlab
phi_EO = abs(L*pi*(n_rotated(2,2)^3*r_rotated(2,2) -
n_rotated(3,3)^3*r_rotated(3,2))*E/lambda)*180/pi/90
phi_angle_EO = angle(L*pi*(n_rotated(2,2)^3*r_rotated(2,2) -
n_rotated(3,3)^3*r_rotated(3,2))*E/lambda)*180/pi
phi_PE = abs(L*pi*(n_rotated(2,2)^3*q_rotated(2,2) -
n_rotated(3,3)^3*q_rotated(3,2))*T/lambda)*180/pi/90
phi_angle_PE = angle(L*pi*(n_rotated(2,2)^3*q_rotated(2,2) -
n_rotated(3,3)^3*q_rotated(3,2))*T/lambda)*180/pi

phi = abs((L*pi*(n_rotated(2,2)^3*r_rotated(2,2) -
n_rotated(3,3)^3*r_rotated(3,2))*E/lambda +
L*pi*(n_rotated(2,2)^3*q_rotated(2,2) -
n_rotated(3,3)^3*q_rotated(3,2))*T/lambda))*180/pi/90

folder = 'C:/Users/superPuTeR/Desktop/Jim/Data/3-13-14 data/1e-
4/';
file_name = strcat(folder, 'transitions.csv');
transition_table = csvread(file_name);
length(transition_table)

D_transitions = transition_table(length(transition_table),2);
D_phase_change = ((D_transitions)/4)*pi/2;
lambda = 632.8e-9;
L = 1e-2;
    D2 =
eps(2,2)*lambda*D_phase_change/(L*pi*(n_rotated(2,2)^3*r_rotated(
2,2) - n_rotated(3,3)^3*r_rotated(3,2)))


qvalue = 0;     % set qvalue = 1 if using Q-value to find current
and D2
                % set qvalue = 0 if using transitions to find
current and D2

if qvalue == 0
    D2 =
eps(2,2)*lambda*D_phase_change/(L*pi*(n_rotated(2,2)^3*r_rotated(
2,2) - n_rotated(3,3)^3*r_rotated(3,2)))
    I = abs(D2*complex(0,1)*2*pi*f*width*thick)
elseif qvalue ==1
    I = 51.3556e-6      % plug in Iout and D2 from Mathematica
Q-value workbook
    D2 = -2.39262e-3*complex(0,1)
end


sum32 = 0;
sum22 = 0;
for k = 1:6
    sum32 = p_rotated(3,k)*d(2,k) + sum32;
    sum22 = p_rotated(2,k)*d(2,k) + sum22;
```

```
end
for x = 1:length(transition_table)

    transitions = transition_table(x,2);
    phase_change = (transitions/4)*pi/2;

    T_numerator = (D2*L*pi*(n_rotated(2,2)^3*r_rotated(2,2) -
n(3,3)^3*r_rotated(3,2)) - eps(2,2)*lambda*phase_change);
    T_denominator = L*pi*(d(2,2)*n_rotated(2,2)^3*r_rotated(2,2)
- d(2,2)*n_rotated(3,3)^3*r_rotated(3,2) -
n_rotated(2,2)^3*q_rotated(2,2)*eps(2,2) +
n_rotated(3,3)^3*q_rotated(3,2)*eps(2,2));

    T = abs(T_numerator/T_denominator);
    T = (T_numerator/T_denominator);
    T_table(x,1) = abs(T);



    T_test =
lambda*phase_change/(L*pi*(n_rotated(2,2)^3*q_rotated(2,2) -
n_rotated(3,3)^3*q_rotated(3,2)));
    T_test_table(x,1) = abs(T_test);
    T_dif = (T_test) - (T);
    transitions_E_test =
abs(L*pi*(n_rotated(2,2)^3*q_rotated(2,2) -
n_rotated(3,3)^3*q_rotated(3,2))*(T_dif)/lambda)*180/pi/90;
    phase_change_E_test = transitions_E_test*pi/2;
    E_test =
lambda*phase_change_E_test/(L*pi*(n_rotated(2,2)^3*r_rotated(2,2)
- n_rotated(3,3)^3*r_rotated(3,2)));
    E_test_table(x,1) = abs(E_test);

    E = ((D2 - d(2,2)*T)/eps(2,2));
    E_table(x,1) = abs(E);
    E_table(x,1) = E;

    V(1,1) = 0;
    V(1,1) = abs(-(E_table(1,1))*1e-3*(transition_table(1,1) -
50));

    if x > 1
        V(x,1) = abs(-(E_table(x,1))*1e-3*(transition_table(x,1)
- transition_table(x-1,1)) + V(x-1,1));
    end

    E_table(x,1) = abs(E);


n_rotated(2,2)^3*(1 + p_rotated(2,2)*sum22)*sum32 +
n_rotated(3,3)^3*(sum22 + p_rotated(3,2)*sum22*sum32) ));
```

```
end


% E_estimates = fitcurve(transition_table(:,1),
E_table(:,1)/1e3/100)

%
% for x = 1:5
%     for y = 1:5
%         for z = 1:5
figure
% subplot(2,1,2)
plot(transition_table(:,1),E_table(:,1)/1e3/100,'o')
% hold on;
% plot(transition_table(:,1),E_test_table(:,1),'b')
hold on;
% plot(transition_table(:,1),abs(E_estimates(:,1) *
cos(E_estimates(:,2) * transition_table(:,1) + E_estimates(:,4))
+ E_estimates(:,3)),'r')
% plot(transition_table(:,1),abs(E_estimates(:,:,1) *
(E_estimates(:,:,2)*transition_table(:,1) +
E_estimates(:,:,4))^E_estimates(:,:,5) + E_estimates(:,:,3)))
grid on;
xlabel('Position (mm)')
ylabel('Longitudinal Electric Field (kV/cm)')
% legend('EO + PE','PE only');
xlim([transition_table(1,1) 100])

figure
% subplot(2,1,2)
plot(transition_table(:,1),V(:,1)/1e3,'o')
% hold on;
% plot(transition_table(:,1),E_test_table(:,1),'b')
hold on;
% plot(transition_table(:,1),abs(E_estimates(:,1) *
cos(E_estimates(:,2) * transition_table(:,1) + E_estimates(:,4))
+ E_estimates(:,3)),'r')
% plot(transition_table(:,1),abs(E_estimates(:,:,1) *
(E_estimates(:,:,2)*transition_table(:,1) +
E_estimates(:,:,4))^E_estimates(:,:,5) + E_estimates(:,:,3)))
grid on;
xlabel('Position (mm)')
ylabel('Longitudinal Electric Potential (kV)')
% legend('EO + PE','PE only');
xlim([transition_table(1,1) 100])

figure
% subplot(2,1,1)
plot(transition_table(:,1),T_table(:,1)/1e6,'o')
% hold on;
```

```matlab
% plot(transition_table(:,1),T_test_table(:,1),'b')
grid on;
xlabel('Position (mm)')
ylabel('Longitudinal Stress (MPa)')
% legend('EO + PE','PE only');
xlim([transition_table(1,1) 100])

figure
% subplot(2,1,1)
plot(transition_table(:,1),transition_table(:,2)/4,'o')
% hold on;
% plot(transition_table(:,1),T_test_table(:,1),'b')
grid on;
xlabel('Position (mm)')
ylabel('Number of  ^\pi/_2  Phase Changes')
% legend('EO + PE','PE only');
xlim([transition_table(1,1) 100])

T_table1(:,2) = T_table(:,1)/1e6;  % in MPa
T_table1(:,1) = transition_table(:,1);
% xlswrite('C:\Users\Jim\Documents\Papers\GRADUATE
RESEARCH\PhD\VanGordon PT Code\Least Squares Curve
Fitting\P6015A\stress.csv', T_table1)

E_table1(:,2) = E_table(:,1)/1e5;  % in kV/cm
E_table1(:,1) = transition_table(:,1);
% xlswrite('C:\Users\Jim\Documents\Papers\GRADUATE
RESEARCH\PhD\VanGordon PT Code\Least Squares Curve
Fitting\P6015A\efield.csv', E_table1)

Ebeam_data(:,1) = transition_table(:,1);
Ebeam_data(:,2) = T_table1(:,2);
Ebeam_data(:,3) = E_table1(:,2);
Ebeam_data(:,4) = V(:,1)/1e3;        % in kV
xlswrite('C:\Users\superPuTeR\Desktop\Jim\Least Squares Curve
Fitting\3-13-14 data\1e-4\1e-4_data.csv', Ebeam_data)
```

D. Matlab Code for Least Squares Curve Fitting

```
clear all;
close all;
clc;
tic;
pause(1);

%%%% simulation parameters
%%%%%%%%%%%%%%%%%%%%%%%%%%%%%%%%%%%%%%%%%%%
total_simulations=1;
generations_to_simulate=50;      %50
end_fitness=1e-5;                 %kunits  was 1e4
number_of_bugs=1000;            %400
show_figure=2;                  %0->nofigure,1->very small
figure, 2->full screen figure
parameter_variation=0.99;       %fraction allowed variability in
the parameters
number_of_shots=1;
%%%%%%%%%%%%%%%%%%%%%%%%%%%%%%%%%%%%%%%%%%%%%%%%%%%%%%%%%%%%%%%%%
%%%%%%%

%%%% swarm behavior parameters. Probably don't mess with.
accel_constant_1=3;             %between 0 and 4. This is
associated with personal best. Global is (4 - this number).
                                 %3 was better then 1.
inertia=0.5;                    %less than 1. big=explore,
small=smooth (0.5>0.8>0.2)
number_of_elements=5;           %parameters being varied
total_elements=8;               %total varied parameters and
constants
%%%%%%%%%%%%%%%%%%%%%%%%%%%%%%%%%%%%%%%%%%%%%%%%%%%%%%%%%%%%%%%%%
%%%%%%%%%

best_bugs=zeros(total_simulations,number_of_elements);
best_bugs_fitness=zeros(1,total_simulations);
shot_location='C:\Users\superPuTeR\Desktop\Jim\Least Squares
Curve Fitting\';
date = '3-13-14 data\';
voltage = '1e-4';
shot_location = strcat(shot_location,date,voltage,'\')
file_location = 'C:\\Users\superPuTeR\\Desktop\\Jim\\Least
Squares Curve Fitting\\';
file_location = strcat(file_location,date,'\',voltage,'\\');
estimated_charge_voltage=0;    %convert to equiv. total estimated
charge

simulation_number=1;
k=1;
```

```matlab
% temp0={'fitness' 'AGD' 'MUN' 'VT' 'CGS' 'MUP' 'TAU' 'COXD' 'KP'
'NB' 'THETA' 'RL' 'BVN' 'JSNE' 'AREA' 'KF' 'VTD' 'BVF' 'WB'
'Lstray1' 'Lstray2'};
temp0={'fitness' 'RL' 'CL' 'a' 'dielectric_loss_tangent_xy'
'dielectric_loss_tangent_z' 'Vin' 'Q' 'Vout'};

while simulation_number<total_simulations+1


[global_best_position,global_best_position_constants,global_best_
fitness1,global_best_shot_fitness]=calibration_script(simulation_
number,
generations_to_simulate,number_of_bugs,accel_constant_1,inertia,n
umber_of_elements,shot_location,file_location,show_figure,estimat
ed_charge_voltage,parameter_variation,end_fitness);
    l=1;
    while l<number_of_shots+1
        global_best_fitness(l,1)=global_best_fitness1;
        l=l+1;
    end


temp1=[global_best_shot_fitness,global_best_position,global_best_
position_constants];
        temp2(simulation_number+(k-
1)*number_of_shots:simulation_number+k*number_of_shots-
1,:)=temp1;
        w=1;
        while w<(total_elements + 2)
            temp3(simulation_number+(k-
1)*number_of_shots:simulation_number+k*number_of_shots-
1,w)=cellstr(num2str(temp2(simulation_number+(k-
1)*number_of_shots:simulation_number+k*number_of_shots-1,w)));
            w=w+1;
        end
        temp=[temp0;temp3];

    xlswrite(strcat(shot_location,voltage,' curve fitting
results.csv'), temp)
        %%%%%%%%%%%%%%%%%%%%%%%%%%%%%%%%%%%%%%

    simulation_number=simulation_number+1;
    k=k+1;
end

toc
```

```matlab
function
[global_best_position,global_best_position_constants,global_best_
fitness,global_best_shot_fitness]=calibration_script(simulation_n
umber,
generations_to_simulate,number_of_bugs,accel_constant_1,inertia,n
umber_of_elements,shot_location,file_location,show_figure,estimat
ed_charge_voltage,parameter_variation,end_fitness)



%*********************** Input Parameters
****************************

Vin_pk = 7.4;                                      %% amplitude of
input voltage sinusoid
                                                   %% 8.1 V for
ebeam
Q = 3255;                                          %% input Q-value


%*****************************************************************
**********



%%%%%%% CONTROL VARIABLES %%%%%%%%
file_name = strcat(shot_location,'1e-4_data.csv');
size_file=xlsread(file_name);
number_samples = numel(size_file(:,1));
samplerate=1.27;                                %sample rate for
simulations
simend=100;                                     %when do the
simulations stop?
training_simend=100;
train_on_stress=1;    %0-no, 1-yes
train_on_efield=1;
train_on_voltage=1;
training_weight=[1 1 1];   %weight to put on [stress efield
voltage];
%%%%%%%%%%%%%%%%%%%%%%%%%%%%%%%%%%%

% temp=size(training_shot);
number_of_shots=1;
shot_number=1;
position_offset=50;
V_charge=3e3;

%%%%%%% SET LIMITS FOR CIRCUIT ELEMENT VALUES %%%%%%%%
%   As with the bug_position and bug_velocity vectors, the
columns in the element_limits matrix are the
%   elements in the circuit model. The order and size is the same
in all three matrixes. The (2) rows in
```

```matlab
%   the element_limits matrix are:  1-  the upper limit of the
individual element value
%                                   2-  the lower limit of the
individual element value
element_limits=zeros(2*number_of_shots,number_of_elements);
%initialize the matrix


while shot_number<number_of_shots+1

    guess=1e9;  %RL  1
    element_limits(shot_number*2-1,1)= 250e9;  %guess/(1-
parameter_variation);         %upper limit of 1st element
    element_limits(shot_number*2,1)= guess*(1-
parameter_variation);           %lower limit of 1st element

    guess=0.1e-12;  %CL 2
    element_limits(shot_number*2-1,2)= 1e-13;         %upper
limit of 2nd element
    element_limits(shot_number*2,2)= 40e-15;          %lower
limit of 2nd element

    guess=0.33;  %a 3
    element_limits(shot_number*2-1,3)= 1;         %upper limit
of 3rd element
    element_limits(shot_number*2,3)= 1;          %lower limit
of 3rd element

    guess=5e-3;  %dielectric_loss_tangent_xy 4
    guess = 5e-4;
    element_limits(shot_number*2-1,4)= guess;         %upper
limit of 4th element
    element_limits(shot_number*2,4)= guess;          %lower
limit of 4th element

    guess=3.4e-3;  %dielectric_loss_tangent_z 5
    guess = 3.4e-4;
    element_limits(shot_number*2-1,5)= guess;         %upper
limit of 5th element
    element_limits(shot_number*2,5)= guess;          %lower
limit of 5th element


    %%%%%%%%%%%%%%%%%%%%%%%%%%%%%%%%%%%%%%%%%%%%%%%%%%%%%%%%%

    shot_number=shot_number+1;
end


%%%%%%%% USED BY PROGRAM %%%%%%%%
% Variable initialization
accel_constant_2=4-accel_constant_1;
```

```
bug_num=1;
global_best_position = zeros(number_of_shots,number_of_elements);
global_best_fitness = 1e30;
shot_fitness = zeros(number_of_shots,1);
global_best_shot_fitness = zeros(number_of_shots,1);
personal_best_position =
zeros(number_of_bugs*number_of_shots,number_of_elements);
personal_best_fitness(number_of_bugs,1) = 10e30;
personal_best_fitness(:,1) = 10e30;
bug_fitness(number_of_bugs,1) = 10e30;
xaxis=[samplerate:samplerate:simend];
%%%%%%%%%%%%%%%%%%%%%%%%%%%%%%%

%%%%%%%%%%%%%%%%%%%%%%%%%%%%%%%%%%%%%%%%%
%   Initialize the position and velocity for the bugs. The
velocity is zero and initialize_bugs takes care of the position.
bug_position =
zeros(number_of_bugs*number_of_shots,number_of_elements);
bug_position =
initialize_bugs(number_of_bugs,number_of_shots,element_limits);
bug_velocity =
zeros(number_of_bugs*number_of_shots,number_of_elements);
%%%%%%%%%%%%%%%%%%%%%%%%%%%%

% %%%% GET TEST DATA %%%%%%%%
shot_number=1;
% training_data_saved=zeros(number_samples,number_of_shots*4);
% size(training_data_saved);

training_data_saved_temp1=size_file;
% training_data_saved_temp2=xlsread('C:\Jim\shot7\2');
% training_data_saved_temp3=xlsread('C:\Jim\shot7\3');
% training_data_saved_temp4=xlsread('C:\Jim\shot7\4');
% training_data_saved_temp5=xlsread('C:\Jim\shot7\5');
% training_data_saved_temp6=xlsread('C:\Jim\shot7\6');
% training_data_saved_temp7=xlsread('C:\Jim\shot7\7');
% training_data_saved_temp8=xlsread('C:\Jim\shot7\8');
% training_data_saved_temp9=xlsread('C:\Jim\shot7\9');
% training_data_saved_temp10=xlsread('C:\Jim\shot7\10');

while shot_number<number_of_shots+1
    if shot_number==1
        n=1;
        while n<5
            training_data_saved(:,n+4*(shot_number-
1))=training_data_saved_temp1(:,n);
            n=n+1;
        end
    end
    if shot_number==2
        n=1;
        while n<5
```

```
            training_data_saved(:,n+4*(shot_number-
1))=training_data_saved_temp2(:,n);
            n=n+1;
        end
    end
    if shot_number==3
        n=1;
        while n<5
            training_data_saved(:,n+4*(shot_number-
1))=training_data_saved_temp3(:,n);
            n=n+1;
        end
    end
    if shot_number==4
        n=1;
        while n<5
            training_data_saved(:,n+4*(shot_number-
1))=training_data_saved_temp4(:,n);
            n=n+1;
        end
    end
    if shot_number==5
        n=1;
        while n<5
            training_data_saved(:,n+4*(shot_number-
1))=training_data_saved_temp5(:,n);
            n=n+1;
        end
    end
    if shot_number==6
        n=1;
        while n<5
            training_data_saved(:,n+4*(shot_number-
1))=training_data_saved_temp6(:,n);
            n=n+1;
        end
    end
    if shot_number==7
        n=1;
        while n<5
            training_data_saved(:,n+4*(shot_number-
1))=training_data_saved_temp7(:,n);
            n=n+1;
        end
    end
    if shot_number==8
        n=1;
        while n<5
            training_data_saved(:,n+4*(shot_number-
1))=training_data_saved_temp8(:,n);
            n=n+1;
        end
```

```
        end
    if shot_number==9
        n=1;
        while n<5
            training_data_saved(:,n+4*(shot_number-
1))=training_data_saved_temp9(:,n);
            n=n+1;
        end
    end
    if shot_number==10
        n=1;
        while n<5
            training_data_saved(:,n+4*(shot_number-
1))=training_data_saved_temp10(:,n);
            n=n+1;
        end
    end

    shot_number=shot_number+1;
end


%%%%%%%%%initialize all paramters being held
constant%%%%%%%%%%%%%%%%%%

num_constants=1;
bug_position1 =
zeros(number_of_bugs*number_of_shots,num_constants);

x=1;
while x < number_of_bugs*number_of_shots+1

    bug_position1(x,1)=Vin_pk;    %input voltage
    bug_position1(x,2)=Q;         %input Q-value
    bug_position1(x,3)=0;         %output voltage

    x=x+1;
end

% repeat for all generations

% Ebeam_data = csvread('C:\Users\Jim\Documents\Papers\GRADUATE
RESEARCH\PhD\VanGordon PT Code\Least Squares Curve
Fitting\Ebeam\Ebeam_data.csv')
% bug_position(1,1) = 25e9;  %R
% bug_position(1,2) = 4e-14;   %C
% bug_position(1,2) = 6.6e-12;
% bug_position(1,3) = 0.20909;  %a
% bug_position(2,1) = 91.2e9;
% bug_position(2,2) = 4.63e-14;
```

```
%************************ Material Constants
****************************
x_rotation_angle = 45;                          %% rotation for
z-cut PT in degrees
                                                %% rotation for
y-cut PT should be made accordingly
                                                %% (45 degree
rotated z-cut = 135 degree rotated y-cut)
y_rotation_angle = 0;                           %% rotation about
y-axis
z_rotation_angle = 0;                           %% rotation about
z-axis

length = 100e-3;                                %% length of PT
in meters
width = 1e-2;                                    %% width of PT in
meters
a = 50e-3;                                       %% length of
input electrode in meters
b = length - a;                                 %% position of
output electrode in meters
thick = 1.5e-3;                                 %% thickness of
PT in meters

rho = 4700;                                     %% mass density
in kg/m^3
                                                %% should be
4,700 kg/m^3 for LiNbO3

BD_dielectric = 150e6;                          %% dielectric
breakdown strength in V/m
                                                %% for LiNbO3
should be ~150 MV/m

T_max = 30 * 10^6;                              %% maximum stress
before crystal will fracture in Pa
                                                %% for LiNbO3
should be between 30 MPa and 120 MPa

c = zeros(6,6);                                 %% initialize
size of c              [N/m^2]
e = zeros(3,6);                                 %% initialize
size of e              [C/m^2]
eps_S = zeros(3,3);                             %% initialize
size of eps_S          [C/(V*m)] aka [F/m]
s = zeros(6,6);                                 %% initialize
size of s              [m^2/N]
d = zeros(3,6);                                 %% initialize
size of d              [C/N]
eps = zeros(3,3);                               %% initialize
size of eps            [C^2/(N*m^2)] aka [F/m]
```

237

```
r = zeros(6,3);                                 %% initialize
size of r                [m/V]
r_rotated = zeros(6,3);                         %% initialize
size of rotated r      [m/V]
p = zeros(6,6);                                 %% initialize
size of p                [unitless]
p_rotated = zeros(6,6);                         %% initialize
size of rotated p      [unitless]
n = zeros(3,3);                                 %% initialize
size of n                [unitless]
n_rotated = zeros(3,3);                         %% initialize
size of rotated n      [unitless]


% set up elastic constants in matrix "c"        %% for LiNb03
should be
c = [2.03   0.53  0.75   0.09  0     0;          %% 2.03   0.53
0.75   0.09  0      0
     0.53   2.03  0.75  -0.09  0     0;          %% 0.53   2.03
0.75  -0.09  0      0
     0.75   0.75  2.45   0     0     0;          %% 0.75   0.75
2.45   0     0      0
     0.09  -0.09  0      0.60  0     0;          %% 0.09  -0.09  0
0.60   0      0
     0      0     0      0     0.60  0.09;        %% 0      0      0
0     0.60   0.09
     0      0     0      0     0.09  0.75];       %% 0      0      0
0      0.09  0.75

 c = c * 10^11;                                  %% c = c * 10^11


% set up piezoelectric constants in matrix "e"  %% for LiNbO3
should be
e = [0        0     0      0     3.70  -2.50;     %% 0       0       0
0     3.70  -2.50
     -2.50  2.50  0      3.70  0     0;          %% -2.50   2.50   0
3.70  0      0
     0.20   0.20  1.30   0     0     0];         %% 0.20    0.20
1.30   0      0      0

e = e * 1;                                       %% e = e * 1


% set up dielectric constants in matrix "eps_S"
% this is for constant strain field             %% for LiNbO3
should be
eps_S = [38.9  0     0;                           %% 38.9  0      0
         0     38.9  0;                           %% 0      38.9  0
         0     0     25.7];                       %% 0      0
25.7
```

```matlab
eps_S = eps_S * 10^-11;                        %% eps_S = eps_S
* 10^-11

% set up dielectric constants in matrix "eps_T"
% this is for constant stress field            %% for LiNbO3
should be
eps_T = [85.2  0      0;                        %% 38.9  0      0
         0     85.2  0;                         %% 0     38.9  0
         0     0      28.7];                    %% 0     0
25.7

eps_T = eps_T * 8.85e-12;                       %% eps_S =
eps_S * 10^-11


% set up dielectric constants in matrix "n"    %% for LiNbO3
should be
n = [2.2910      0             0;               %% 2.2910   0
0
     0           2.2910        0;               %% 0
2.2910  0
     0           0             2.2005];         %% 0        0
2.2005

n = n * 1;                                      %% n = n * 1


% set up electro-optic constants in matrix "r"
% this is for constant strain field            %% for LiNbO3
should be
r = [0       -3.4    7.7;                       %% 0       -3.4
7.7
     0       3.4     7.7;                       %% 0       3.4
7.7
     0       0       28.8;                      %% 0       0
28.8
     0       18.2    0;                         %% 0       18.2
0
     18.2    0       0;                         %% 18.2    0
0
     -3.4    0       0];                        %% -3.4    0
0

r = r * 10^-12;                                 %% r = r * 10^-
12


% set up elastic constants in matrix "p"       %% for LiNb03
should be
p = [0.036  0.072   0.139   0.066   0       0;          %% 0.036
0.072   0.139   0.066   0       0
```

```
        0.072   0.036    0.139    -0.066  0         0;              %% 0.072
0.036   0.139   -0.066  0          0
        0.178   0.178    0.060    0        0        0;              %% 0.178
0.178   0.060   0          0        0
        0.154   -0.154   0         0.30     0        0;              %% 0.154
-0.154  0          0.30     0         0
        0        0        0         0         0.30     0.154;          %% 0
0        0        0         0.30     0.154
        0        0        0         0         0.066    -0.019];        %% 0
0        0        0         0.066    -0.019

 p = p * 1;                                                    %% p = p
* 1


 % rotate matrices accordingly and return matrices to be used in
calculations
 [s, d, eps, r_rotated, p_rotated, n_rotated, q_rotated] =
rotate3D_RSI_paper1(x_rotation_angle, y_rotation_angle,
z_rotation_angle, c, e, eps_T, r, p, n,
bug_position(bug_num,4),bug_position(bug_num,5), Q);
% s;
% d;
% eps;
% r_rotated;
% p_rotated;
% n_rotated;
% q_rotated;

%*****************************************************************
**********

generation=1;
while (generation<generations_to_simulate+1) &
(global_best_fitness > end_fitness)

    %%%%% simulate PT for all bugs %%%%%%%%%
    shot_number=1;
    while shot_number < number_of_shots+1
       bug_num=1;
       while bug_num < number_of_bugs+1

          % line below is for varying dielectric loss factor
%         [s, d, eps, r_rotated, p_rotated, n_rotated, q_rotated]
= rotate3D_RSI_paper1(x_rotation_angle, y_rotation_angle,
z_rotation_angle, c, e, eps_T, r, p, n,
bug_position(bug_num,4),bug_position(bug_num,5), Q);

        R = bug_position(bug_num,1);
        C = bug_position(bug_num,2);
%         R = 50e9;
%         C = 0.04e-12;
```

240

```matlab
        stress = zeros(number_samples:2);
        efield = zeros(number_samples:2);
        potential = zeros(number_samples:2);
        bug_file = zeros(number_samples,4);
        num = 1;

        % find f_operating
        %%%%%%%%%%%%%%%%%%%%%%%%%%%%%%%%%%%%%%%%%%%%%%%%%%%%%%%%%
        ZL = @(f) 1/(1/complex(R,0)+1/complex(0,-1/(2*pi*f*C)));
        j = complex(0,1);
        k22 = sqrt(d(2,2)^2/(s(2,2)*eps(2,2)));
        sbar = s(2,2)*(1-k22^2);
        dbar = d(2,2)*(1-1/k22^2);
        omega = @(f) 2*pi*f;
        k = @(f) omega(f)*sqrt(rho*s(2,2));
        kbar = @(f) omega(f)*sqrt(rho*sbar);

        delta = @(f) s(2,2)*kbar(f)*sin(kbar(f)*b)*cos(k(f)*a) +
sbar*k(f)*sin(k(f)*a)*cos(kbar(f)*b);
        alpha11 = @(f) -
1/(delta(f)*cos(k(f)*a))*sbar*cos(kbar(f)*b)*sin(k(f)*a)*(cos(k(f
)*a)-1) - 1/(k(f)*cos(k(f)*a));
        beta11 = @(f) 1/delta(f)*s(2,2)*sin(k(f)*a)*(1-
cos(kbar(f)*b));
        alpha12 = @(f)
1/delta(f)*sbar*cos(kbar(f)*b)*(cos(k(f)*a)-1);
        beta12 = @(f) -1/delta(f)*s(2,2)*cos(k(f)*a)*(1-
cos(kbar(f)*b));
        alpha22 = @(f)
1/delta(f)*sbar*sin(kbar(f)*b)*(cos(k(f)*a)-1);
        beta22 = @(f) -
1/(delta(f)*cos(kbar(f)*b))*s(2,2)*sin(kbar(f)*b)*cos(k(f)*a)*(1-
cos(kbar(f)*b)) + 1/(kbar(f)*cos(kbar(f)*b));


        gamma1 = @(f) 1/2 + d(3,2)/(thick*dbar)*(alpha12(f)*(1-
cos(kbar(f)*b))-alpha22(f)*sin(kbar(f)*b));
        Z2 = @(f) 1/((1-k22^2)*b)*(b-
beta22(f)*k22^2*sin(kbar(f)*b) + beta12(f)*k22^2*(1-
cos(kbar(f)*b)))*b/(j*omega(f)*eps(2,2)*width*thick);

        n_f = @(f) abs(gamma1(f)*ZL(f)/(ZL(f) + Z2(f)));

        f_operating = fminbnd(@(f) (-n_f(f)),50e3,80e3);
        %%%%%%%%%%%%%%%%%%%%%%%%%%%%%%%%%%%%%%%%%%%%%%%%%%%%%%%

        ZL = 1/(1/complex(R,0)+1/complex(0,-
1/(2*pi*f_operating*C)));


        lambda = 632.8e-9;
```

```matlab
        L = 1e-2;
        length_num = 1;


[Tin,Tout,voltage,E2,E3,Iin,Vout,Iout,f_resonant,xformer_ratio,Pout,Qout,Pin,Qin,Sin,Sout,gamma1] =
PT_solver(rho,s,d,eps,ZL,Vin_pk,f_operating,length,width,thick,a);


        for x = 1:number_samples
            l = training_data_saved(x,1)/1e3;  %  convert from mm
to m for T(l) and E(l)
            stress(length_num,1) = (l)*1e3;  % in mm
            stress(length_num,2) =
bug_position(bug_num,3)*abs(Tout(l - 0.05))/1e6;  % in MPa
            efield(length_num,1) = (l)*1e3;  % in mm
            efield(length_num,2) =
bug_position(bug_num,3)*abs(E2(l - 0.05))/1e5;  %  in kV/cm
            potential(length_num,1) = (l)*1e3;  % in mm
            potential(length_num,2) =
bug_position(bug_num,3)*abs(voltage(l - 0.05))/1e3;    %  in kV
            phi_EO(length_num,1) =
abs(L*pi*(n_rotated(2,2)^3*r_rotated(2,2) -
n_rotated(3,3)^3*r_rotated(3,2))*(E2(l))/lambda)*180/pi/90;
            phi_PE(length_num,1) =
abs(L*pi*(n_rotated(2,2)^3*q_rotated(2,2) -
n_rotated(3,3)^3*q_rotated(3,2))*(Tout(l))/lambda)*180/pi/90;
            phi_total(length_num,1) =
abs(L*pi*((E2(l))*(n_rotated(2,2)^3*r_rotated(2,2) -
n_rotated(3,3)^3*r_rotated(3,2)) +
(Tout(l))*(n_rotated(2,2)^3*q_rotated(2,2) -
n_rotated(3,3)^3*q_rotated(3,2)))/lambda)*180/pi/90;
            length_num = length_num + 1;
        end
%           l = training_data_saved(number_samples,1)/1e3;
%           potential(length_num-1,1) = (l)*1e3;  % in mm
%           potential(length_num-1,2) = abs(voltage(l))/1e3;
%  in kV

            bug_file(:,1) = stress(:,1);
            bug_file(:,2) = stress(:,2);
            bug_file(:,3) = efield(:,2);
            bug_file(:,4) = potential(:,2);

            file_name = strcat(file_location,sprintf('Bug
Files\\test%03d.csv', bug_num + number_of_bugs*(shot_number-1)));
            csvwrite(file_name, bug_file);

%                bug_num
            bug_num=bug_num+1;
        end
```

```matlab
        shot_number=shot_number+1;
    end


    %compare results for each bug
    bug_num=1;
    while bug_num<number_of_bugs+1

        bug_fitness=0;
        efield_residuals = 0;
        efield_total = 0;
        stress_residuals = 0;
        stress_total = 0;
        voltage_residuals = 0;
        voltage_total = 0;
        stress_R_squared = 0;
        efield_R_squared = 0;
        voltage_R_squared = 0;
        shot_number=1;
        shot_fitness = zeros(number_of_shots,1);

        while shot_number<number_of_shots+1
            file_name = strcat(file_location,sprintf('Bug
Files\\test%03d.csv', bug_num + number_of_bugs*(shot_number-1)));
            if exist(file_name)==0
                swarm_data = ones(20,4)*5e9;
                bad = 1

            else
                swarm_data = csvread(file_name);
                if size(swarm_data) == [0,0]
                    swarm_data = ones(20,4)*5e9;
                    fprintf('Error, file is empty.')
                end
                delete(file_name);    %HERE HERE HERE
            end

            stress_mean =
mean(training_data_saved(:,2+(shot_number-1)*4));
            efield_mean =
mean(training_data_saved(:,3+(shot_number-1)*4));
            voltage_mean =
mean(training_data_saved(:,4+(shot_number-1)*4));

            if train_on_stress==1
                bug_fitness = bug_fitness + sum((swarm_data(:,2)-
training_data_saved(:,2+(shot_number-
1)*4)).^2)*training_weight(1);
                shot_fitness(shot_number,1) =
shot_fitness(shot_number,1) + sum((swarm_data(:,2)-
training_data_saved(:,2+(shot_number-
1)*4)).^2)*training_weight(1);
```

```matlab
                stress_residuals = stress_residuals +
sum((swarm_data(:,2)-training_data_saved(:,2+(shot_number-
1)*4)).^2)*training_weight(1);
                stress_total = stress_total +
sum((training_data_saved(:,2+(shot_number-1)*4) -
stress_mean).^2)*training_weight(1);
            end
            if train_on_efield==1
                bug_fitness = bug_fitness + sum((swarm_data(:,3)-
training_data_saved(:,3+(shot_number-
1)*4)).^2)*training_weight(2);
                shot_fitness(shot_number,1) =
shot_fitness(shot_number,1) + sum((swarm_data(:,3)-
training_data_saved(:,3+(shot_number-
1)*4)).^2)*training_weight(2);
                efield_residuals = efield_residuals +
sum((swarm_data(:,3)-training_data_saved(:,3+(shot_number-
1)*4)).^2)*training_weight(2);
                efield_total = efield_total +
sum((training_data_saved(:,3+(shot_number-1)*4) -
efield_mean).^2)*training_weight(2);
            end
            if train_on_voltage==1
                bug_fitness = bug_fitness + sum((swarm_data(:,4)-
training_data_saved(:,4+(shot_number-
1)*4)).^2)*training_weight(3);
                shot_fitness(shot_number,1) =
shot_fitness(shot_number,1) + sum((swarm_data(:,4)-
training_data_saved(:,4+(shot_number-
1)*4)).^2)*training_weight(3);
                voltage_residuals = voltage_residuals +
sum((swarm_data(:,4)-training_data_saved(:,4+(shot_number-
1)*4)).^2)*training_weight(3);
                voltage_total = voltage_total +
sum((training_data_saved(:,4+(shot_number-1)*4) -
voltage_mean).^2)*training_weight(3);
            end

            stress_R_squared = 1 - stress_residuals/stress_total;
            efield_R_squared = 1 - efield_residuals/efield_total;
            voltage_R_squared = 1 -
voltage_residuals/voltage_total;

            shot_number=shot_number+1;
        end


        %is it a personal best?
        if bug_fitness< personal_best_fitness(bug_num,1)
            personal_best_fitness(bug_num,1)=bug_fitness;
```

```
            shot_number=1;
            while shot_number<number_of_shots+1
                personal_best_position(bug_num +
number_of_bugs*(shot_number-1),:)=bug_position(bug_num +
number_of_bugs*(shot_number-1),:);
                shot_number=shot_number+1;
            end
        end;

        %is it a global best?
        if bug_fitness < global_best_fitness
            global_best_fitness=bug_fitness;
            shot_number=1;
            while shot_number<number_of_shots+1

global_best_position(shot_number,:)=bug_position(bug_num+number_o
f_bugs*(shot_number-1),:);

global_best_position_constants(shot_number,:)=bug_position1(bug_n
um+number_of_bugs*(shot_number-1),:);
                global_best_shot_fitness = shot_fitness;
                global_best_voltage =
swarm_data(number_samples,4);

global_best_position_constants(shot_number,3)=global_best_voltage
;
                global_best_stress_R_squared = stress_R_squared;
                global_best_efield_R_squared = efield_R_squared;
                global_best_voltage_R_squared =
voltage_R_squared;
                shot_number=shot_number+1;
            end
        end

        %the "two equations" for swarm optimization. update
velocity and position
        shot_number=1;
        while shot_number < number_of_shots+1
            bug_velocity(bug_num+number_of_bugs*(shot_number-
1),:)= bug_velocity(bug_num+number_of_bugs*(shot_number-
1),:)*inertia +
rand(1)*accel_constant_1*(personal_best_position(bug_num+number_o
f_bugs*(shot_number-1),:)-
bug_position(bug_num+number_of_bugs*(shot_number-1),:)) +
rand(1)*accel_constant_2*(global_best_position(shot_number,:)-
bug_position(bug_num+number_of_bugs*(shot_number-1),:));
            bug_velocity(bug_num+number_of_bugs*(shot_number-
1),:)=
constrain_velocity(bug_velocity,element_limits,bug_num,shot_numbe
r,number_of_bugs);
            shot_number=shot_number+1;
        end
```

```
        shot_number=1;
        while shot_number < number_of_shots+1
            bug_position(bug_num+number_of_bugs*(shot_number-
1),:)= bug_position(bug_num+number_of_bugs*(shot_number-1),:) +
bug_velocity(bug_num+number_of_bugs*(shot_number-1),:);
            [bug_position(bug_num+number_of_bugs*(shot_number-
1),:),element_limits]=
constrain_position(bug_position,element_limits,bug_num,shot_numbe
r,number_of_bugs);
            shot_number=shot_number+1;
        end

        %output to screen
            simulation_number
            generation
            bug_num
            global_best_fitness

        bug_num=bug_num+1;
    end;



    close all;

    shot_number=1;
    while shot_number<number_of_shots+1

        %Offset and get training data %%%%
        training_data_saved_temp=zeros(number_samples,4);
        k=1;
        while k<5
%
training_data_saved_temp(:,n)=training_data_saved(:,n+4*(shot_num
ber-1));

training_data(:,k)=training_data_saved(:,k+4*(shot_number-1));
            k=k+1;
        end
%
training_data=offset_training_data(training_data_saved_temp,globa
l_best_position,shot_number,simend,samplerate,1,number_of_bugs);
        %%%%%%%%%%%%%%%%%%%%%%%%%

        % line below is for varying dielectric loss factor
%        [s, d, eps, r_rotated, p_rotated, n_rotated, q_rotated]
= rotate3D_RSI_paper1(x_rotation_angle, y_rotation_angle,
z_rotation_angle, c, e, eps_T, r, p, n,
global_best_position(shot_number,4),
global_best_position(shot_number,5), Q);
```

```
        swarm_data1 =
simulation(shot_location,file_location,global_best_position,globa
l_best_position_constants,1,number_samples,1,shot_number,training
_data_saved,rho,s,d,eps,ZL,Vin_pk,f_operating,length,width,thick,
a,b,r_rotated,p_rotated,n_rotated,q_rotated);

        global_best_fitness
        global_best_voltage
        R = global_best_position(shot_number,1)
        C = global_best_position(shot_number,2)
        a1 = global_best_position(shot_number,3);
        diel_const_xy = global_best_position(shot_number,4);
        diel_const_z = global_best_position(shot_number,5);
        global_best_stress_R_squared
        global_best_efield_R_squared
        global_best_voltage_R_squared



        if show_figure==0
            if train_on_voltage==1
                figure
                plot(swarm_data1(:,1),swarm_data1(:,4)/a1,'b')
                hold on;
                grid on;
                plot(training_data(:,1),training_data(:,4),'ro')
%                 legend('Swarm Solution','X-Ray Data')
                xlabel('Position (mm)')
                ylabel('Voltage (kV)')
                title('PT Output Voltage')
                axis([position_offset  simend
0.5*min(training_data(:,4))  2*max(training_data(:,4))])
                text(0,-
max(training_data(:,4))/7,strcat(mat2str(global_best_shot_fitness
(shot_number,1)/1e8,4), ' e8'))
                text(0,-
max(training_data(:,4))/4,mat2str(global_best_position(shot_numbe
r,:),3))
            end;

            pause(1);   %pause for a second

        else
            % Output best swarm solution so far and compare to
the training data

%             figure;
%             temp=get(0,'ScreenSize');
%             if show_figure==1
%                 set(gcf,'Position',[1 1 10 10])
%             else
```

```matlab
%                   set(gcf,'Position',[10 10 temp(3)*.8
temp(4)*.8])
%               end

            if train_on_stress==1
%                   subplot(2,2,1)
                figure
%                 fig = figure;
%
set(fig,'units','normalized','outerposition',[0.5 0 0.5 1]);
                plot(swarm_data1(:,1),swarm_data1(:,2)/a1,'b')
                hold on;
                grid on;
                plot(training_data(:,1),training_data(:,2),'ro')
                legend('Swarm Solution','Optical Data')
                xlabel('Position (mm)')
                ylabel('Stress (MPa)')
                title('Longitudinal Stress')
                axis([position_offset  simend
0.5*min(training_data(:,2))  2*max(training_data(:,2))])
            end

            if train_on_efield==1
%                   subplot(2,2,2)
                figure
%                 fig = figure;
%                 set(fig,'units','normalized','outerposition',[0
0 0.5 1]);
                plot(swarm_data1(:,1),swarm_data1(:,3)/a1,'b')
                hold on;
                grid on;
                plot(training_data(:,1),training_data(:,3),'ro')
                legend('Swarm Solution','Optical Data')
                xlabel('Position (mm)')
                ylabel('Electric Field (kV/cm)')
                title('Longitudinal Electric Field')
                axis([position_offset  simend
0.5*min(training_data(:,3))  2*max(training_data(:,3))])
            end;

            if train_on_voltage==1
%                   subplot(2,2,3)
                figure
%                 fig = figure;
%                 set(fig,'units','normalized','outerposition',[0
0 1 1]);
                plot(swarm_data1(:,1),swarm_data1(:,4)/a1,'b')
                hold on;
                grid on;
                plot(training_data(:,1),training_data(:,4),'ro')
%                 legend('Swarm Solution','X-Ray Data')
                xlabel('Position (mm)')
```

```matlab
                ylabel('Voltage (kV)')
                title('PT Output Voltage')
                axis([position_offset  simend
0.5*min(training_data(:,4))  2*max(training_data(:,4))])
                text(0,-
max(training_data(:,4))/7,strcat(mat2str(global_best_shot_fitness
(shot_number,1)/1e8,4), ' e8'))
                text(0,-
max(training_data(:,4))/4,mat2str(global_best_position(shot_numbe
r,:),3))
            end;


        pause(1);    %pause for a second
    end

    output_file_name =
strcat(strcat(shot_location,'training'),num2str(shot_number),'.cs
v');
    csvwrite(output_file_name, training_data);
    output_file_name =
strcat(strcat(shot_location,'swarm'),num2str(shot_number),'.csv')
;
    csvwrite(output_file_name, swarm_data1);

%
save(strcat('C:\Jim\training',num2str(shot_number),'.tab'),'train
ing_data','-tabs','-ascii');
%
save(strcat('C:\Jim\swarm',num2str(shot_number),'.tab'),'swarm_da
ta1','-tabs','-ascii');

    shot_number=shot_number+1;
    end



    generation;
    generation=generation+1;
end;
```

```
function bug_position =
initialize_bugs(number_of_bugs,number_of_shots,element_limits)
% This function initializes the bug positions. The method we
chose is to randomly
% choose values between the predefined limits. The returned
vector is the initialized
% positions.

temp=size(element_limits);
number_of_elements=temp(2);
bug_position(number_of_bugs*number_of_shots,number_of_elements)=0
;
%
bug_position2(number_of_bugs*number_of_shots,number_of_elements)=
0;
%
% VT = [12 12 12 12];  %added
% TAU = [2e-5 2e-5 2e-5 2e-5];  %added
% NB = [2e15 2e15 2e15 2e15];  %added
% THETA = [0.5 0.5 0.5 0.5];  %added

shot_number=1;
while shot_number<number_of_shots+1

    bug_num=1;
    while bug_num<number_of_bugs+1
        %Do for every element in the row
        n=1;
        while n < number_of_elements+1
            bug_position(bug_num +(shot_number-
1)*number_of_bugs,n)=unifrnd(element_limits(shot_number*2,n),elem
ent_limits(shot_number*2-1,n));
            n=n+1;
        end;
%
%           n=1;
%           bug_position2(bug_num +(shot_number-
1)*number_of_bugs,n)=unifrnd(element_limits(shot_number*2,n),bug_
position2(bug_num,6));
%
%           n=3;  %added
%           random_num=randi([1 4],1,1,'double');  %added
%           bug_position2(bug_num +(shot_number-
1)*number_of_bugs,n)= VT(1, random_num);  %added
%
%           n=6;  %added
%           random_num=randi([1 4],1,1,'double');  %added
%           bug_position2(bug_num +(shot_number-
1)*number_of_bugs,n)= TAU(1, random_num);  %added
%
%           n=9;  %added
%           random_num=randi([1 4],1,1,'double');  %added
```

```
%           bug_position2(bug_num +(shot_number-
1)*number_of_bugs,n)= NB(1, random_num);  %added
%
%           n=10;  %added
%           random_num=randi([1 4],1,1,'double');  %added
%           bug_position2(bug_num +(shot_number-
1)*number_of_bugs,n)= THETA(1, random_num);  %added
%

        bug_num=bug_num+1;
    end;

    shot_number=shot_number+1;
end
% bug_position=bug_position2;
```

```
function
temp1=constrain_velocity(bug_velocity,element_limits,bug_num,shot
_number,number_of_bugs)


temp=size(element_limits);
number_of_elements=temp(2);


element_num=1;
while element_num <number_of_elements + 1

    lowerl=element_limits(shot_number*2,element_num);
    upperl=element_limits(shot_number*2-1,element_num);

    if bug_velocity(bug_num+number_of_bugs*(shot_number-
1),element_num)>lowerl*10^(log10(upperl/lowerl)/3)
        bug_velocity(bug_num+number_of_bugs*(shot_number-
1),element_num)=lowerl*10^(log10(upperl/lowerl)/3);
    end;
    if bug_velocity(bug_num+number_of_bugs*(shot_number-
1),element_num)<-lowerl*10^(log10(upperl/lowerl)/3)
        bug_velocity(bug_num+number_of_bugs*(shot_number-
1),element_num)=-lowerl*10^(log10(upperl/lowerl)/3);
    end;

    element_num=element_num+1;
end;

temp1=bug_velocity(bug_num+number_of_bugs*(shot_number-1),:);
```

```
function
[temp1,element_limits]=constrain_position(bug_position,element_li
mits,bug_num,shot_number,number_of_bugs)

temp=size(element_limits);
number_of_elements=temp(2);

    element_num=1;
    while element_num <number_of_elements+1

        if bug_position(bug_num+number_of_bugs*(shot_number-
1),element_num)>element_limits(shot_number*2-1,element_num)
            bug_position(bug_num+number_of_bugs*(shot_number-
1),element_num)=element_limits(shot_number*2-1,element_num);
        end;

        if bug_position(bug_num+number_of_bugs*(shot_number-
1),element_num)<element_limits(shot_number*2,element_num)
            bug_position(bug_num+number_of_bugs*(shot_number-
1),element_num)=element_limits(shot_number*2,element_num);
        end;

        element_num=element_num+1;
    end;


    if bug_position(bug_num+number_of_bugs*(shot_number-
1),1)>element_limits(shot_number*2-1,1)
        bug_position(bug_num+number_of_bugs*(shot_number-
1),1)=element_limits(shot_number*2-1,1);
    end;

    temp1=bug_position(bug_num+number_of_bugs*(shot_number-1),:);
```

```
function sim_data =
simulation(shot_location,file_location,bug_position,bug_position1
,bug_num,number_samples,number_of_bugs,shot_number,training_data_
saved,rho,s,d,eps,ZL,Vin_pk,f_operating,length,width,thick,a,b,r_
rotated,p_rotated,n_rotated,q_rotated)

        R = bug_position(bug_num,1);
        C = bug_position(bug_num,2);
        Vin_pk = bug_position1(bug_num,1);

        matrix = zeros(2500*5:10);
        stress = zeros(101:2);
        efield = zeros(101:2);
        potential = zeros(101:2);
        num = 1;

        % find f_operating
        %%%%%%%%%%%%%%%%%%%%%%%%%%%%%%%%%%%%%%%%%%%%%%%%%%%%%%%%%%%
%         ZL = @(f) 1/(1/complex(R,0)+1/complex(0,-
1/(2*pi*f*C)));
        ZL = @(f) 1/(1/complex(R,0)+1/complex(0,-1/(2*pi*f*C)));
%         ZL = @(f) R;
        j = complex(0,1);
        k22 = sqrt(d(2,2)^2/(s(2,2)*eps(2,2)));
        sbar = s(2,2)*(1-k22^2);
        dbar = d(2,2)*(1-1/k22^2);
        omega = @(f) 2*pi*f;
        k = @(f) omega(f)*sqrt(rho*s(2,2));
        kbar = @(f) omega(f)*sqrt(rho*sbar);

        delta = @(f) s(2,2)*kbar(f)*sin(kbar(f)*b)*cos(k(f)*a) +
sbar*k(f)*sin(k(f)*a)*cos(kbar(f)*b);
        alpha11 = @(f) -
1/(delta(f)*cos(k(f)*a))*sbar*cos(kbar(f)*b)*sin(k(f)*a)*(cos(k(f
)*a)-1) - 1/(k(f)*cos(k(f)*a));
        beta11 = @(f) 1/delta(f)*s(2,2)*sin(k(f)*a)*(1-
cos(kbar(f)*b));
        alpha12 = @(f)
1/delta(f)*sbar*cos(kbar(f)*b)*(cos(k(f)*a)-1);
        beta12 = @(f) -1/delta(f)*s(2,2)*cos(k(f)*a)*(1-
cos(kbar(f)*b));
        alpha22 = @(f)
1/delta(f)*sbar*sin(kbar(f)*b)*(cos(k(f)*a)-1);
        beta22 = @(f) -
1/(delta(f)*cos(kbar(f)*b))*s(2,2)*sin(kbar(f)*b)*cos(k(f)*a)*(1-
cos(kbar(f)*b)) + 1/(kbar(f)*cos(kbar(f)*b));


        gamma1 = @(f) 1/2 + d(3,2)/(thick*dbar)*(alpha12(f)*(1-
cos(kbar(f)*b))-alpha22(f)*sin(kbar(f)*b));
```

```matlab
        Z2 = @(f) 1/((1-k22^2)*b)*(b-
beta22(f)*k22^2*sin(kbar(f)*b) + beta12(f)*k22^2*(1-
cos(kbar(f)*b)))*b/(j*omega(f)*eps(2,2)*width*thick);

        n_f = @(f) abs(gamma1(f)*ZL(f)/(ZL(f) + Z2(f)));

        f_operating = fminbnd(@(f) (-n_f(f)),50e3,80e3);
        %%%%%%%%%%%%%%%%%%%%%%%%%%%%%%%%%%%%%%%%%%%%%%%%%%

%         ZL = 1/(1/complex(R,0)+1/complex(0,-
1/(2*pi*f_operating*C)));
        ZL = 1/(1/complex(R,0)+1/complex(0,-
1/(2*pi*f_operating*C)));
%          ZL = R;

        lambda = 632.8e-9;
        L = 1e-2;
        length_num = 1;


[Tin,Tout,voltage,E2,E3,Iin,Vout,Iout,f_resonant,xformer_ratio,Po
ut,Qout,Pin,Qin,Sin,Sout,gamma1] =
PT_solver(rho,s,d,eps,ZL,Vin_pk,f_operating,length,width,thick,a)
;


        for x = 1:number_samples
            l = training_data_saved(x,1)/1e3;  %  convert from mm
to m for T(l) and E(l)
            stress(length_num,1) = (l)*1e3;  % in mm
            stress(length_num,2) = abs(Tout(l - 0.05))/1e6;  % in
MPa
            efield(length_num,1) = (l)*1e3;  % in mm
            efield(length_num,2) = abs(E2(l - 0.05))/1e5;  %  in
kV/cm
            potential(length_num,1) = (l)*1e3;  % in mm
            potential(length_num,2) = abs(voltage(l - 0.05))/1e3;
%  in kV
            phi_EO(length_num,1) =
abs(L*pi*(n_rotated(2,2)^3*r_rotated(2,2) -
n_rotated(3,3)^3*r_rotated(3,2))*(E2(l))/lambda)*180/pi/90;
            phi_PE(length_num,1) =
abs(L*pi*(n_rotated(2,2)^3*q_rotated(2,2) -
n_rotated(3,3)^3*q_rotated(3,2))*(Tout(l))/lambda)*180/pi/90;
            phi_total(length_num,1) =
abs(L*pi*((E2(l))*(n_rotated(2,2)^3*r_rotated(2,2) -
n_rotated(3,3)^3*r_rotated(3,2)) +
(Tout(l))*(n_rotated(2,2)^3*q_rotated(2,2) -
n_rotated(3,3)^3*q_rotated(3,2)))/lambda)*180/pi/90;
            length_num = length_num + 1;
        end
%             l = training_data_saved(number_samples,1)/1e3;
```

255

```
%              potential(length_num-1,1) = (l)*1e3;   % in mm
%              potential(length_num-1,2) = abs(voltage(l))/1e3;
%  in kV

           bug_file(:,1) = stress(:,1);
           bug_file(:,2) = stress(:,2);
           bug_file(:,3) = efield(:,2);
           bug_file(:,4) = potential(:,2);

           file_name = strcat(file_location,sprintf('Bug
Files\\test_final.csv', bug_num + number_of_bugs*(shot_number-
1)));
           csvwrite(file_name, bug_file);




if exist(strcat(shot_location,'Bug Files\test_final.csv'))==0
    sim_data = ones(2500,4)*5e9;
    bad = 1

else
    sim_data = csvread(strcat(shot_location,'Bug
Files\test_final.csv'));

    if size(sim_data) == [number_samples,4]
    else
        sim_data = ones(2500,4)*5e9;
        bad = 2

    end
end

delete(file_name);
```

Bibliography

[1]   R. Talman, *Accelerator X-Ray Sources*. John Wiley & Sons, 2007.

[2]   J. Faure, Y. Glinec, A. Pukhov, S. Kiselev, S. Gordienko, E. Lefebvre, J.-P. Rousseau, F. Burgy, and V. Malka, "A laser–plasma accelerator producing monoenergetic electron beams," *Nature*, vol. 431, no. 7008, pp. 541–544, Sep. 2004.

[3]   B. Wolf, *Handbook of Ion Sources*. CRC Press, 1995.

[4]   R. C. Runkle, T. A. White, E. A. Miller, J. A. Caggiano, and B. A. Collins, "Photon and neutron interrogation techniques for chemical explosives detection in air cargo: A critical review," *Nuclear Instruments and Methods in Physics Research Section A: Accelerators, Spectrometers, Detectors and Associated Equipment*, vol. 603, no. 3, pp. 510–528, May 2009.

[5]   ATLAS Collaboration, "Observation of a new particle in the search for the Standard Model Higgs boson with the ATLAS detector at the LHC," *Physics Letters B*, vol. 716, no. 1, pp. 1–29, Sep. 2012.

[6]   D. A. Jaffray, J. J. Battista, A. Fenster, and P. Munro, "X - ray sources of medical linear accelerators: Focal and extra - focal radiation," *Medical Physics*, vol. 20, no. 5, pp. 1417–1427, Sep. 1993.

[7]   B. K. Das and A. Shyam, "Development of compact size penning ion source for compact neutron generator," *Review of Scientific Instruments*, vol. 79, no. 12, pp. 123305 –123305–4, Dec. 2008.

[8]   M. F. Hawthorne, "The Role of Chemistry in the Development of Boron Neutron Capture Therapy of Cancer," *Angew. Chem. Int. Ed. Engl.*, vol. 32, no. 7, pp. 950–984, Jul. 1993.

[9]   Jiashi Yang, *An Introduction to the Theory of Piezoelectricity*. New York: Springer, 2005.

[10] Jiashi Yang, *Analysis of Piezoelectric Devices*. New Jersey: World Scientific, 2006.

[11] J. W. Judy, D. L. Polla, and W. P. Robbins, "A linear piezoelectric stepper motor with submicrometer step size and centimeter travel range," *IEEE Trans. Ultrason., Ferroelectr., Freq. Control*, vol. 37, no. 5, pp. 428–437, 1990.

[12] D. Kalamatianos, P. E. Wellstead, J. M. Edmunds, and P. Liatsis, "Active alignment for two-beam interferometers," *Rev. Sci. Instrum.*, vol. 77, no. 1, pp. 013103–013103–13, 2006.

[13] T.-J. Liu, "A Smart Translation From the Response of the Piezoelectric Transducer to a Real-Time Ventilating Signal for the Release of Cooking Fumes," *IEEE Sensors J.*, vol. 7, no. 2, pp. 197–203, 2007.

[14] C. S. Lynch, "Strain compensated thin film stress gauges for stress wave measurements in the presence of lateral strain," *Rev. Sci. Instrum.*, vol. 66, no. 12, pp. 5582–5589, 1995.

[15] C. Rosen, "Analysis and Design of Ceramic Transformers and Filter Elements," Ph.D. Dissertation, Syracuse University, Syracuse, New York, 1956.

[16] C. Rosen, "Analysis And Design Of Ceramic Transformers And Filter Elements," Syracuse University, 1956.

[17] Jiashi Yang, "Piezoelectric transformer structural modeling - a review," *Ultrasonics, Ferroelectrics and Frequency Control, IEEE Transactions on*, vol. 54, no. 6, pp. 1154–1170, Jun. 2007.

[18] M. A. Kemp, "The ferroelectric plasma thruster," Ph.D. Dissertation, University of Missouri, 2008.

[19] A. Benwell, "A high voltage piezoelectric transformer for active interrogation," Doctor of Philosophy, University of Missouri, Columbia, MO USA, 2009.

[20] B. B. Gall, "Investigation and Optimization of a High Voltage Piezoelectric Particle Accelerator," Master of Science thesis, University of Missouri, Columbia, MO USA, 2012.

[21]   J. A. VanGordon, B. B. Gall, S. D. Kovaleski, E. A. Baxter, R. Almeida, and J. W. Kwon, "High voltage production from shaped piezoelectric transformers and piezoelectric transformer based circuits," in *Power Modulator and High Voltage Conference (IPMHVC), 2010 IEEE International*, 2010, pp. 334–337.

[22]   J. A. VanGordon, B. B. Gall, S. D. Kovaleski, E. A. Baxter, B. H. Kim, J. W. Kwon, and G. E. Dale, "Electrical analysis of piezoelectric transformers and associated high-voltage output circuits," in *Pulsed Power Conference (PPC), 2011 IEEE*, 2011, pp. 475 –479.

[23]   A. Benwell, S. Kovaleski, and M. Kemp, "A resonantly driven piezoelectric transformer for high voltage generation," in *IEEE International Power Modulators and High Voltage Conference, Proceedings of the 2008*, 2008, pp. 113 –116.

[24]   A. Benwell, S. Kovaleski, T. Wacharasindhu, J. W. Kwon, and E. Baxter, "Flashover prevention of high voltage piezoelectric transformers," in *Pulsed Power Conference, 2009. PPC '09. IEEE*, 2009, pp. 1112 –1115.

[25]   Yu-Hsiang Hsu, Chih-Kung Lee, and Wen-Hsin Hsiao, "Electrical and mechanical fully coupled theory and experimental verification of Rosen-type piezoelectric transformers," *Ultrasonics, Ferroelectrics and Frequency Control, IEEE Transactions on*, vol. 52, no. 10, pp. 1829–1839, 2005.

[26]   A. Benwell, M. Kemp, and S. Kovaleski, "A High-Voltage Piezoelectric Transformer for Active Interrogation," *Journal of Nuclear Materials Management*, vol. 37, no. 1, pp. 42–47, 2008.

[27]   B. Gall, S. D. Kovaleski, J. A. VanGordon, P. Norgard, A. Benwell, B. H. Kim, J. W. Kwon, and G. E. Dale, "Investigation of the Piezoelectric Effect as a Means to Generate X-Rays," *IEEE Trans. Plasma Sci.*, vol. 41, no. 1, pp. 106 –111, Jan. 2013.

[28]   J. S. Yang and X. Zhang, "Extensional vibration of a nonuniform piezoceramic rod and high voltage generation," *International Journal of Applied Electromagnetics and Mechanics*, vol. 16, pp. 29–42, 2002.

[29]   G. Ivensky, I. Zafrany, and S. Ben-Yaakov, "Generic operational characteristics of piezoelectric transformers," *IEEE Trans. Power Electron.*, vol. 17, no. 6, pp. 1049–1057, 2002.

[30]   Kuo-Tsai Chang, "Effects of load resistances on step-up voltage gains of Rosen-type piezoelectric transformer," in *Industrial Technology, 2005. ICIT 2005. IEEE International Conference on*, 2005, pp. 1080–1085.

[31]   M. Quillec, *Materials for optoelectronics*. Boston: Kluwer Academic Publishers, 1996.

[32]   R. W. Boyd, *Nonlinear Optics*. Academic Press, 2008.

[33]   M. Bass, C. DeCusatis, J. Enoch, V. Lakshminarayanan, G. Li, C. MacDonald, V. Mahajan, and E. V. Stryland, *Handbook of Optics, Third Edition Volume V: Atmospheric Optics, Modulators, Fiber Optics, X-Ray and Neutron Optics*. McGraw Hill Professional, 2009.

[34]   T. S. Narasimhamurty, *Photoelastic and electro-optic properties of crystals*. Plenum Press, 1981.

[35]   A. Garzarella, S. B. Qadri, T. J. Wieting, and D. H. Wu, "Piezo-induced sensitivity enhancements in electro-optic field sensors," *J. Appl. Phys.*, vol. 98, no. 4, pp. 043113–043113–6, 2005.

[36]   P. Norgard and S. Kovaleski, "An electrooptic probe to determine internal electric fields in a piezoelectric transformer," *Rev. Sci. Instrum.*, vol. 83, no. 2, pp. 025106–025106–7, 2012.

[37]   Wolfram, *Mathematica 7*. 2008.

[38]   *COMSOL Multiphysics*. COMSOL, 2013.

[39]   J. F. Nye, *Physical Properties of Crystals: Their Representation by Tensors and Matrices*. Clarendon Press, 1957.

[40]   R. S. Weis and T. K. Gaylord, "Lithium niobate: Summary of physical properties and crystal structure," *Appl. Phys. A*, vol. 37, no. 4, pp. 191–203, Aug. 1985.

[41]   "IEEE Standard on Piezoelectricity," *ANSI/IEEE Std 176-1987*, 1988.

[42] K. Nakamura and Y. Adachi, "Piezoelectric transformers using LiNbO3 single crystals," *Electron. Comm. Jpn. 3*, vol. 81, no. 7, pp. 1–6, 1998.

[43] P. C. Chou, *Elasticity: tensor, dyadic, and engineering approaches*. Princeton, N.J: Van Nostrand, 1967.

[44] M. H. Sadd, *Elasticity: Theory, Applications, and Numerics*. Academic Press, 2009.

[45] A. V. Mezheritsky, "Elastic, dielectric, and piezoelectric losses in piezoceramics: how it works all together," *IEEE Trans. Ultrason., Ferroelectr., Freq. Control*, vol. 51, no. 6, pp. 695–707, 2004.

[46] J. R. Teague, R. R. Rice, and R. Gerson, "High‑frequency dielectric measurements on electro‑optic single crystals," *Journal of Applied Physics*, vol. 46, no. 7, pp. 2864–2866, Sep. 2008.

[47] K. Nassau, H. J. Levinstein, and G. M. Loiacono, "Ferroelectric lithium niobate. 2. Preparation of single domain crystals," *Journal of Physics and Chemistry of Solids*, vol. 27, no. 6–7, pp. 989–996, Jun. 1966.

[48] F. T. Ulaby, E. Michielssen, and U. Ravaioli, *Fundamentals of applied electromagnetics*, 6th ed. Boston: Prentice Hall, 2010.

[49] K. Uchino and S. Hirose, "Loss mechanisms in piezoelectrics: how to measure different losses separately," *IEEE Transactions on Ultrasonics, Ferroelectrics and Frequency Control*, vol. 48, no. 1, pp. 307–321, Jan. 2001.

[50] K. Wong, *Properties of Lithium Niobate*. London: INSPEC, 2002.

[51] B. Gall, S. D. Kovaleski, J. A. VanGordon, P. Norgard, B. Kim, J. W. Kwon, and G. E. Dale, "High voltage piezoelectric system for generating neutrons," in *2013 19th IEEE Pulsed Power Conference (PPC)*, 2013, pp. 1–5.

[52] J. M. Lafferty, Ed., *Foundations of vacuum science and technology*. New York: Wiley, 1998.

[53] R. Jenkins, R. W. Gould, and D. Gedcke, *Quantitative x-ray spectrometry*. New York: M. Dekker, 1981.

[54]   G. Zschornack, *Handbook of X-ray data*. New York: Springer, 2006.

[55]   G. F. Knoll, *Radiation detection and measurement*. Oxford: Wiley & Son, 2010.

[56]   W. D. Ehmann and D. E. Vance, *Radiochemistry and nuclear methods of analysis*. New York: Wiley, 1991.

[57]   L. A. Currie, "Limits for qualitative detection and quantitative determination. Application to radiochemistry," *Anal. Chem.*, vol. 40, no. 3, pp. 586–593, Mar. 1968.

[58]   J. A. VanGordon, S. D. Kovaleski, P. Norgard, B. B. Gall, and G. E. Dale, "Measurement of the internal stress and electric field in a resonating piezoelectric transformer for high-voltage applications using the electro-optic and photoelastic effects," *Review of Scientific Instruments*, vol. 85, no. 2, p. 023101, Feb. 2014.

[59]   K. K. Sharma, *Optics: principles and applications*. Amsterdam ; Boston: Academic Press, 2006.

[60]   D. Malacara, Ed., *Physical optics and light measurements*. Boston: Academic Press, 1988.

[61]   R.-Y. Yang, Y.-K. Su, M.-H. Weng, C.-Y. Hung, and H.-W. Wu, "Characteristics of coplanar waveguide on lithium niobate crystals as a microwave substrate," *J. Appl. Phys.*, vol. 101, no. 1, pp. 014101–014101–5, Jan. 2007.

[62]   M. A. Kemp, S. D. Kovaleski, B. T. Hutsel, A. Benwell, and J. M. Gahl, "Particle Swarm Optimization of Pulsed Power Circuit Models," *IEEE Trans. Plasma Sci.*, vol. 36, no. 5, pp. 2722 –2729, Oct. 2008.

[63]   J. VanGordon, "Hefner Model Parameters for Power IGBTs under Pulsed Power Conditions," Master of Science thesis, University of Missouri, Columbia, MO USA, 2010.

[64]   M. Yamada, N. Nada, M. Saitoh, and K. Watanabe, "First‐order quasi‐phase matched LiNbO3 waveguide periodically poled by applying an external field for efficient blue second‐harmonic generation," *Applied Physics Letters*, vol. 62, no. 5, pp. 435–436, Feb. 1993.

[65] R. Coelho and J. Debeau, "Properties of the tip-plane configuration," *Journal of Physics D: Applied Physics*, vol. 4, no. 9, pp. 1266–1280, Sep. 1971.

[66] The MathWorks, Inc., *MATLAB*. .

[67] J. H. Wilson, M. Beal-Hodges, and B. P. Keating, *Regression Analysis : Understanding and Building Business and Economic Models Using Excel*. [New York, N.Y.] [222 East 46th Street, New York, NY 10017]: Business Expert Press, 2012.

[68] A. Sommerfeld, "About the production of the continuous x-ray spectrum," *Proc Natl Acad Sci U S A*, vol. 15, no. 5, pp. 393–400, May 1929.

[69] E. Acosta, X. Llovet, and F. Salvat, "Monte Carlo simulation of bremsstrahlung emission by electrons," *Applied Physics Letters*, vol. 80, no. 17, pp. 3228–3230, Apr. 2002.

[70] P. J. Statham, "The generation, absorption and anisotropy of thick-target bremsstrahlung and implications for quantitative energy dispersive analysis," *X-Ray Spectrom.*, vol. 5, no. 3, pp. 154–168, Jul. 1976.

[71] E. Storm, "Calculated Bremsstrahlung Spectra from Thick Tungsten Targets," *Phys. Rev. A*, vol. 5, no. 6, pp. 2328–2338, Jun. 1972.

[72] J. G. Chervenak and A. Liuzzi, "Experimental thick-target bremsstrahlung spectra from electrons in the range 10 to 30 keV," *Phys. Rev. A*, vol. 12, no. 1, pp. 26–33, Jul. 1975.

[73] M. Aydinol, R. Hippler, I. McGregor, and H. Kleinpoppen, "Angular distribution of X-radiation following electron bombardment of free atoms," *J. Phys. B: At. Mol. Phys.*, vol. 13, no. 5, p. 989, Mar. 1980.

[74] J. A. Bearden and United States, *X-ray wavelengths and x-ray atomic energy levels*. Washington, D.C: U.S. Dept. of Commerce, National Bureau of Standards : For sale by the Supt. of Docs., U.S. G.P.O, 1967.

VITA

James "Jim" VanGordon was born on December 30, 1984 in Butler, Missouri, USA. He received his B.S. and M.S. in Electrical Engineering from the University of Missouri in May 2008 and December 2010, respectively. His M.S. thesis was entitled "Hefner Model Parameters for Power IGBTs under Pulsed Power Conditions" and was supported by Los Alamos National Laboratory. He will earn his Ph.D. in May 2014. His Ph.D. research was supported by the Nuclear Regulatory Commission, Qynergy, Inc., the Office of Naval Research, and Los Alamos National Laboratory.

Jim has presented his research at several international conferences and a national workshop. At the time of this work, he has co-authored at least 13 conference papers, two peer-reviewed journal papers, and has another journal paper in review. He has been awarded the 2010 High Voltage Association Student Excellence Award, 2012 University of Missouri Graduate Student Association Outstanding Graduate Student Award, 2012 Conference on the Application of Accelerators in Research and Industry Student Poster Award, and 2012 Review of Scientific Instruments Outstanding Referee.

Jim has been an active volunteer Lieutentant/EMT of the Boone County Fire Protection District where he began firefighting/EMS in 2005. He has also been a Technical Information Specialist for Missouri Task Force 1 Urban Search and Rescue Team since 2009. Jim married Monika Gołębiowska of Wrocław, Poland in September 2012. After graduation, Jim will be employed as a Physical Electronics Engineer for bioMérieux, Inc. in Hazelwood, Missouri.